Imperial College London

Characterisation, Enhancement and Impact of Temporal Intensity Contrast in Multi-Terawatt Laser Systems

James A. Fullalove
April 2023

Submitted in part fulfilment of the requirements for the degree of
Doctor of Philosophy of the Imperial College London, Department of Physics and
the Diploma of Imperial College, April 2023

Declaration

I submit for the award of Doctor of Philosophy of Imperial College London and hereby declare that this thesis is my own original work, unless specifically cited or referenced in this text.

The copyright of this thesis rests with the author. Unless otherwise indicated, its contents are licensed under a Creative Commons Attribution 4.0 International Licence (CC BY).
Under this licence, you may copy and redistribute the material in any medium or format for both commercial and non-commercial purposes. You may also create and distribute modified versions of the work. This on the condition that you credit the author.
When reusing or sharing this work, ensure you make the licence terms clear to others by naming the licence and linking to the licence text. Where a work has been adapted, you should indicate that the work has been changed and describe those changes.
Please seek permission from the copyright holder for uses of this work that are not included in this licence or permitted under UK Copyright Law.

James Fullalove, April 2023

Abstract

Unwanted features in high intensity, $> 10^{12}$ Wcm^{-2}, laser pulses such as discrete prepulses or spontaneous emission from laser amplifiers can pre-ionise a target before the arrival of the main pulse. This produces expanding "preplasmas" which can significantly alter the subsequent laser-matter interaction. Here we identify key sources of 'low-contrast' features in the temporal intensity profile of the Cerberus laser system at Imperial College arising from scattered light in chirped pulse amplification (CPA) stretcher and compressor subsystems and optical parametric amplifiers (OPA). To characterise these, we have developed an extended third order autocorrelator utilising cross-polarised wave gating, enabling 'artefact-free' pulse measurement. To suppress these unwanted features, we have developed techniques for spatially filtering and homogenising spatiotemporal distortions, including spatial chirp and angular dispersion from OPA stages. A contrast enhancement scheme using cylindrical dielectric hollow core fibres is shown to be a capable spatial filter at ∼180µJ, 1.2ps which also demonstrates transmission >75%, approaching that of conventional spatial filters, and is highly effective in removing astigmatism and spatial chirp. We also explored reintroduction of controlled discrete prepulses, and quantified their effect on electron and proton acceleration and x-rays generation from targets irradiated at relativistic intensities $> 10^{19}$ Wcm^{-2}. Experiments are presented investigating the interaction between >10 TW pulses and thin metallic foils. We observe ∼5 times enhancement in the maximum energy of accelerated protons by addition of a 2.75×10^{-4} relative contrast prepulse arriving 60ps before the main pulse, with evidence for self-focusing in the preplasma, to a predicted focal spot of ∼1.6µm. Finally, we describe development of an off-harmonic optical probe based on supercontinuum emission to investigate plasma dynamics close to the target surface. An "off wavelength" probe, with ∼600nm spectral width was generated from an aqueous ZnCl solution, and light centred at 630nm used to produce high contrast interferograms.

Contents

1 Introduction **1**

1.1 Oraganisation of Thesis 2

1.2 Contributions, Publications and Outputs of Thesis 5

2 Generating Short Optical Pulses **7**

2.1 Fundamentals of High Power Laser Systems 7

2.1.1 Chirped Pulse Amplification (CPA) 9

2.1.2 Solid State Amplification 11

2.1.3 Nonlinear Optics 12

2.2 Temporal-Intensity Pulse Contrast 16

2.2.1 Origin of Prepulse in a Laser System 16

2.2.2 Contrast Enhancement Techniques 20

3 Short Pulse Diagnostics **22**

3.1 Autocorrelation 23

3.2 Frequency-Resolved Optical Gating (FROG) 24

3.2.1 Cerberus FROG 25

3.3 Extended Third Order Autocorrelator (XTOAD) 29

3.3.1 XTOAD Diagnostic Overview 32

3.3.2 Results and Discussion 35

4 The Cerberus Laser System at Imperial College London **44**

4.1 Mode-locked Nd:Glass Master Oscillator 48

4.2 ps-OPA Pump Beamline 51

4.3 ps-OPA Stages . . . 58
4.3.1 ps-OPA Seed Pulse . . . 58
4.3.2 ps-OPA Pump Pulse . . . 59
4.3.3 ps-OPA Results . . . 60
4.4 ns-OPA Beamline . . . 65
4.5 ns-OPA Stages . . . 68
4.6 Nd:Glass Amplifier Beamline . . . 68

5 Contrast Enhancement Technique using Hollow Core Fibre 70
5.1 Experimental Setup . . . 74
5.2 Characterising Hollow Core Fibre as a Spatial Filter . . . 76
5.2.1 100 µm Diameter Fibre Characterisation . . . 77
5.2.2 200 µm Diameter Fibre Characterisation . . . 82
5.3 Characterising Hollow Core Fibre as as Spatiospectral filter . . . 88
5.4 Conclusion . . . 100

6 Laser-Plasma Interactions 103
6.1 The Pondermotive Force . . . 103
6.2 Target Normal Sheath Acceleration . . . 105
6.2.1 Influence of Contrast upon TNSA . . . 108

7 Target Areas 110
7.1 MAGPIE . . . 110
7.2 Multi-Terawatt Target Area . . . 111
7.2.1 Target Area Laser Diagnostics . . . 111
7.2.2 Cerberus Interferometry Beamline . . . 115

8 Effect of a Discrete Prepulse on Laser-Plasma Interactions 119
8.1 Cerberus Prepulser . . . 121
8.2 Effect of a Discrete Prepulse on Particle and X-ray Emission Spectra . . . 122
8.2.1 Results and Discussion . . . 126
8.3 Source Size Measurement . . . 143
8.3.1 X-Ray Source Size Measurements . . . 143

8.3.2 Proton Source Size Measurements . . . 151
8.4 Conclusion . . . 154

9 Supercontinuum-Source Based Optical Probe **156**
9.1 Supercontinuum Generation . . . 160
9.1.1 Filamentation in liquids . . . 161
9.2 Experimental Setup . . . 162
9.3 Supercontinuum Source Characterisation . . . 163
9.4 Wavelength Selectable Interferometry . . . 167
9.4.1 On-Shot Off-Harmonic Interferometry . . . 170
9.5 Conclusion and Further Work . . . 172

10 Conclusion **174**
10.1 Further Work: Phase Conjugate OPCPA Beamline . . . 175

Bibliography **176**

List of Tables

5.1 Attenuation length z_{att}, where $e^{-\alpha_{nm}z} \rightarrow e^{-1}$, for low order eigenmodes (figure 5.1) in hollow core fibre with core diameters of 100 µm, 120 µm and 200 µm. . . . 82

5.2 Spatial chirp parameterisation of the oscillator and ps-OPA stages before and after careful alignment to minimise spatial chirp. 93

5.3 Spatial chirp parametrisation before and after spatial filtering with a 100 µm diameter, 210 mm long cylindrical dielectric HCF. 94

8.1 Two-temperature fitting parameters, described in equation 8.2, for the measured x-ray spectrum spectra obtained by adding an artificial prepulse, with relative intensity contrast of 2.75×10^{-4}, at a relative time prior to the main Cerberus laser pulse, of focused intensity of $5\pm1\ \times10^{18}$ Wcm^{-2} (2 J, 750 fs), in interactions with 14 µm Al foils. 130

List of Figures

2.1 Layout of a simple two parallel diffraction grating Treacy compressor involved in CPA. 10

2.2 Diagram of the operation of the OPA process. A low intensity seed pulse is temporally and spatially overlapped with a high intensity, high frequency, pump wave in a nonlinear crystal. This corresponds to a transfer of energy from the pump to the seed and the production of a third, idler, wave produced as the frequency difference between pump and seed. 14

2.3 Typical temporal profile of a high power laser, illustrating commonly observed contrast features. Image credit: Nicholas Stuart [36]. 16

3.1 Schematic diagram of the Cerberus FROG 26

3.2 Example FROG data showing the measured and retrieved FROG traces. Upper left: measured taken with the Cerberus frog, upper right: analysed using the FROGed algorithm by Matthew Streeter [72], lower left: retrieved pulse vs time, lower right: retrieved pulse vs wavelength. The Frog retrieval error in this measurement was 0.012. 28

3.3 The formation of 'ghost' prepulses in a third order autocorrelator due to convolution of the first and second harmonics of a pulse with a trailing postpulse. A postpulse following the main pulse is initially suppressed by the intensity-dependent SHG process, however this postpulse remains during the correlation of the fundamental and 2ω beams to produce an artefact ahead of the main pulse in the THG signal. Image credit: Nicholas Stuart [36]. 31

3.4 Schematic diagram of the extended third-order autocorrelator diagnostic (XTOAD). 32

3.5 The temporal intensity profile of Cerberus laser OPCPA front end (15/12/2022), characterised using the XTOAD diagnostic up to a dynamic range of 10^{10}, over a temporal window ∼1.35 ns. Several features are evident on this plot, including three major prepulses; one at 249 ps at a relative contrast of 10^{-5}, concluded to be an artefact of the diagnostic, and two at 440 and 192 ps which are indicative of real prepulses, produced by double-passed optics in the laser beamline. The plot also shows a broad ∼ns-duration pedestal at a relative contrast of $\sim 10^{-9}$, produced by fluorescence in the front end ns-duration OPA stages and a triangular feature extending ∼ 200 ps ahead of the main pulse up to a relative contrast of 10^{-5}, characteristic of incoherent scattered light in CPA stretchers. 36

3.6 Artefact (grey) versus artefact free (red) contrast characterisation of the Cerberus front-end. A 10^{10} dynamic range is achieved in the X-TOAD. We can conclude that an 80 ps prepulse with 3×10^{4} contrast is a measurement artefact by comparison of two autocorrelator traces with and without a probe pulse contrast enhancement. 39

3.7 XTOAD photomultiplier tube response, measuring two pulses of the same energy, attenuated by two different factors. A region of linear response was identified between ∼0.02 to ∼1.5 V. 42

3.8 The measured attenuation factor for the 8 neutral density, centered at $\lambda_0 = 351$ nm, filters used to maintain the XTOAD signal within the linearity range of the PMT. 42

3.9 High dynamic range, 7.8×10^{11}, temporal intensity characterisation of the Cerberus laser system OPCPA front end (15/12/2022) measured with the XTOAD diagnostic 43

4.1 Simplified schematic diagram of the Cerberus laser system “front-end”. Seed pulses from an Nd:Glass master oscillator (GLX 200HP, Time Bandwidth Systems), are divided between two beamlines; a short pulse, 10 Hz ‘seed’ beamline and a ‘long pulse’ beamline which is further amplified by Nd:YLF gain storage amplifiers to pump two, two-stage OPAs. The stages are divided by an initial ‘ps-OPA’ (OPA1 and OPA2) and then a ‘ns-OPA’ (OPA3 and OPA4), separated by an Öffner-pattern stretcher, which provide the first $\sim 10^8$ gain. Final amplification of the main pulse, up to ∼1 J, occurs through a series of up to three Nd:Glass flashlamp amplifiers, before subsequent compression delivering up to ∼10 TW peak pulse power. 46

4.2 Schematic view of the Cerberus oscillator (GLX 200HP, Time Bandwidth Systems). A double-pumped (800 nm) Nd:Glass crystal amplifies light into a SESAM mode-locked optical cavity, generating a 70 MHz train of 5 nJ, ∼250 fs sech^2 pulses with a spectral bandwidth ∼4.7 nm. Image credit: Nicholas Stuart [36]. 48

4.3 Spectral profile of the Cerberus oscillator (GLX 200HP, Time Bandwidth Systems), centered at $\lambda_0 = 1053.5$ nm with a measured bandwidth of 4.7 nm. Note: The spectrometer used here (Oceanoptics USB4000) gave a +1.5 nm spectral offset. . . 49

4.4 Cerberus Nd:Glass master oscillator (GLX 200HP, Time Bandwidth Systems) frequency locking stability over a 25 hour operational period. Drifts in temperature over time were corrected using a piezoelectric stage attached to one of the cavity end mirrors kept the cavity frequency stable to $\pm 3.91\ Hz$ over 22.5 hours 50

4.5 The spectral profile of the pulse amplified by the front end regenerative amplifier. The amplifier is based on a linear optical cavity, centered around a diode pumped Nd:YLF gain module. Significant gain narrowing produced over 43 round passes within the cavity is compensated for by a low-finesse, 500 um thick intracavity etalon, which enhances the bandwidth and produces the central dip seen in the spectrum. 52

4.6 The oscilloscope trace of top) the regenerative amplifier rolling over into energy saturation bottom) oscillator pulse train, measured at ∼70 MHz 53

4.7 The total output energy and %RMS energy stability measured across ∼20 minutes of operation, with respect to the current applied across the Nd:YLF gain module at the centre of the Regen cavity. 53
4.8 The output energy stability of the Cerberus linear regenerative amplifier over 1 hour of operation, stable to <1% RMS. This figure displays the recorded output energy at a sampling rate of 1/400 pulses, or once per second. 54
4.9 The gain from the first Nd:YLF flashlamp pumped gain storage amplifier in the Cerberus pump chain. 55
4.10 Spatial profile of the amplified pump pulse a) before and b) after spatial filtering using a vacuum spatial filter (VSF). The telescope arrangement of the spatial filter inverts the spatial profile of the beam from a) to b). 56
4.11 FROG retrieval of the ps-OPA pump beam. Top left: the measured spectrogram obtained using the Cerberus FROG, top right: retrieved FROG trace from FROGed code, bottom left: temporal, and bottom right: spectral profiles of the retrieved FROG trace. Retrieval error of 0.014. 57
4.12 Schematic diagram of the ps-OPA stages at the front end of the Cerberus laser system. A ∼5 nJ pulse is amplified through two successive OPA stages for a total gain factor of $\sim 2 \times 10^6$. Image credit: Nicholas Stuart [36]. 58
4.13 FROG measurement of the Cerberus OPA seed pulse. Upper left: measured taken with the Cerberus frog, upper right: analysed using the FROGed algorithm by Matthew Streeter [72], lower left: retrieved pulse vs time, lower right: retrieved pulse vs wavelength. The Frog retrieval error in this measurement was 0.012. . . . 59
4.14 the amplified pulse energy and energy stability over ∼600 shots, obtained from OPA1 with respect to the pump energy. 61
4.15 the amplified pulse energy and energy stability over ∼600 shots, obtained from OPA2 with respect to the pump energy. 61
4.16 Spectral profiles of OPA1 with respect to increasing pump energy. 62
4.17 Spectral profiles of OPA1 with respect to increasing pump energy. 63
4.18 The signal energy of the ps-OPA stages, a) OPA1 and b) OPA2, over <1 hour operation. 64
4.19 Spatial profile VSF3 out, super-Gaussian 66

4.20 The performance of a 2-passed 9.5 mm diameter Nd:YLF flashlamp amplifier relative to the setting of the pulsed power drive system which controls the voltage applied across the flashlamps 67

5.1 Linear propagation, LP_{mn}, eigenmodes supported by cylindrical hollow waveguides (from Y. Gao et al. [108]) 73

5.2 A schematic diagram of the ps-OPA stages in the Cerberus laser system, with the addition of a temporary beampath for characterising hollow core fibre. The beam is image relayed from the output of OPA2 to the back focal length of a lens which focuses light into the hollow core fibre. 75

5.3 HCF mounted on translation stages 76

5.4 a) the spatial profile (taken as the viewfield of a Dataray, WinCamD-LCM – 1" CMOS Beam Profiler) of the image of the amplified signal pulse at the second stage of the OPAs, b) the OPA signal pulse spatial profile post filtering with 300 mm, a = 100 um hollow core fibre. 78

5.5 transmission efficiency of a 100 µm diameter, 250 mm long HCF with respect to the $2w$ beam diameter of a Gaussian beam injected at focus into the fibre. 79

5.6 Transmission efficiency of the signal of OPA2 through 100 µm diameter, 250 mm long HCF translated along the optical axis around a ∼64 diameter µm focal spot produced by an F/50 focused input. top) the diverging beam diameter, bottom) distance from focal spot. 79

5.7 The effect on measured transmission efficiency of small translation in the a) horizontal and b) vertical axes on the input of a beam into 300 mm HCF. 80

5.8 Spatial profile of HCF output with 2.3 mm z offset from the optimum input position, larger divergence at input increases the amount of the beam that is coupled into scattering modes - (profile from WinCamD-LCM). 81

5.9 Damage sustained by the input face of 100 µm diameter fibre due to the focused laser intensities at input over a period of ∼3 weeks. 82

5.10 Nearfield spatial profiles of the OPA2 signal beam a) before and b) after modal filtering using a 200 µm diameter, 300 mm long HCF. Here, the nearfield ellipticity was improved from 0.82 to 0.99. 83

5.11 Farfield spatial profiles of the OPA2 signal beam a) before and b) after modal filtering using a 200 µm diameter, 300 mm long HCF. 84

5.12 M^2 measurements, analysed with "laserbeamsize 1.9.4" by Scott Prahl [112], of the OPA2 signal beam a) before and b) after modal filtering using a 200 µm diameter, 300 mm long HCF. Significant astigmatism was present in the beam prior to modal filtering, which was successfully removed by the HCF. 85

5.13 The dependence of transmission efficiency through a 200 µm diameter, 300 mm long HCF with respect to translating the input along the optical axis, z, for an focused beam at input (∼F/100) with Rayleigh length ∼10 mm. 86

5.14 Transmission efficiency dependence for a 200 µm diameter, 300 mm long HCF by translating the input face of the fibre in the perpendicular axis, a)x and b)y, of the focused beam at input (F# ∼ 100). 87

5.15 Dynamic time warping (DTW) calibration used to callibrate a 2D imaging spectrometer using a reference spectrum obtained from an Oceanoptics usb2000+ spectrometer, compensating for a subtle aberration found in the 2D imaging spectrometer. Left: illustration of the DTW algorithm (image credit to XantaCross, Wikimedia commons). Right: DTW calibration for the 2D imaging spectrometer, comparing reference spectra of the Cerberus oscillator measured by both devices. . 90

5.16 Spatial chirp measurements of the output of the ps-OPA stages, a) oscillator, b) OPA1, c) OPA2 using a 2D imaging spectrometer. Black lines represent the peak intensity for slices along the image in position and wavelength, from which the linear fit (red lines) gives the spectral dispersion, $dx_0/d\lambda$ and frequency gradient $d\lambda_0/dx$. 92

5.17 Spatiospectral profile of the a) OPA1 and b) OPA2 signals after careful alignment to reduce the spatial chirp in the system. Black lines represent the peak intensity for slices along the image in position and wavelength, from which the linear fit (red lines) gives the spectral dispersion, $dx_0/d\lambda$ and frequency gradient $d\lambda_0/dx$. 93

5.18 The spatiospectral profile of OPA2 signal beam before (a) and after (b) spatial filtering with a 100 µm diameter, 210 mm long cylindrical dielectric HCF. In each figure the degree of linear spatial dispersion and frequency gradient is shown. . . . 94

5.19 The spatiospectral profile of OPA2 signal beam before (a) and after (b) spatial filtering with a 100 µm diameter, 125 mm long cylindrical dielectric HCF. Only the centre of each beam profile was selected using a ∼90 µm slit at the image plane of the fibre. Black lines represent the peak intensity for slices along the image in position and wavelength, from which the linear fit (red lines) gives the spectral dispersion, $dx_0/d\lambda$ and frequency gradient $d\lambda_0/dx$. 95

5.20 FROG retrieval of the OPA2 signal pulse. Top left: the measured spectrogram obtained using the Cerberus FROG, top right: retrieved FROG trace from FROGed code, obtained by mirroring the measured trace around delay = 0 from t = $0 \rightarrow -\infty$, which gave a retrieval error of 0.025. Bottom left: temporal, and bottom right: spectral profiles of the retrieved FROG trace. 98

5.21 FROG retrieval of the OPA2 signal pulse, post filtering with 200 µm diameter, 300 mm long HCF. Top left: the measured spectrogram obtained using the Cerberus FROG, top right: retrieved FROG trace from FROGed code, obtained by mirroring the measured trace around delay = 0 from t = $0 \rightarrow -\infty$, which gave a retrieval error of 0.023. Bottom left: temporal, and bottom right: spectral profiles of the retrieved FROG trace. 99

6.1 An outline of the TNSA mechanism. As the leading edge of a high power laser pulse is focused onto a thin (∼5 - 50 µm thick) metallic foil, the surface of the foil is ionised by intensities greater than 10^{12} Wcm^{-2}, creating an expanding preplasma at the front of the target. Electrons pondermotively accelerated by the main pulse may then travel through the target as 'hot electrons', escaping from the rear side and establishing a high electric field between the electron beam and the rear of the target due to charge seperation. This electric field will ionise the rear surface, accelerating ions in the direction pointing normal to the target. From Roth et al. [4] 106

7.1 SE: Calibration of peak voltage measured by the compressor energy meter against directly measured energy. Each data point x represents a single shot, this data was taken over a time scale of several weeks 112

7.2 Schematic diagram of the single-shot, second order autocorrelator in the multi-terawatt target area. A small portion of the compressed laser pulse is taken and split between two beamlines, which are then cylindrically focused to overlap inside of a 1.5 mm thick beta-barium borate (BBO) non-linear crystal. The crossing angle between the two pulses encodes a time delay onto the SHG signal from the nonlinear stage, from which we can measure the temporal duration of an experimental pulse. Image credit: Samuel Eardley [15]. 114

7.3 Single-shot, second order SHG autocorrelation of the Cerberus 10 Hz OPCPA front-end, with a FWHM pulse duration measured at 680 fs, assuming a Gaussian temporal pulse shape. 114

7.4 Farfield image of the Cerberus main pulse, taken using a microscope objective at the centre of the multi-terawatt target chamber. 115

7.5 Schematic diagram of the Cerberus optical probe beamline and the Nomarski interferometer. An optical probe beam passes through the centre of the main target chamber, at which point the beam is imaged by a series of optics onto a CCD camera. A Wollaston prism, visible polariser combination is used to divide the beam into two and interfere a region of the optical probe which passed through the interaction region with an undisturbed part of the spatial profile. Image credit: Samuel Giltrap [125]. 117

7.6 Top a) snapshot of a Cerberus Nomarski interferogram, this image has been contrast enhanced to clearly show interference fringes. Bottom b) relative contrast, taken from the unmodified interferogram, of the fringes produced by the interferometer Wollaston prism, rotated at 45°. 118

8.1 Schematic view of Cerberus Prepulser, which adds an arbitrary discrete prepulse with a relative intensity from 1:10^{-5} to 1:1, to the main pulse of the Cerberus laser system at a relative temporal position of up to 10 ns. Image credit: Samuel Eardley [15]. 121

8.2 Diagram of the multi-terawatt lab target chamber setup for characterising the emission spectra of charged particles and x-rays for interactions between a $\sim 10^{18}$ Wcm^{-2} intensity focused laser pulse with an artificial $\sim 10^{-5}$ relative contrast prepulse included in the temporal intensity profile, incident at an angle of 15°, with 14 µm Al foils. Two magnetic spectrometers were included, one in the axis normal to the target rear surface to measure protons accelerated by the TNSA mechanism and one along the laser axis to measure the spectrum of electrons directly accelerated by the laser beam, with a multi-layer image plate stack to characterise the x-ray spectrum in the laser axis. Additionally, a single-hit x-ray photon counter (Andor DX434-BN) was aligned with line of sight to the target. An optical probe beam provided plasma interferometry measurements normal to the front surface of the target. Image credit: Samuel Eardley [15]. 124

8.3 Proton energy spectra obtained by adding an artificial prepulse, with relative intensity contrast of 2.75×10^{-4}, at a relative time prior to the main Cerberus laser pulse, of focused intensity of $5 \pm 1 \times 10^{18}$ Wcm^{-2} (2 J, 750 fs), in interactions with 14 µm Al foils. A clear increase in the maximum particle energy can be seen for prepulse delays around 60 ps. A low energy cutoff is imposed for proton energies <1 MeV. 127

8.4 The maximum recorded proton energies obtained by adding an artificial prepulse, with relative intensity contrast of 2.75×10^{-4}, at a relative time prior to the main Cerberus laser pulse, of focused intensity of $5 \pm 1 \times 10^{18}$ Wcm^{-2} (2 J, 750 fs), in interactions with 14 µm Al foils. The maximum particle energy is observed to peak for prepulse with up to 60 ps relative to the main pulse. 128

8.5 Electron energy spectra obtained by adding an artificial prepulse, with relative intensity contrast of 2.75×10^{-4}, at a relative time prior to the main Cerberus laser pulse, of focused intensity of $5 \pm 1 \times 10^{18}$ Wcm^{-2} (2 J, 750 fs), in interactions with 14 µm Al foils. A clear enhancement of the electron spectrum can be seen for prepulse delays around 60 ps. 129

8.6 The a) maximum energy and b) hot electron temperature of electron spectra obtained by adding an artificial prepulse, with relative intensity contrast of 2.75×10^{-4}, at a relative time prior to the main Cerberus laser pulse, of focused intensity of $5\pm1\ \times10^{18}$ Wcm^{-2} (2 J, 750 fs), in interactions with 14 µm Al foils. The maximum electron energy was observed for a prepulse 60 ps before the main pulse, whilst T_{eHOT} was seen to peak for a prepulse 50 ps before the main pulse. 129

8.7 The total energy in the hard (>10 keV) x-ray spectrum obtained by adding an artificial prepulse, with relative intensity contrast of 2.75×10^{-4}, at specific time ahead of the Ceberus main laser pulse ($5\pm1\ \times10^{18}$ Wcm^{-2}), calculated by integrating the image stack x-ray PSL with respect to photon energy. 131

8.8 The temporal profile of Cerberus OPCPA front end, characterised with an effective dynamic range of $\sim10^8$, using a third order autocorrelator, the XTOAD described in section 3.3, without XPW contrast enhancement engaged. Several important features can be seen on this plot including a) the discrete prepulse artificially introduced by the Cerberus Prepulser, at 65 ps before the main pulse with a relative contrast of 2.75×10^{-4} and a temporal FWHM of 3.7 ps. Two additional discrete prepulses are also observed by the scan, b) a 10^{-5} artefact produced in the diagnostic and c) a $\sim 10^{-6}$ relative contrast produced by internal reflections inside of the Cerberus prepulser. The broad 10^{-7} relative contrast pedestal is produced by fluorescence in the front end ns-OPA stages, at 10^{-7} the pedestal is an order of magnitude more intense than is typically measured for the system, this likely a factor of this contrast scan and not representative of typical system performance. Additionally, a 200 ps duration broad 'triangular' pedestal is visible up to a relative contrast of 10^{-4} due to uncompressible incoherent scattered light inside of the front end CPA stretcher. 133

8.9 Interferograms showing the plasma expansion from the front of a 15 µm thick Al foil at -8ps relative to the Cerberus main pulse for two shots, a) (4.9±1.2)×10^{18} Wcm^{-2} focused intensity, with no additional prepulse and b) (5.2±1.3) × 10^{18} Wcm^{-2} where an artificial prepulse, with relative intensity contrast of 2.75×10^{-4}, was included 60ps ahead of the Ceberus main laser pulse. Both a) and b) show bright self emission close to the interaction region which obscures density measurements close to the face of the target whilst b) shows significant diffraction from the optical probe beam across the front surface of the target. 135

8.10 Electron density at the front of a a 15 µm Al foil, 8 ps before the arrival of the main pulse (4.9±1.2×10^{18} Wcm^{-2}). The electron density profile is comprised of a composite of 1D Helios hydrodynamic simulations (blue) and experimental interferometry results (orange). The threshold for laser self-focusing in the preplasma (pink) as well as the relativistic critical surface (green) are also indicated. 137

8.11 Composite electron density profile density at the front of a 15 µm Al foil, 8 ps before the arrival of the main pulse (5.2±1.3 ×10^{18} Wcm^{-2}) where a prepulse of 2.75×10^{-4} contrast was introduced at -60 ps relative to the main pulse. The electron density profile is comprised of combined 1D Helios hydrodynamic simulations (purple) and interferometry results (blue). The threshold for self-focusing, taken from the exponential fit of interferometry data between 65 - 90 µm from the target surface (pink), as well as the relativistic critical surface (neon green) are also indicated. 138

8.12 Helios model of electron density in a 14 µm thick Al foil, showing the radial expansion of preplasma produced by a 4.9±1.2×10^{18} Wcm^{-2} focused intensity laser pulse. The main pulse arrives on this figure at 0.25 ns. 139

8.13 PROPACEOS Al opacities [17] 140

8.14 The radial velocity of preplsma expanding from the front of the target at -8 ps relative to the main pulse, calculated from the radial distance of the plasma from the target, given a specific expansion time, for two shots, a) (4.9±1.2)×10^{18} Wcm^{-2} focused intensity, with no additional prepulse and b) (5.2±1.3)×10^{18} Wcm^{-2} where an artificial prepulse, with relative intensity contrast of 2.75×10^{-4}, was included 60ps ahead of the Ceberus main laser pulse. 141

8.15 Knife-edge source size measurement technique. The size of the penumbral region, R_p, is determined by the source size, S, where S' is the footprint of the source at a viewing angle θ, p is the distance from the source to the knife-edge and q is the distance from the knife-edge to the detector. 144

8.16 X-ray source size diagnostic layout, two tungsten carbide ball bearings (WCBBs) were used to create a sharp knife-edge for prenumbral measurements. X-rays produced at TCC were detected using Fuji BAS-MS image plate, with signal to noise improvement provided by two (∼45 mT) Neodymium (Nd) plate magnets to deflect charged particles. 145

8.17 Image plate scan showing the penumbral shadows cast by two, orthogonally oriented tungsten carbide ball-bearing after a Cerberus shot upon 15 µm thick aluminium. Streaks can be seen upon the image plate caused by charged particles. The black box on the left image shows the direction in which the lineout was taken. The lineout shows the real data (red line) along with a smoothed profile (blue line) which assisted in measuring the transition width. The penumbra width was estimated to be 11.5×1.5 pixels, yielding a measured source size of 34.9×4.8 µm. 146

8.18 Source-size measurements of x-rays produced in the interaction between the Cerberus main laser pulse ($\sim 10^{18}$ Wcm^{-2}) and both 15 µm (blue), and 5 µm (red) thick Al foils. 147

8.19 Source-size measurements of x-rays produced in the interaction between the Cerberus main laser pulse ($\sim 10^{18}$ Wcm^{-2}) and 15 µm thick Al foil, without a prepulse (blue) and with the inclusion of a discrete 2×10^{-4} relative contrast prepulse, ∼50 ps before the main beam (red). 149

8.20 Source-size measurements of x-rays produced in the interaction between the Cerberus main laser pulse ($\sim 10^{18}$ Wcm^{-2}) and 5 µm thick Al foil, without a prepulse (blue) and with the inclusion of a discrete 2×10^{-4} relative contrast prepulse, ∼50 ps before the main beam (red). 150

8.21 (a) the spatial profile, recorded using one layer of RCF (Gafchromic EBT2) of a proton beam generated by the Cerberus main laser pulse ($\sim 10^{18}$ Wcm^{-2}) and 15 µm thick Al foil. The grid pattern on (a) was produced by a woven copper mesh, placed between the Al foil and the RCF. A lineout on (a) shows a penumbral transition, (b), which can be measured to extract the effective proton source size given at that point in the spatial profile of the proton beam. 152

8.22 Source size measurements, in units of µm, of a proton beam accelerated by a 3.4 J, 6.8×10^{18} Wcm^{-2} focused intensity laser pulse onto 15 µm Al foil. The a) vertical and b) horizontal source sizes were observed to vary across the spatial profile of the proton beam. 153

8.23 Source size measurements, in units of µm, of a proton beam accelerated by a 9.8×10^{18} focused intensity laser pulse with a $\sim2\times10^{-4}$ relative contrast prepulse, 50 ps prior, pulse onto 15 µm Al foil. The a) vertical and b) horizontal source sizes were observed to vary across the spatial profile of the proton beam. 154

9.1 Optical probe image of a laser-target interaction with a 15 µm thick Al foil viewed edge on. The probe light was centered at 527 nm, with a pulse duration of ∼500 fs. Figure a) shows the target geometry prior to the shot, whilst figure b) shows the optical probe image ∼10 ps before the main pulse arrives, the interaction is obscured by bright self-emission from the target, integrated over 100ms by the camera exposure time. 157

9.2 TR: Layout of the setup used to acquire spectra for analysis of the supercontinuum source's spectral stability. A holographic diffuser was used to spatially smooth the pulses in order to isolate the overall pulse-to-pulse spectral stability. Image credit: Timothy Robinson [138] 159

9.3 Total energy generated in a supercontinuum source with ∼600 nm spectral range, with respect to the input energy of a 1054 nm, 500fs driving pulse. The supercontinuum generation efficiency was observed to begin to saturate at high input energies, with a predicted saturated energy of 710±60 µJ. 164

9.4 The spectral profile of a supercontinuum generated by a ∼40 mJ energy, 500 fs FHWM duration, pulse centered at 1054 nm. The black line represents the 20-point moving average supercontinuum spectrum, averaged measured over 50 shots, whilst the shaded area shows the standard deviation at each wavelength. 165

9.5 Comparison between the spectra measured for supercontinuum generation with a ∼40 mJ pulse energy (red), where an HR mirror was used to remove residual >1 µm light, and the spectrum generated for ∼10 mJ pulse energy, where IR light was not removed (grey). By comparing the two profiles, it is clear that an HR mirror introduces spectral fringes into the supercontinuum profile. 166

9.6 The measured spatial profiles (WinCamD-LCM) of the a) input λ_0= 1054 nm, ∼80 GW input light and the b) generated supercontinuum, collimated and propagated a distance of ∼1 m. The 'triangular' profile on a) is produced by imperfect spatial filtering in a VSF stage, where a imprint on the spatial apodiser is left on the beam. 167

9.7 Optical probe images captured with the supercontinuum source. These images were taken following a Cerberus laser shot onto 15 µm Al foil, with the target remnants seen in frame. Optical probe images were recorded with a) the full supercontinuum spectrum, b) a 527 nm interference filter and c) a 630 nm interference filter. No fringes were produced on images a) and b) as the interferometer's Wollaston prism rotated out for these shots. 169

9.8 Top: contrast enhanced snapshot of figure 9.7c, to clearly show interference fringes. Bottom: the relative contrast of a 120 µm lineout from the target surface from figure 9.7c. 170

9.9 Off-harmonic optical probe images of a Cerberus laser shot onto a 15 µm thick Al foil. a) pre-shot background image, and b) the optical probe image on-shot with a relative timing to approximately coincide with the arrival of the laser pulse. . . . 171

9.10 Self-emission spectrum measured from a Cerberus shot onto a 15 µm Al foil. A bright self-emission peak is seen at the second harmonic (527 nm) as well as a small peak above background, centered at 656 nm. 172

10.1 Overview of the phase-conjugate OPCPA principle, taking the idler from an OPA as the signal for amplification, as the idler has the opposite sign chirp to the seed (-ve) it can be recompressed by a positive dispersion grating pair. Image credit: Nicholas Stuart [36]. 177

Chapter 1

Introduction

Lasers are exceptional tools for scientific experiments, able to deliver discrete packets of energy, or continuous beams, for a wide range of specified experimental requirements. This is due in large part to the broad parameter space that different laser architecture can cover. Specific laser systems are often optimised for parameters including peak intensity, pulselength, repetition rate, average power, spectral bandwidth and temporal pulse shape which fulfil experimental roles in a vast number of high intensity use cases from research experiments in nuclear fusion [1], high energy density laboratory astrophysics [2], compact particle acceleration [3]–[5], probing extreme processes [6], radiography [7] to industrial applications [8]. High power laser systems in particular, are typically optimised for high focused intensities and high temporal contrast, the ratio between the peak intensity of the laser pulse and the unwanted background noise. These factors allow us to reach high electric field and relativistic intensity requirements for laser-matter experiments, particularly where the laser is used as a driver for particle acceleration, where the laser intensity determines much of the energy spectrum and flux of generated particles as well as the acceleration regime [9].

Large national facility scale laser systems such as Orion at AWE Aldermaston or Vulcan at the Central Laser Facility repeatedly deliver focused intensities of the order 10^{21} Wcm^{-2}, each is built to similar design with a peak pulse energy of approximately 500 J over a temporal pulse duration of 500 fs using hybrid OPCPA-Nd:Glass architecture [10], [11]. The front-end design of Vulcan and Orion is similar to that of the Cerberus laser system at Imperial College London, which as a university based laser system, designed to explore laser-matter interactions at an intensity-space

of approximately 10^{19} Wcm^{-2}. This intensity means that the Cerberus laser is an appropriate system for experiments involving x-ray, electron and ion beam acceleration and can also be used as a platform to develop new techniques and diagnostics relevant to these larger systems.

Ion acceleration is commonly achieved via laser interaction with a thin (∼10 µm) metallic foils, such as aluminium. However, laser driven ionisation of such a target has been observed to occur at intensities of the order 10^{9} - 10^{12} Wcm^{-2} [12]. Low intensity discrete pulses (arriving before the main peak of the laser) or poorly resolved contrast above this threshold can pre-ionise the target, producing a 'preplasma' which expands before the arrival of the main pulse and which may significantly alter the interaction and even prevent ion acceleration from occurring. Poor temperal contrast has previously been identified to arise from processes including scattered light in chirped pulse amplification (CPA) stretcher and compressor subsystems [13] as well as parametric fluorescence in optical parametric amplifiers [14]. As laser development moves towards higher peak power and greater focused intensities, we expose ourselves to increasing vulnerabilities stemming from low intensity background noise generated early in the amplification chain which can then be amplified above a target's ionisation threshold. The next generation of high power laser systems [11], such as the Extreme Light Infrastructure (ELI) projects or the The Vulcan 2020 upgrade project are moving to exawatt (10^{15} W) peak powers. Characterising the temporal intensity contrast of a laser pulse, and the effect that this has on plasma physics experiments is therefore of paramount importance, for current experimental work and also for future-proofing the next generation of laser technology.

1.1 Oraganisation of Thesis

This project aimed to characterise the temporal intensity contrast of the Cerberus laser system at Imperial College London, particularly investigating sources in the system which may contribute to degradation in the contrast. By identifying these sources in the laser system, we can take steps to prevent these detrimental effects from manifesting or develop "filtering" or noise suppression techniques specific to these components in the system. Finally, for an ideal 'ultra-high' contrast beam there may be utility in reintroducing well controlled and characterised low contrast elements of the temporal beam profile, where our ability to improve the contrast of the pulse also allows us to intentionally manipulate those low-contrast elements, and their influence on the subsequent

plasma dynamics.

The Cerberus laser at Imperial College is an OPCPA/flashlamp pumped Nd:Glass hybrid architecture system built towards design specifications of high temporal-intensity contrast ratio, scalability and flexibility in providing drivers and probe capabilities for a range of experiments. The system, so named Cerberus for its three beamlines, divides output between a 'long-pulse' 20 J, 1.4 ns beamline for plasma diagnostics, a high power 10 TW, 500 fs main beam for laser-target interactions and a interferometry probe beamline in the second harmonic, or off-harmonic wavelengths. A full description of the Cerberus laser can be found in chapter 4, which includes an overview of the laser as well as examples of the operational performance of the system. As an Nd:Glass hybrid-OPCPA system, Cerberus' architecture bears similarity to larger facility class laser systems such as the Orion laser at AWE Aldermaston and the Vulcan laser at the Central Laser Facility, the so-called hybrid approach of primary OPCPA front end with flashlamp pumped Nd:Glass amplifiers at the final stage to bring the beam to full power. This allows the laser system to function in the manner of a developmental test bed for technologies directly relevant to the advance of high power systems elsewhere in the country.

In chapter 3 we will discuss the development of two diagnostics for characterising the Cerberus laser pulse, firstly a scanning frequency resolved optical gating (FROG) diagnostic, designed and built by the author for characterising pulses involved in picosecond (ps) time domain optical parametric amplification. We will also discuss an extended third order autocorrelator (X-TOAD), utilising a cross-polarised wave generation (XPW) contrast enhancement technique for 'artefact-free' third order autocorrelation, designed and built by Dr. Nicholas Stuart with additional characterisation and dynamic range improvements by the author. The temporal contrast characterisation and analysis presented in this chapter was additionally performed by the author.

In chapter 5, we present a technique for laser beam spatial mode filtering using few 10s of cm lengths of air-filled hollow core fibre with core diameters in the few 100 micron range. Hollow core fibre is an effective tool for spatially filtering and homogenising spatiotemporal distortions, including spatial chirp and angular dispersion, in a ps-domain laser pulse and also for improving the pointing stability of a beam as it propagates downstream through a complex, multi-element alignment sensitive optical beamlines. The investigation in this chapter was conducted solely by the author, with supply of two dielectric cylindrical waveguides kindly provided by Prof. John

Tisch and with helpful advice at the start of the project by Dr. Daniel Walke.

In chapter 8 we discuss two laser-contrast sensitive experiments, involving use of the Cerberus laser system at high focused intensities to generate secondary sources of protons, electrons and x-rays from thin ∼few µm aluminium foils. The first experiment, described in 8.2, investigated the effect of introducing a discrete low-contrast prepulse to the temporal intensity profile, measuring the effect this has on the emission spectra of charged particles (mainly protons and electrons) and x-rays. This experiment was principally designed by Dr. Samuel Eardley [15], with the role of the author mainly consisting of aligning and optimising the Cerberus laser system for the experiment. After this initial experiment, however a further investigation began, led by the author which first involved a detailed re-characterisation of the artificial prepulse (using the XTOAD diagnostic, discussed in chapter 3.3) and additional simulations and interferometry measurements of the preplasma electron densities prior to the arrival of the main laser pulse. Initial electron density retrieval using the image analysis routine "Interpret" developed by Jason Cole [16] was supplemented in regions where the interometry data could not be retrieved using Helios 4.4.0, a 1D radiation-magnetohydrodynamics code [17]. The data presented in section 8.2.1 is a combination of this Helios modelling and a careful re-analysis of the interferometry data taken by Dr. Samuel Eardley to eliminate artefacts in the electron density profile due to noise in the interferogram. The analysis of the Helios and interferometry data was completed in joint collaboration by Samuel Eardley and the author. The second experiment described in chapter 8, section 8.3, was principally led by Dr. George Rowland [18], characterised the source size for x-rays and protons generated by laser-plasma interactions with the Cerberus laser system for several different target geometries. As with the previous experiment, the author was primarily involved in delivering well characterised laser pulses to target of repeated specified energy and pulse duration.

Finally, in chapter 9, we present progress on developing an 'off-harmonic optical probe' for laser-plasma interferometry at wavelengths not obscured by bright second-harmonic self-emission at the laser-plasma interaction region. A liquid-cell supercontinuum source, previously demonstated on the system at much lower energy by Dr. Timothy Robinson [19] was reproduced and characterised for higher peak power driving pulses. The viability of laser-plasma interferometry with this supercontinuum source was then investigated in a laser-target interaction, with assistance by Dr. Samuel Eardley and Dr. Nicholas Dover.

Funding for this studentship was secured from an EPSRC iCASE award, with additional funding provided by the AWE for transfer of research outputs between AWE Aldermaston and Imperial College London.

1.2 Contributions, Publications and Outputs of Thesis

Over the course of this PhD, a significant fraction of my work has also been in fulfilment of other theses from students in our experimental group. Results obtained in collaboration with the author have led to the publication of Theses from Dr. Samuel Eardley [15] and Dr. George Rowland [18]. In the second case, the author was responsible for key areas of beamline design, including synchronising the Cerberus laser system long pulse beamline with the optical probe pulse and an external Nd:YAG laser system for investigating laser-launched flyers. Additionally, the delivery of diagnostic laser pulses has resulted in a recent publication [20], with an additional paper submitted and pending peer review. Finally, the author has been involved in an experiment investigating ion acceleration from the front surface of nanostructed subtrate targets, which has influenced further investigations in this area.

Publications involving the author:

- D.R. Russell, G.C. Burdiak, J.J. Carroll-Nellenback, J.W.D. Halliday, J.D. Hare, S. Merlini, L.G. Suttle, V. Valenzuela-Villaseca, S.J. Eardley, J.A. Fullalove, G.C. Rowland, R.A. Smith, A. Frank, P. Hartigan, A.L. Velikovich, J.P. Chittenden, and S.V. Lebedev, "Perpendicular Subcritical Shock Structure in a Collisional Plasma Experiment", Phys. Rev. Lett. 129, 225001 (Published 22 November 2022) [20]

Submitted, pending review:

- Russell, Danny; Burdiak, Guy; Carroll-Nellenback, Jonathan; Halliday, Jack; Hare, Jack; Merlini, Stefano; Suttle, Lee; Valenzuela-Villaseca, Vicente; Eardly, Sam; Fullalove, James; Rowland, George; Smith, Roland; Frank, Adam; Hartigan, Patrick; Velikovich, Alexander; Chittenden, Jeremy and Lebedev, Sergey, "Observation of subcritical shocks in a collisional laboratory plasma: scale dependence near the resistive length, " Journal of Plasma Physics (submitted 04 April 2023)

Papers currently in preparation:

- N.H. Stuart, J.A. Fullalove, D.I. Hillier, N.W. Hopps and R.A. Smith, "Efficient and Stable Cross-Polarised Wave Generation of Picosecond Pulses for Artefact-free Measurement of Laser Pulse Contrast, " in preparation for submission to Applied Physics B
- J.A. Fullalove and R.A. Smith, "A Spatiospectral Filtering Technique using Hollow Core Fibre for Contrast Enhancement of ps-doman OPA," in preparation for submission to Optics Letters
- S.J. Eardley, J.A. Fullalove, G.R. Rowland and R.A. Smith, "Effect of Low Intensity Prepulse on Particle and X-ray emission from Foil Targets," in preparation for submission to Applied Physics Letters

Chapter 2

Generating Short Optical Pulses

2.1 Fundamentals of High Power Laser Systems

In order to achieve a high focused intensity at target, the design of high power laser systems seeks to optimise the peak power, spectral bandwidth and temporal pulse shape.

From the perspective of high peak power laser systems, developments in laser technology have marked major milestones and spurred leaps in the maximum focused intensities for experiments. From the demonstration of the first pulsed system [21] to mode-locked oscillators capable of generating picosecond duration short pulses [22], [23], techniques such as chirped pulse amplification (CPA) [24] have facilitated access to even higher peak powers. Today, there are more than fifty systems worldwide of 'petawatt-class' or above in commissioning or operation [11] able to access intense physical regimes for experiments.

A laser pulse will propagate with a minimum pulse duration given by the time-bandwidth product

$$TBP = \Delta\nu \cdot \tau_0 \tag{2.1}$$

where $\Delta\nu$ is the spectral bandwidth of a pulse and τ_0 is the minimum pulse duration corresponding to that spectral bandwidth. The time-bandwidth product is a specific factor depending on the pulse profile, where $TBP \simeq 0.44$ for Gaussian pulse profiles.

One of the simplest ways we can approximately relate the electric field of a one-dimensional

linearly polarised plane-wave, propagating through space, is

$$E(z,t) = A_0(t)\exp[i(\omega t - kz)] \tag{2.2}$$

where k is the wavenumber in a material of refractive index n, where $k = \frac{n(\omega)\omega}{c}$, and ω is the instantaneous angular frequency of the optical carrier wave. For a Gaussian pulse, the time varying field envelope is given in the form

$$A_0(t) = A\exp\left(-t^2/2\tau_0^2\right) \tag{2.3}$$

The full width at half maximum intensity profile can be found from this equation, therefore, as $\Delta\tau_0 = \tau_0\sqrt{4ln(2)}$. The evolution of a Gaussian pulse as it propagates through space is determined by the spectral phase, a factor of the form $\varphi(\omega) = \exp(-ik(\omega)z)$. we can Taylor expand the phase of a laser about the central frequency, ω_0, to understand how that pulse propagates

$$\varphi(\omega) = \varphi_0 + \frac{d\varphi}{d\omega}\Big|_0(\omega-\omega_0) + \frac{1}{2}\frac{d^2\varphi}{d\omega^2}\Big|_0(\omega-\omega_0)^2 + \frac{1}{6}\frac{d^3\varphi}{d\omega^3}\Big|_0(\omega-\omega_0)^3 + ... \tag{2.4}$$

where $\varphi_0 = -k(\omega)z$. For long propagation distances we can approximate the following relations:

$$\frac{d\varphi}{d\omega}\Big|_0 = \varphi^{(1)} = -\tau_{group}, \tag{2.5}$$

The group time delay (GTD), τ_{group} here, is related to the group velocity, the speed of the pulse envelope propagating distance of z, as $\tau_{group} = z/v_{group}$. We can also find,

$$\frac{d^2\varphi}{d\omega^2}\Big|_0 = \varphi^{(2)} = -\frac{d\tau_{group}}{d\omega} \simeq \left(\frac{d\omega}{dt}\right)^{-1}, \tag{2.6}$$

$\varphi^{(2)}$ also gives group time delay dispersion (GTDD), This is equivalent to the group velocity dispersion and described the variation in the GTD with respect to frequency or wavelength.

$$D_\lambda = \frac{2\pi c}{\lambda^2}\,\frac{d^2\varphi}{d\omega^2}\Big|_0 = \left(\frac{2\pi c}{\lambda^2}\right)\varphi^{(2)} \tag{2.7}$$

Third order dispersion is often parameterised as

$$D_{3,\lambda} = \left(\frac{2\pi c}{\lambda^2}\right)^2 \left.\frac{d^3\varphi}{d\omega^3}\right|_0 = \left(\frac{2\pi c}{\lambda^2}\right)^2 \varphi^{(3)} \tag{2.8}$$

typically presented in units of $\mathrm{fs/nm^2}$.

One way the phase of a pulse can be manipulated is via the CPA technique, where second order phase produces a linear 'chirp' allowing temporal stretching of the pulse and access to higher amplification regimes.

2.1.1 Chirped Pulse Amplification (CPA)

When the laser induced damage threshold (LIDT) is exceeded, damage may occur through thermal heating of conduction band electrons or laser ablation [25]. Bulk damage (e.g. to a laser rod) in these cases is usually induced by self-focussing, where the nonlinear refractive index of a material is modified by intense EM fields, the so-called optical Kerr effect [26], proportionally to the intensity ($\Delta n = n_2 I$). An intense Gaussian spatial profile induces spatial variation transverse to the optical axis, where the change in refractive index is greatest at the centre of the pulse and decreases radially outwards and produces a lens-like variation in the refractive index causing a pulse with a Gaussian spatial profile to 'self-focus' inside of the propagation medium. The LIDT of optics presents a challenge for laser amplification, imposing a limit on the maximum pulse intensity of the system. In order to reduce the likelihood of damaging the system the intensity of the beam must therefore be carefully managed or in some cases significantly reduced. Up-expansion of the beam spatially and amplifying in progressively larger and larger aperture gain media is one possible solution however this can quickly become prohibitively expensive and technically unwieldy.

The most commonly used method to circumvent nonlinear optical damage in a short pulse (sub picosecond to 10s of femtosecond) laser system is chirped pulse amplification (CPA), first demonstrated for a laser system by Strickland and Mourou [24], which couples path-dependent spectral dispersion to the pulsewidth. CPA works in three stages, an initially short (ps to fs) laser pulse is temporally broadened – stretched, safely amplified below the LIDT and then recompressed to high peak power. The pulse is either stretched or compressed by manipulating the group velocity dispersion (GVD) of the pulse, either with material properties of a medium through which light

propagates (e.g. in an optical fibre or block of glass) or a combination of pairs of optics such as prisms or diffraction gratings. In the latter case, light is spectrally dispersed by the first optic and recollimated by the second, a geometric view (figure 2.1) intuitively shows frequency-dependent time delay of the the pulse, with the instantaneous frequency either rising or falling along the temporal profile, positively or negatively chirped.

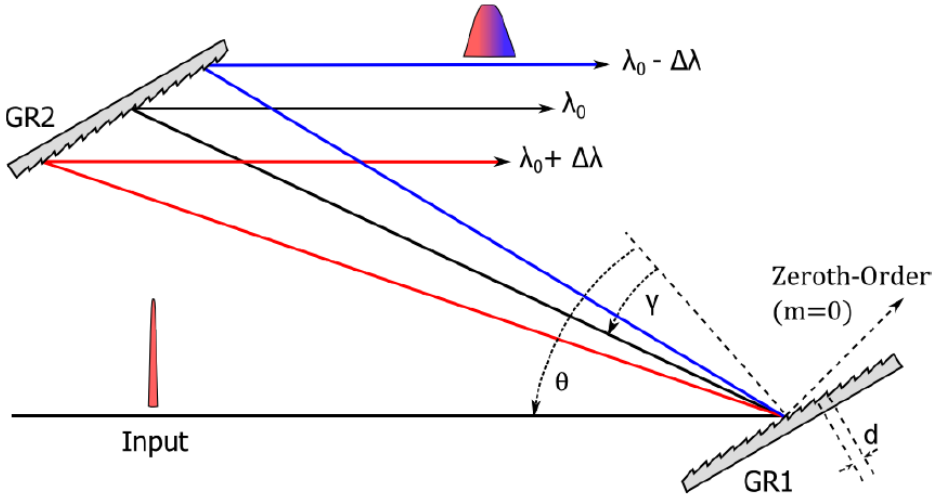


Figure 2.1: Layout of a simple two parallel diffraction grating Treacy compressor involved in CPA.

There are several common instances of two-grating CPA subsystems stretchers such as Treacy [27], Martinez [28] or Öffner [29], [30] designs. The first case, a Treacy compressor, is the simplest example; this consists of two diffraction gratings arranged such that the chromatic dispersion of light incident upon the first is compensated for by the second. Light of central wavelength λ_0, incident upon a diffraction grating of groove separation d, at an incidence angle θ, is determined by orders of constructive interference;

$$m\lambda_0 = d\left(\sin\theta + \sin\gamma\right), \tag{2.9}$$

where m is the diffraction order and γ is the angle of the diffracted ray to the normal of the grating. Therefore, as shown in figure 2.1, for a Treacy compressor the path length of longer wavelengths is greater than short wavelength light producing a temporal walkoff of the laser pulse from high to low frequencies, or negative chirp. In terms of the spectral phase, we can

write

$$\varphi(\omega) = -\frac{1}{2}\varphi^{(2)}(\omega - \omega_0)^2 + \frac{1}{2}(\gamma_2 G_{eff})(\omega - \omega_0)^2 \tag{2.10}$$

where G_{eff} is the effective separation of the two diffraction gratings. The second term of this expression gives us the group time delay dispersion, $\gamma_2 G_{eff}$, from which we may derive the additional pulse duration due to this temporal walkoff [31], Δt, given by,

$$\Delta t = \frac{G_{eff}\lambda_0 \Delta\lambda}{c(dcos\gamma)^2}, \tag{2.11}$$

where $\Delta\lambda$ is the bandwidth of the laser pulse. Often in laser systems the compressor is subsequently 'double-passed' by retroreflecting the beam in the opposite direction back along the optical path to further temporally stretch the pulse and compensate for spatial chirp that manifests due to chromatic dispersion.

Other grating geometries, for instance Martinez and Öffner, positively chirp a pulse with the insertion of a telescope between the two diffraction gratings. In typical laser systems a pulse is stretched in a Martinez or Öffner initially producing a positively chirped pulse that can later be recompressed in a Treacy compressor which does not possess material components such as telescopic lenses that may incur damage. The minimum possible compressed pulse duration is related by the time-bandwidth product, determined by the pulse envelope at FWHM. A Gaussian pulse has a time bandwidth product of ≈ 0.441, while for a sech^2 pulse the time-bandwidth product is ≈ 0.315. By combination of CPA techniques with amplification using solid state gain media or optical parametric amplification, CPA has allowed high power lasers to access increasingly high power regimes since its demonstration in 1985. High power lasers have been demonstrated to amplify to the petawatt level, potentially as high as 5.4 PW [32], accessing successively more extreme interaction regimes as a consequence.

2.1.2 Solid State Amplification

Laser gain media amplifies laser light by process of stimulated emission, where a material is excited to a higher energy state and, instead of spontaneously decaying to a lower energy state, the decay is stimulated by the interaction of a 'seed' photon. Population inversion is achieved by pumping the gain media to excite it to this higher energy state, typically using optical sources such

as external lasers, flashlamps or diode pumping in the case of solid state gain media. The energy levels of the gain media that electrons can transition between determine the possible emission frequencies, called the gain bandwidth. Where the wavelength of light propagating through gain media overlaps with the gain bandwidth stimulated emission can occur.

However the process is also known to be inherently inefficient, much of the pump energy is not well absorbed or lost to heating the crystal lattice. This loss in efficiency arises due to the "quantum defect", which is the energy difference between pump photon and laser photon due to the difference in the transitions between energy bands in the gain media. Moreover, as this process relies upon a system which will over time decay, amplified spontaneous emission (ASE) occurs in the media when it is in its excited state where the spontaneous transition from a high energy state to a lower band is greatly increased by the degree of population inversion of the gain media. The relaxation time in which the population falls to $1/e$ of its excited value is often of the order a few μs, for example Ti:Sapphire at 800 nm exists at an upper level for around 3.2 μs [33]. This ASE commonly contributes to a noise background of the laser pulse.

Gain bandwidth in a real world system is both finite and non-uniform, for amplification of broadband pulses the gain bandwidth can spectrally reshape the pulse by preferentially amplifying around the central lasing frequency over the wings of the pulse spectrum. This process, known as gain-narrowing, leads to a reduction in the bandwidth of the laser and reduces the temporal compressibility of a laser, reflected in the time-bandwidth product. In the case of high gain, bandwidth reduction can be significant, for example Nd:YLF which can limit minimum pulse duration to ∼1ps. There do however exist gain media such as titanium-doped sapphire (Ti:S), which has a sufficiently broad gain bandwidth to achieve fs-domain pulses. For instance, systems such as the Gemini laser at the Central Laser Facility in Oxfordshire are specified at a 30 fs pulse duration [10]. Gain-narrowing effects can be mitigated using pulse-shaping techniques or alternative amplification methods capable of preserving bandwidth, for example optical parametric amplification.

2.1.3 Nonlinear Optics

Nonlinear amplification techniques potentially provide "inversion free" broadband amplification with less background noise levels due to ASE from solid state amplification. At high intensities

materials react nonlinearly to light propagating through them. Whilst this can result in undesirable effects such as self-focusing, it can also be a potent tool for optical techniques. A high order expansion of the material polarisation (dipole moment per unit volume), P(E), yields;

$$P(E) = \epsilon_0(\chi^{(0)}E + \chi^{(2)}E^2 + \chi^{(3)}E^3 + \chi^{(4)}E^4 + ...), \tag{2.12}$$

where χ^n is the electric susceptibility of the nth order, ϵ_0 is the permittivity of free space and in the presence of an electric field E. Nonlinear processes include second harmonic generation (SHG), Third Harmonic Generation (THG), Sum and Difference Frequency Generation (SFG and DFG).

Optical Parametric Amplification (OPA)

OPA is a second-order process dependent upon the total electromagnetic field and material polarisation defined by the $\chi^{(2)}$ coefficient. Second-order processes are a consequence of a three-wave process, where the electric field at a point in the crystal is constituted of multiple waves with distinct frequencies. Due to the second order material polarization, energy can be coupled from one wave into another, providing a mechanism by which a so-called pump wave can transfer energy into a signal wave. OPA can be referred to as difference frequency generation (DFG) as in a non-degenerate case where the pump and signal are not harmonics of one-another, the difference in frequency leads to the third wave in the three-wave process:

$$\omega_p = \omega_s + \omega_i, \tag{2.13}$$

where the three waves are denoted as p, the high energy, high frequency pump wave, s, the amplified signal, and i, the residual idler with frequency determined by the difference between the other two waves.

The parametric nature of this process means that ideally no energy is coupled into the gain medium, however wavelength-dependent material refractive index can limit the efficiency of OPA. Differences in dispersion at different wavelengths cause the phase difference between the pump and signal to accrue, even causing the transfer to energy to reverse when the waves are π radians

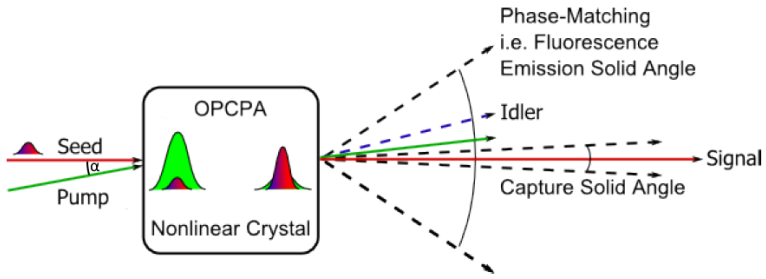


Figure 2.2: Diagram of the operation of the OPA process. A low intensity seed pulse is temporally and spatially overlapped with a high intensity, high frequency, pump wave in a nonlinear crystal. This corresponds to a transfer of energy from the pump to the seed and the production of a third, idler, wave produced as the frequency difference between pump and seed.

out of phase. The phase matching condition is satisfied when

$$\hbar \boldsymbol{k_s} + \hbar \boldsymbol{k_i} = \hbar \boldsymbol{k_p}. \tag{2.14}$$

To enforce this condition, birefringent crystals which are tuned to minimise the difference in the refractive indices of signal and pump waves propagating along the fast and slow axes are typically used to implement an OPA.

For wave-vectors of corresponding signals, this condition can be imposed by propagating the seed and pump beams at a noncollinear angle, α, through the crystal (figure 2.2), useful especially in the case of amplifying broadband signals where the phase-matching condition becomes

$$2k_p k_s \cos\alpha = k_p^2 + k_s^2 – k_i^2. \tag{2.15}$$

Therefore the finite bandwidth of the signal pulse, reflected in variation of k_s does not break this condition.

The OPA process may yield very high gain stages, a total of 10^5 at the front end of the Cerberus laser, and is therefore suitable for initial amplification of an oscillator signal starting from the ∼few nJ level. In high power laser systems OPA can be combined with CPA (OPCPA) in front end amplification stages where the pulse is stretched before further amplification via OPA. Due to a low noise floor and broad spectral acceptance associated with OPA this can result in generation of mJ level broadband pulses starting from a few nJ seed.

Self Phase Modulation

Another nonlinear optical process, involving $\chi^{(3)}$ nonlinearity, is the optical Kerr effect [26], where the refractive index of a material is modified by the intensity of a pulse propagating through that material due to the combination of the ordinary refractive index, n_0, and the nonlinear index, n_2, as

$$n = n_0 + n_2 I \tag{2.16}$$

The optical Kerr effect can result in self focusing due to variation in the refractive index across the spatial intensity profile of a Gaussian laser pulse approximating lens-like behaviour. Additionally, a change in the refractive index of the medium will modulate the phase of the pulse propagating through it. From the instantaneous phase of a laser pulse, $\varphi(t) = \omega t - kz$, and $k = n(\omega)\frac{\omega}{c}$, we can see that a modification of the refractive index modulates the phase of the optical wave carrier as

$$\phi = -\omega_0 n_2 I(t) z/c \tag{2.17}$$

For SPM of a pulse with a Gaussian temporal pulse-shape with intensity, I_0, and a FWHM pulse duration, $2\sqrt{ln2}\tau$, a shift in the instantaneous frequency, ω_0, is equivalent to

$$\omega(t) \simeq \omega_0 + \frac{4\pi L_{spm} n_2 I_0}{\lambda_0 \tau} t \tag{2.18}$$

Where L_{spm}, is the propagation length corresponding to a phase change at the peak of the pulse by 1 radian, $L_{spm} \simeq c/\omega_0 |n_2| I_0$.

The laser B integral, the total nonlinear phase shift a beam experiences due to the change in the intensity-dependent nonlinear refractive index, can be used to estimate an approximate threshold for problematic nonlinear effects to emerge. Laser systems are typically designed to limit the accumulated B integral to <3. The B-integral can be calculated for a pulse travelling through a material for a given distance, z, as

$$B = \frac{2\pi}{\lambda_0} \int n_2 I(z) dz \tag{2.19}$$

2.2 Temporal-Intensity Pulse Contrast

High power lasers can act as compact particle accelerators, often used in experiments as drivers for x-ray radiation, high energy electrons, protons and ions and neutrons [3], [5], [34]. One of the main mechanisms for ion acceleration is via target normal sheath acceleration (TNSA), described in chapter 6. The efficiency of TNSA depends upon the incident laser intensity and the target thickness. In addition to this, a steep density gradient on the rear surface of the target is also important to reduce ion density scale lengths [35]. Pre-ionisation by poor temporal intensity contrast may lead to significant preplasma formation and expansion before the arrival of the main pulse which can prevent efficient ion acceleration.

2.2.1 Origin of Prepulse in a Laser System

Contrast degradation arises from several different sources in a high power laser system which, as seen in figure 2.3, each produce distinctive features on the temporal profile of the laser pulse. These include discrete pulses due to back-reflections from optics, a *ns*-duration noise pedestal from parametric amplifiers and an exponential (or triangular on a logarithmic plot) feature at a relative contrast up to 10^{-5} resulting from residual phase terms as a by-product of CPA. Temporal intensity contrast is commonly measured using third order autocorrelation techniques, described in chapter 3.

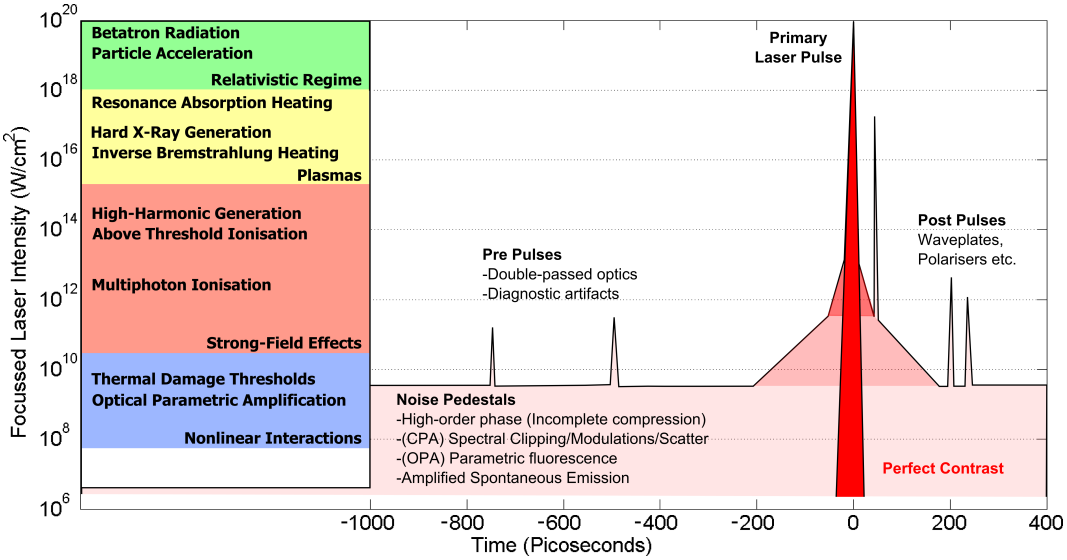


Figure 2.3: Typical temporal profile of a high power laser, illustrating commonly observed contrast features. Image credit: Nicholas Stuart [36].

Amplified Spontaneous Emission

As described in section 2.1.2, ASE is produced due to the spontaneous transition of electrons in population-inverted gain media to a lower level. ASE commonly originates in solid-state amplifiers but is also seeded at the first stages of laser oscillators [37], this background radiation is subsequently amplified by additional solid-state amplifiers leading to an ASE-pedestal with a temporal duration of up to ∼100 µs before the main pulse. ASE-pedestals commonly satisfy the ablation threshold for metallic foils with focussed intensities of order 10^9 to 10^{12} Wcm^{-2}. ASE above the ionisation threshold can produce this effect on a scale of ns before the arrival of the main pulse, the resultant preplasma forming an exponential density gradient extending hundreds of microns in front of the intended interaction surface [38].

Discrete Prepulses

A fraction of the light which is internally reflected rather than transmitted though thin optics such as waveplates or polarisers can cause post-pulses delayed behind the main beam a distance equal to the optical thickness of the optic. In the case however where elements of an optical chain are double-passed, back-reflections back along the beampath instead then propagate ahead of the main beam.

Post-pulses may additionally be transmitted ahead of the main pulse due to the Fourier symmetry within the final stage of compression. If the main pulse of a laser is sufficiently stretched, as before compression, it may temporally overlap and interfere with a post-pulse. If propagating through a medium this will result in self-phase modulation (SPM) through the optical Kerr effect. Intensity modulation of a stretched pulse directly correlates to a spectral modulation due to chirp and therefore when the pulse is recompressed, the Fourier transform performed by the compressor will result in two satellite pulses, a prepulse and post-pulse, either side of the main pulse [39], [40].

CPA Pedestal

A distinctive triangular pedestal is near-ubiquitously observed across many high power laser systems, including prominent facility systems ([36], [41]–[44]), with a 30-50 ps FWHM to a relative contrast ratio of up to 10^{-4}. This pedestal is often well above the threshold for field

ionisation and can also produce significant heating or ablation of the target. Due to its duration, this may result in severe modulation of the initial conditions ahead of the interaction with the main pulse [41].

Investigations have shown the pedestal originates as a result of scatter and surface irregularities from large optics in an imaging stretcher [41], consistent with theoretical predictions of high frequency spectral phase modulation [45]. The temporal profile of the triangular pedestal can be predicted due to the sum contributions of spectral phase noise from each optic in a stretcher [45], however other optics in a system contribute a negligible amount compared to diffractive optics, particularly diffraction gratings, towards the magnitude of the pedestal.

The phase noise contributions of a diffraction grating with spatially varying small-scale surface irregularities $\delta z(x)$ has been shown [46] to be related by

$$\delta\phi(\omega) = \frac{4\pi}{\lambda(x)\cos\gamma}\delta z(x), \tag{2.20}$$

which introduces an additional exponential term, $\propto \exp(i\overline{\delta z(x)}\ 2k/\cos\gamma)$, to the electric field.

Individual wavelength components within the beam scatter from the diffraction gratings within a range of angles around the main diffraction order which correspond to longer and shorter path lengths through the stretcher. The temporal profile of a wavelength component reveals a noise pedestal of scattered light exponentially rising at the base either side of that component. When the full spectrum of the pulse is considered this therefore forms incoherent spectral noise beneath the chirped pulse. Larger angles of scatter result in a broader noise pedestal, however wide angle scatter falls beyond the acceptance angle for the stretcher optics and subsequent optics in the system, limiting the temporal window of the noise pedestal.

Imaging stretchers, such as the Martinez or Öffner, are particularly vulnerable to scatter in this way. These systems relay the image of the first diffraction grating, and therefore the scattered light, further down the beampath. This increases the acceptance angle for scattered light, increasing the magnitude and duration of the contrast pedestal.

High Order Phase and Angular Divergence

Some elements of a laser system may introduce phase terms into the main pulse which cannot be compensated for and lead to temporal lengthening or asymmetry. Such incompressible phase

takes the form of high order phase terms such as third order dispersion or incoherent phase noise which act to either reduce the compressibility of the main pulse or introduce a distinctive and significant prepulse pedestal. Further broadening of the main pulse occurs in the case where the pulse exceeds the B-integral threshold in media. CPA subsystems are typically employed for manipulating only the second order phase of a pulse without the use of an active high-order phase control system (e.g. a dazzler), incompressible phase noise due to SPM therefore will broaden the final pulse [47].

High order phase terms originate due to chromatic dispersion through optical components or residual third order dispersion from CPA subsystems due to antiparallelism between diffractive optics [48], [49]. The architecture of CPA systems imposes strict alignment requirements as small angular deviations in the alignment of dispersive optics, such as diffraction gratings, have been shown to introduce pulse-front tilt [50], phase shift [51] and incompressible high order phase. Poor spatial quality contributes to non-ideal ray paths in a stretcher system, causing parts of the beam to acquire non-linear chirp terms that may not be properly compensated by the compressor [52].

Spatiotemporal couplings manifest from both spatial and temporal dependence on spectral components of the pulse, for example in the case of residual angular divergence from CPA subsystems [48], [49], [53] or from nonlinear amplification stages [54]. These couplings manifest most strongly as pulse duration of the laser decreases, a consequence of an increasingly broad bandwidth, therefore becoming increasingly prevalent in high power laser systems. In particular, noncollinear optical parametric amplification (n-OPA), due to the mismatch between the pulse fronts of the signal and pump pulses, has been shown to impose spatiospectral effects such as spatial chirp, angular dispersion and pulse front tilt in cases where the physical length of the pulses ($u \times \tau$) is less than the diameter of the beam [54]. Whilst spatiotemporal/spatiospectral distortions are often negligible in many parts of the front end of a laser system due to the often small beam size, these effects become more prevalent post-amplification and can limit the final intensities brought to target.

2.2.2 Contrast Enhancement Techniques

Due to the great influence of intensity contrast on laser interactions, there has been much effort to improve the contrast of a laser pulse by either inhibiting the formation of the contrast pedestal or by filtering prepulse-components from the beam. Optical shuttering with fast Pockels cells, nonlinear temporal enhancement using SHG and cross polarized wave generation (XPW) or relativistic filtering methods such as plasma mirrors work in the latter way; techniques that gate or attenuate specific components of a pulse profile. Meanwhile, an understanding of how prepulse components originate can inform the design of a high power laser system by either engineering out these sources or investigating alternate high-contrast system architectures.

Scatter from stray dust particles in a system has been shown to degrade the spatial quality of a beam and, in CPA subsystems, introduce incoherent phase noise. Cleaning diffraction gratings has been proven a simple and markedly effective way of maintaining contrast [41]. Indeed, careful selection of the optics in stretcher systems for good surface quality [55], or low manufacture-defect diffraction gratings [46], [56] go a long way to improve the overall contrast of the system. Additionally, maintaining the surfaces of optics reduces back-reflections, anti-reflection coatings and wedged optics are also widely used for the same effect.

The diameter of pulses propagating through CPA stretches has also recently been shown to mitigate the formation of the characteristic CPA pedestal. Analytical modelling by Roeder et al. [57], has shown that incoherent scatter and phase noise can be reduced by increasing the beam diameter relative to the size of the optics through either a folded or an unfolded stretcher design.

Pockels cells are optical shutters which actively filter the temporal intensity profile by gating light through the system within short (>1ns), electronically defined, intervals. When a high DC voltage is applied across the cell it acts as a half waveplate. In combination with a polariser it rejects light at the initial polarisation of the beam, only when the Pockels cell is active is light transmitted. The rise-time of Pockels cell drivers can be of ns-duration, as such Pockels cells are often used to enhance contrast by suppressing the long ASE pedestal or unamplified prepulses arriving well ahead of the main pulse [58].

Nonlinear techniques such as SHG are intensity dependent, their efficiency being greatest at the most intense parts of a pulse and suppressing low-intensities. Cross-polarised wave generation (XPW) is a third order nonlinear process which yields a wave polarised perpendicularly to the

input [59], [60]. The generated wave scales nonlinearly, relative to the intensity of the original pulse cubed, therefore enhancing the contrast of the pulse. Via this process, an intensity contrast of $10^{-10}\ Wcm^{-2}$ has been demonstrated for a Ti:Sapphire 1.2 mJ, 42 fs system [60]. This process is however limited by low efficiencies (10% in the referenced instance) and is often unsuitable at high intensities due to optical damage and unwanted nonlinearity in solid media.

Plasma mirrors are a high intensity solution to contrast enhancement, designed to only reflect the most intense portion of a pulse. Light is loosely focused onto an otherwise transmissive surface, typically a dielectric [61], with a field ionisation threshold only reached by the most intense parts of the pulse. Prepulse elements ariving onto the mirror prior to ionisation are transmitted whilst the thin plasma layer that forms from the leading edge will reflect the remainder of the beam from the critical surface. Plasma mirrors have been shown to enable large focused intensities with very high levels of contrast [62] however these also introduce significant loss at the final stage before the interaction and, due to their size and complexity requirements, can be beyond the scope for inclusion into smaller or lower power systems.

Choice of amplifier has a large effect upon contrast. The long timescale µs - ns ASE pedestal present from flashlamp-pumped solid-state amplifiers is avoided with short pump pulse OPA as the primary form of amplification. OPA stages do not impose gain-narrowing, increasing the transform-limited pulse duration, and due to their nonlinear process amplification only occurs when both seed and pump overlap within the crystal, allowing for exact temporal windowing of the gain to limit fluorescence.

Chapter 3

Short Pulse Diagnostics

The implicit challenge of temporally characterising a "short" pulse is that, much like the flash of a camera, the exposure or probe must also be on the timescale of the event, or ideally shorter in order to resolve details of the pulse envelope as well as the overall duration. As the event in this instance is the temporal profile of a laser, which is often by design as short as possible (on the order of picoseconds to femtoseconds), it becomes challenging to capture the time evolution of a pulse accurately. Short (ps to hundreds of fs domain) and ultrashort (few fs) pulses, with femtosecond timescale durations, are too fast to be characterised by conventional electronic detectors such as photodiodes with rise/fall times on nanosecond to few 10s of ps timescales [63].

In this chapter we will discuss temporal intensity pulse characterisation techniques using intensity autocorrelation, as well as two new diagnostics which have been developed on the Cerberus laser system. Firstly, a scanning FROG was designed and built by the author for characterising pulses involved in ps-domain optical parametric amplification stages, with pulse lengths varying from $\sim$1 - 10 ps, and with spectral bandwidths varying from $\sim$0.6 - $>$10 nm. We will also discuss a an extended third order autocorrelator (X-TOAD), designed and built by Nicholas Stuart with additional characterisation and dynamic range improvements by the author, presenting a high contrast ($> 10^{11}$), artefact-free method of characterising laser pulse temporal intensity through utilisation of a cross-polarised wave (XPW) contrast enhancement technique.

3.1 Autocorrelation

Intensity autocorrelation has become a widespread technique for characterising ps-duration, or shorter, pulses; first developed in 1967 [64], autocorrelation introduces a gating of two pulses (often replicas of the same pulse created with a beam splitter) with a relative time delay between each other, overlapped in space and time, in a nonlinear crystal or other non linear process. A nonlinear process occurs most efficiently only when the pulses are overlapped, therefore from the intensity response to varying delay, the temporal duration of the pulse, assumed to be symmetric and ideally of known shape, most typically Gaussian, can be reconstructed. Designs of autocorrelators involve different $\chi^{(2)}$ and $\chi^{(3)}$ processes such as polarisation rotation or second harmonic generation (SHG) [65], [66]. The retrieved trace from a second order autocorrelator is given by the correlation of two pulses, each identical but one time gated with a known delay,

$$E_{sig}(t,\tau) \propto E(t)E(t-\tau), \tag{3.1}$$

for a Gaussian pulse, where τ is the relative delay between the reference and the gate pulse, the duration of the pulse being measured can be shown to be a factor $\sqrt{2}$ less than the second order autocorrelation trace.

However, autocorrelation correlates a pulse with itself and is therefore a time symmetric process for "simple" 2nd order non-linear methods. Not only does this assume an inherently symmetric temporal pulse profile but from an autocorrelated trace temporal features that occur before or after the main laser pulse cannot be distinguished. This means that information from complex temporal profiles such as low intensity prepulses or the effects of high order phase are not uniquely resolved. Additionally, autocorrelation does not yield the temporal phase of the pulse, information often valuable in optimisation and control of short pulse and ultrafast systems. Additionally, due to the convolution of the reference and gate pulse, autocorrelation results in a measured signal pulse with a broader FWHM pulse duration than the pulse we want to measure. We are required to make an assumption of the temporal shape of our reference in order to determine the FWHM pulse duration at input. The relationship between the FWHM duration of the autocorrelator signal, Δt_{ac}, and the input pulse is

$$\Delta t_{Gauss} = \frac{\Delta t_{ac}}{1.411} \tag{3.2}$$

$$\Delta t_{Sech^2} = \frac{\Delta t_{ac}}{1.543} \tag{3.3}$$

for pulses with a Gaussian or Sech^2 profile respectively.

Autocorrelators can be designed as "scanning", where the relative delay between the reference and gating pulse is determined by adjusting their relative path length using a linear translation stage, or "single-shot", in which case, for SHG-autocorrelators the delay varies across the spatial profile of the signal pulse, determined by the crossing angle of two fundamental beams. Scanning autocorrelators are less practical for low repetition rate systems (<10 Hz) due to the time a scan would take. For single-shot systems, or for systems where it is important to measure the temporal profile of a specific shot, single-shot autocorrelators are used. Here, the reference pulses are split and cylindrically focused through the nonlinear crystal, where the crossing angle imposes the relative delay. The temporal window of a scanning autocorrelator is determined by the crossing angle, θ,

$$\Delta t|_{max} = \frac{\gamma L_D sin(\theta/2)}{c} \tag{3.4}$$

where γ is a pulse shape dependent factor and L_D is the width of the detector.

A Single-shot autocorrelator used as an on-shot diagnostic for characterising the compressed pulse duration of the Cerberus laser system is described in section 7.2.1.

3.2 Frequency-Resolved Optical Gating (FROG)

The simple addition of a 2D imaging spectrometer to spectrally resolve a second-order autocorrelation trace led to the development of Frequency-Resolved Optical Gating (FROG). A FROG is able to simultaneously resolve the temporal and frequency domain, and analysis of a FROG trace allows us to characterise not only the temporal intensity profile but also the spectral phase of a laser pulse. A good overview of the diagnostic, can be found in [67]. The FROG was designed to measure short (few-ps to sub-ps) pulse durations, and has been shown to be effective at characterising pulses even down to the attosecond (sub-fs) timescale [68]. There are other conceptually similar designs to the FROG such as GRENOUILLE [69] or diagnostics for similar purpose such as the SPIDER [70] which uses a temporal interferogram in concert with a known spectrogram.

For a FROG based upon an SHG autocorrelator device, the measured FROG trace of a pulse is

$$I_{FROG}(\omega,\tau) = \left| \int_{\infty}^{\infty} E(t)E(t-\tau)exp(-i\omega t)\ dt \right|^2 \tag{3.5}$$

for a pulse with instantaneous frequency ω. As with autocorrelation, the retrieved SHG-FROG trace is time-symmetric and therefore requires additional characterisation to resolve the direction of time ambiguity. SHG-FROGs are able to reconstruct traces of low energy pulses (>5 pJ) with a low noise floor due to overdetermination of the pulse (a FROG trace is an N×N array from which we measure N intensity and N phase points) [67].

Extracting both the pulse intensity and phase from FROG trace is a two-dimensional phase retrieval problem, in typical processes solved algorithmically by making an initial guess of the electric field and comparing that to the retrieved FROG trace, calculating an error based on the difference between the measured and retrieved traces. The retrieval algorithm iterates to reduce this error until the simulated electric field converges to fit the observed data to within some specified tolerance.

3.2.1 Cerberus FROG

A scanning SHG-FROG was designed and built by the author for measuring pulses in the ps-OPA stages of the Cerberus laser system, described in detail in chapter 4.3. The diagnostic was intended to be able to characterise the seed, pump and signal beamlines of the ps-OPA stages, therefore the design requirements for the diagnostic were set by the pulse parameters; a minimum energy requirement of <5 nJ at 250 fs, which is temporally stretched and amplified over two successive stages to 180 µJ, with a 1.2 ps pulse duration and a maximum bandwidth <15 nm. We were also particularly interested in high order phase in the pump beamline which has a bandwidth of ∼0.6 nm and a FHWM pulse duration of ∼10 ps. A schematic diagram of this diagnostic is shown in figure 3.1. An SHG-autocorrelator was chosen for simplicity as well as the low nonlinear interaction threshold of SHG (<1 pJ [71]). This diagnostic has been used to measure the pulses with input parameters of <5 nJ pulse energy and 1.2 ps duration.

A beam propagating into the FROG may first be apodised using a 2 mm diameter serrated aperture, to enforce a beam size at input which produces a known focal volume further down the diagnostic and to reduce the effect of pointing instabilities in the input beam, before it is

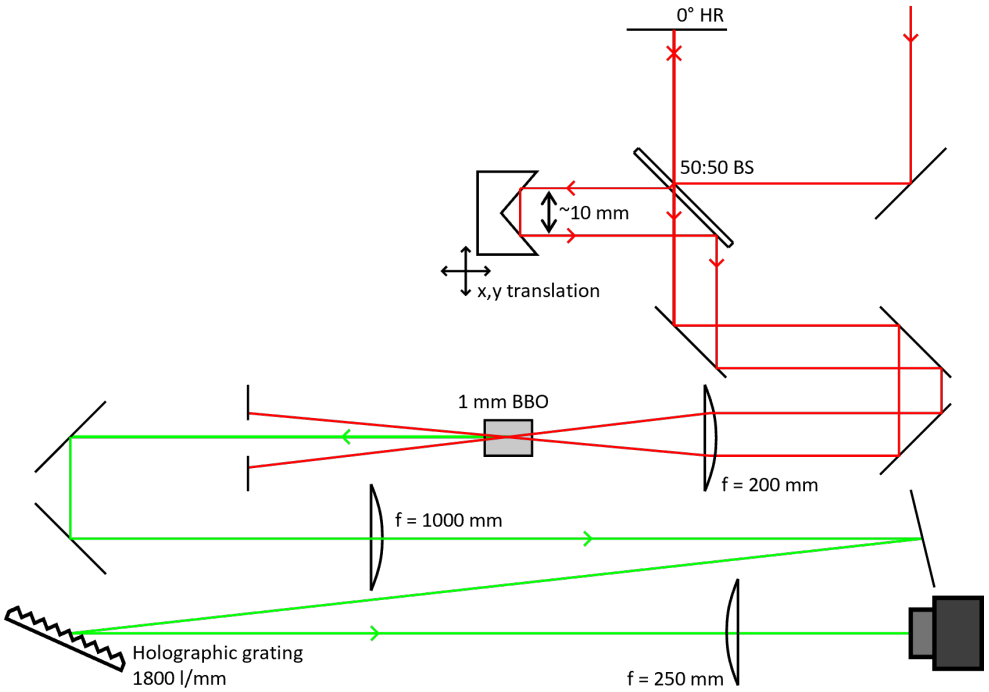


Figure 3.1: Schematic diagram of the Cerberus FROG

split using a 50:50 beamsplitter into two beamlines, both the transmitted and reflected beams are retroreflected back to the beamsplitter, however a hollow roof prism mirror (THORLABS 1×1", protected silver) is used to introduce spatial separation between the beamlines. The beamsplitter reflection is from one side of this optic, therefore the initially transmitted pulse was expected to propagate twice the distance through the substrate. Whilst some degree of dispersion due to the beamsplitter substrate is expected, the pulses we aim to measure are relatively low bandwidth so dispersion is not expected to be significant. The roof mirror is mounted on a two-axis translation stage, able to adjust the beam seperation and the relative timing between the two pulses. A dovetail translation stage in the axis orthogonal to the incoming beam may be used to vary the beam separation by up to ∼10 mm to optimise the interaction region between the two beams in the nonlinear crystal and the spatial separation between them and the SHG signal. A motorised translation stage (Thorlabs MT1-Z8) controls the relative delay between the two pulses. With a maximum travel distance of 12 mm, this affords the diagnostic a temporal window of ∼80 ps. The two beams are focused by a ϕ1", f = 200 mm PCX lens to be spatially overlapped within a 6x6 mm aperture, 1mm thick type I BBO crystal, cut at 23.4°, AR coated at 515+1030 nm. For a pulse with an input beam waist of ∼2 mm at $1/e^2$, this focusing geometry was chosen for a Rayleigh length of ∼14.6 mm and an interaction region of approximately 5.7 mm, both far

larger than the crystal length in order to minimise spatial effects in the SHG signal due to lateral walkoff between the two fundamental pulses. The SHG signal produced at overlap is spatially separated from the fundamental beams due to the crossing angle imposed by the roof mirror and the focusing lens, to reduce background noise the fundamental beams are blocked by an aperture down stream from the SHG crystal.

The spectrometer portion of the Cerberus FROG was designed with the condition that it should resolve the spectral profiles of pulses with bandwidth ranging from <0.6 nm to <12 nm. The spectrometer was designed to maximise the resolution, whilst focusing the bandwidth onto the active area of the detector (12 bit camera - Allied vision Alvium 1800 U-158m), $L_D = 4.98 \times 3.74$ mm (pixel width = 3.45 µm). A collimating lens with an f = 1000 mm focal length imaged the SHG signal inside the BBO crystal, this gave an effective slit width of ≈99 µm, calculated from the approximate focal volume and crossing angle of the two beams, within which the SHG signal was generated. A holographic 1800 l/mm grating was used to spectrally disperse the pulse before it was focused to the detector using an f = 200 mm plano-convex lens. A rough calculation of the spectrometer resolution suggested a $\Delta\lambda|_{min}$ ∼0.25 nm. Additionally, unlike FROGs used to measure the spectral phase of compressed or ultrafast pulses, here the direction of time ambiguity present in an SHG-FROG trace is not an issue as we know the direction of chirp of the input pulse.

Temporal intensity and phase retrieval was performed using the FROGed code written by Matthew Streeter [72]. This code is able to switch between several different retrieval algorithm methods in order to get best fit between the measured FROG trace and the reconstructed electric field, including the Data Constraints method, Generalized Projections method [73] and the Genetic Algorithm method. By switching between different retrieval algorithms after a given number of iterations, the FROGed software is able to avoid local minima in the retrieval error which would prevent the code converging at the correct soultion. The switch between retrieval methods happens when there is no change in the residual error over a specified number of iterations. A final residual error of 0.02 or less was shown to correspond to a good level of confidence in the retrieval [72].

Figure 3.2 show an example FROG retrieval measurement of ∼5 nJ pulse produced by an Nd:Glass oscillator (GLX 200HP, Time Bandwidth Systems), centered at 1053.5 nm, which has been tem-

porally stretched from 250 fs to 1.2 ps ps duration using a 30 cm long high-index H-ZF7LA (SF6) bulk glass stretcher, in a four passed geometry. From the algorithm, we can find the temporal (figure 3.2 bottom left) and spectral (figure 3.2 bottom right) profiles of the retrieved FROG trace, giving a measurement of the pulse duration and bandwidth, which can be cross-referenced with previous measurements, and spectral phase, discussed in chapters 4 and 5.

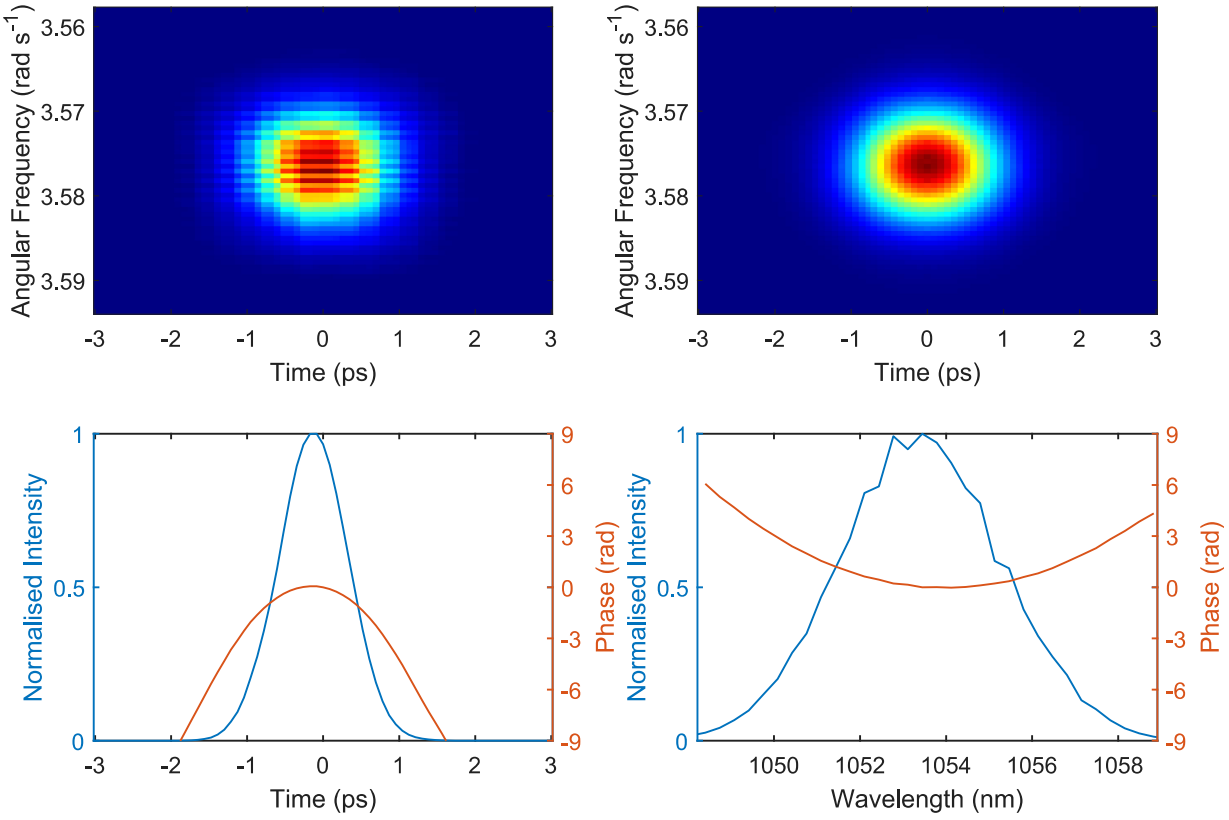


Figure 3.2: Example FROG data showing the measured and retrieved FROG traces. Upper left: measured taken with the Cerberus frog, upper right: analysed using the FROGed algorithm by Matthew Streeter [72], lower left: retrieved pulse vs time, lower right: retrieved pulse vs wavelength. The Frog retrieval error in this measurement was 0.012.

For the FROGed algorithm to converge on the correct result, we need to be quite selective with the data we put in; correctly processing the raw data for the algorithm not only improves the final residual error but also accounts for shot-to-shot variations in the energy and spectrum of the input beam, which can introduce asymmetries in the measured FROG trace. Raw data was prepared for analysis using a code written by the author, which performed background subtraction, against a reference image, of the spectrum at each step of the delay stage and combined the measured spectra into a single spectrogram. Specific parameters for the FROGed algorithm,

such as the spectral and temporal resolution of the spectrogram, were accurately calculated from the motorised translation stage positions and a reference spectrum, measured using a separate calibrated spectrometer. Lastly, the temporal and spectral centres of the spectrogram were found by fitting a Gaussian model across the peak of the spectrogram, for known resolution. However, the peak temporal and spectral profiles of the spectrogram were often not a perfect Gaussian, due to their actual shape or because of fluctuation in the energy of the input beam, which would have resulted in offset between the fitted central frequency or delay error and the true values. An SHG-FROG spectrogram should be symmetric around t = 0, therefore an error in the position of the spectrogram means that the FROGed algorithm would try and generate an electric field that matched the data, and generate non-physical phase. To reduce the effect of this error, the centre of the delay was manually identified based upon the known temporal profile of the pulse, which was previously measured by N. Stuart using a third order autocorrelator [36]. These spectrograms were then mirrored around t = 0 and the retrieved FROG data for the mirrored -ve and +ve temporal sides of the pulse was compared in order to make general predictions for the spectral phase. This process is described in more detail in chapter 5.

3.3 Extended Third Order Autocorrelator (XTOAD)

Whilst autocorrelation can give a useful measurement of the temporal pulse duration and FROGs can also measure spectral phase, there is a significant need to diagnose the temporal intensity profile of the laser to high dynamic range in order to measure the contrast of a laser pulse and to detect the presence of any (typically unwanted) features on the temporal intensity profile preceding the main pulse which may affect laser interactions. As prepulses and contrast pedestals can have a significant effect on laser-target interactions, for interactions with focused light impinging upon thin (∼10 µm) metallic foils, features preceding the main pulse with intensity greater than 10^9-10^{12} Wcm^{-2} may pre-ionise the target ahead of the main laser interaction [12]. High power laser systems with a focused intensity 10^{19} - 10^{21} Wcm^{-2} therefore ideally require diagnostics with a minimum 10^8 - 10^{10} dynamic range.

One common diagnostic used for this purpose is the third order autocorrelator, which is able resolve the temporal profile to high dynamic range (up to $\sim 10^{11}$) without making symmetric assumptions. First reported by Luan et al. at Imperial College [74], third order autocorrelation

works similarly in principle to second-order autocorrelation however in place of correlating the measured pulse with itself, the gate pulse is instead the second harmonic of the fundamental. This involves a two-stage process where the fundamental frequency (1ω) is first frequency doubled to the second harmonic (2ω), the residual fundamental and the 2ω are then overlapped in the final stage to drive sum frequency generation to produce a third harmonic (3ω) signal from which the temporal intensity profile of the measured pulse may be inferred. Unlike second-order autocorrelation, by taking the second harmonic we create a "sharper" and "cleaner" gate pulse providing a shorter (and typically less temporally structured) probe which breaks the time symmetry of the autocorrelation and thus removes the direction-of-time ambiguity. Second harmonic generation is intensity-dependent, therefore the gate pulse duration is approximately a factor $\sqrt{2}$ less than the fundamental for a Gaussian input pulse and the intensity of background noise features are reduced by the square of their initial contrast ratio, resulting in a shorter temporal duration and higher contrast gate pulse. As with noncollinear second-order autocorrelation, the process is background free; the 3ω signal is only produced when both fundamental and 2ω beams are present and overlapped. Furthermore, if noncollinear phase matching is used then the resulting wavevector of the 3ω signal is not in the beampath of either fundamental or 2ω beams, removing both them and the scatter they may produce in the crystal from the measurement.

Much like second order autocorrelators, third order autocorrelators also exist in scanning and single-shot geometries. Scanning third order autocorrelators typically achieve a higher dynamic range, with a greater temporal window, whilst for measuring the contrast of a specific pulse as an on-shot diagnostic, involved in an experiment, single-shot third order autocorrelators are used. A high very dynamic range scanning diagnostic (up to 10^{11}), the Third Order Autocorrelator Device (TOAD), has previously been developed at Imperial college. This has been used to characterise the contrast of different laser oscillator designs [37] as well as the front end temporal intensity profiles of several high power laser facilities in the UK [36]. Also available is the commercial "SEQUIOA" third-order autocorrelator (Amplitude Technologies), which is able to resolve the temporal intensity profile of a single pulse, with a noise floor limited dynamic range typically of $\sim 10^9$.

Although background noise features in the second harmonic are suppressed, they nonetheless remain present in the 2ω beam, though reduced by the square of their ratio compared to the peak intensity of the pulse. In particular, low-intensity noise features such as postpulses can

have a detrimental affect on the contrast measurement by producing artefacts in the contrast measurement. Postpulses may arise due to double-passed optical systems or internal reflections from thin flat, parallel optics such as waveplates and polarisers. Due to the sheer complexity of a laser system where there may be hundreds of optics along the total beampath, with a significant number of postpulses potentially present in the temporal intensity profile. For example, a thin optic with an antireflection coating of (good commercial quality) reflectivity R$\sim$ 0.1%, for example, would introduce a postpulse of order 10^{-6} relative contrast. Correlation of the measured pulse with these postpulses in the gate pulse means that they can be correlated with the peak signal and produce an artefact in the temporal profile prior to the main pulse in the contrast scan with a similar profile to the postpulse, this is illustrated in figure 3.3. These artefact prepulses can sometimes be identified by the presence of a corresponding postpulse with a squared greater magnitude at the opposite point in time from the main pulse. However, due to the number of postpulses often present in contrast scans from large laser systems, there is often an opportunity for misidentifying the correct postpulse or introducing bias, trying to correlate real prepulses to postpulses in order to report a greater contrast of a scan. Real prepulses may also be hidden beneath overlapping noise features or artefact prepulses.

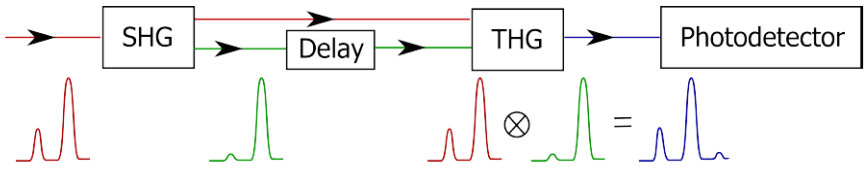


Figure 3.3: The formation of 'ghost' prepulses in a third order autocorrelator due to convolution of the first and second harmonics of a pulse with a trailing postpulse. A postpulse following the main pulse is initially suppressed by the intensity-dependent SHG process, however this postpulse remains during the correlation of the fundamental and 2ω beams to produce an artefact ahead of the main pulse in the THG signal. Image credit: Nicholas Stuart [36].

Removing these artefacts requires further contrast enhancement of the 2ω pulse, one method of achieving this is to introduce an additional cross-polarised wave generation (XPW) stage into the 2ω beampath prior to the THG stage. XPW is a technique using a nonlinear crystal with third-order anisotropy, where for an input wave of given polarisation, a new wave with polarisation orthogonal to the input may be generated. The generated wave has cubic dependence on the intensity of the input pulse, providing contrast enhancement with twofold benefit; a factor $\sqrt{3}$ shortening of pulse duration and further suppression of low intensity pulse features. XPW

is sometimes used for contrast enhancements of sub-100 fs laser systems [75] with efficiencies reported of up to 33% for 650 µJ pulses with an input 25 fs duration [76]. The challenge of incorporating this technique however lies in the threshold intensity for the process, for ps-domain pulses use of XPW is typically limited by the surface damage threshold of the the nonlinear crystal which often approaches the XPW interaction threshold intensity.

In the next section we will discuss the design of a novel extended third order autocorrelator diagnostic (XTOAD) for artefact-free high dynamic range ps-domain pulse temporal intensity characterisation, utilising a focusing beam geometry to achieve efficient and stable implementation of an XPW stage operating at 527 nm. By comparing contrast measurements with and without the XPW process engaged, we are able to clearly identify postpulse artefacts in the contrast plot.

3.3.1 XTOAD Diagnostic Overview

An extended third order autocorrelator, here named the XTOAD, incorporating XPW contrast enhancement of the 2ω signal was designed by Nicholas Stuart with supervision by R.A. Smith working at Imperial College London. A schematic diagram of the diagnostic is shown in figure 3.4. The XTOAD provides a method of "artefact-free" temporal intensity contrast characterisation up to a high dynamic range ($> 10^{10}$) by utilising efficient XPW in the 2ω beamline of the diagnostic. The diagnostic requires only 5 µJ of input energy for up to 2 ps duration pulses, centred at 1054 nm wavelength to achieve the above results.

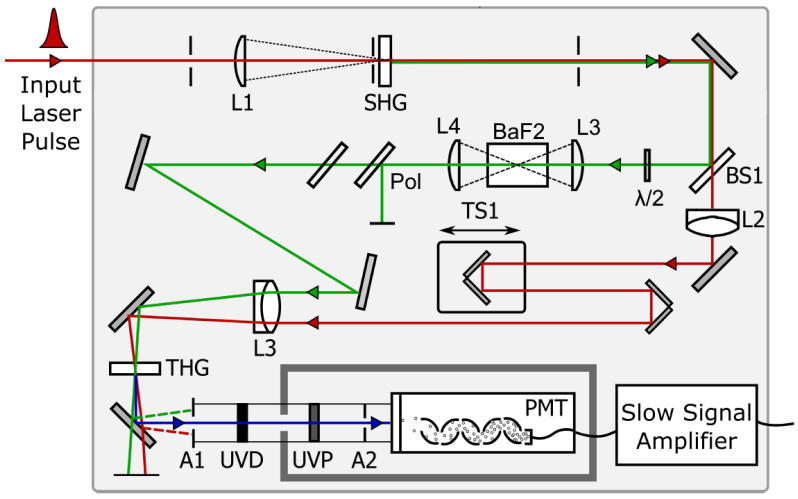


Figure 3.4: Schematic diagram of the extended third-order autocorrelator diagnostic (XTOAD).

Light injected into the diagnostic is first apodised using a 1.7 ± 0.1 mm diameter serrated aperture. Typically the input beam is set to overfill the serrated aperture to select the most intense portion of the spatial profile. It is then focused through a pinhole before the first SHG stage, a 1.5 mm type I BBO, set slightly back from the focal point, operating at ∼35 % efficiency. Apodisation here spatially filters the beam profile and helps insulate against minor changes in the beam pointing into the diagnostic. It also helps to avoid generation of elliptical beams from marginal rays that are not able to be birefringently phase matched. After the first nonlinear stage, the harmonics are separated with a 0.5° wedged dichroic mirror. The residual fundamental light is recollimated and propagated along a motorised translation stage (Thorlabs LTS300/M) with an effective travel length of 230 mm (max 300 mm), which set the the maxium temporal window of the diagnostic, 1.4 ns. The diagnostic was aligned such that the path lengths of the fundamental and 2ω beams are equal at the centre of the translation stage, for the purposes of capturing postpulses to confirm their corresponding artefacts are removed by the XPW stage. The 2ω beam, converted in the SHG stage is picked off using a 0.5° wedged dichroic mirror, a $\lambda/2$ waveplate rotates the polarisation orthogonally before the beam is focused with an f/30 lens into a 25 mm thick [011] oriented BaF_2 crystal. BaF_2 is commonly used for XPW applications [75] however for applications of ps-duration pulses the surface damage threshold is often reached before the XPW nonlinear interaction threshold. To circumvent this, we use a focusing geometry with a short, 5 mm, confocal parameter. The bulk damage threshold of BaF_2, experimentally measured at an intensity threshold of ∼1 $TWcm^{-2}$ with a 2ps, 527 nm pulse, is greater than the the surface damage threshold. The bulk damage threshold measurement was defined at the point where the XPW efficiency began to slowly decrease after 500 shots. The focusing geometry results in a 50 µm focal spot size, therefore the collimating lens after the BaF_2 crystal creates a magnification of x0.53 to counteract the greater divergence of the XPW beam as it is created within a smaller focal volume and to match the accepted phase matching tolerance of the THG crystal. Finally, the orthogonally polarised XPW signal is isolated using two high extinction polarisers (>10,000:1).

The XPW conversion efficiency was characterised by Nicholas Stuart. The nonlinear interaction threshold was experimentally found to be ∼200 $GWcm^{-2}$, with the process reaching the point of saturation at ∼600 $GWcm^{-2}$ with 25 ± 9% efficiency. For pulses centered at 527 nm, of approximately 2 ps duration, a maximum efficiency of orthogonally polarised light generated was

$37 \pm 7.5\%$, at 2.18 µJ input. We have been able to produce $\sim 35 \pm 9\%$ efficiency over long term operation, found to be robust over multiple days without causing optical damage to the BaF_2 crystal.

At the final nonlinear stage the fundamental and 2ω pulses are both recombined as a pair of parallel co-propagating beams and focused using a 200 mm lens into a type II 1.5 mm BBO THG stage, producing a 3ω, 351 nm signal. A 5° noncollinear angle is used to spatially separate the fundamental and 2ω beams from the THG signal, which also has the effect of reducing the background scattered light. A larger noncollinear angle would further improve background noise reduction however this would limit the nonlinear interaction length and reduce the signal level, impacting the overall dynamic range. The THG stage is type II phase-matched, meaning the polarisation required for the 2ω beam is parallel to the fundamental. Measurements can be taken with and without the XPW process running by switching out the waveplate and polarisers either side of the BaF_2 crystal so that the unconverted light instead drives the THG process. This allows us to compare contrast scans taken by the diagnostic with and without the XPW stage engaged, to validate the XPW contrast enhancement process and artefact removal.

Once spatially separated from the fundamental and 2ω beams, the 3ω is further isolated from residual scatter and background light by a combination of a 351 nm laser line dielectric mirror and short pass colour filters. Lastly, an iris is used as a tight aperture which can be adjusted to discriminate spatially between the 3ω signal and background noise. The 3ω signal is measured using a high-gain, low-noise photomultiplier tube (PMT). A set of ten calibrated neutral density filters mounted in a computer controlled wheel are used to keep the 3ω signal within the linearity range of the PMT. Finally, the PMT voltage signal is measured by an oscilloscope (Tektronix DPO3054) which passes this measurement to the diagnostic software. The XTOAD is automated using software written by Nicholas Stuart which controls the translation stage movement and records the PMT output voltage at each step along a scan and applies the current attenuation of the filter in place to determine the absolute intensity of the pulse. This software can be modified to change the temporal window of the scan as well as dynamically change the diagnostic scanning resolution (in fs) and the time between steps of the translation stage.

3.3.2 Results and Discussion

In this section we present the results of the characterisation and performance of the XTOAD diagnostic, demonstrating up to 37% XPW conversion efficiency of 2 ps 527 nm laser pulses, routine operation quite robust to optical damage, and up to 7×10^{11} dynamic range third order autocorrelation. Design and initial alignment of the XTOAD was done by Nick Stuart along with XPW efficiency measurements whilst characterisation of the photomultiplier tube, filters and dynamic range enhancements were performed by the author. Additionally, the contrast scans presented in this chapter were similarly taken by the author. The output of this work has led to a paper, currently in preparation.

This diagnostic was used to characterise the contrast of the Cerberus laser system OPCPA front end, described in detail in section 4. The front end of Cerberus is composed of four OPA stages arranged in two sets of two. The first, ps-OPA stages, have a combined gain factor of $\sim$15 $\times 10^4$ across a temporal gain window of 6 ps set by the duration of the 2ω pump pulse. The output of the ps-OPAs is temporally stretched to 1.8 ns in an Öffner stretcher before additional amplification by a factor $\sim$200 gain in the ns-OPA stages, which have a gain window of 1.4 ns. For the following measurements, the laser propagated through the full OPCPA front end of the system and then the glass amplifier beamline. However, whilst the beam propagated through the Nd:glass gain media to match dispersion in normal operation, the flashlamps for high gain were not in operation. The pulse was compressed in a Treacy configuration z-compressor to an optimum duration of 500$\pm$50 fs using a pair of gold holographic 1741 l/mm gratings. The Cerberus laser is used for laser-plasma interactions with a focused pulse intensity $\sim 10^{19}$ Wcm^{-2}, therefore as features in the temporal intensity profile of $\sim 10^{12}$ Wcm^{-2} are known to impact these interactions we therefore require a dynamic range of at least 10^8. A contrast scan measured with the XTOAD with a temporal window of 1.3 ns, achieving a dynamic range $\sim 10^{10}$, of the Cerberus laser front end is shown in figure 3.5. From this we are able to identify key features in the temporal intensity profile of the laser.

Of particular note is a 'triangular' noise pedestal, rising $\sim$ 200 ps prior to the main pulse to a contrast ratio of approximately 10^{-4}. This pedestal, previously described in chapter 1, has been shown to originate from incoherent scatter and surface irregularities from large optics in imaging stretchers, such as the Cerberus front end Öffner stretcher[41], consistent with theoret-

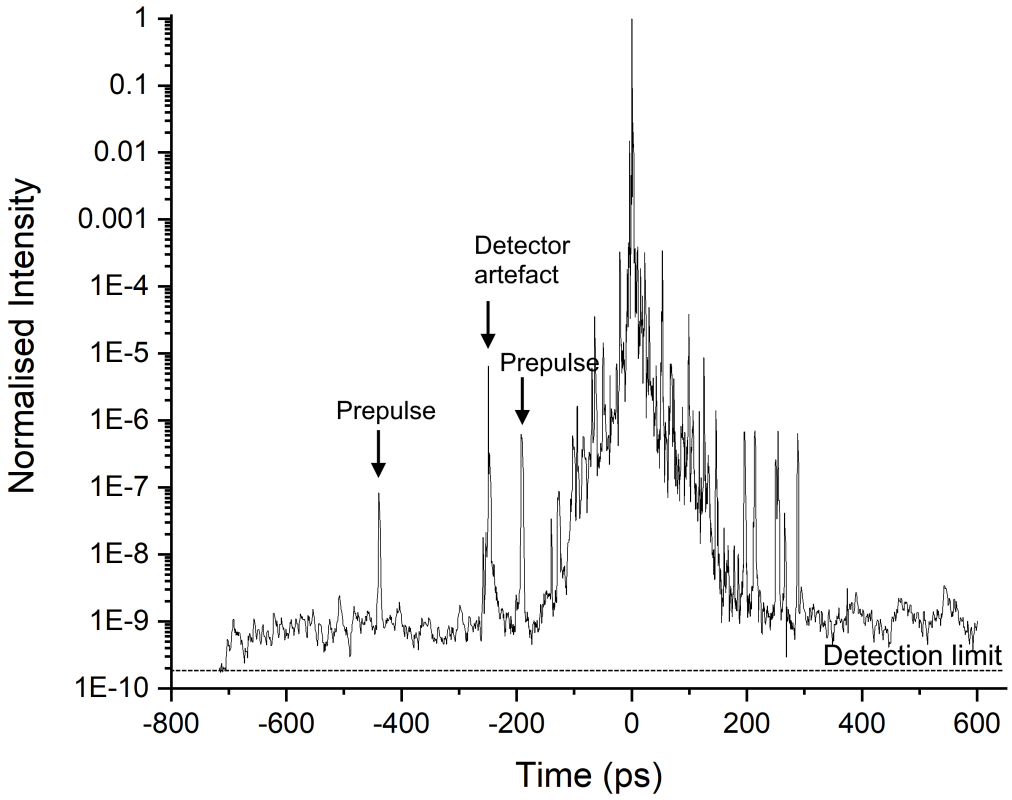


Figure 3.5: The temporal intensity profile of Cerberus laser OPCPA front end (15/12/2022), characterised using the XTOAD diagnostic up to a dynamic range of 10^{10}, over a temporal window ∼1.35 ns. Several features are evident on this plot, including three major prepulses; one at 249 ps at a relative contrast of 10^{-5}, concluded to be an artefact of the diagnostic, and two at 440 and 192 ps which are indicative of real prepulses, produced by double-passed optics in the laser beamline. The plot also shows a broad ∼ns-duration pedestal at a relative contrast of $\sim 10^{-9}$, produced by fluorescence in the front end ns-duration OPA stages and a triangular feature extending ~ 200 ps ahead of the main pulse up to a relative contrast of 10^{-5}, characteristic of incoherent scattered light in CPA stretchers.

ical predictions of high frequency spectral phase modulation [45]. The temporal profile of the triangular pedestal is mainly produced due to the spectral phase noise from surface irregularities in the diffraction gratings [45]. The impact of this feature on laser-plasma interactions is further discussed in section 6.

With a dynamic range of $\sim 10^{10}$, we are first able to identify a broad >ns duration noise pedestal at a relative contrast of 10^{-9}, approximately 10^{-10} Wcm^{-2}, representing parametric fluorescence from the ns-duration OPA gain stages. Parametric fluorescence produces a noise pedestal with a temporal width of the same order as the temporal gain window of the OPA stages of the

front end, in turn determined by the OPA pump pulse duration. We would therefore expect two sources of parametric fluorescence, from the ps-OPAs with a total width ∼6 ps and from the ns-OPAs, which have a gain window of approximately 1.4 ns. Fluorescence from the ps-OPAs is likely obscured in this contrast scan due to the magnitude of the CPA pedestal, the ps-OPA fluorescence was previously characterised with a temporal intensity contrast of 3×10^{-9}, rising 1.3 ps before the main pulse [14]. Additionally the temporal window of the XTOAD is not broad enough, in the current configuration, to observe the start of the ns-OPA fluorescence pedestal, however the measurement in figure 3.5 does correspond to previous measurements of the pedestal, observed at a relative contrast between 10^{-8} and 10^{-10} across several scans. This difference in relative contrast of the ns-OPA fluorescence background is likely due to differences in the pump depletion of the ns-OPAs [36]. In figure 3.5, there is a visible modulation in the fluorescence pedestal from roughly 250 ps after the main pulse, persisting until the end of the scan. This is likely an artefact of the scan, with an approximate period of 1.3 minutes, rather than a feature of the fluorescence background. There are several explanations for this feature, including slow variation of laser power due to cooling loop cycling or due to air currents in the laboratory caused by air-conditioning units, both of which have a similar timescale to the 1.3 minute period observed.

A large prepulse is observed on figure 3.5, -4 ps ahead of the main pulse with a relative contrast of 1.48×10^{-2}. Usually a prepulse of this magnitude would be highly significant, however here it was introduced by a thin waveplate placed in front of the diagnostic for this particular scan and was not present on any scans without the waveplate in the beamline. However, several other prominent discrete prepulses were observed consistently across several diagnostic scans. In total, there are three major prepulses ahead of the main pulse, at 440 ps at a relative contrast of $\sim 10^{-7}$, 249 ps at 10^{-5} and 192 ps at 10^{-6} contrast. These prepulses account for path length in vacuum of 132, 74.7 and 57.6 mm respectively, which could correspond to internal double-passed reflections from optics with thickness ∼44, 24.9, 19.2 mm, assuming a ∼1.5 refractive index. It was particularly important to identify the sources of these prepulses, at they may potentially have an effect on laser-plasma interaction experiments. Several candidate optics were considered, inside of the XTOAD diagnostic itself and in the system. A postpulse in the 2ω arm of the detector will create an apparent prepulse in the scan, to avoid this most of the optics in the green arm are wedged, with the exception of a thin $\lambda/2$ waveplate and BaF_2 crystal. A 25 mm

thick BaF_2 (n = 1.48 at 527 nm [77]) will produce a prepulse at 247 ps, which corresponds well to the 10^{-5} prepulse which we observe throughout contrast measurements. For purposes of understanding the diagnostic, it was practical to leave the BaF_2 crystal in place for each scan. A 532 nm $\lambda/2$ Waveplate (Thorlabs) has an unmounted thickness of 2.01 mm, comprised of two combined multi-order crystalline quartz wave plates for a total of 4 surfaces. The antireflective coating these optics are supplied with is quoted as R<0.25%, from this and the refractive index of crystalline quartz (n = 1.46 at 527 nm [78]) we would anticipate two prepulses at 19.5 ps and 9.8 ps at a contrast of $\sim 6.25 \times 10^{-6}$ from the exterior surfaces and the boundary between the two crystals. A prepulse at 19.5 ps would correlate closely to a minor prespulse observed at 21 ps however the contrast measured of this, 3.30×10^4, was two orders of magnitude greater than the predicted prepulse contrast. SHG crystals in third order autocorrelators are known to produce artefacts in the measured contrast plot [36], a 1.5 mm BBO crystal at 527 nm would produce a prepulse at ∼16.8 ps, whilst this is not observed in the contrast plot the relative contrast of the SHG artefact (10^{-6}) would be obscured by the CPA pedestal if it was not eliminated by the XPW stage.

The discrete prepulses observed at 450 and 200 ps were found to closely coincide with double-passed lengths of the Cerberus pre-pulser, a component of the system at the output of the front end which can be used to add an intentional, discrete prepulse up to 2 ns ahead of the main laser pulse. A schematic layout of the optics, as well as its role in charged particle and x-ray acceleration experiments is, further described in section 8.1.

By comparing contrast scans with and without the XPW process engaged, we can identify which prepulse features were removed and thus clearly identify them as artefacts. Figure 3.6 shows two contrast scans, one where the XPW signal was selected as the gate pulse and another (grey) where the residual, non-rotated, light was used. By comparing the two temporal intensity profiles, We can identify an artefact prepulse at ∼80 ps. Additionally, we saw the removal of postpulse artefact at ∼60 ps after the main pulse. This correlates to the artefact that would be produced by the Cerberus prepulser, which aligned at the time to introduce an artefact of 60 ps. This postpulse is a known artefact and thus its removal is expected and a further verification of the diagnostic.

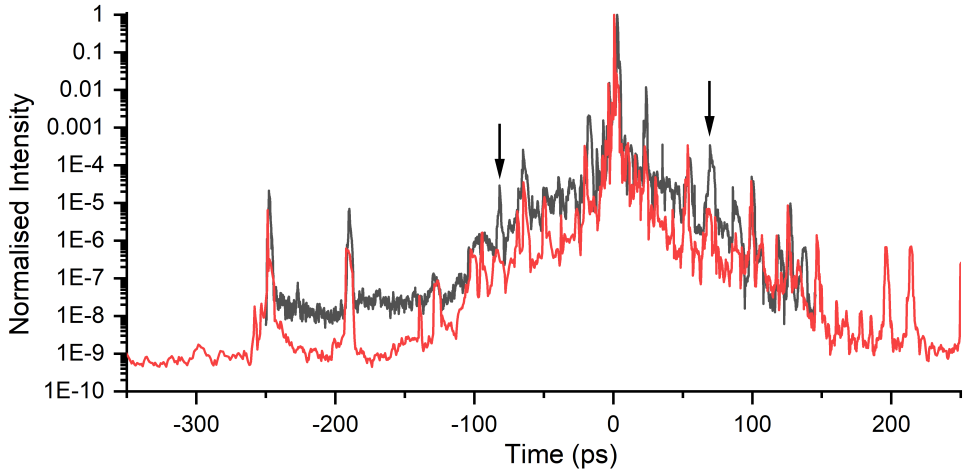


Figure 3.6: Artefact (grey) versus artefact free (red) contrast characterisation of the Cerberus front-end. A 10^{10} dynamic range is achieved in the X-TOAD. We can conclude that an 80 ps prepulse with $3{\times}10^{4}$ contrast is a measurement artefact by comparison of two autocorrelator traces with and without a probe pulse contrast enhancement.

We can improve the dynamic range by optimising two key factors; by increasing the signal intensity of the THG stage or by reducing the noise floor of the diagnostic. In the design stage of the diagnostic, this amounted to carefully optimising the nonlinear interaction lengths, phase matching, focal lengths, etc. in relation to the maximum energy through the diagnostic. Obviously, a high signal intensity follows a high energy, which itself is limited by the optical damage thresholds at each stage, e.g. $<$ 20-30 µJ to the SHG for $<$500 fs pulse durations. One method to increase dynamic range would be a smaller focused spot size of the fundamental and 2ω beams in the THG stage. However, the angular tolerance of the THG process limits the mimimum confocal parameter; for THG in type II BBO, this is equal to 10.0 mrad·cm for light centered at 1054 nm and 0.4 mrad.cm for light centered at 527 nm. A high interaction energy also runs the risk of surpassing the nonlinear threshold for self-focusing or filamentation. It was therefore important to optimise the confocal parameter for the XPW stage, too long a focal length and the focusing angle would become comparable to the Kerr self-focus strength, resulting in filamentation, however too short and we limit the input energy due to the bulk damage threshold. During the alignment and operation of the XTOAD, we observed filamentation inside of the BaF_2 crystal by the formation of Kerr rings around the XPW signal. These rings are indicative of filamentation and are produced by the diffraction patterns when a filament with a super-Gaussian spatial profile collapses, saturating the $\chi^{(3)}$ process in the nonlinear media [79]. Filamentation marks a

breakdown in the stability of the XPW process and therefore sets a fundamental limit, on the input beam energy, defined by the critical power, when self-focusing dominates over the beam divergence;

$$P_{crit} = \frac{\alpha\lambda^2}{4\pi n_0 n_2} \tag{3.6}$$

where n_2 is the nonlinear refractive index of a medium and α is a dimensionless parameter, given as $\alpha \approx 1.90$ for Gaussian beams. For $\lambda = 527$ nm, the critical power of light propagating through BaF2 was calculated to be ∼0.93 MW, or 0.47 µJ at 500 fs.

By overfilling the serrated aperture, combined with a pinhole before the first SHG stage, we propagate a pseudo flat-top spatial profile beam through the diagnostic. As the laser intensity is more uniform across the spatial profile of the beam, this reduces susceptibility to self-focusing, and therefore filamentation in the BaF_2 crystal, which allowed us to increase the XPW stage energy for greater conversion efficiency. Additionally, flat top-beam profiles have been shown to improve the efficiency of XPW stages [76].

Lastly, the THG stage crystal was imaged with an alignment camera to ensure good spatial overlap of the fundamental and 2ω pulses. This camera could also be used to monitor the beam profile of the XPW stage signal. Where any fluorescence occurred, this would correspond to obvious intensity fluctuations on the camera. Scanning third order autocorrelators typically achieve a higher dynamic range measurement of the temporal intensity profile of a laser, however this measurement is averaged over many shots and therefore is indicative of average performance. Factors including gain in amplifier stages or pointing changes in the laser will affect the temporal profile on a shot-to-shot basis. Improving the energy stability of the laser system (RMS energy stability <1%) meant that we could push the XPW stage closer to the critical power limit without risking fluctuations of the laser energy exceeding this limit. As filamentation in the BaF_2 crystal could be quickly observed on the XTOAD alignment camera, it was possible to make precise adjustments to the energy into the diagnostic using a waveplate-polariser combination and identify the threshold at which filamentation began to occur and then step back from that to an operational input energy. The steps taken to improve the stability of the Ceberus laser system are discussed more in section 4.

In order to reduce the diagnostic noise floor, the XTOAD design accounted for sources of scattered light and electrical noise. As described in section 3.3.1, scattered light was spatially separated

from the fundamental and SHG beams due to the 5° noncollinear angle used in the THG stage, in combination with a combination of a 351 nm laser line dielectric mirror, short pass colour filters and a tight aperture before the PMT. A low electrical noise PMT was used to record the signal. PMTs prduce a "dark current" which is determined by the following factors:

$$\text{Output } (V\omega^{-1}) = \text{Transimpedance gain } (VA^{-1}) \times \text{Sensitivity } (A\omega^{-1}) \times \text{tube gain.} \quad (3.7)$$

The dark current for the XTOAD PMT (Thorlabs PMM01-1) was measured to be 0.57±0.05 mV The PMT voltage is read by an oscilloscope (Tektronix DPO3054) which feeds the maximum voltage on the trace to the XTOAD software to be recorded. To reduce the impact of laser energy fluctuation on the PMT signal voltage, the oscilloscope is set to to average over a given number, typically 16, of datapoints. The PMT response is also dependent on the number of photons hitting the detector, this is globally nonlinear, with a successively lower output voltage as the PMT begins to saturate. There is, however, a region where the PMT response linearly varies with the signal onto the detector. This "linearity range" was characterised by measuring the PMT response for pulses with two given levels of attenuation, figure 3.7, and found to be in the region of ∼0.02 - 1.5 V, measured at 50Ω resistance. This data was collected by noting the momentary PMT signal as measured by the oscilloscope, itself averaging over 16 data points, and therefore the error represented on figure 3.7 is determined by the standard deviation of ten measurements of the same voltage. A 12-Position motorised filter wheel (THORLABS FW212C) was used to maintain the THG signal intensity onto the PMT to within the linearity range. The attenuation factor for 9 filters used was experimentally measured, shown in figure 3.8.

It was necessary to carefully align through the translation stage which determines the delay between the fundamental and 2ω gate pulse so that the movement did not cause the fundamental and 2ω beams to spatially walk off from one another. Such spatial walk-off would reduce the efficiency of the SFG process away from the point at which the stage was aligned and, depending on where this point was on the stage, could potentially reduce either the dynamic range by reducing the intensity of the main pulse or could also mask prepulses or postpulses as spatial walkoff at the extreme ends of the stage would decrease the measured contrast of these pulses. In the latter case, this could result in mis-identification of real or artefact prepulses by reducing the relative contrast between them and their corresponding post pulse, for example where one ought

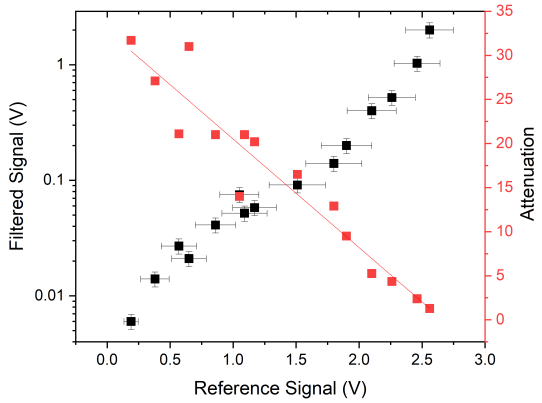


Figure 3.7: XTOAD photomultiplier tube response, measuring two pulses of the same energy, attenuated by two different factors. A region of linear response was identified between ∼0.02 to ∼1.5 V.

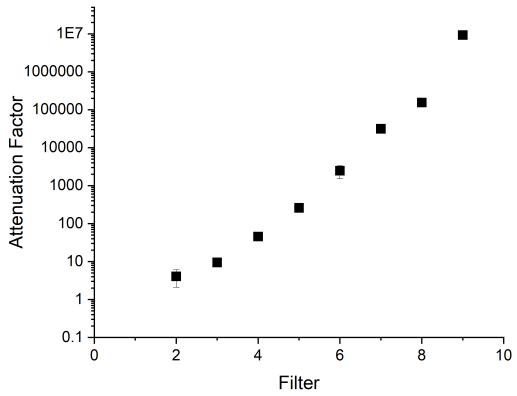


Figure 3.8: The measured attenuation factor for the 8 neutral density, centered at $\lambda_0 = 351$ nm, filters used to maintain the XTOAD signal within the linearity range of the PMT.

to be two orders of magnitude higher than the other, walk-off of the stage reduces the SFG signal at that point by an order of magnitude or more. The translation stage was carefully aligned in the first instance however the alignment camera can also be used to monitor the overlap of the fundamental and 2ω beams. The interval between data collection was also set so there was some time after the stage had stopped moving before the measurement was taken, reducing the impact of the stage wobbling after it came to rest.

The contrast of an OPCPA laser system is highly influenced by the operation of the OPA stages, where pointing instabilities, beam wander or thermal effects can have a significant effect on the energy stability, bandwidth and wavefront of the laser. A contrast scan, with a ∼1.4 ns temporal window can take up to $>$ 2 hours to complete. Whilst we can take steps to reduce this, such as varying the step size of the translation stage, the time between steps and the averaging duration, poor system performance can introduce additional noise or impact the front end performance, decreasing the maximum signal intensity. With steps taken to achieve stable operation of the OPCPA front end (RMS energy drift ∼1% over 2 hours of operation) the energy input did not vary into the diagnostic and there was no requirement to pause the scan in order to reoptimise the OPA stages, something which produces discontinuities on the contrast plot. Long-term drift was prevented with the aid of a frequency-lock on the oscillator cavity, by allowing the system to reach thermal equilibrium and identifying a stable regime in which to run the OPA stages, each

described in section 4.

This careful optimisation yielded a maximum dynamic range of 7.8×10^{11}, shown in figure 3.9, an improvement by four orders of magnitude over the initial diagnostic results. With this dynamic range, the XTOAD is shown to be an applicable and effective temporal intensity characterisation diagnostic for high power laser systems with up to 10^{22} Wcm^{-2} focused intensities, including many of the highest power laser facilities worldwide [11].

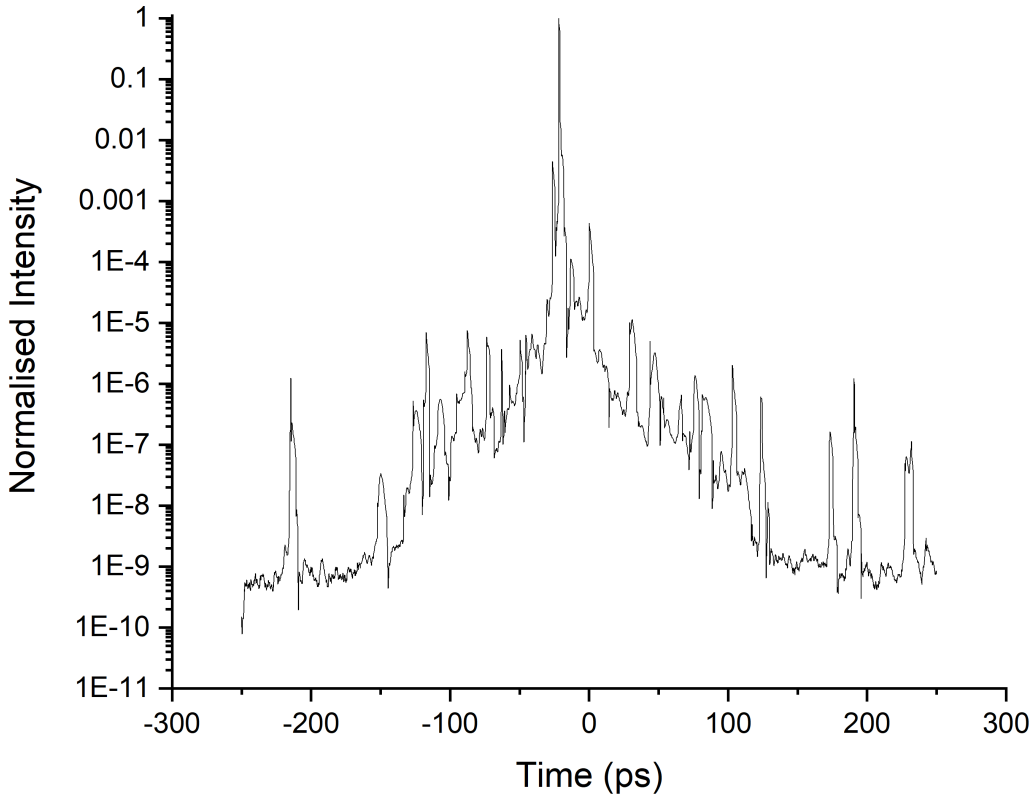


Figure 3.9: High dynamic range, 7.8×10^{11}, temporal intensity characterisation of the Cerberus laser system OPCPA front end (15/12/2022) measured with the XTOAD diagnostic

Chapter 4

The Cerberus Laser System at Imperial College London

The Cerberus laser system at Imperial College London is aptly named for its three main beamlines. The first of these is used to generate long-pulse, high energy light for shock physics experiments or to deliver diagnostic beams (up to 20 J, 1.2 ns) to the adjacent MAGPIE z-pinch facility [20], [80] and also for use as a optical pump beam for large aperture OPA stages, to amplify the second and third beamlines. These two, are 'high-contrast' short pulse beamlines, based on an OPCPA/flashlamp pumped Nd:Glass hybrid architecture, consisting of a primary multi-terawatt (∼10 TW), 500 fs beam for laser-target interactions, generating x-rays and accelerating hot (>10 keV) electrons and up to 10 MeV proton beams. The primary, main-pulse, is supplemented by a secondary ∼TW beamline for interferometry and other active probing and diagnostic applications, A schematic diagram of the system is shown in figure 4.1. The overall design of the system was developed by Prof. R.A. Smith in discussion with Prof. S. Lebedev who mapped out the end-user requirements for Magpie Z-Pinch diagnostics in 2008. Funding was secured from EPSRC by Prof R.A. Smith and Prof Lebedev in 2009 and the 1^{st} arm of the system (a narrowband green beamline for multi-point Thompson scattering) was delivered to target in 2010. The short pulse arm of the system was developed over 2009-2011, with construction of the long pulse pump beam line, seeded by a linear regenerative amplifier (described later in this chapter) primarily by R.A. Smith. The two-stage picosecond time domain optical parametric amplification (OPA) subsystems, were installed by R.A. Smith, S. Patankar, D. Bigourd and N.

Stuart, with a design based upon initial modelling by G.C.H. New, D. Bigourd and S. Patankar [81] with several later key improvements later made by N. Stuart [36]. The CPA subsystems we shall describe later were designed and modelled by S. Patankar [81] using the code CPTrace (M. Mason [82]) and installed by S. Patankar and N. Stuart [81].

The author of this thesis has been responsible for the Cerberus laser system as the primary laser operator since June 2019. During this time, those duties have been to maintain and operate the system for experimental campaigns, including key alignment and repairs to damage which arose over time. In this chapter we will describe the design and operational parameters of the Cerberus laser system. In addition, we will present the results of an investigation into potential sources of contrast degradation across the system, such as high order spectral phase manifesting in the long-pulse beamline or stretchers and compressors. Lastly, we have characterised the performance of the gain stages on the system, including the flashlamp-pumped amplifiers and OPA stages, to measure their energy and spectral stability when operated at different levels of gain.

The Cerberus laser is seeded by a single mode-locked Nd:Glass master oscillator (GLX 200HP, Time Bandwidth Systems), which produces 5 nJ, 250 fs pulses centered at 1053.5 nm with excellent temporal intensity contrast ($> 1 : 10^9$) [37]. This oscillator is a basis for the OPCPA "front-end" of the laser system, as pulses output from the oscillator are divided between two beamlines; a short pulse, 10 Hz 'seed' beamline for high contrast amplification up to ∼10 TW pulse powers and a 'long pulse' beamline which undergoes additional amplification to deliver pump pulses to the primary front-end, which is comprised of two, two-stage type-I degenerate noncollinear OPAs. The stages are divided by an initial 'ps-OPA' (OPA1 and OPA2) and then a 'ns-OPA' (OPA3 and OPA4), separated by an Öffner-pattern stretcher. By seeding both the short pulse and the OPA pump beamlines from the same source, we are able to 'optically-lock' the pump and seed beams based on their relative path length and achieve stable operation, as shown later in this chapter, over several hours.

Both seed and pump beamlines are temporally stretched prior to amplification. The 10 Hz seed beamline is four-passed through a 300 mm long H-ZF7LA (SF6) bulk glass stretcher to 1.2 ps, whilst the the OPA pump pulse is stretched to a duration of ∼240 ps in a single-grating folded Martinez stretcher [28] before further amplification inside of a linear regenerative cavity where a diode pumped 3mm diameter, 80 mm long Nd:YLF rod provides a total gain of 10^6 over 43

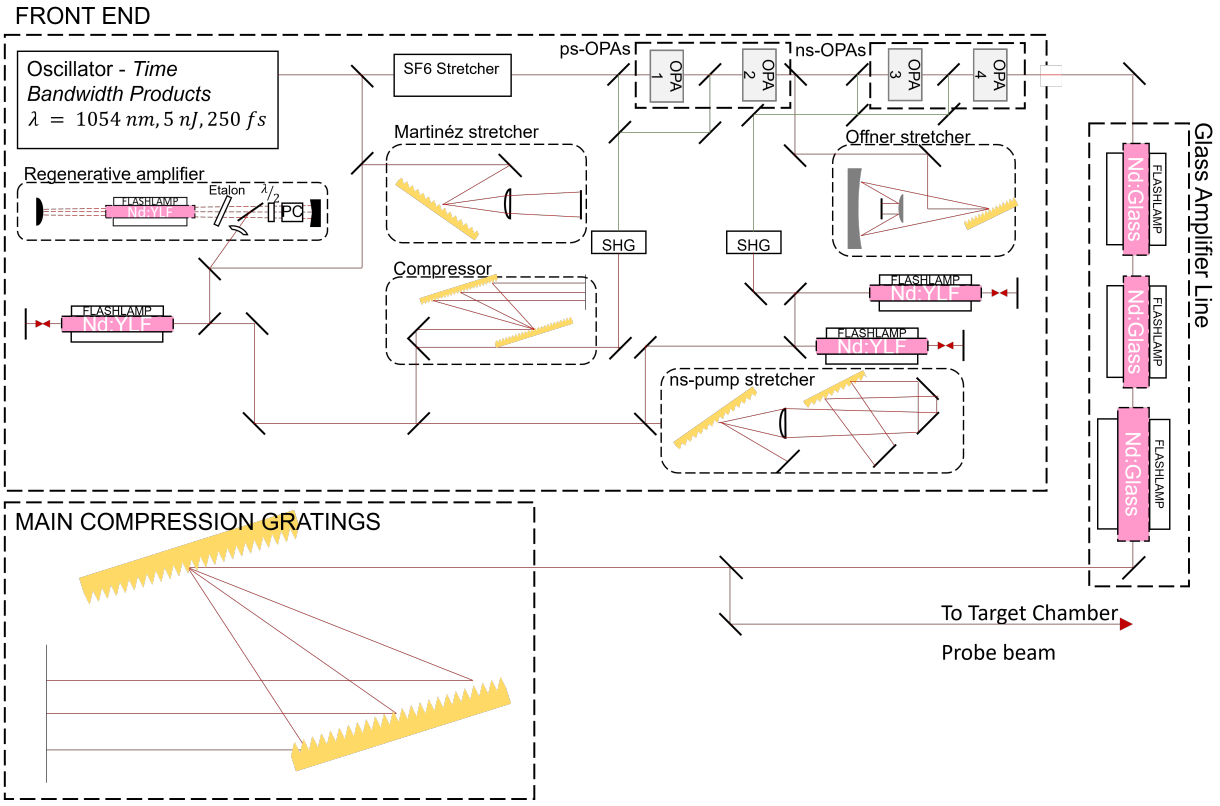


Figure 4.1: Simplified schematic diagram of the Cerberus laser system "front-end". Seed pulses from an Nd:Glass master oscillator (GLX 200HP, Time Bandwidth Systems), are divided between two beamlines; a short pulse, 10 Hz 'seed' beamline and a 'long pulse' beamline which is further amplified by Nd:YLF gain storage amplifiers to pump two, two-stage OPAs. The stages are divided by an initial 'ps-OPA' (OPA1 and OPA2) and then a 'ns-OPA' (OPA3 and OPA4), separated by an Öffner-pattern stretcher, which provide the first $\sim 10^8$ gain. Final amplification of the main pulse, up to ~1 J, occurs through a series of up to three Nd:Glass flashlamp amplifiers, before subsequent compression delivering up to ~10 TW peak pulse power.

round trips inside of the optical cavity, producing up to ~3 mJ pulses of ~80 ps FWHM duration (due to gain narrowing effects in Nd:YLF). In addition to amplification, the Regen (when run into the energy saturation regime) is a fixed point in the system, where the output is to a great extent insensitive to fluctuations in beam energy or pointing at the input, this provides a stable platform for the long-pulse beamline and amplification up to the energies required for pumping the front-end OPA stages. A 10 Hz selection of the Regen output is further amplified by a chain of Nd:YLF gain-storage flashlamp pumped amplifiers, each operated in a double-pass configuration in order to maximise each gain stage. ~30 mJ is extracted from the first 7.5 mm rod diameter Nd:YLF flashlamp stage (termed BMI 1), which is split at a ratio 1:2, with ~10 mJ from pump beamline compressed to ~10 ps with a parallel-grating configuration compressor to pump the first two ps-OPA stages (OPA1 and OPA2). The remaining ~20 mJ is propagated along a 6.9

m, 23 ns optical delay stage to account for additional path length in the seed beamline before it is stretched in a parallel two-grating configuration pulse stretcher to ∼1.4 ns.

The ∼5 nJ, 1.2 ps stretched oscillator seed pulse is amplified by two successive degenerate, noncollinear OPAs, achieving a large gain factor of 10^4 through the first 6.5 mm long type I BBO crystal stage and then subsequent lower additional gain of ∼15 through 2 mm type I BBO. The second gain stage, OPA2, is operated in an oversaturated regime for energy stability, causing spectral reshaping and enhancing the bandwidth of the pulse. This ∼200 μJ signal is temporally stretched to a duration of 1.8 ns, with ∼200 ps/nm positive chirp, in an Öffner stretcher designed by M. Mason and S. Patankar [83] before further short pulse amplification in the ns-OPA stages.

Meanwhile, the 1.4 ns duration long-pulse beam is amplified by two subsequent Nd:YLF flashlamp amplifiers, each arraigned in a double-passed configuration. After energy losses in the ns-pump beamline stretcher, a 7.5 mm rod diameter Nd:YLF gain-stage amplifies the stretched pulse from 4 mJ up to 40 mJ before a final 9.5 mm rod diameter Nd:YLF flashlamp, rated to produce up to 400 mJ pulse energy with very good energy stability (0.5% RMS) over sustained operation. The signal from this amplifier stage can either be directed to the Cerberus long pulse beamline, which operates as a driver for shock physics experiments and plasma diagnostics on the adjacent MAGPIE z-pinch facility (described in more detail in chapter 7), or used to pump the final ns-OPA stages (OPA3 and OPA4). Up to 75 mJ pump light, in the second harmonic, amplifies a stretched 1.8 ns pulse first up to 50 mJ in OPA 3 (12 mm BBO type I phase matching) and finally up to an energy of 8 mJ in OPA 4 (8 mm BBO type I phase matching) with ∼4 nm spectral bandwidth and <1% RMS energy stability.

To access the relativistic regime for laser-plasma interactions, and achieve the focused laser intensities required for ion acceleration, we finally amplify the 10 Hz OPCPA front end pulse up to energies of >1 J using a series of Nd:Glass flashlamp amplifiers. Up to three Nd:Glass flashlamp amplifiers can be operated independently, including two 7 mm diameter rod amplifiers, each with ∼4 factor single pass gain, and a single 16 mm diameter rod amplifier with up to ×15 single-pass gain. At the end of the Nd:Glass amplifier chain, the beam is split using a $\lambda/2$ waveplate-polariser combination between two 'high-contrast' short pulse beamlines (described in section 7); the 'main' Cerberus beamline, whereupon the beam propagates into the Cerberus multi-terawatt target chamber for further amplification, compression and use in laser-plasma

experiments with a focused intensity of $\sim 10^{19}$ Wcm^{-}2, and a supplemental 'interferometry' beamline, where the pulse is compressed to 500 fs for plasma interferometry.

4.1 Mode-locked Nd:Glass Master Oscillator

A mode-locked Nd:Glass master oscillator (GLX 200HP, Time Bandwidth Systems) produces a train of pulses (5 nJ, 250 fs, 70 MHz) centred at 1053.5 nm. Passive modelocking is governed by an intracavity semiconductor saturable absorber mirror (SESAM) which attenuates ASE from the diode-pumped Nd:Glass gain media and gives the system an excellent temporal contrast and near ideal sech^2 temporal profile, measured up to $1 : 10^9$ relative contrast [37]. A schematic view of the oscillator cavity is shown in figure 4.2, within the cavity are components which allow adjustment of the power, central wavelength and repetition rate. The oscillator cavity is initially seeded by the amplified spontaneous emission (ASE) of a diode-pumped Nd:Glass slab, CW pumped by two diode lasers (up to 2 W, 804 nm). Light from spontaneous emission initially builds up within the cavity until modelocking is initiated by a random noise spike in the ASE, whereupon modelocking is subsequently governed by a SESAM end cavity mirror. A SESAM is a semiconductor layer deposited over a highly reflective mirror, which preferentially reflects higher intensity light from within the cavity thereby suppressing ASE buildup and preferential reflection of higher intensity. The modelocked pulse duration is determined by the impulse response of the SESAM, the time taken for valence electrons to be excited into the conduction

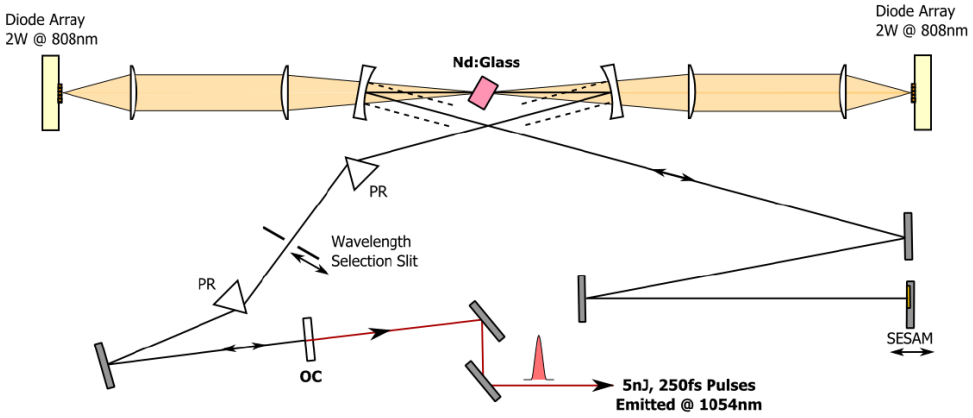


Figure 4.2: Schematic view of the Cerberus oscillator (GLX 200HP, Time Bandwidth Systems). A double-pumped (800 nm) Nd:Glass crystal amplifies light into a SESAM mode-locked optical cavity, generating a 70 MHz train of 5 nJ, ∼250 fs sech^2 pulses with a spectral bandwidth ∼4.7 nm. Image credit: Nicholas Stuart [36].

band and then decay, and the emission bandwidth of the cavity gain media, and the degree of intra-cavity dispersion compensation. Nd:Glass has a central gain wavelength of 1054 nm, however the central wavelength of the oscillator can be tuned by a pair of intra-cavity dispersion compensation prisms with a mechanical slit between them. The output of the Cerberus oscillator was chosen to be 1053.5 nm, a compromise between the central gain wavelengths of the two solid state gain media used on the system, Nd:Glass; 1054 nm, and Nd:YLF; 1053 nm. The spectral bandwidth was measured to be 4.7 nm (figure 4.3), for a modelocked pulse this would correspond to a transform limited pulse duration of 248 fs, given a sech^2 temporal profile. The temporal profile of the oscillator was measured using a second order SHG autocorrelator (the front end of the Cerberus FROG, described in chapter 3) with a FWHM sech^2 pulse duration of 251±5 fs, which is in good agreement with the previous published value of 255 fs [36].

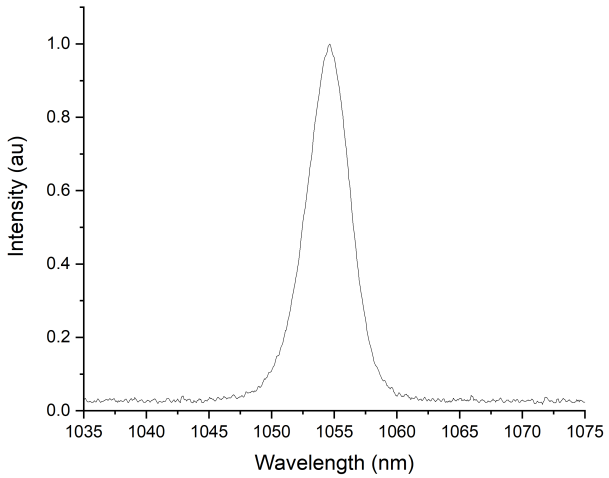


Figure 4.3: Spectral profile of the Cerberus oscillator (GLX 200HP, Time Bandwidth Systems), centered at $\lambda_0 = 1053.5$ nm with a measured bandwidth of 4.7 nm. Note: The spectrometer used here (Oceanoptics USB4000) gave a +1.5 nm spectral offset.

The output of the oscillator is split into two pulse trains, a Pockels cell is used to switch out a 10 Hz seed beamline from the 70 MHz oscillator pulse train, the remainder of which will be subsequently amplified, at 400 Hz, to the few mJ level and then used as a pump for the front-end OPA stages. By taking the pulses for seed and pump beamlines from the same oscillator as opposed to seeding from a separate source, the relative time delay between the two is only dependent on the optical path length of the system, 'optically locking' the beamlines to reduce timing fluctuations in the system that might otherwise be induced by electrical delay or timing jitter that would be present

in a system seeded and pumped by two separate light sources. Without electrical timing jitter, the relative delay can be precisely controlled by optomechanical elements for stability over long (up to 20 hour) operations.

As a consequence of optically locking the pump and seed timing though, it becomes very important to stabilise the oscillator pulse train frequency as drift due to thermal effects in the lab throughout the day can cause the cavity to expand, increasing the period between the pump and seed pulses which are switched out from the oscillator pulse train at different times. The global timing of the system is controlled by a rubidium atomic clock timing module (Stanford Research Systems DG645, Rb timebase option) which governs the Pockels cell switching out pulses from the seed beamline to the pump beamline. If the system is optically locked it expects a fixed period between seed and pump pulses, if, due to the cavity expanding, this period becomes too great then the pump may fall outside of the OPA gain window. In order to prevent this, the pulse train frequency is monitored by a photon counter (Stanford Research Systems SR400). Any deviation from the frequency set point, averaged over a 0.5 second counting window, is counteracted using a piezoelectric actuator (Thorlabs PAS009) which adjusts the cavity length accordingly. Figure 4.4 shows stable operation of the oscillator over long operation: despite varying lab temperature, the piezoelectric actuator keeps the oscillator pulse train frequency at a given setpoint of $70,004,000\ Hz$ with only a standard deviation of $\pm 3.91\ Hz$ during a period of 22.5 hours.

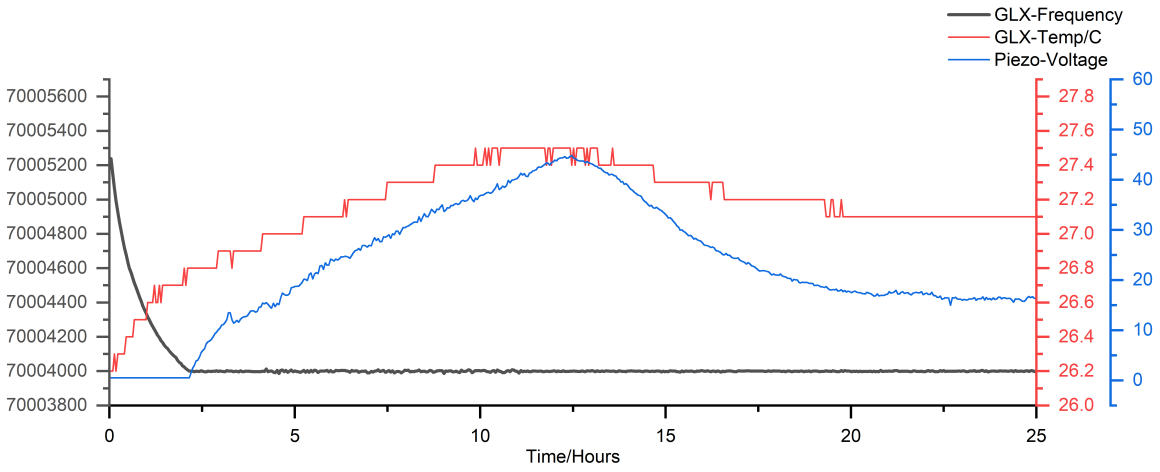


Figure 4.4: Cerberus Nd:Glass master oscillator (GLX 200HP, Time Bandwidth Systems) frequency locking stability over a 25 hour operational period. Drifts in temperature over time were corrected using a piezoelectric stage attached to one of the cavity end mirrors kept the cavity frequency stable to $\pm 3.91\ Hz$ over 22.5 hours

4.2 ps-OPA Pump Beamline

Light from the oscillator is split between two beamlines, using a fast (∼1ns rise time) Pockels cell, into a 10 Hz pulse train to seed the first nonlinear OPA stages, and a pump beamline which is subsequently temporally stretched and re-amplified. The following section outlines the OPA pump beamline which runs parallel to the seed beamline, amplifying pulses in order to pump the nonlinear OPA stages on the system and seed the long-pulse beamline which is delivered to our adjacent experimental target areas.

The pump beam is first stretched in a folded Martinez stretcher [28] to ∼240 ps (+147 ps/nm chirp). The stretcher is operated in a four-passed folded Martinez layout with a single 1740 lines/mm gold holographic diffraction grating (Spectrogon), light incident at a 70.2° angle is captured by a 2" diameter, 1m focal length acromatic doublet lens onto a flat 2" HR retro mirror, giving a 2.8 m total effective grating separation.

Once stretched, the pulse is injected into a regenerative amplifier cavity comprised of a convex mirror (f = -5 m) and a concave mirror (f = 2 m), arranged in a linear geometry either side of a 3 mm diode-pumped Nd:YLF module (Northrop Grumman RBA35-1C2). Pulses are actively switched in and out of the cavity using a a quarter waveplate and a fast BBO Pockel cell which determines the number of round trips the pulses take, for 43 round passes inside of the pump is amplified up to ∼3 mJ, a factor 10^6 gain with a single-pass gain of ∼1.25. Nd:YLF imposes significant gain narrowing effects however, over the 43 round passes within the cavity the bandwidth of the Regen signal is reduced to only 0.4 nm for an unmodified cavity. To account for this, a low-finesse, 500 um thick intracavity etalon was introduced, slightly attenuating the central amplified wavelength and thereby broadening the spectral wings of the pulse. This had the result of increasing the FWHM bandwidth of the output by a factor of ∼1.6, from 0.4 nm to 0.63 nm, improving the energy stability of that cavity as well as enabling a shorter pulse length for the front end OPA pump. Custom in-house antireflectivity coatings (titanium dioxide (TiO_2) + magnesium fluoride (MgF_2)) were also developed by Prof Roland Smith to limit the loss due to multiple passes through the etalon, these demonstrated high damage threshold (14 J cm^{-2}, 1.4 ns, 1053 nm) demonstrating optimum performance of >0.02% surface reflectivity.

The Regen ouputs up to ∼3 mJ pulses of ∼80 ps duration, stable to <1% RMS energy stability over long term (∼6 hrs) laser operation, this stability is crucial as instabilities seeded in the

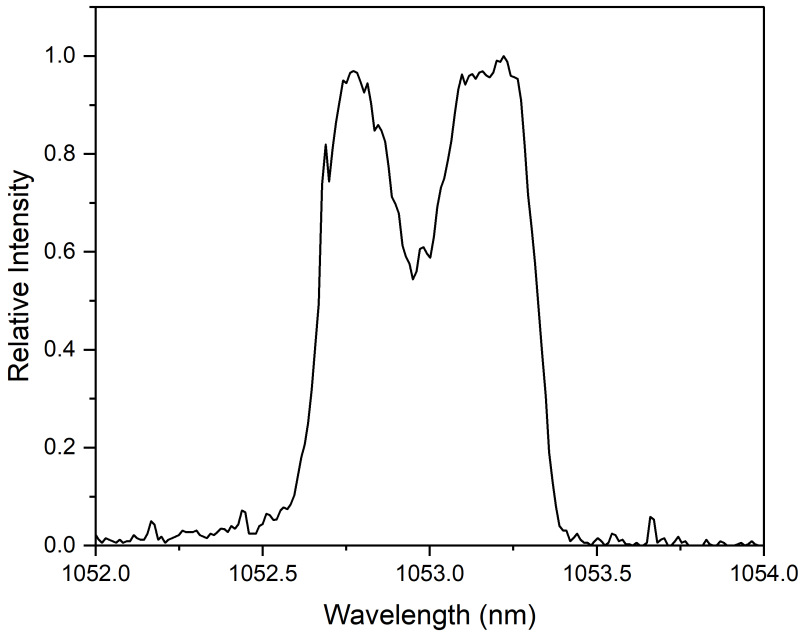


Figure 4.5: The spectral profile of the pulse amplified by the front end regenerative amplifier. The amplifier is based on a linear optical cavity, centered around a diode pumped Nd:YLF gain module. Significant gain narrowing produced over 43 round passes within the cavity is compensated for by a low-finesse, 500 um thick intracavity etalon, which enhances the bandwidth and produces the central dip seen in the spectrum.

Regen can significantly affect the energy stability of the OPA stages. The Regen cavity optical rails are made of 1" thick Invar rods which have a low thermal expansion coefficient to minimise thermal drift due to changes in the lab temperature. The optimum number of round trips inside of the cavity was determined by the number needed for the signal to reach saturation within a set limit for the diode module current, as the number of round trips determines the path length of the beamline relative to the seed. However, this has been since fixed at 43 round passes, seen on the top oscilloscope trace of figure 4.6.

The Regen is operated in a saturated regime for greatest energy stability, by controlling the power of the input seed from the pump beamline Martinéz stretcher and the single pass gain inside of the cavity. The seed power is set by a waveplate before the pump beamline Martinez stretcher, using the stretcher grating as a polariser and the single-pass gain can be controlled by changing the diode current applied across the Nd:YLF gain stage. As can be seen from figure 4.7, increasing the total gain also improves the stability of the output of the Regen, to a maximum $\sim$0.5 %RMS

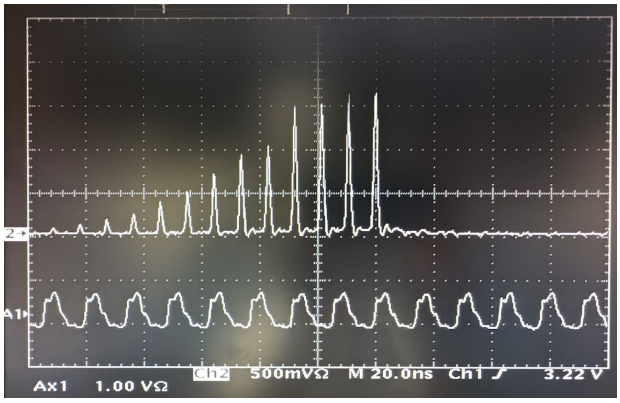


Figure 4.6: The oscilloscope trace of top) the regenerative amplifier rolling over into energy saturation bottom) oscillator pulse train, measured at ∼70 MHz

energy stability over ∼20 minutes of laser operation. Additionally, the highest energy stability was found when the seed power was set at the minimum point where the Regen round passes still began to roll off into saturation.

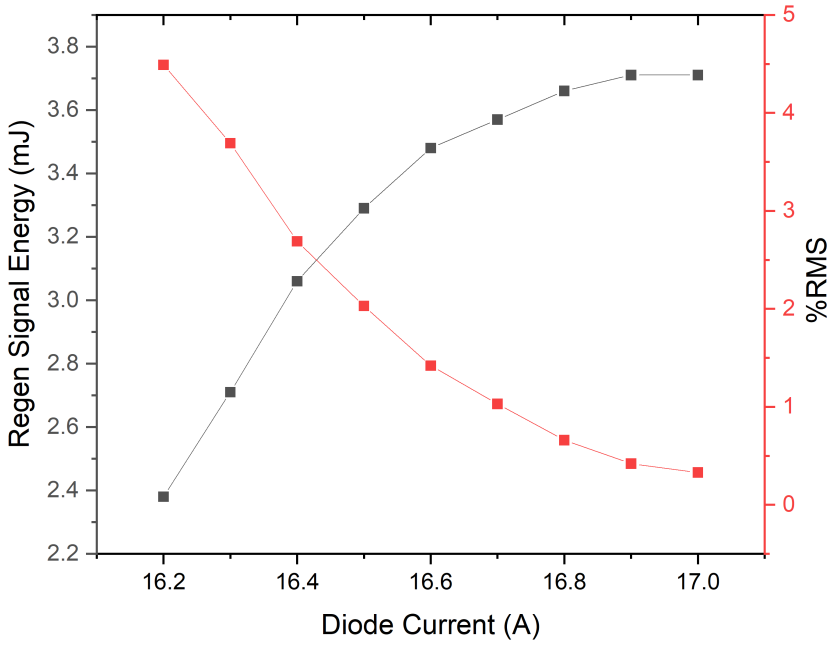


Figure 4.7: The total output energy and %RMS energy stability measured across ∼20 minutes of operation, with respect to the current applied across the Nd:YLF gain module at the centre of the Regen cavity.

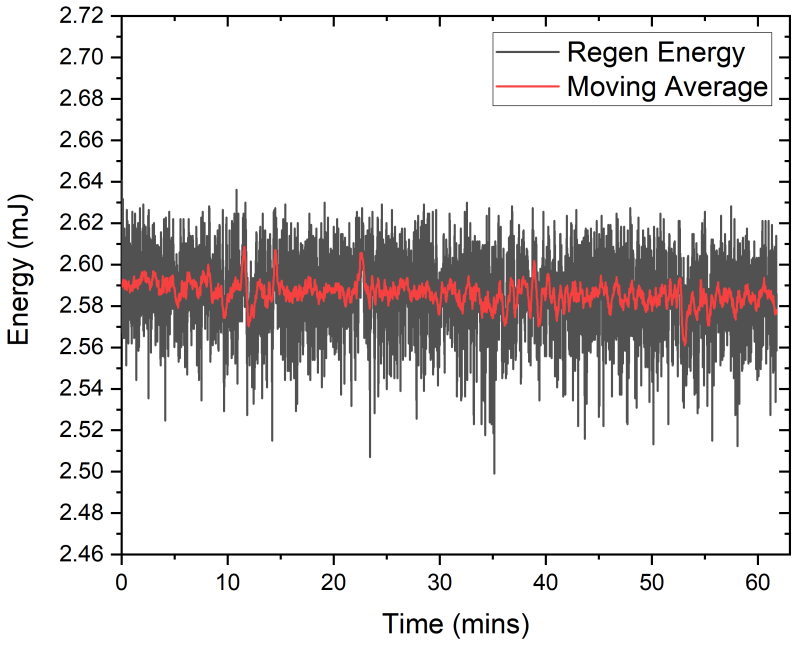


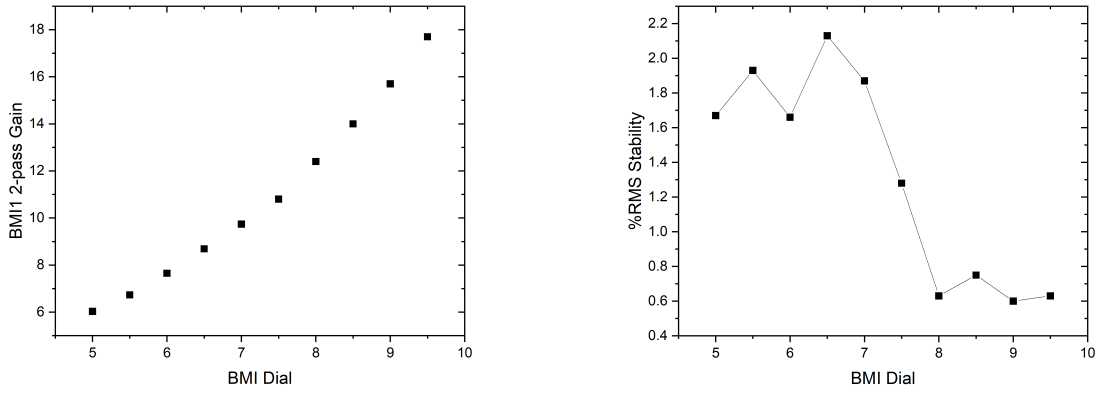
Figure 4.8: The output energy stability of the Cerberus linear regenerative amplifier over 1 hour of operation, stable to <1% RMS. This figure displays the recorded output energy at a sampling rate of 1/400 pulses, or once per second.

As a precaution, a Terbium Gallium Garnet (TGG) Faraday rotator and polariser prevent the amplified output of the Regen back-propagating to the Martinéz stretcher and oscillator and damaging earlier components in the system.

To reach the energy required to pump the OPA stages, we next amplify with a succession of larger aperture 10Hz Nd:YLF flashlamp amplifiers, each operated in a double-pass configuration in order to maximise each gain stage. Nd:YLF was chosen as the gain media for the pump beamline as its cross-sectional gain is greater than Nd:Glass; $\sigma(10^{21}\ cm^2) = 142$ versus $\sigma(10^{21}\ cm^2) = 34$ [36], and matches the central gain bandwidth well. Nd:YLF does cause appreciable gain narrowing, as seen in the Regen, which would make it unsuitable for final amplification; however, it is a good candidate for narrowband pump beams, and being crystalline, has good thermal conductivity and can be run at 10 Hz enabling real time optimisation of the system front end. While contrast is of paramount importance for the main beam, OPA affords some forgiveness in the pump beam's contrast. The OPA process only occurs when both seed and pump are temporally overlapped, and whilst parametric fluorescence is non-zero [14] ASE present in the pump is largely not present in the amplified signal. This means we are free to use 'cruder', and less exacting amplification

process for our pump beam including flashlamp amplifiers. The time for a flashlamp to reach population inversion is 'long timescale' compared to the rest of the system.

At the first Nd:YLF amplification stage (BMI 1), a 7.5 mm rod diameter is flashlamp pumped at a level needed to to amplify to signal to ∼30 mJ. The amplifier is double-passed by retroreflecting the beam back through and using a Faraday rotator to separate the input and output beams. The Faraday rotator is also important as Nd:YLF is birefringent, therefore the input polarisation must be carefully set to match the rod axis, and circular polarisation (as used to double pass a glass amplifier) must be avoided. For a ∼3 mJ, 0.8% RMS Regen signal, figure 4.9 shows the double-pass gain and percentage RMS stability of the amplified pulse over an operating period of several minutes. From this, we see that the gain rises with increased voltage applied over the flashlamps as we would expect. However the %RMS stability of the amplified pulse appears to operate at two levels, dropping to a more stable operation (∼0.65% RMS) as the BMI dial passes 7.5.

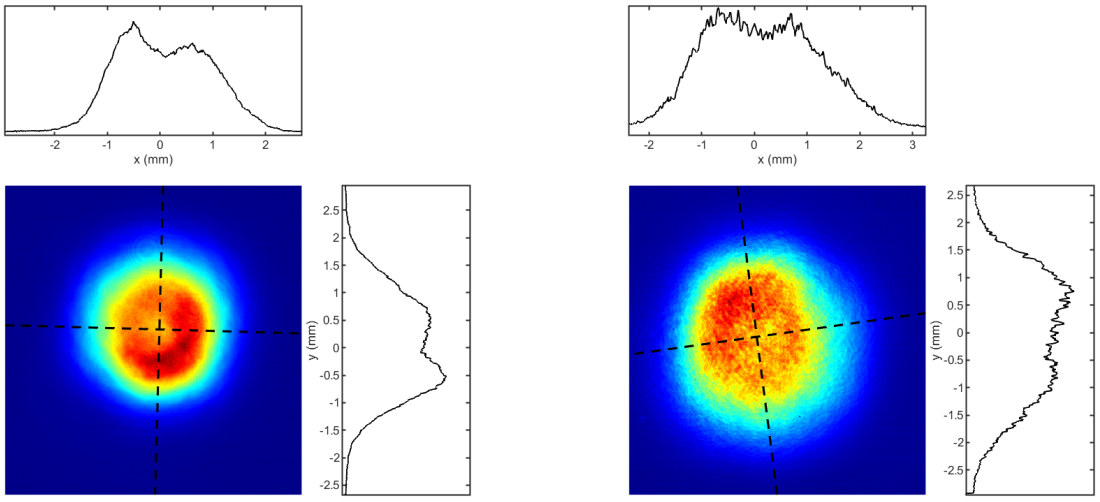


(a) (b)

Figure 4.9: The gain from the first Nd:YLF flashlamp pumped gain storage amplifier in the Cerberus pump chain.

Vacuum spatial filters (VSFs) are used between each major stage of the pump beamline in order to recover the spatial quality of the pump beam, a crucial feature for efficiency and good spatial quality in the OPA process, "the quality of the amplified signal is directly related to the temporal and spatial intensity distribution of the pump pulse" [84]. By focusing through a pinhole under vacuum, high spatial frequencies at the Fourier plane, which resolve away from the centre of the optical axis, are blocked. VSFs are commonly used in conjunction with serrated aperture

transmission masks, where the high spatial frequency structure of the serrated edge is filtered by the VSF, producing a pseudo top-hat spatial beam profile which allows for good spatial profile matching and smooth amplification in the subsequent OPA stages in the system. Figure 4.10 shows spatial profile enhancement due to the VSF after the output of the first Nd:YLF amplifier.



(a) (b)

Figure 4.10: Spatial profile of the amplified pump pulse a) before and b) after spatial filtering using a vacuum spatial filter (VSF). The telescope arrangement of the spatial filter inverts the spatial profile of the beam from a) to b).

From the output of this VSF, the ∼30 mJ output of the first amplifier is split 1:2, ∼10 mJ is taken to pump the first two ps-OPA stages: first compressed for the ps-OPAs are compressed to ∼10 ps with a paralell-grating configuration compressor, folded around a single 1740 lines/mm gold holographic diffraction grating (Spectrogon) and double-passed with a total efficiency of ∼40%. The temporal profile of the compressed pump pulse was measured using the second-order autocorrelator front end of the Cerberus FROG (described in 3.2) which gave a FWHM compressed pulse duration of 12.2±0.8 ps. The compressed ps-OPA pump pulse was characterised using the Cerberus FROG (described in section 3.2). Figure 4.11 shows the FROGed retrieval of the ps-OPA pump beam for the measured spectrogram obtained using the Cerberus FROG, which gives a retrieved FROG trace with an associated dimensionless retrieval error of 0.014, which is comfortably below the threshold for 'good retrieval', set at 0.02. High order spectral phase is clearly visible on the retrieved FROG data, most likely due to the intracavity elalon in

the regenerative amplifier which spectrally reshapes the Regen bandwidth over 43 round trips. High order phase in the OPA pump will transfer to the idler but not the seed beam in the OPA, therefore this was not expected to have significant negative impact on the ps-OPA performance. High order phase does affect the recompressibility of the pump, the time bandwidth product for the pump pulse ($\Delta\lambda$ = 0.6 nm) was predicted to be 2.71 ps. However the pump pulse is not designed to be fully compressed, as a longer pump duration provides smooth gain across the seed pulse in the OPA stages.

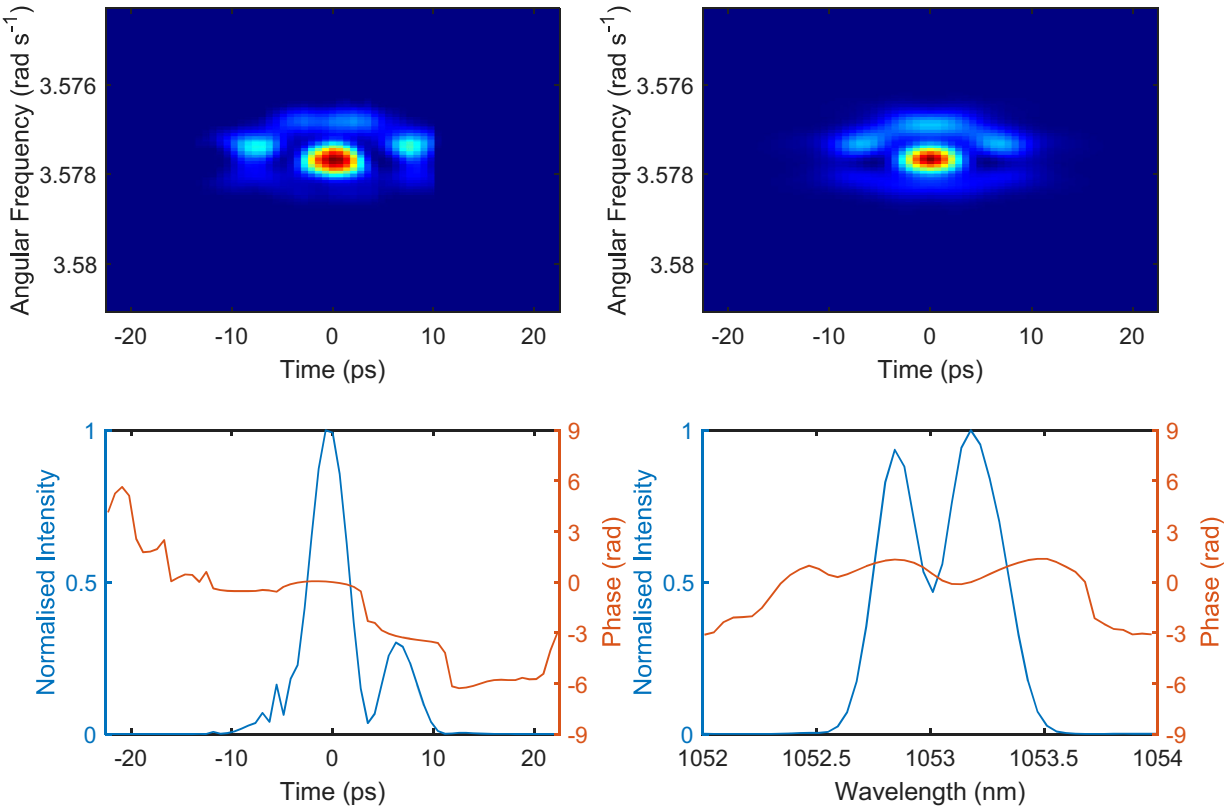


Figure 4.11: FROG retrieval of the ps-OPA pump beam. Top left: the measured spectrogram obtained using the Cerberus FROG, top right: retrieved FROG trace from FROGed code, bottom left: temporal, and bottom right: spectral profiles of the retrieved FROG trace. Retrieval error of 0.014.

4.3 ps-OPA Stages

The ps-OPA provides initial high gain stages for the Oscillator seed pulse, up to $\sim 2 \times 10^6$. Figure 4.12 shows a schematic view of the ps-OPA beamline, consisting of two degenerate OPA amplifiers each with a 6 ps gain window; a 1.2 ps pulse duration seed is amplified first by a 6.5 mm type I BBO crystal where a 5 nJ seed is amplified with a gain factor of $\sim 10^4$, followed by a 2 mm type I BBO stage with a $\times 16$ gain.

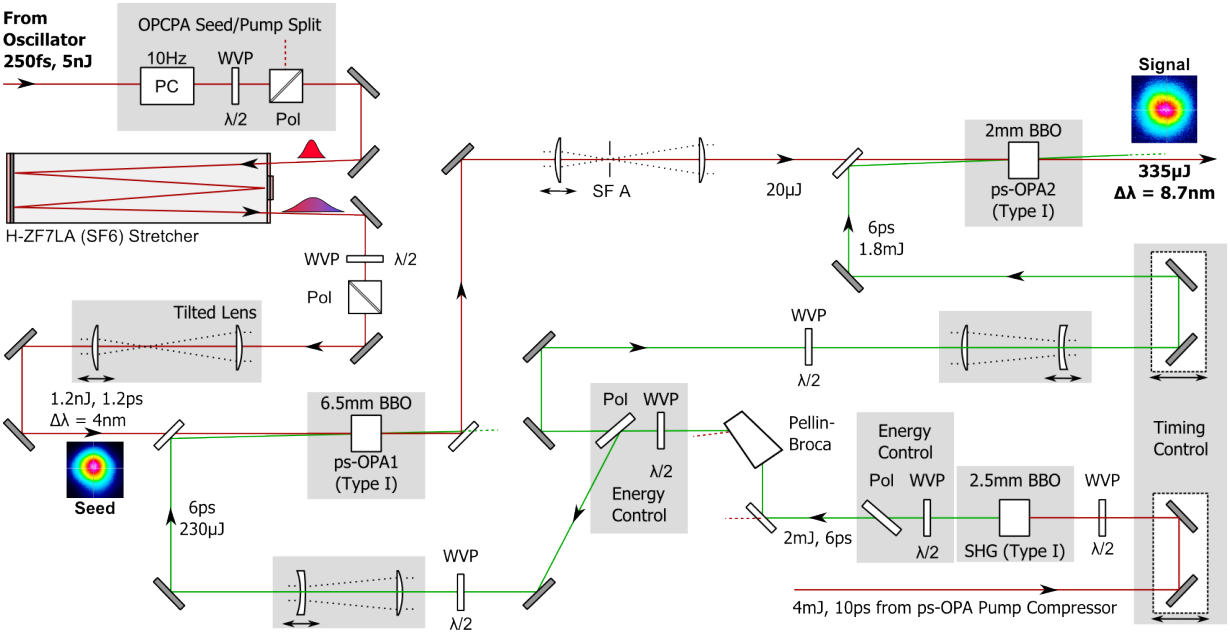


Figure 4.12: Schematic diagram of the ps-OPA stages at the front end of the Cerberus laser system. A ~5 nJ pulse is amplified through two successive OPA stages for a total gain factor of $\sim 2 \times 10^6$. Image credit: Nicholas Stuart [36].

4.3.1 ps-OPA Seed Pulse

The 10 Hz selection of the Oscillator, to seed the ps-OPA stages, is first temporally stretched from 250 fs to 1.2 ps (corresponding to a chirp of 1.06 THz/ps) using a 30 cm long high-index H-ZF7LA (SF6) bulk glass stretcher, four passed using highly reflective mirror surfaces coated directly onto the glass block ends for a total internal propagation length of 1.2 m, with transmission efficiency >73% in a four-pass geometry. During the annealing process, due to internal stress of the SF6 block, a slight cylindrical lensing term was introduced corresponding to approximately a f = -20 m cylindrical defocus in the vertical plane. This is accounted for by introducing an astigmatism term into a subsequent up-expansion telescope by tilting the first lens the first lens vertically to

compensate for the cylindrical focus and collimate the beam. This pulse was characterised using the Cerberus FROG, with the retrieved FROGed tace shown in figure 4.13. The retrieved trace shows smooth second-order linear chirp due to the SF6 glass stretcher.

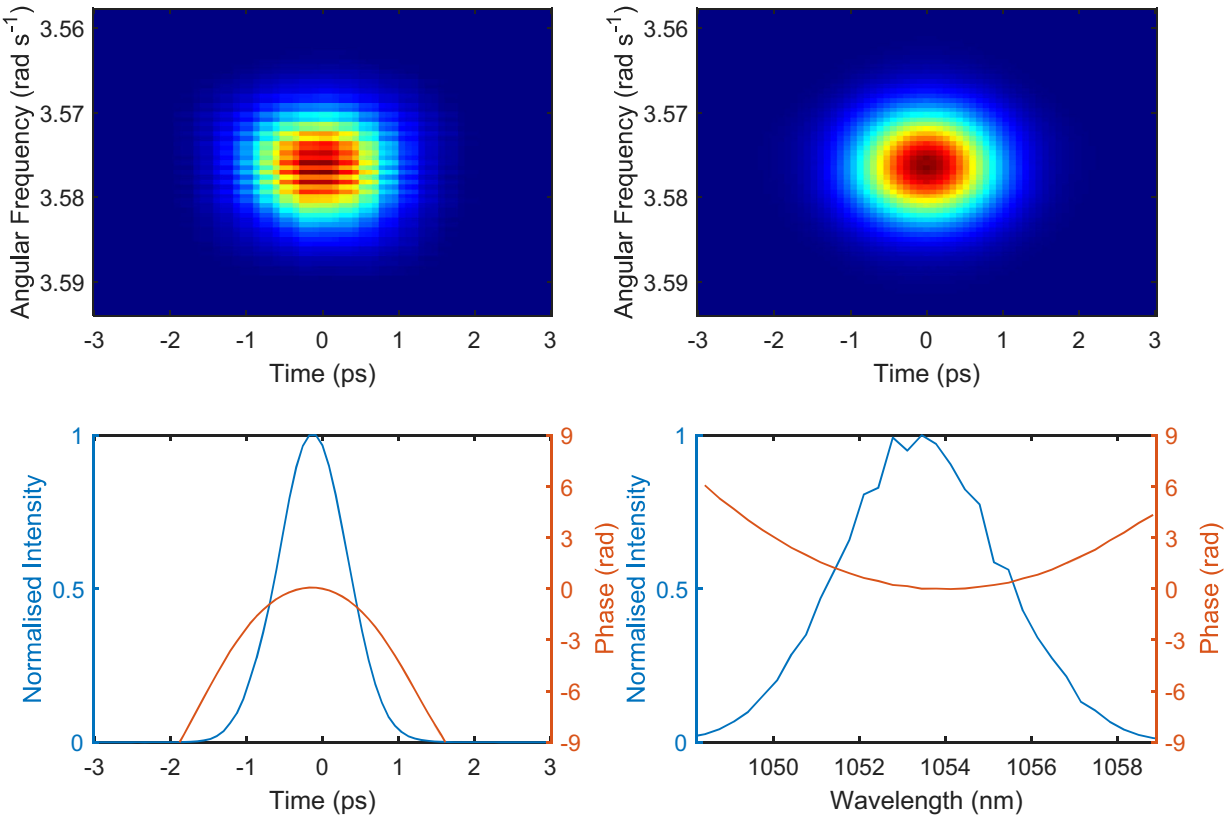


Figure 4.13: FROG measurement of the Cerberus OPA seed pulse. Upper left: measured taken with the Cerberus frog, upper right: analysed using the FROGed algorithm by Matthew Streeter [72], lower left: retrieved pulse vs time, lower right: retrieved pulse vs wavelength. The Frog retrieval error in this measurement was 0.012.

4.3.2 ps-OPA Pump Pulse

Each stage is pumped by the second harmonic of the pump beamline produced before each stage via SHG. The compressed ∼10 ps, 4 mJ pump beam is frequency doubled in a 2.5 mm BBO SHG stage, at an efficiency of ∼60% corresponding to compressed pump pulses up to 2 mJ, 6 ps. The pump duration was chosen to be significantly longer than the stretched seed such that it is temporally smooth over the duration of the seed, and therfore should not produce any modulation of the chirped signal's spectrum. Given the maximum pump energy for the 2.5 mm BBO, due to damage threshold of the coatings, as given by the manufacturer, is quoted at 2.5 GW cm^2, ∼7.5

mJ.The ps-OPA SHG signal was measured with an energy stability of 0.6% RMS over a period of >1 hour, which helps to provide a stable gain platform for the ps-OPAs

4.3.3 ps-OPA Results

In the initial two-stage ps-OPAs a 1.2 ps signal is amplified by a compressed 6 ps pump pulse achieving a gain of 10^4 through OPA1 (6.5 mm BBO) and then subsequent lower additional gain of 15 through OPA2 (2 mm BBO). Somewhat obviously, OPA (a parametric process) is heavily dependent upon the laser parameters: principally the beam intensity, spectrum, pointing and relative delay between seed and pump pulses and as such we need to actively control these parameters in order to optimise, and keep optimised, the OPA stages whilst the laser is operational. Timing control counteracts small scale timing drift due to thermal effects in the system such as the Regen cavity length changing due to thermal effects. Timing can be controlled with a global delay stage and delay stage for OPA2 which together allow the relative timing to be adjusted seperately for each stage. Turning pump mirrors before each stage can be used to adjust beam pointing to ensure good spatial overlap. Good spatial matching prevents the manifestation of detrimental effects such as parametric fluorescence and spatial chirp in such cases where the pump pulse does not overlap with the signal. Finally, the energy split from the SHG signal to pump each stage is controlled in two parts, rejection after the SHG stage and waveplate split OPA 1 and 2 pump energy.

Figure 4.14 and figure 4.15 show the amplified pulse energy and energy stability over ∼600 shots, obtained from OPA1 and OPA2 respectively as the input pump energy was varied.

The ps-OPAs are operated in a noncollinear geometry with a phase matching angle of ∼3.65°/0.064 rad. The non-collinear angle between pump and seed, whilst in some applications is used in order to increase the phase-matching bandwidth, here simply allows the residual pump light to be easily picked off from the beamline. The direction of the non-collinear angle was also chosen to be in the direction of spatial walkoff to limit this effect. Between the OPA stages, the beam is up-expanded using a telescope with a spatial filter, which was included to eliminate wide-angle parametric fluorescence emission that may seed the remaining down-stream amplifiers.

Using a two-stage configuration such as this, specifically where the high gain first stage ($\sim 10^4$) operating below saturation is supplemented by a saturated lower gain second stage (∼15) we limit

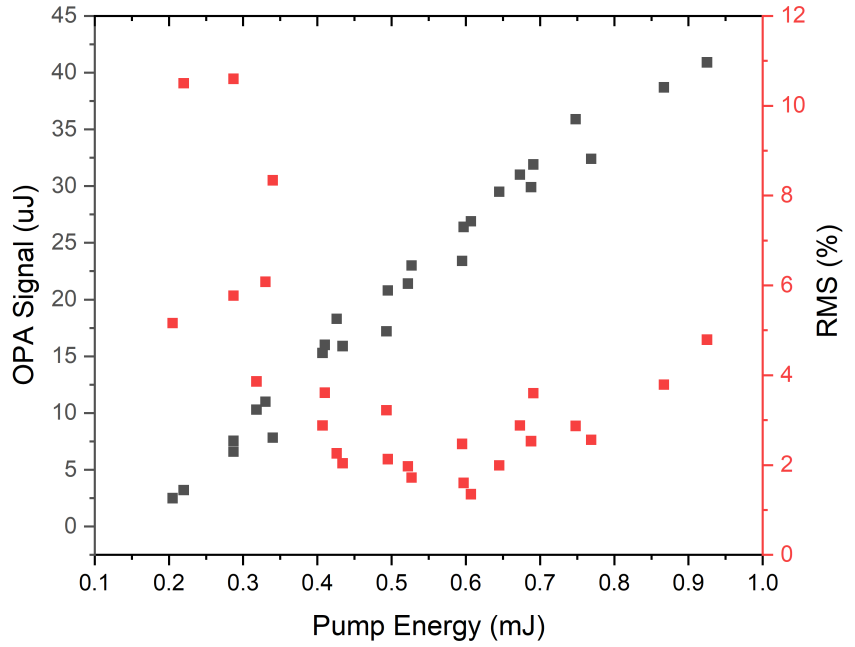


Figure 4.14: the amplified pulse energy and energy stability over ~600 shots, obtained from OPA1 with respect to the pump energy.

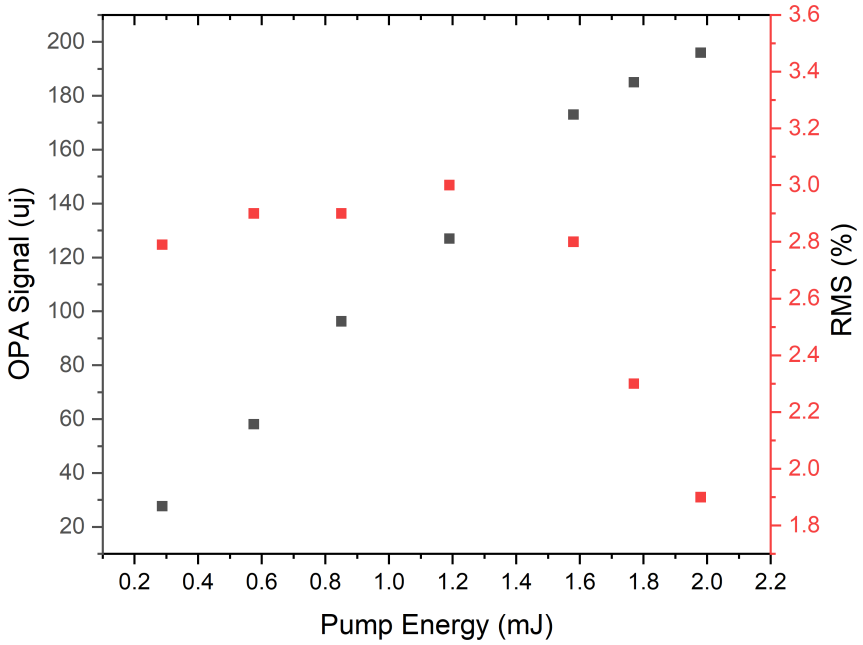


Figure 4.15: the amplified pulse energy and energy stability over ~600 shots, obtained from OPA2 with respect to the pump energy.

parametric fluorescence [14] and generate additional bandwidth and increase energy stability by operating near the saturation/pump depletion regime [85]. However the saturation regime causes the spectrum to be reshaped – enhancing the wings of the Gaussian spectral profile. The spectral gain profile of an OPA stage is determined by the pump pulse, a Gaussian pump pulse will not produce uniform spectral gain and instead the intensity peak of the pulse is preferentially amplified, leaving less gain out in the wings of the Gaussian. As the process begins to saturate, high intensity components of the pulse are subject to back-conversion as energy is coupled from the signal into the pump wave whilst the wings of the Gaussian spectral profile are amplified. This enhances the bandwidth of the pulse [85]. Figures 4.16 and 4.17 shows the bandwidth enhancement of the OPA signal with increasing pump energy.

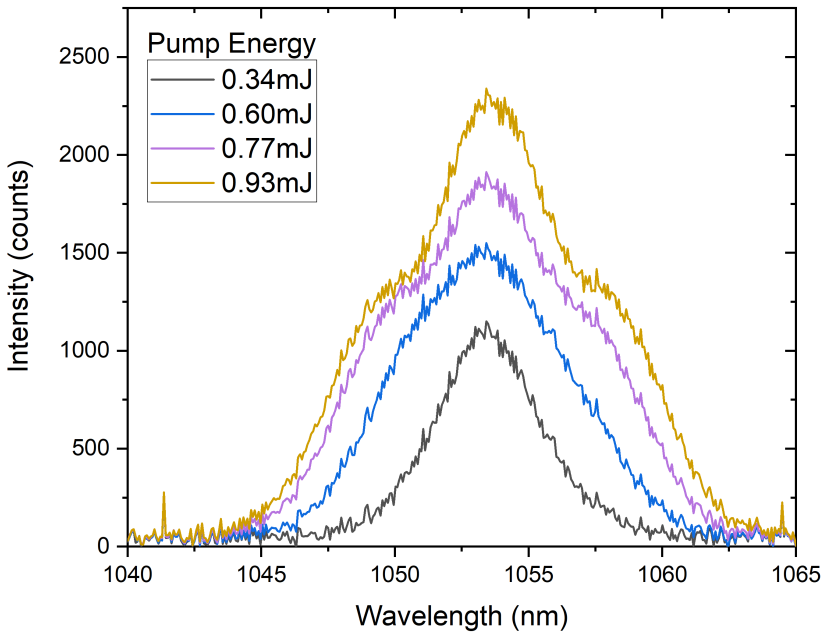


Figure 4.16: Spectral profiles of OPA1 with respect to increasing pump energy.

The shot-to-shot variation of the ps-OPA pump beam and OPA2 signal positions were measured using a WinCamD-LCM beam wander calibration measurement, taking the beam centroid positions at 10 Hz operation over a period of 600 s and then calculating the RMS deviation of the centroid position. From this measurement, the beam pointing stability of the OPA1 pump was found to wander by 40.46 µm within the crystal and the OPA2 pump beam by 69.1 µm.

Stable operation of the ps-OPAs over 50 minutes operation is shown in figure 4.18, with a <2%

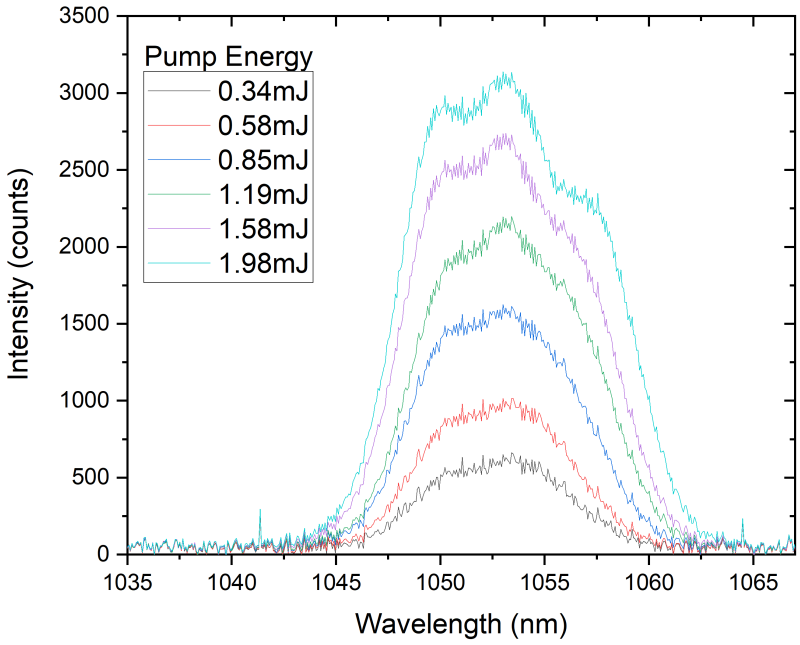
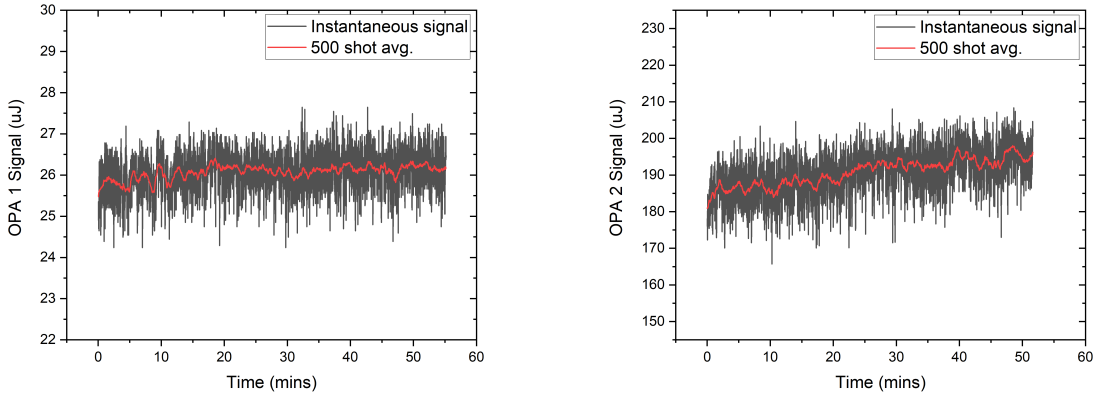


Figure 4.17: Spectral profiles of OPA1 with respect to increasing pump energy.

RMS energy stability over this operational period.



(a) (b)

Figure 4.18: The signal energy of the ps-OPA stages, a) OPA1 and b) OPA2, over <1 hour operation.

4.4 ns-OPA Beamline

The amplified and temporally windowed ∼200 μJ signal pulse from the ps-OPAs is temporally stretched with ∼200 ps/nm chirp in an Öffner-configuration stretcher [30], [86] to a duration of 1.8 ns before the final front-end ns-OPA amplification stages. In this Öffner configuration, light is injected at a grating angle of 77° onto a 1740 lines/mm multilayer dielectric coated reflective diffraction gratings (Plymouth Grating Laboratory). Rather than a lens, light is focused onto a retroreflecting focal plane by a combination concave and convex mirror pair which gives an effective grating spacing of 1.14 m. Rather than optimising the grating angle for dispersion, the diffraction gratings were instead oriented at a steeper grating angle of 77 degrees to prevent bandwidth clipping on the optics which otherwise degrades contrast. The supported bandwidth acceptance of the Öffner is ∼20 nm, limited by the size of the optics, and their associated cost.

The stretcher is four-passed in similar manner to the Regen Martinéz and as with the Regen Martinéz stretcher, we invert the beam after the second pass by focusing with a lens onto a flat retro-mirror to spatially invert the effect of aberrations on the beam profile.

The remaining ∼20 mJ, from the pump beamline split between the ps and ns OPA pump, is propagated along a 6.9 m, 23 ns optical delay stage to account for additional path length in the seed beamline before it is stretched in a parallel two-grating configuration pulse stretcher to ∼1.4 ns.

Two 1740 lines/mm gold holographic gratings (Jobin Yvon) are aligned in a parallel arrangement with ∼59° incidence angle and ∼5.6 m grating separation which add negative dispersion to stretch the pulse. This is the opposite chirp direction to the seed pulse, however, as the pump beam is narrowband (<1 nm bandwidth) this has little effect upon the ns-OPA stages. The incidence angle is a limitation of the gratings used, the efficiency of which drops off at large angles, due to this factor and the narrow pump bandwidth the large grating separation is required to compensate, in this arrangement the stretcher operates with a transmission efficiency of ∼25%.

Beam drift can produce significant misalignment in this stretcher as a combination of the long internal beampath in conjunction with the 6.9 m optical delay prior to injection. Misalignment reduces the transmission efficiency and may also introduce spatiotemporal couplings into the beam such as spatial chirp. An active beamsteering system is therefore used to compensate for this and the injection onto the first grating is controlled monitored and actively adjusted with a

motorised mirror (Newport Agilis AG-M100).

A combined serrated aperture and VSF cuts the output of the long pulse stretcher to a super-Gaussian beam profile (figure 4.19) which is image relayed through two subsequent lamp pumped 10Hz double-passed Nd:YLF amplifiers, BMI 2 and BMI 3. Image relay is an important concept in laser design where the spatial profile of the laser at one point is relayed along the beamline using a series of telescopes, it is especially important where a given spatial profile is necessary. In this case, a super-Gaussian spatial profile draws uniform gain across the profile from the amplifiers but also is less susceptible to self-focusing inside of the laser rods, potentially causing damage.

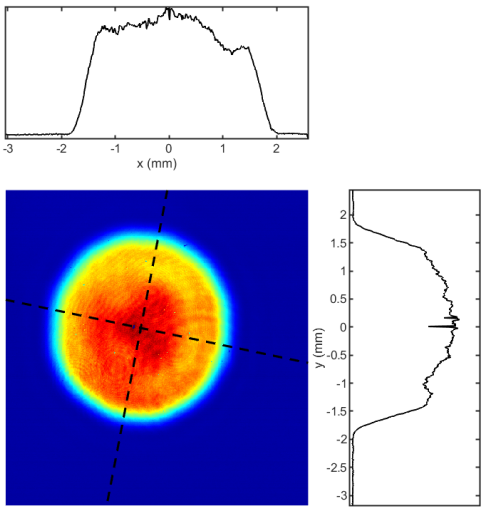


Figure 4.19: Spatial profile VSF3 out, super-Gaussian

The two subsequent gain stages that follow are double-passed Nd:YLF flashlamp amplifiers, in a similar configuration to that which was described previously a 7.5 mm rod diameter stage amplifies the stretched pulse from 4 mJ up to 40 mJ before final amplification at a 9.5 mm Nd:YLF rod diameter stage, rated to produce up to 400 mJ with very good energy stability up to 0.5% RMS over sustained operation. BMI 2 shares a common pulsed power drive system with BMI 1, meaning the two must be operated in concert. The first amplified is limited to <30 mJ in order to prevent damaging the in-line Faraday rotator, this places a limit on the performance of the second amplifier.

BMI 3 operates on a separate driver circuit to the other two amplifiers on the system, this allows for flexibility in the way we run the laser but also affords a degree of freedom in how the amplifier

is seeded. Although the amplifier is rated up to ∼400 mJ, only 180 mJ is practically required for good operation of the ns-OPA stages, we typically limit the output by running at a lower dial setting which preserves the lifetime of the amplifier. Figure 4.20 shows the performance of BMI 3 for a fixed input analogous to typical laser parameters during normal operation of the system (8.5 dial, 19.3 mJ input). We demonstrate here a 2-pass gain up to and exceeding a factor of 10 for an amplified pulse energy comfortably above the required 180 mJ.

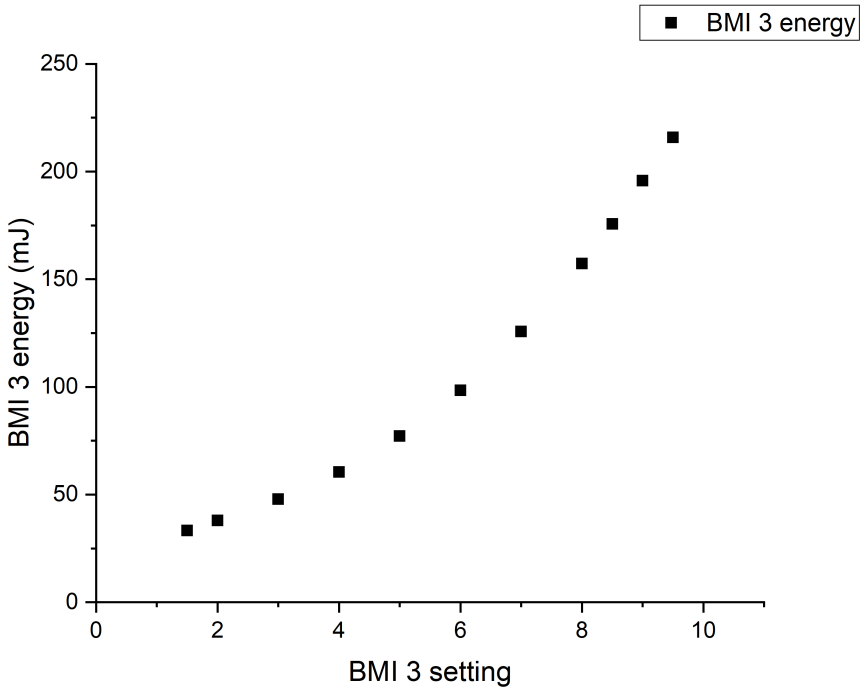


Figure 4.20: The performance of a 2-passed 9.5 mm diameter Nd:YLF flashlamp amplifier relative to the setting of the pulsed power drive system which controls the voltage applied across the flashlamps

BMI 3 energy stability was shown to be highly dependent on stability of the input beam, with the stability seen to be dependent dependent upon the input % RMS. Unlike BMI 1 and 2 which both demonstrate levels of energy stability associated with the driver setting, BMI 3 is driven on a separate circuit. This provides evidence that minor instabilities in the BMI 1 and 2 are seeded by the driver circuit.

4.5 ns-OPA Stages

The stretched seed output of the Öffner is injected into two further OPA stages, OPA 3 and 4. The stages are pumped by the long pulse beamline which is frequency doubled in using a 30 mm type-II phase matching KDP stage with conversion efficiency of ∼60%. Up to 25 mJ of pump light amplifies the Offner output in OPA 3 (12 mm BBO type I phase matching) and up to 50 mJ is used for pumping OPA 4 (8 mm BBO type I phase matching) up to an energy of 8 mJ, ∼4 nm spectral bandwdith with <1% RMS stability.

4.6 Nd:Glass Amplifier Beamline

Amplification to ∼1 J is accomplished using a series of Nd:Glass flashlamp amplifiers. we finally amplify the 10 Hz OPCPA front end pulse up to energies of >1 J using a series of Nd:Glass flashlamp amplifiers. Up to three Nd:Glass flashlamp amplifiers can be operated independently, including two 7 mm diameter rod amplifiers, each with ∼4 factor single pass gain, and a single 16 mm diameter rod amplifier with up to ×15 single-pass gain. The beam is image-relayed by several VSF telescopes througout this stage in order to maintain a super-Gaussian pulse shape which suppress self-focusing and formation of hot-spots from any dusty/slightly damaged optics that may imprint high spatial frequencies on to the beam profile.

A strong magnetic Faraday isolater sits at the end of the glass beamline, in order to reject back-propagating light which can be reflected back along the beampath by plasma in the main target area. If not rejected, this light may potentially damage sensitive optics upstream.

The front-end terminates where these pulses are split using a $\lambda/2$ waveplate-polariser combination between two beamlines. Typically the energy split is set to be approximately 1:2, with the majority of the light being sent to an adjacent lab for further amplification, compression and use in experiments. The remainder of the energy is directed to the 'interferometry beamline', where it is first compressed to 500±50 fs using a pair of 22 cm wide, 1740 lines/mm gold holographic gratings (Jobin Yvon) operated in a Treacy-style configuration with an effective grating distance of ∼2.3 m, with a 14 nm spectral acceptance. At the output of the pulse compressor, the large ∼2" beam diameter is down-collimated by an f = 500, f = -200 mm lens pair to a beam diameter, at $1/e^2$, of 10±1 mm. The interferometry beamline provides either a measurement of the OPCPA

front-end temporal intensity contrast, by directing light into the Cerberus X-TOAD diagnostic (described in 3.3) or can be sent through to the multi-terawatt target area to be used as an optical probe for plasma electron density measurements, described later in this chapter in section 7.2.2.

The Cerberus main pulse beamline undergoes final amplification through a liquid-cooled 500 mm diameter Nd:Glass flashlamp pumped amplifier with a gain factor of ∼20 before compression to ∼10 TW pulse energies using a pair of 28.5 cm wide, 1740 lines/mm multilayer dielectric coated diffraction gratings (Plymouth Grating Laboratories) operated in a z-configuration, with a total transmission efficiency of ∼60%. Dielectric coatings provide a high damage threshold for sub-ps pulse compression, approximately four times that of gold holographic diffraction gratings. Theoretically this compressor is capable of supporting up to 20 J input pulse energies, however the acquired B-integral of compressing pulses at this energy would reach the threshold for nonlinearity. Current plans for an upgrade to the Cerberus laser system involve compressing under vacuum in order to avoid self-phase modulation or self-focusing before the beam reaches the target. The vacuum compressor chamber designed by Timothy Robinson [19], constructed from aluminium with internal dimensions of 2.80 × 0.93 × 0.5 m (length, width, height), has been delivered to the multi-terawatt lab at the time of writing and is awaiting installation.

Chapter 5

Contrast Enhancement Technique using Hollow Core Fibre

Spatial filtering techniques help to regain good beam quality; necessary for delivering a high focused laser intensity, as well as to prevent aberrations or hot-spots in the spatial profile leading to damage in optical systems. Moreover, problematic spatiotemporal couplings may manifest in a laser due to unwanted aberrations or non-optimal spatial profiles. Without the ability to filter these unwanted couplings from a laser, small pulse-distortions such as pulse-front tilt, angular dispersion and poor spatial quality, originating from user misalignment, amplifiers or beam pointing instabilities quality can propagate along a beampath, to the detriment of the final focused pulse intensity. Therefore there is need to maintain (or recover) the spatial, temporal and spectral quality of a pulse as it propagates along the beamline. In an effort to examine possible pathways for improving the temporal-intensity pulse contrast of the Cerberus laser system we have explored the use of cylindrical dielectric waveguides, hollow core fibre (HCF), as a tool to modally filter and homogenise the spatiospectral profile of Gaussian laser pulses generated from noncollinear optical parametric amplification (OPA) stages.

As discussed in section 2.2.1, sources of spatial chirp and angular dispersion from noncollinear optical parametric amplifiers (OPAs) and high order phase due to non-ideal optical paths through stretchers and compressors introduce spatiotemporal couplings which reduce the focused intensity of a laser. In the case of noncollinear OPA, spatial mismatch between the signal and pump pulses due to the noncollinear geometry has been shown to impose spatial chirp, angular dispersion and

pulse front tilt [54]. Additionally, high gain OPA often requires long (> 5 mm) nonlinear crystals where lateral and temporal walkoff between the pump and seed beams due the noncollinear angle and relative group velocities of the beams propagating in media, exacerbates the spatial mismatch between the pump and seed beams. Noncollinear OPA stages may manifest spatiotemporal couplings such as angular dispersion and pulse front tilt, these factors may be compounded in stretchers and compressors which are highly susceptible to internal misalignment. Poor spatial quality in the input due to aberrations present in the beam or pointing instabilities will affect the effective input angle and contribute to non-ideal ray paths in a stretcher system, causing parts of the beam to acquire non-linear chirp terms that may not be properly compensated by the compressor. Additionally, antiparallelism of the gratings can introduce uncompressible quadratic chirp terms, angular dispersion and pulse-front tilt [50], [51], [87] and attempting to compensate for spatial chirp in CPA systems further introduces high order phase which limits the minimum compressed pulse duration and minimum focal spot size [52], [88].

There are several different methods which enable spatial filtering or amplitude modulation of the front end pulses of a laser system, including inserting pinholes at the focal plane of a telescope such as with vacuum spatial filters (VSFs), Acousto-Optic pulse modulation (Dazzlers) [89], cross-polarised wave generation (XPW) [90], Bragg gratings [91], or through gain shaping in OPA stages [92]. However, many of these techniques are complex, expensive or difficult to integrate into systems with the parameter space of the Cerberus laser system, such as with the case of XPW where in ps-domain systems the crystal damage threshold approaches the threshold for the nonlinear process or Bragg gratings which are themselves susceptible to user-induced grating misalignment errors. VSFs, however, are commonly used to recover the laser beamfront spatial quality, which use a pinhole to filter high order spatial modes from the beam at the focal plane of a telescope. At the Fourier plane, high order spatial frequencies do not focus to within the pinhole diameter and are therefore removed from the spatial profile. VSFs are compatible with high power lasers systems as the beam is often focused partly or completely under vacuum, preventing breakdown of air at the focus. There is some complexity associated with installing VSFs into a laser system, as they require vacuum pumps and plumbing to operate. Loss or degradation in the vacuum can result in a steep drop in the beam spatial quality, energy and stability due to the laser breaking down in air at the focus.

In this section, we present a technique leveraging the modal filtering and waveguide properties

of hollow core fibre with core diameters in the few 100 micron range for spatially filtering and homogenising spatiotemporal distortions including spatial chirp and angular dispersion and improving the pointing stability of a beam. Hollow core fibre confines light to within a central region bounded by higher refractive index media. Whereas optical step-index fibres confine light via total internal reflection (TIR), a hollow waveguide cannot confine light via this mechanism, in the case where the wavelength of the propagating light is much smaller than the diameter of the core region, rays are instead confined within the waveguide by grazing incidence reflection (GIR) from the outer layer at small angles. Hollow core fibre has applications in laser systems specifically in the field of ultrashort and few-cycle pulses. Precise control of the internal conditions of gas-filled hollow fibres allows precise control of the nonlinearity of the waveguide and is therefore also applicable for nonlinear processes inside of the fibre such as pulse compression [93]–[95], high harmonic generation [96] and supercontinuum generation [97]. Hollow waveguides are also considered good candidates for temperature insensitive [98], low-latency telecommunications, as signals travelling across them are unimpeded by the speed of light in materials [99], with optical signals measured as propagating a factor 3.2 times faster than in silica glass fibre [100]. HCF covers range of fibres, defined by their internal structures, such as photonic crystal fibres (HCPCF) [101], [102], Bragg fibres [103], and oxide glasses [104]. However in the remainder of this section, HCF here refers to hollow cylindrical dielectric waveguides.

A description of an electromagnetic wave decomposed into eigenmodes propagating within multimodal hollow metal and dielectric cylinders was presented by Marcatili et al. in 1964 [99], with further formalism introduced by J. Degnan in 1973, describing a set of eigenmodes, called linearly polarised modes [105]. Eigenmodes, e_{mn}, for a fibre of radius a, these can be expressed in a cylindrical coordinate system (r, θ, z) as

$$e_{nm}(r,\theta,z) = A_{nm} e^{i(\beta_{nm} z - \omega t)} e^{-\alpha_{nm} z} J_n\left(\frac{u_{nm} r}{a}\right) e^{in\theta}, \tag{5.1}$$

Where J_n is a Bessel function of the first kind and u_{nm} is its m^{th} root, normalised by an amplitude coefficient A_{nm} and with propagation constant β_{nm}. High spatial frequencies in the input beam decompose to high orders of this Bessel function and therefore experience greater transmission

loss due to the attenuation coefficient:

$$\alpha_{nm} = \left(\frac{u_{nm}}{k}\right)^2 \frac{1}{a^3} \frac{\varepsilon + 1}{2\sqrt{\varepsilon - 1}} \tag{5.2}$$

where ϵ is the dielectric permittivity. High spatial frequencies are thus preferentially attenuated as a beam propagates along HCF and the beam profile at the end of the fibre will increasingly tend towards the near-Gaussian LP_{01} mode which experiences least attenuation. In this way HCF can act as a spatial filter in an optical system. Spatial filtering by modal attenuation using HCF was first demonstrated by Mahieu et al. [106], who reported modal attenuation of high spatial frequencies to recover good wavefront quality for HHG experiments at the LUCA facility [107], a <150 mJ energy, 200 ps pulse duration, $\lambda_0 = 795$ nm Ti:Sapphire laser system.

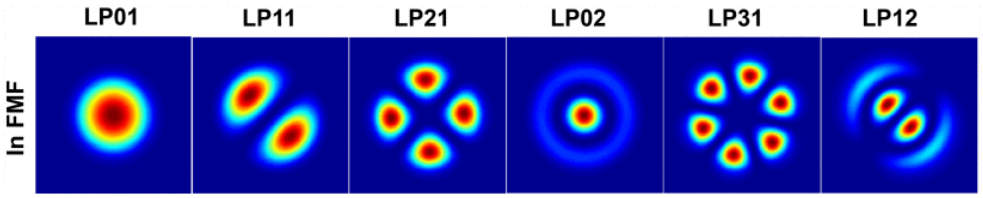


Figure 5.1: Linear propagation, LP_{mn}, eigenmodes supported by cylindrical hollow waveguides (from Y. Gao et al. [108])

The output of HCF is dependent upon the energy from the beam at focus, coupled into the LP eigenmodes, therefore any spectral variation across the spatial profile of the beam before input would not be conserved in the lowest order near Gaussian mode. In the case of a spatially chirped beam, or one with angular divergence, this implies that spatiospectral couplings would be homogenised by the HCF. Additionally, whilst beam wander or pointing instabilites earlier in the system may affect the coupling efficiency into the HCF, the pointing of light propagating from the output is fixed by the waveguide nature of the HCF. HCF therefore potentially increases the robustness of the beam pointing, diminishing the effects of beam wander or pointing instabilities from prior points in the beamline, though potentially at the expense of energy variation, if not then compensated by saturation of a later amplification stage. In the case where thermal changes to the system can cause significant beam wander, potentially introducing aberrations into the beam profile, HCF will both dampen the thermal-induced beam wander as well as modally filter existing aberrations in the beam. Increased pointing stability additionally reduces angular pointing changes into stretcher/compressor systems which potentially prevents unwanted high

order phase from developing due to sub-optimal internal paths through the CPA subsystems.

Since the start of this experimental work, there have been new publications reporting modal and spatiospectral filtering using HCF. An angular dispersion compensation scheme has been demonstrated by Cirmi et al. [109], as a method of minimising angular chirp present in an idler pulse in broadband (∼1.8 to 2.3 µm, 340 nm FWHM bandwidth) noncollinear OPA. No residual angular chirp was detected of the initially measured ∼1.8° external angular chirp, without adverse effects to the spectral and spatial profiles or significant change to the retrieved spectral phase. A similar angular dispersion scheme has also been presented by Hu et al. [110] using a combination of dispersive prisms and HCF. Prisms are first used to correct the angular dispersion of an idler beam (2.59 mJ pulse energy, 400 nm bandwidth centred at 1250 nm), resulting in only spatial chirp at the input of a hollow core fibre. For initial angular dispersion, measured as ∼72.4 µrad/nm at 1250 nm (an external angle difference of ∼1.66° over 400 nm), again no residual angular dispersion was measured at the output of a 300 µm core diameter, 250 mm long hollow core fibre.

5.1 Experimental Setup

As noncollinear OPA stages have been shown to manifest spatiotemporal couplings, including spatial chirp and angular dispersion, we investigated spatial filtering and beam homogenisation techniques using HCF at the output of the ps-OPA stages on the front end of the Cerberus laser system (described in detail in section 4.3). These stages consist of two, degenerate OPA amplifiers each with a 6 ps gain window; a 1.2 ps pulse duration seed is amplified first by a 6.5 mm type I BBO crystal where a 5 nJ seed is amplified with a gain factor of $\sim 10^4$, followed by a 2 mm type I BBO stage with a ×16 gain. The ps-OPAs are operated in a noncollinear geometry with a phase matching angle of ∼3.65°/0.064 rad. OPA2 is operated in an oversaturated regime for improved energy stability (described in chapter 4), causing spectral reshaping in the centre of the pulse not present in the outer wings. The output of the ps-OPA stages is propagated into an all-reflective Öffner stretcher where it is stretched to 1.8 ns pulse duration before further amplification in two ns-OPA stages. The ps-OPA stages were selected for this investigation as the small beam sizes used, in combination with short pulse lengths made them most susceptible to wavefront mismatch and walkoff. In addition, the ps-OPA output leads directly into the Cerberus Öffner stretcher,

which is sensitive to spatial quality and pointing.

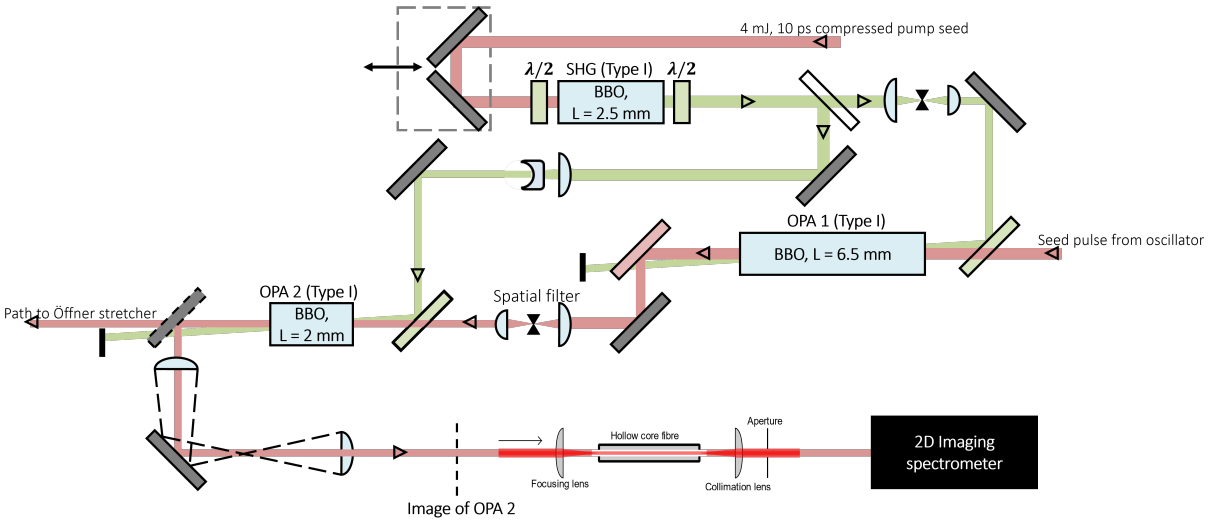


Figure 5.2: A schematic diagram of the ps-OPA stages in the Cerberus laser system, with the addition of a temporary beampath for characterising hollow core fibre. The beam is image relayed from the output of OPA2 to the back focal length of a lens which focuses light into the hollow core fibre.

A schematic overview of the experiment is shown in figure 5.2, the signal beam from OPA2 was imaged to the back focal plane of a lens to inject into a cylindrical dielectric hollow core fibre. Two different fibres were used in this experiment, glass capillary fibres of L = 250 mm, radius a = 100 µm and L = 300 mm, a = 200 µm respectively. In the case of the 100 µm core, the fibre was successively cleaved to shorter lengths, namely 250 mm, 210 mm and 127.5 mm, over the course of this experiment. This was partly to investigate the efficiency of the fibre as a filter with respect to the fibre length and also as a result of damage to the input face, described later in section 5.2.1. The HCF was mounted, resting between two stainless steel rods cut to the length of the fibre and loosely secured to two translation stages placed at the input and output ends of the fibre (figure 5.3). Using flexible o-rings to secure the fibre mount to the translation stages allowed independent control in the x,y axes normal to the direction of propagation and joined to a common z-translation, this permitted independent translation of the input and output ends of the fibre, allowing adjustments to be made to either end whilst keeping the other as a fixed point. In a "production" version of this system, removing most of these degrees of freedom would be useful for creating a fixed point for beam position, beam profile and propagation direction.

The energy coupled from the input beam into given modes of the HCF is sensitive to the spatial distribution of the beam at the input, particularly to the beam waist of the input with respect to

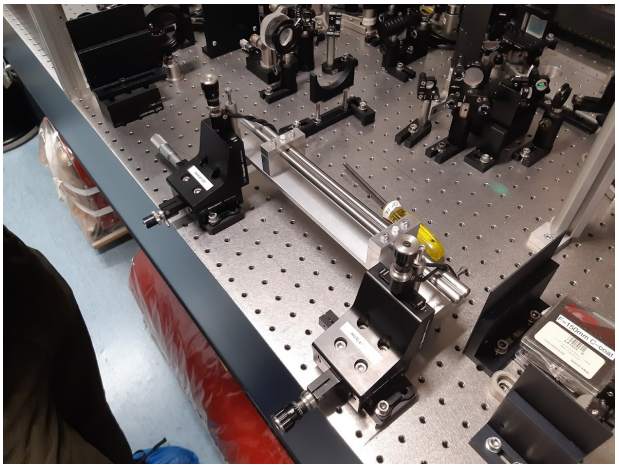


Figure 5.3: HCF mounted on translation stages

the fibre diameter and the angle between the input beam and the fibre input face. Maximising LP_{01} (the lowest order Gaussian mode) for best transmission of a Gaussian beam focused at the input of radius a, to a focus of $w = 0.645$a, ∼98% of energy can be coupled into LP_{01} [106], therefore for 100 µm diameter fibre, an f = 100 mm, ∼F/50, focal length plano-convex lens was selected, giving a focused beam diameter at focus of ∼68.1 µm. For 200 µm diameter fibre, a 200 mm focal length plano-convex lens was used - due to changes in the system alignment between the 100 µm fibre characterisation and the 200 µm fibre, the beam waist at the output of OPA2 had changed by a small amount, therefore resulting in a focused diameter at input of 122 µm, F/90. The divergence of the beam at the output from the hollow core fibre is determined by the internal diameter of the fibre, for 100 µm diameter fibre this was experimentally measured at an angle of 1.37° and collimated using an f = 100 mm plano-convex lens. Similarly, for 200 µm core diameter fibre the full divergence angle was measured to be 0.59° ± 0.005° and collimated using an f = 200 mm plano-convex lens.

5.2 Characterising Hollow Core Fibre as a Spatial Filter

High power laser systems commonly use spatial filtering techniques to preserve or recover the spatial quality of the beamfront spatial profile as it propagates through the front end of the system. However, spatial filtering techniques are ultimately limited by their efficiency, and whilst energy may be recouped in later amplification stages, the degree of filtering must be chosen such that the benefit of spatial filtering outweighs the energy lost in the filtering process. Vacuum

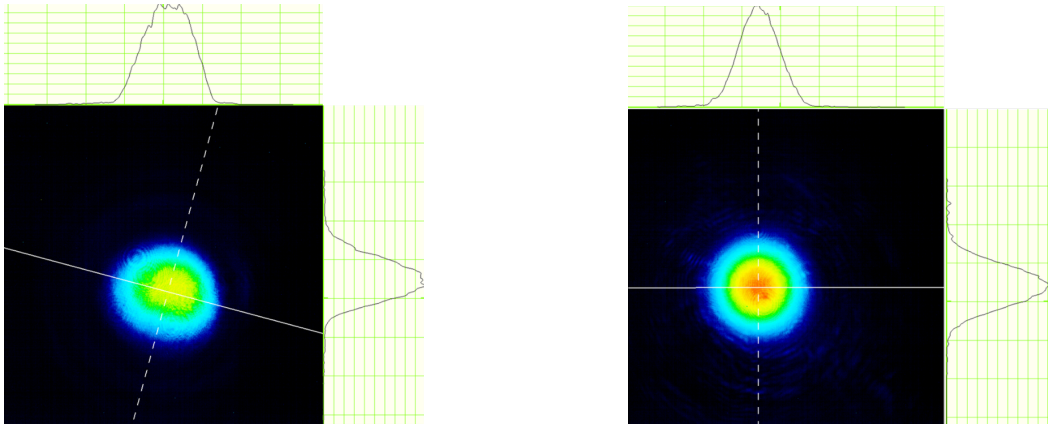
spatial filters, for example, provide a reasonable level of high spatial frequency filtering combined with a good transmission efficiency of >80%. The first step to characterising HCF for use in the front end of a laser was to characterise the spatial filtering and transmission efficiency, this included characterising the input dependence for the fibre with respect to angular divergence of the fibre input face around the laser focal spot. Thermal effects on the system, general beam wander and minor user misalignment can cause the beam pointing to change by small amounts on timescales of hours to months and whilst the fibre may have good transmission efficiency when carefully aligned, it is important to identify what the effect of these pointing changes will be.

Theoretical predictions of transmission efficiency through cylindrical dielectric HCF are very high ($> 90\%$), however this is difficult to achieve experimentally due to non-ideal focus at the point of coupling into the fibre core. For real systems the need for spatial filtering arises because the beam is, in fact, not a perfect Gaussian and the dynamics of coupling a non-Gaussian beam profile into HCF therefore differs from theoretical predictions. Experimentally observed transmission efficiencies are lower than theoretical expectations due to the practical limits of high spatial frequencies in the beam preventing good coupling of the beam waist at the HCF input, particularly astigmatic effects, which have significantly reduce HCF coupling efficiency [105] . Previous reports for spatial filtering using hollow core fibre have ranged between 36 - 78% efficiency based upon the fibre diameter and type of fibre used [106], [109], [111]. Mahieu et al observed 78% transmission efficiency for fibre with core radius $a \simeq 125$ µm and length $L = 300$ mm (E <150 mJ, $\tau \simeq$200 ps, $\lambda_0 \simeq$795 nm, repetition rate 20 Hz) [106], Cirmi et al measured 36% transmission efficiency for a = 63 µm and $L = 220$ mm, (10.7 uJ, $\Delta\lambda$ =340 nm) [109] and Hu et al. measured 67% for a = 300 µm, $L = 250$ mm [110].

5.2.1 100 µm Diameter Fibre Characterisation

We first characterised the 250 mm long, 100 µm diameter fibre for spatial quality enhancement and transmission efficiency. The spatial quality enhancement was assessed in addition to the dependence on transmission efficiency when translating the fibre around the focused input, horizontally, vertically and in the optical axis. Good alignment through the fibre was checked by comparing the nearfield profiles, recorded by a beam profiler (WinCamD-LCM – 1" CMOS Beam Profiler), at the back focal length of the focusing lens and the collimated output of the

fibre. Transmission was characterised in a similar manner, by measuring the beam energy at each point with an energy meter (GENTEC QE12SP), averaged across 100 laser pulses at 10 Hz, which allowed calculation of the average recorded energy, peak-to-peak stability and %RMS stability. Shown in figure 5.4, the HCF is successful at filtering the nearfield spatial profile, with the output of the HCF closely resembling the LP_01 mode. The ellipticity, the ratio of the beam waist along the semi-major to semi-minor axes, also improved from from 0.88 to 1.00. The maximum transmission efficiency, after careful alignment, was measured at 51.1 %.



(a) (b)

Figure 5.4: a) the spatial profile (taken as the viewfield of a Dataray, WinCamD-LCM – 1" CMOS Beam Profiler) of the image of the amplified signal pulse at the second stage of the OPAs, b) the OPA signal pulse spatial profile post filtering with 300 mm, a = 100 um hollow core fibre.

This transmission efficiency was observed to be sensitive to coupling into the HCF, which is largely determined by the focused beam waist at input, where for a Gaussian beam in order to maximise LP_01, best coupling is predicted at a focused 2w beam diameter at $1/e^2$ intensity of 64.5 μm [106]. To verify this, several focusing lenses were used in order to vary the focused spot diameter at the input of the HCF, a best form f = 50 mm lens was used in addition to three plano-convex focusing lenses with, f = 75 mm, f = 100 mm and f = 150 mm focal lengths as well as a two lens system with a f = 300 mm meniscus lens in combination with a f = 150 mm PCX lens in order to vary the focal spot size by a small amount around the predicted maximum. From these lenses, the focused beam size was calculated based upon the beam waist at input and the effective focal length of the focusing lens. Results showed reasonable agreement with theoretical predictions, as shown in figure 5.5, the peak transmission corresponded to a focused $2w$ beam diameter at injection of 66.2 μm. This differs slightly from the predicted focal spot waist, and could be explained due to a systematic error in the calculated focal spot waist due to

slight divergence in the input beam or M^2 value of the OPA signal deviating from 1.0. The error bars on figure 5.5, and similar graphs in this section, is representative of the standard deviation of OPA2 signal energy and the differences in the maximum transmission efficiency achieved when aligning the HCF from scratch several times within a short time of one another.

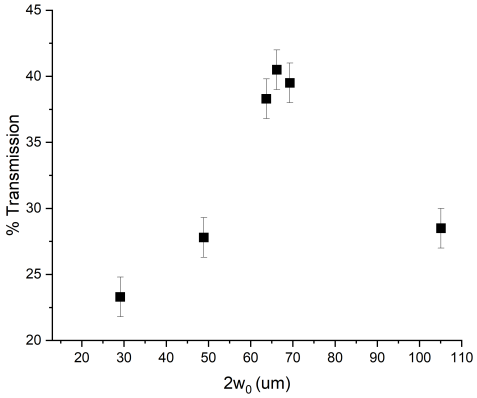


Figure 5.5: transmission efficiency of a 100 µm diameter, 250 mm long HCF with respect to the $2w$ beam diameter of a Gaussian beam injected at focus into the fibre.

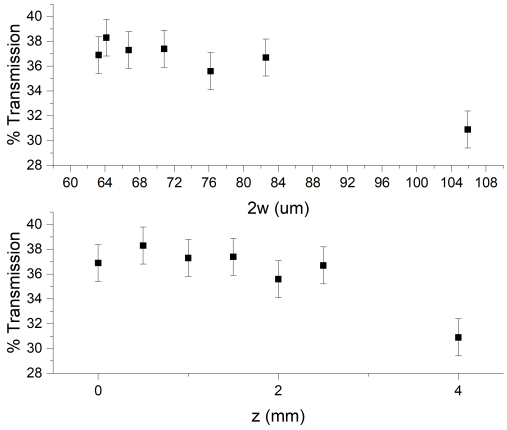
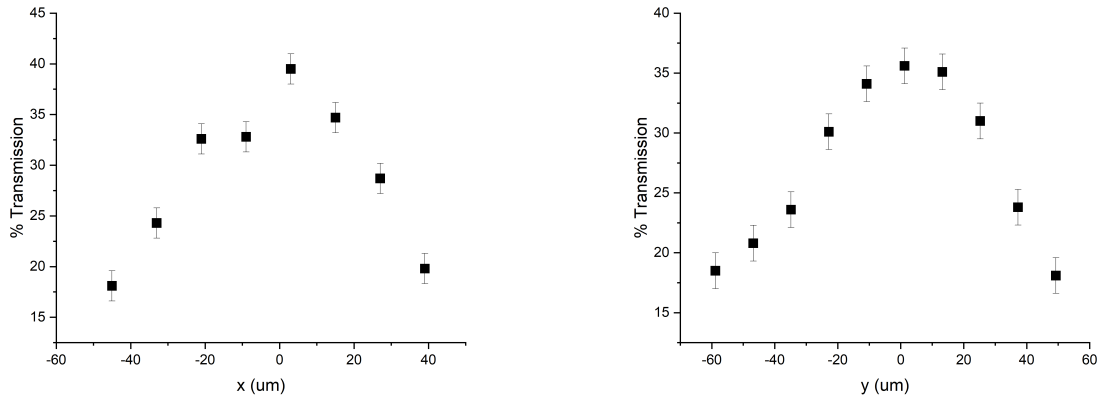


Figure 5.6: Transmission efficiency of the signal of OPA2 through 100 µm diameter, 250 mm long HCF translated along the optical axis around a ∼64 diameter µm focal spot produced by an F/50 focused input. top) the diverging beam diameter, bottom) distance from focal spot.

There are 5 degrees of freedom associated with the fibre alignment, the fibre is secured between two translation stages which move independently, translating and rotating the fibre in the directions perpendicular to the optical axis (x & y) and are locked together in the optical axis, translating in z. Transmission efficiency is mostly dependent upon the coupling at the input, with the translation stage closest to the output then adjusted to optimise propagation through the HCF. The alignment sensitivity of HCF was investigated by translating the input face of the fibre in z, along the axis of propagation, through the focus and translating the fibre input and the optical axis, x & y. Figure 5.6 shows the transmission efficiency of OPA2 signal, focused at ∼F/50 with a focused beam diameter of 63.3 µm, with respect to the beam diameter at input due to translating the input of the HCF away from the position of best focus. The results show symmetrical behaviour either side of focus, suggesting that the beam waist at input dominates coupling over the convergence or divergence of the beam. A focused beam diameter of 63.3 µm corresponds to a Rayleigh length of 2.98 mm, at this point the coupling efficiency is seen to de-

crease by roughly 10%, which approximately corresponds to the difference in coupling efficiency observed due to the focal spot diameter in figure 5.5. The difference in transmission efficiency between figures 5.5 and 5.6 is likely due damage at the input of this fibre, this is discussed in more detail further into this section. Shown in figure 5.7, translation of the fibre input in x and y was observed to strongly influence the coupling into the HCF, due to the fibre core diameter, small adjustment at input reduced the efficiency of coupling into the fibre and also thus the transmission of the pulse. Within the core diameter, the transmission efficiency quickly drops off, when the fibre input is translated half of the focal spot diameter in the x and y axes, transmission falls by 30% and 28% respectively. Additionally, transmission efficiency in the x axis falls by 22% and 60% when the fibre input is translated a quarter and half of the fibre diameter from the input and efficiency in the y axis falling by 17% and 45% for the same translation.



(a) x (b) y

Figure 5.7: The effect on measured transmission efficiency of small translation in the a) horizontal and b) vertical axes on the input of a beam into 300 mm HCF.

In addition to reducing the transmission efficiency through the HCF, misalignment was also responsible for observably degrading the output beam quality; reduction in the quality of the mode was observed and scatter was introduced around the central mode. The nearfield profile of the HCF output is shown in figure 5.8, showing the profile of scattered light produced by a fibre translated in z, 2.3 mm from focus. The scattered light output from the hollow core fibre was observed to quickly diverge, with an full angle of $\sim 5.0°$, forming a ring around the central mode. Due to the far larger divergence in the scattering angles, the scattered light from the fibre can however be attenuated (using a similar method to [106]) by placing an aperture at the back focal

length of the collimating lens. Light scattered into the HCF cladding was less attenuated than light travelling down the core, therefore the proportion of scattered light effectively increased the observed transmission efficiency when measured on a photodiode or energy meter alone, therefore precise alignment through HCF requires an alignment camera looking at the spatial profile of the output.

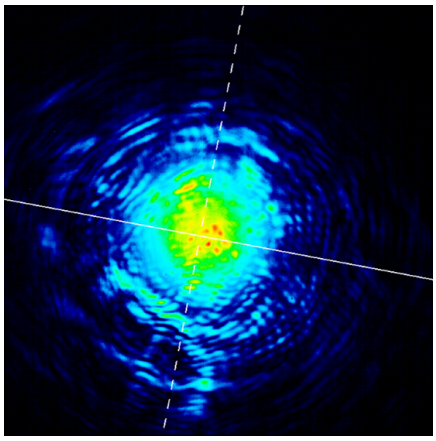


Figure 5.8: Spatial profile of HCF output with 2.3 mm z offset from the optimum input position, larger divergence at input increases the amount of the beam that is coupled into scattering modes - (profile from WinCamD-LCM).

The maximum coupling efficiency was found to be decreasing over time, from >50% to ∼40% over ∼3 weeks, due to damage accumulated on the input face of the fibre. To achieve a beam diameter at input of ∼64 µm, it was necessary to focus the OPA2 signal strongly. As such the focused intensity of OPA2 signal was comparable to the surface damage threshold of fused silica glass at ∼3 J/cm^{-2}. The OPA2 signal was capable of causing damage when focused, but was not above the threshold to cause bulk damage to the fibre as it propagated through it. Therefore, procedures were set at the outset of the experiment to try to limit damage to the HCF by initially aligning at lower power, using the Cerberus oscillator signal, and scaling to high power once alignment was set. However, subsequent pointing changes in the beam caused the slow formation of damage at the face of the fibre, shown in figure 5.9.

Moving to a larger fibre core diameter would allow a greater focused beam diameter, below the damage threshold of the fibre. Whilst a larger fibre core diameter was ultimately the solution to this issue, due to wait times on optical components, the 100 µm diameter fibre was initially cleaved to a shorter length to remove damaged areas. Modal attenuation scales as $a^{-3} \times L$, therefore as the fibre was cleaved to shorter lengths, transmission efficiency correspondingly increased, from

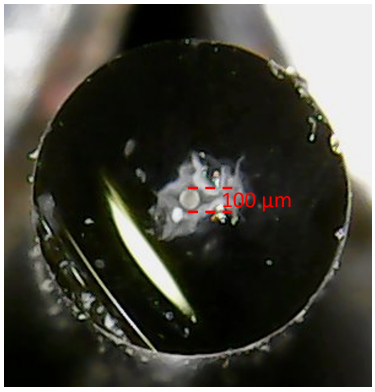


Figure 5.9: Damage sustained by the input face of 100 µm diameter fibre due to the focused laser intensities at input over a period of ∼3 weeks.

a peak of ∼50% for 250 mm fibre to >70% for 127.5 mm fibre.

Table 5.1 compares the attenuation lengths, z_{att}; defined as where $e^{-\alpha_{nm}z} \rightarrow e^{-1}$, for several low order linearly polarised modes in HCF. Whilst these results indicate that a 120 µm diameter fibre would be a good candidate for use due to its shorter attenuation lengths, ultimately 200 µm diameter fibre was chosen due to robustness against damage and availability. 200 µm is not as strong a modal filter as smaller diameter fibres, however strong spatial filtering is not required at this stage in the system and the waveguide nature of the fibre should still produce a useful fixed point and homogenisation.

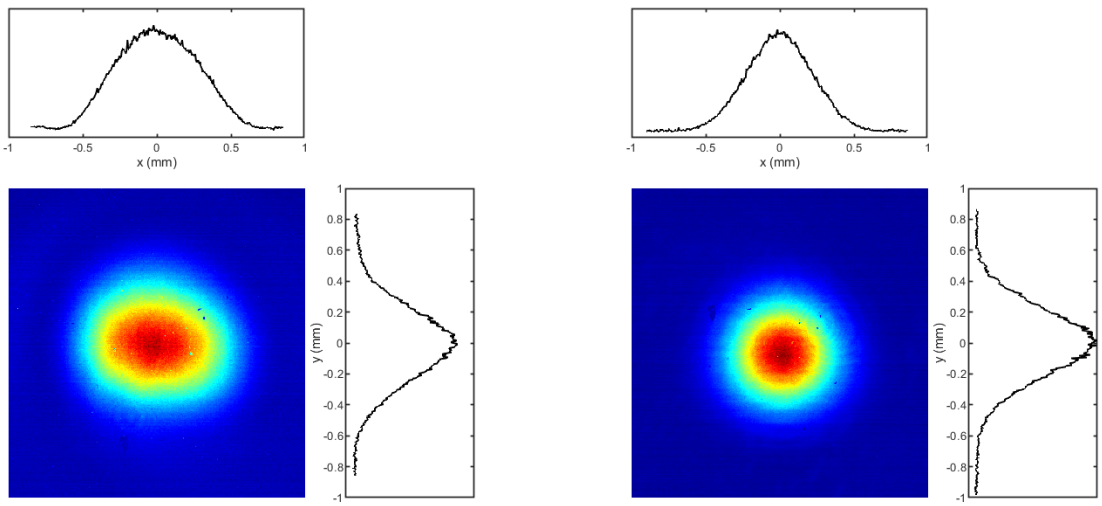
u_{nm}	a = 100 µm	a = 120 µm	a = 200 µm
0,1	4.15 m	7.18 m	33.3 m
0,2	0.79 m	1.36 m	6.31 m
0,3	0.32 m	0.55 m	2.57 m

Table 5.1: Attenuation length z_{att}, where $e^{-\alpha_{nm}z} \rightarrow e^{-1}$, for low order eigenmodes (figure 5.1) in hollow core fibre with core diameters of 100 µm, 120 µm and 200 µm.

5.2.2 200 µm Diameter Fibre Characterisation

Once a 200 µm core diameter fibre was procured, it was characterised in a similar manner to the previous fibre, firstly investigating the performance as a spatial filter. The comparison between the nearfield and farfield input and output of 200 µm HCF is shown in figures 5.10 and 5.11, both figures showing clear strong spatial enhancement of the beam despite a larger core diameter. Since the LP_{01} mode closely resembles a Gaussian, we may roughly characterise the degree of spatial filtering of the HCF output based upon the ellipticity of the profile and the R^2 fit, comparing

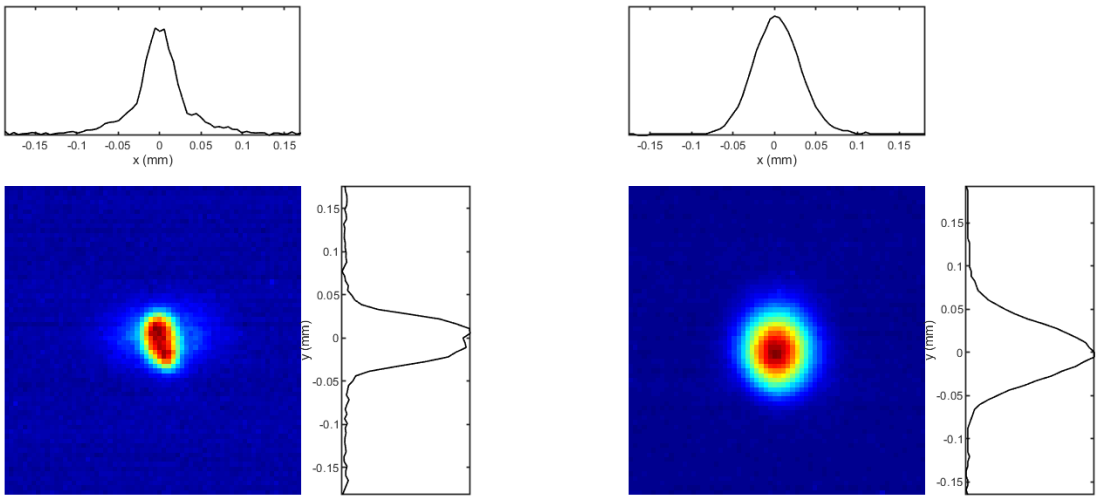
the measured beam profile against a 2D Gaussian fit which imposes a constant radius, equal to that of the average of the x and y radii of the nearfield. From these parameters, we observe improvement to the nearfield spatial profile from an ellipticity, the ratio of the semi-major to semi-minor beam axis widths, of 0.821 to 0.988 and an improvement in the R^2 fit from 0.973 to 0.987. Whilst the R^2 parameter does show some improvement, this value was also seen to be largely affected by low level background noise, of a similar level in both figures 5.10a and 5.10b. The OPA2 farfield was captured both at the input of the HCF and by focusing the fibre output, seen in figure 5.11. Here especially, the spatial filtering qualities of HCF can be observed, with the R^2 fit of the input, 0.931, improved to 0.993, demonstrating key filtering of spatial frequencies in the input beam.



(a) (b)

Figure 5.10: Nearfield spatial profiles of the OPA2 signal beam a) before and b) after modal filtering using a 200 µm diameter, 300 mm long HCF. Here, the nearfield ellipticity was improved from 0.82 to 0.99.

A comparison of the M^2 value between the input and output beams from HCF also allows us to quantify our ability to remove aberrations from a beam. The M^2 value of OPA2 signal was measured before and after filtering using the HCF, by measuring the beam waist through 5 different points within the Rayleigh length of the focal spot produced with an f = 200 mm focal length lens and 5 more points outside of twice the Rayleigh length. The focused beam diameter was measured for several points around the focal plane, taking the $2w$ beam waist of a Gaussian

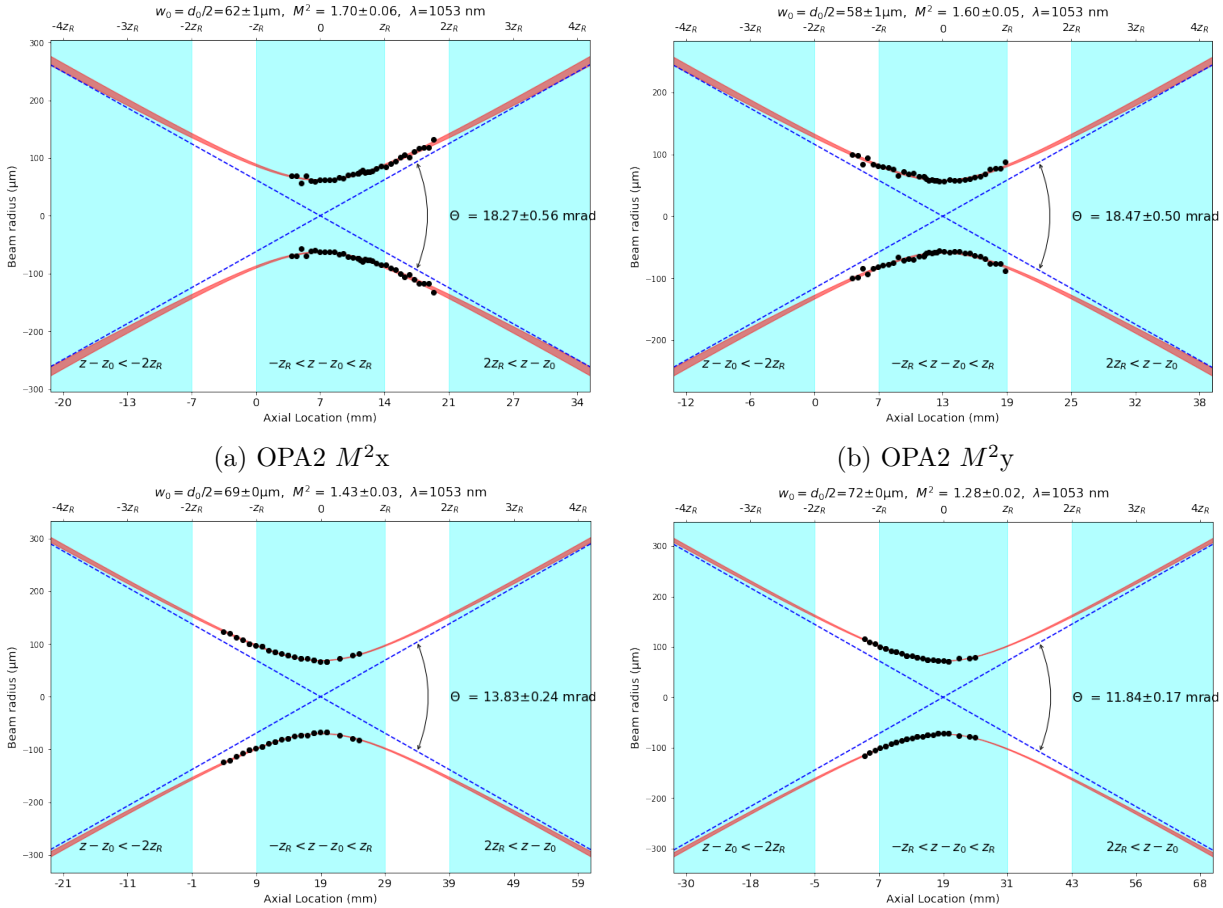


(a) (b)

Figure 5.11: Farfield spatial profiles of the OPA2 signal beam a) before and b) after modal filtering using a 200 µm diameter, 300 mm long HCF.

fit of the of semi-major and semi-minor (x & y) axes. Typically for M^2 measurements, the D4σ beam waist is used however here, due to the fitting technique, it was convenient to calculate the $2w$ beam waist instead, which for a sufficiently Gaussian spatial profile, approximates to D4σ. The M^2 fitting analysis was performed using the python library, "laserbeamsize 1.9.4" by Scott Prahl [112], shown in figure 5.12. A degree of astigmatism was observed at the focus of the unmodified OPA2 signal, characterised by the difference in the M^2 value in the x & y axes of M_x^2 = 1.70 ± 0.06 and M_y^2 = 1.60 ± 0.05. The distance between points of best focus in the x and y axes was measured to be 6.42 mm, a significant fraction of the Rayleigh length ($z_R \simeq 10.7$ mm). The astigmatic term present is likely a result of user misalignment of a telescope lens-pair just before OPA1. The SF6 glass stretcher block, used to stretch the oscillator pulse from 250 fs to 1.2 ps, introduces an f = -20 m cylindrical lens term due to internal stress which was reduced to a large extent by careful annealing of the glass in a long thermal cycle to near the yield point, but could not be removed completely in this way. This cylindrical term is counteracted by tilting the first lens of the telescope to minimise the beam divergence through the ps-OPAs. This alignment process may cause a residual astigmatic term due to subtle user-misalignment. Whilst non-ideal for routine operation, the presence of this astigmatism at the time of measurement did offer an opportunity to showcase the use of HCF to remove aberrations in the system. Whilst a difference

in the M^2 value at output in the x, y axes was present, $M_x^2 = 1.43 \pm 0.03$ and $M_y^2 = 1.28 \pm 0.02$, the astigmatism was highly suppressed with a difference between the x, y focal planes of 0.288 mm post HCF.



(a) OPA2 M^2x (b) OPA2 M^2y

(c) HCF M^2x (d) HCF M^2y

Figure 5.12: M^2 measurements, analysed with "laserbeamsize 1.9.4" by Scott Prahl [112], of the OPA2 signal beam a) before and b) after modal filtering using a 200 µm diameter, 300 mm long HCF. Significant astigmatism was present in the beam prior to modal filtering, which was successfully removed by the HCF.

Transmission efficiency with respect to the input translation of the fibre in x, y, z was also characterised similarly as to section 5.2.1. Scanning across the length of the translation stage, the efficiency changed slowly with z due to the larger Rayleigh length, ∼42 mm, associated with the longer focal length of the focusing lens. For practical alignment, and finding the position of best focus, the 200 µm fibre shared some similarities to more standard VSF alignment. As the HCF input was translated further from the position of best focus, x, y translation produced a 'squashing and stretching' effect on the output nearfield, similar to a pinhole filter away from

best focus. This enabled good initial alignment through the fibre with confidence, in addition to the longer Rayleigh length decreasing the chance for small changes in the collimation of the beam to affect transmission. Figure 5.13 shows a single peak in transmission efficiency and we did not observe two positions of best coupling during this scan, which indicates that astigmatism may not have been present during this measurement. Figure 5.14 shows the rapid drop off in coupling efficiency due to angular misalignment of the input. This raises questions as to the limits of utility for hollow core fibre in a laser system prone to wandering during warm up, especially considering one of the aims of integrating HCF is to have a fixed point in the beamline which reduced the need for the laser to warm up to thermal equilibrium, though that could be addressed using an auto-alignment system optimising fibre throughput. There was an observed difference in the x, y translation dependence, with the transmission efficiency falling off by only $\sim$21% in the x axis as the input was translated half of the focused beam diameter, compared to a fall in transmission of $\sim$44% in y. We would expect symmetric behaviour in x and y for a Gaussian focal spot therefore this observed difference may be due to the astigmatism of the beam at the input.

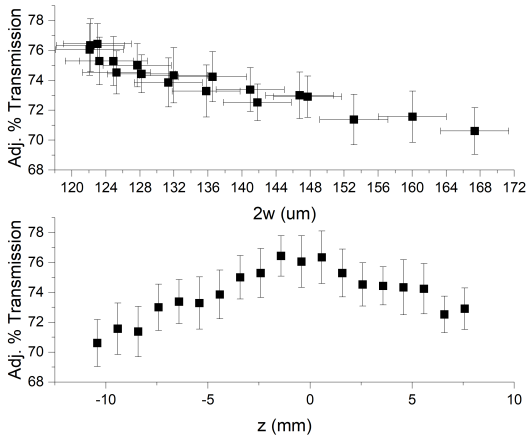
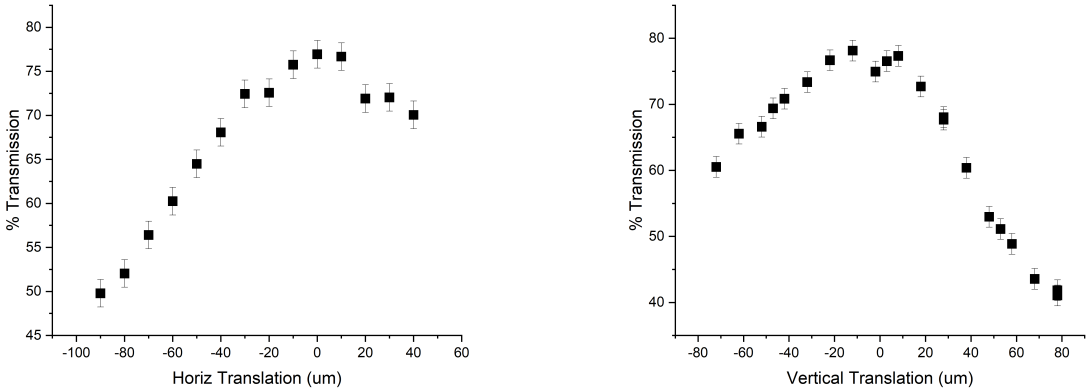


Figure 5.13: The dependence of transmission efficiency through a 200 µm diameter, 300 mm long HCF with respect to translating the input along the optical axis, z, for an focused beam at input ($\sim$F/100) with Rayleigh length $\sim$10 mm.

Much less scattered light was observed from the output of the HCF for the 200 µm diameter fibre compared to the 100 µm diameter fibre. This is perhaps due to the larger Rayleigh length, combined with greater angular tolerances in x, y, improving the robustness of coupling to the core, with less light coupling into the cladding as a result. It is also likely that the scatter seen previously may have been exacerbated by damage at the input face of the 100 µm diameter fibre.



(a) x (b) y

Figure 5.14: Transmission efficiency dependence for a 200 µm diameter, 300 mm long HCF by translating the input face of the fibre in the perpendicular axis, a)x and b)y, of the focused beam at input (F# $\sim$ 100).

Due to thermal effects in the laser system or due to the gain from the ps-OPA stages, the waist of the OPA signal may change by a small amount, amounting to a change from up to 2.7 mm $1/e$ beam waist diameter to 2.2 mm over a system warmup time of $\sim$1.5 hours, amounting to a change of the predicted focal spot change from 99 µm to 122 µm within this time. With an optimum coupling at $w/a = 0.64$, however based upon z-dependence (figure 5.13), assuming a symmetric response to focused beam diameter at coupling, the corresponding drop in transmission efficiency would be <5%, which is recoverable by subsequent amplification stages in the laser system.

Fine alignment into the fibre was required for alignment to peak transmission efficiency however once good throughput was achieved, the transmission mode was shown to be stable over periods of operation lasting hours, and proved to be resilient to beam wander and shot-to-shot variation. The HCF remained in good alignment and would not require adjustment to rediscover the LP_{01} mode when the system was restarted on subsequent days. Whilst the transmission efficiency was observed to be sensitive to deviation in the beam pointing, an average transmission of >75% efficiency with an RMS stability of 2.5% (comparable to normal operation of the ps-OPAs) was achieved over several hours of operation.

5.3 Characterising Hollow Core Fibre as as Spatiospectral filter

By coupling into the LP eigenmodes at focus, HCF effectively homogenises any spectral variation across the spatial profile of a laser, removing spatial chirp and angular dispersion from the beam. In this section we will attempt to quantify the degree to which spatial chirp, and other spatiospectral couplings, are removed from the output of the ps-OPA stages. Whilst angular dispersion has an arguably greater effect on the temporal-intensity contrast of a laser system [49], the two are often coupled [113] and therefore we can infer angular dispersion compensation from spatial chirp reduction (handily an easier measurement). Additionally knowing the spatial chirp of the ps-OPA signal is also a practical measurement. When the Cerberus Öffner stretcher is aligned, we check alignment so that there is no spatial chirp present at the output, qualitatively measured by ensuring the spatial profile at output is consistent when portions of the beam at the stretcher Fourier plane are blocked. If there is preexisting spatial chirp present, then this alignment would minimise that chirp at the detriment of potentially introducing uncompressible high order phase [52].

Spatial chirp can be parameterised by two characteristics, the "frequency gradient", $d\omega_0/dx$, and the "spatial dispersion", $dx_0/d\omega$ [114]. We define ω_0 as the peak intensity of the frequency spectrum for a given position on the spatial profile, where the frequency gradient is the slope of that peak frequency across the spatial profile. Conversely x_0 is the position of peak intensity across a slice of the profile for a fixed frequency, and spatial dispersion is thus characterised by the spatial peak intensity distribution for the spectrum of the pulse. If no spatial chirp is present in the beam, both of these parameters are zero however, crucially, these terms are not the reciprocal of each other and are produced as a consequence of different factors; whereas spatial dispersion is a direct consequence of angular dispersion in the system, the frequency gradient is manifested due to the indirect consequence of both angular dispersion alone and angular dispersion coupled to spatial dispersion. Spatial dispersion is typically a more useful metric to quantify the angular dispersion present in a beam, whilst frequency gradient is often an important parameter for pulse shaping applications, as it determines the mapping of spatial modulation to spectral modulation [114]. Spatial chirp relates to angular dispersion, $\beta = d\theta_0/d\omega$, such that for a beam propagating

a distance L, the change in spatial dispersion due to the angular dispersion is

$$\Delta\left(dx_0/d\omega\right) = \beta L \tag{5.3}$$

A 2D imaging spectrometer was designed and built by the author to measure the spatiospectral profile of the signal pulse. This diagnostic went through two iterations, initially imaging the output of the HCF. A blazed holographic 1800 l/mm diffraction grating (grating angle, $\theta_m - \theta_i = 18.6°$) was used to disperse the light before it was focused at the Fourier plane using a cylidrical lens with measured focal length $f_f = 75.3$ mm recorded with a beam profiler (Thorlabs BC106N-VIS). The spectrum of the beam was resolved in the horizontal, x, axis with the spatial variation measured in the orthogonal direction, the ps-OPA stages are operated in a vertical noncollinear-OPA geometry and therefore spatial chirp effects due to pulse-front mismatching and lateral beam walkoff will most strongly manifest in this plane [54]. For measurements of the OPA2 signal alone, the beam was imaged relayed from the crystal to the approximate position of where the fibre output would be. The imaging spectrometer was characterised by cross-correlation with another spectrometer (Oceanoptics usb2000+), however during analysis we discovered that a minor aberration was present in the measured spatiospectral profile due to a slight misalignment in the beam profiler relative to the incoming angle of the beam which tilted the measured spectrum. Whilst the simplest solution would have been to realign the diagnostic and recapture the data, lab access during this time was restricted due to the 2020 COVID pandemic. As such, the aberration was corrected by matching the central imaging spectrometer spectrum to a reference spectrum from the Oceanoptics spectrometer and mapping the distortion of the first to the second. We used a dynamic time warping (DTW) algorithm [115], [116], which works according the the principle shown in figure 5.15, 'warping' a data set to match a reference waveform. By using this algorithm, we not only compensated for aberration present in the imaging spectrometer data but also accommodated any variation in the spectral structure between the imaging spectrometer data and the reference spectrometer as a result of the difference in slit width between the two spectrometers.

Before quantifying the reduction of spatial chirp using the HCF, we first characterised the spatial chirp, here spatial dispersion, present in the ps-OPA seed pulse and in the output of each ps-OPA stage. The spatiospectral beam profiles of each of these, shown in figure 5.16, were taken from

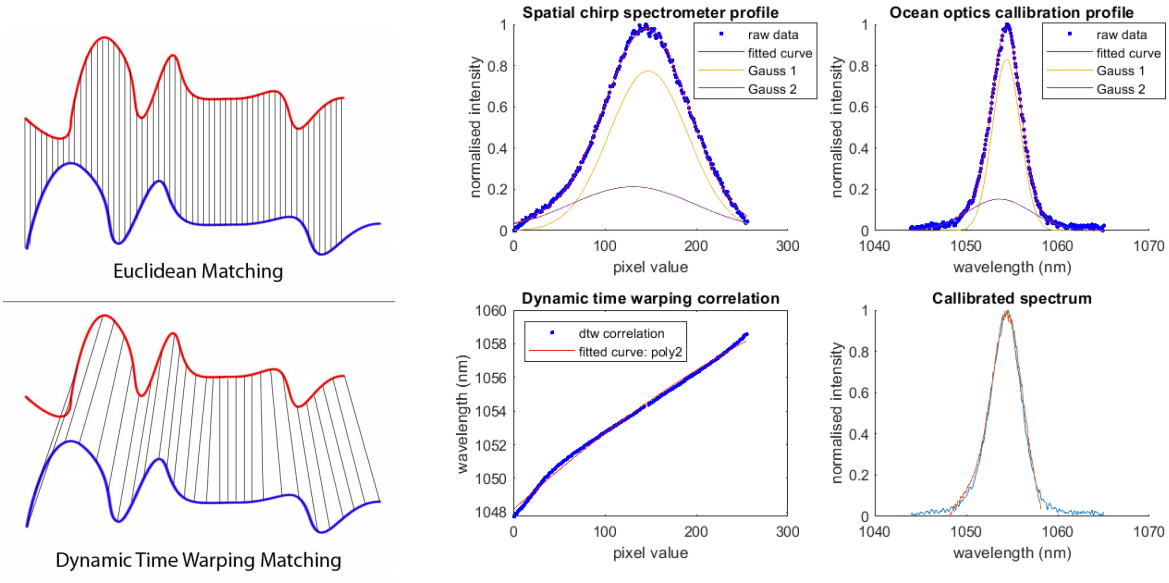


Figure 5.15: Dynamic time warping (DTW) calibration used to callibrate a 2D imaging spectrometer using a reference spectrum obtained from an Oceanoptics usb2000+ spectrometer, compensating for a subtle aberration found in the 2D imaging spectrometer. Left: illustration of the DTW algorithm (image credit to XantaCross, Wikimedia commons). Right: DTW calibration for the 2D imaging spectrometer, comparing reference spectra of the Cerberus oscillator measured by both devices.

the output of OPA2 and image-relayed to the 2D imaging spectrometer. Firstly the pump beams for both ps-OPAs were blocked, then OPA1 was run independently and finally both stages were run together. For each of these measurements, we calculated the spatial dispersion and frequency gradient within the FWHM of beam profile using analysis software written by the author which took slices out of the profile in frequency and spatial axes and found the peak intensity based upon fitting a super-Gaussian profile to the spectrum, based on the Gaussian order (up to 3) which returned the highest r^2 fit. This method was necessary due to the nonlinearity and oversaturation of the ps-OPA stages which could produce complex spectral profiles.

Minor spatial dispersion was observed in the Oscillator spatiospectral profile, $dx_0/d\lambda = 3.03 \times 10^{-3} mm/nm$, which may represent either a systematic error in the diagnostic alignment or be indicative of subtle alignment drift in the dispersive elements of the master oscillator (Time Bandwidth Products GLX-200HP). Analysis of OPA1 and OPA2, indicated the presence of linear spatial dispersion in OPA1 of $dx_0/d\lambda = 2.92 \times 10^{-2}$ mm/nm and in OPA2 of $dx_0/d\lambda$ = -1.04×10^{-2} mm/nm. Accounting for the measured spatial dispersion the in oscillator, from equation 5.3, this corresponds to an angular dispersion of 16.0 µrad/nm manifesting in OPA1. The spatial

dispersion measured in the OPA2 signal is less than that observed in OPA1, this may partially be explained by the difference in beam waist (a larger beam will exhibit spatial chirp more strongly) however this does not fully account for the difference in the measured spatial dispersion. One possible explanation for this is the up-expansion telescope between the two OPA stages which inverts the beam and therefore would invert the direction of spatial dispersion. Both stages are operated with the same noncollinear angle between the pump and seed beams, therefore angular dispersion generated in OPA2 may compensate for angular dispersion present in the OPA1 beam. If angular dispersion generated by OPA2 did act in the opposite direction of OPA1, this would indicate a spatial dispersion of -3.96$\times 10^{-2}$ mm/nm manifesting in OPA2, representing an angular dispersion of $\approx$ -21.6 µrad/nm. However, only taking the sum spatial dispersion present in the OPA2 signal would indicate an angular dispersion in the OPA2 signal of $\approx$ 7.65 µrad/nm. These angular dispersion values are consistent with the residual angular dispersion observed due to stretcher/compressor misalignment [49], which is concerning as this increases the likelihood that alignment of a stretcher or compressor would inadvertently introduce high order phase terms when trying to correct the angular dispersion or chirp observed at the output.

In order to extract higher gain from a low energy seed pulse, the OPA1 stage the beam waists of the pump and seed overlapped within the cyrstal are significantly smaller than in OPA2. Therefore, the amplification process may be more susceptible to pointing changes in the beam, with poor spatial overlap producing the greater spatial dispersion observed in this stage compared to OPA2. Additionally, the crystal length of OPA1 (6.5 mm BBO) is long enough that temporal walkoff between the pump and seed beams manifests due to group velocity mismatch. For type-I degenerate OPA with the fundamental pulse centered at λ_0=1053 nm, the GVM is calculated at 88.5 fs/mm, considering the crystal length and the noncollinear angle, which amounts to a temporal walkoff between the signal and pump pulses of 0.575 ps in OPA1 and 0.177 ps in OPA2. This calculated GVM is well within the expected gain window, set by the pump pulse duration $\sim$6 ps. However, imperfect compression of the pump pulse in the ps-pump compressor or modulation in the pump pulse envelope could result in spatiotemporal couplings in the pump pulse such as pulse-front tilt [48] which would affect the spatial overlap between the pump and seed beams. The group velocity mismatch also results in further amplification of the higher frequency trailing end of the chirped seed pulse, which results in an effective shift in the central wavelength of the pulse, observed in figure 5.16 by the shift in the central wavelength measured in the oscillator,

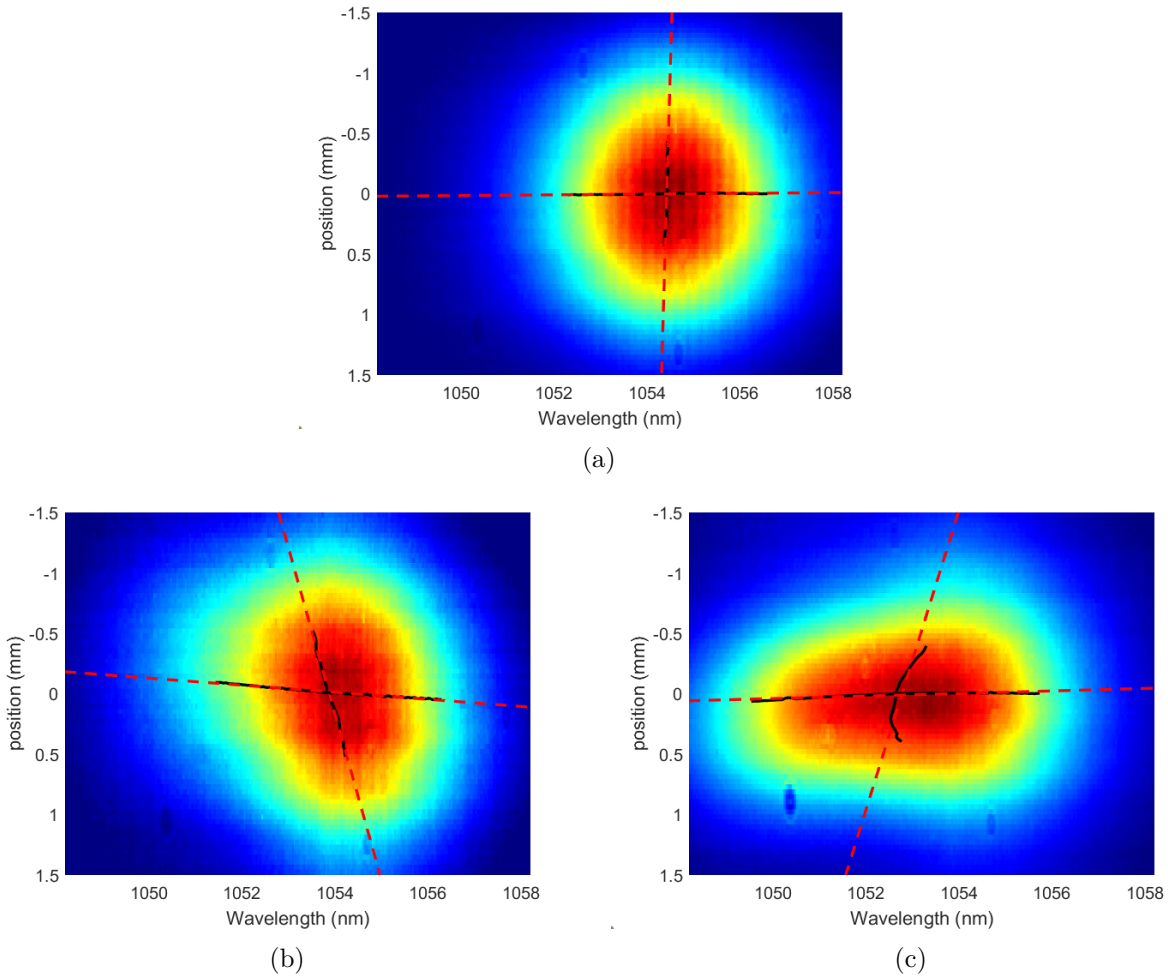


Figure 5.16: Spatial chirp measurements of the output of the ps-OPA stages, a) oscillator, b) OPA1, c) OPA2 using a 2D imaging spectrometer. Black lines represent the peak intensity for slices along the image in position and wavelength, from which the linear fit (red lines) gives the spectral dispersion, $dx_0/d\lambda$ and frequency gradient $d\lambda_0/dx$.

OPA1 and OPA2. Finally, OPA2 displays a non-linear frequency gradient. This is due to the fact that OPA2 is operated in an oversaturated regime in order to increase the energy stability of the signal, causing spectral reshaping with additional bandwidth created in the centre of the pulse, towards the peak intensity.

With careful alignment, using the 2D imaging spectrometer as a reference, it was found that the beam pointing and relative temporal delay between the pump and seed beams in each stage could be operated in such a way as to minimise spatial chirp in the ps-OPA stages. Figure 5.17, shows the retrieved imaging spectrometer profiles of these 'optimised' pulses, with a spatial dispersion of 8.62×10^{-3} mm/nm ($\approx$ 4.71 µrad/nm angular dispersion) measured in OPA1 and -4.32×10^{-4} mm/nm ($\approx$ 0.07 µrad/nm) in OPA2. The OPA2 spatiospectral profile is shows

particular improvement over the previous result, however there is some concern that, if OPA2 is compensating for spatial chirp manifested by OPA1, the spatial dispersion of OPA2 is 'overcompensated' to minimise the spatial dispersion measured on the spectrometer and may be present elsewhere in the system. Table 5.2 shows a comparison of spatial chirp parameters before and after optimisation.

	FWHM (mm)	λ_0 (nm)	$d\lambda_0/dx$ (nm/mm)	$dx_0/d\lambda$ (mm/nm)
Oscillator	0.93	1054.4	-7.49×10^{-2}	-3.03×10^{-3}
OPA1 (pre-optimisation)	1.10	1053.9	0.73	2.92×10^{-2}
OPA1 (post-optimisation)	1.04	1054.3	0.22	8.62×10^{-3}
OPA2 (pre-optimisation)	0.84	1052.6	-0.81	-1.04×10^{-2}
OPA2 (post-optimisation)	0.64	1053.3	-2.96×10^{-2}	-4.32×10^{-4}

Table 5.2: Spatial chirp parameterisation of the oscillator and ps-OPA stages before and after careful alignment to minimise spatial chirp.

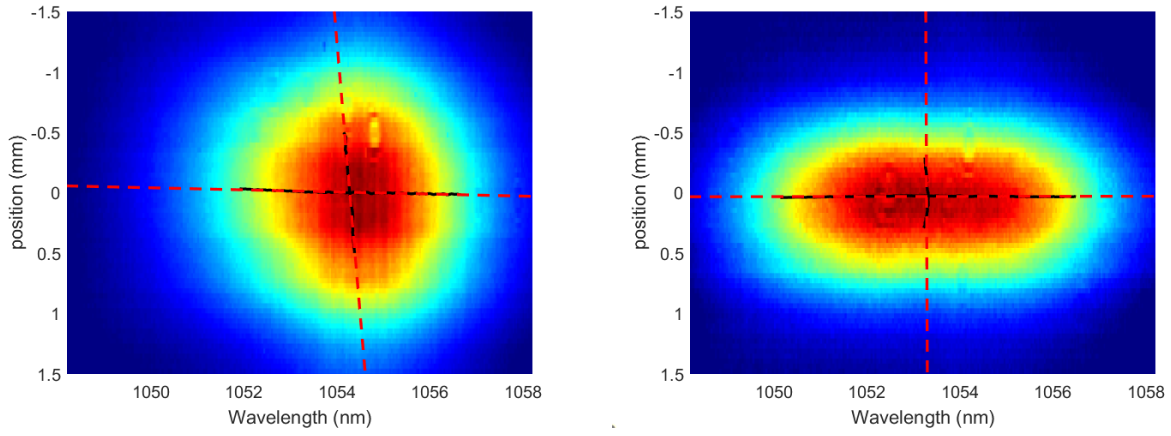


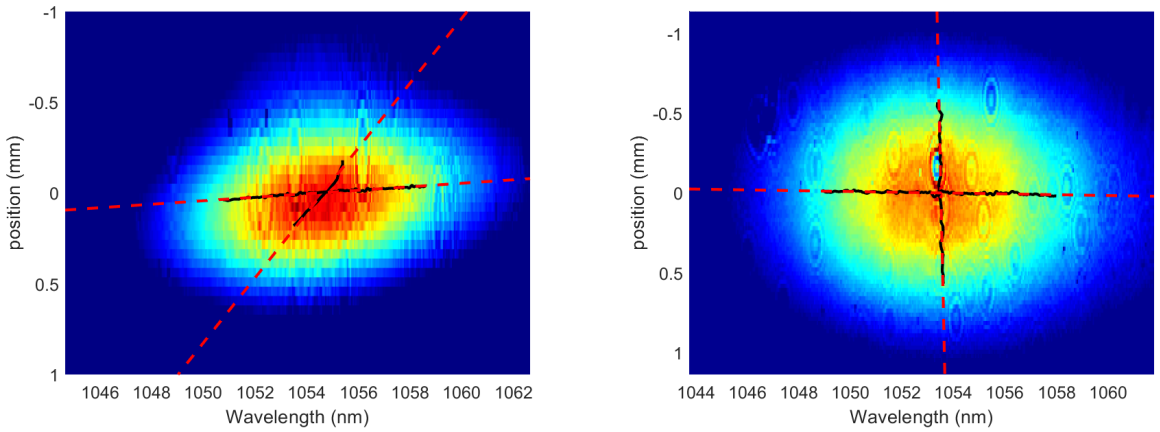
Figure 5.17: Spatiospectral profile of the a) OPA1 and b) OPA2 signals after careful alignment to reduce the spatial chirp in the system. Black lines represent the peak intensity for slices along the image in position and wavelength, from which the linear fit (red lines) gives the spectral dispersion, $dx_0/d\lambda$ and frequency gradient $d\lambda_0/dx$.

With the spatial chirp manifesting in the ps-OPA stages quantified, we moved on to characterising the spatial chirp reduction in the output of OPA2 using HCF. Figure 5.18 shows the spatiospectral profile of OPA2 signal before and after spatial filtering with an $a = 100$ µm diameter, $L = 210$ mm cylindrical dielectric HCF. To minimise error due to system alignment or OPA efficiency, both measurements were taken within under an hour of each other. To measure the OPA2 signal, the image of the beam at the OPA2 crystal was relayed into the 2D imaging spectrometer, whilst to measure the output of the HCF, the image at the back focal plane of the collimating

lens was instead taken. Due to the different lens pairs used to image these two parts of the system, we measure a difference in the FWHM of the spatial profile for the OPA2 signal and the HCF output with the spectrometer. To account for this, we have parameterised the spatial chirp here, normalised to the position of the beam profile, with an adjusted spatial dispersion, $dx'_0/d\lambda$, and a frequency gradient, $d\lambda_0/dx'$, where the position on the beam profile is quantified as proportion of total beam waist, $x' = x/FWHM$. We also note that in this case the spatial profile of the filtered beam is inverted by the focusing and collimating lenses either side of the HCF, therefore for clarity the spatial dispersion and frequency gradient are presented as magnitudes. Analysis of the OPA2 signal yields a normalised spatial dispersion of 2.53×10^{-2} mm/nm and a normalised frequency gradient of 2.09 nm/mm, where the spatial dispersion corresponds to an angular divergence of 13.8 µrad/nm. After spatial filtering with HCF, we observed significant improvement in the spatial chirp of the pulse, with the residual spatial dispersion measured as 2.07×10^{-3} mm/nm and the frequency gradient measured as 0.12 nm/mm, reduced by a factor of 12.2 and 17.9 respectively.

	FWHM (mm)	λ_0 (nm)	$d\lambda_0/dx$ (nm/mm)	$dx_0/d\lambda$ (mm/nm)
Pre-HCF	0.30	1054.4	2.1	-2.5 × 10^{-2}
Post-HCF	0.85	1053.8	0.12	2.1×10^{-3}

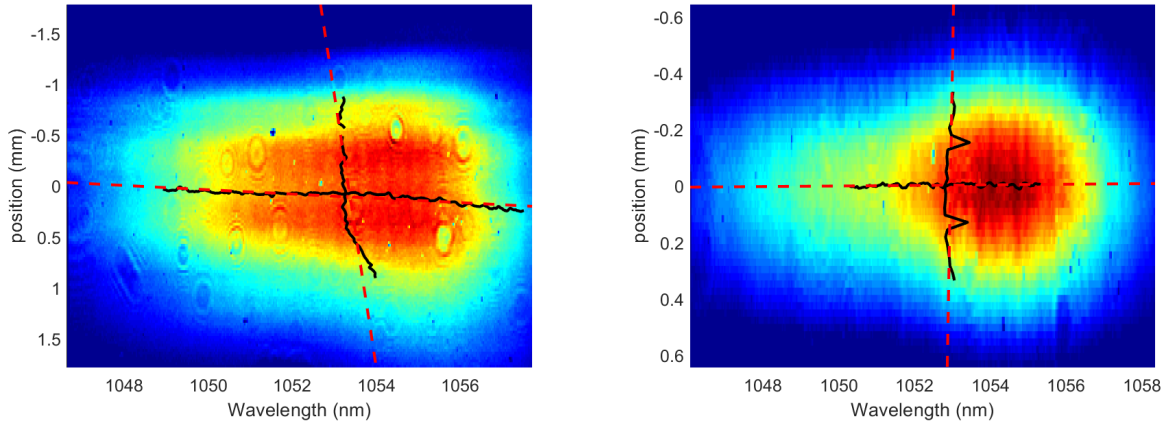
Table 5.3: Spatial chirp parametrisation before and after spatial filtering with a 100 µm diameter, 210 mm long cylindrical dielectric HCF.



(a) (b)

Figure 5.18: The spatiospectral profile of OPA2 signal beam before (a) and after (b) spatial filtering with a 100 µm diameter, 210 mm long cylindrical dielectric HCF. In each figure the degree of linear spatial dispersion and frequency gradient is shown.

By imaging the HCF output, the imaging spectrometer averaged the spectral profile of the beam across every point in the x axis, which allowed measurement of the total spatial chirp but resulted in loss of fine structure data for the spectrum at specific points. To measure the spatial chirp of a specific slice of the x axis, the imaging spectrometer was redesigned to propagate the OPA2 signal or the HCF output onto a ∼90 µm width slit at the spectrometer image plane. The image of the slit was collimated using a cylindrical lens with a measured focal length $f_c = 49.3$ mm before similar dispersion using a holographic 1800 l/mm diffraction grating and the spectrum resolved onto the beam profiler (Thorlabs BC106N-VIS) using a $f_f = 75.3$ mm cylindrical lens. In this configuration, the imaging spectrometer resolution was calculated to be $\Delta\lambda_{min} = 0.4$ nm, sufficient for measuring spatiospectral structure in a > 10 nm bandwidth pulse.



(a) (b)

Figure 5.19: The spatiospectral profile of OPA2 signal beam before (a) and after (b) spatial filtering with a 100 µm diameter, 125 mm long cylindrical dielectric HCF. Only the centre of each beam profile was selected using a ∼90 µm slit at the image plane of the fibre. Black lines represent the peak intensity for slices along the image in position and wavelength, from which the linear fit (red lines) gives the spectral dispersion, $dx_0/d\lambda$ and frequency gradient $d\lambda_0/dx$.

With this new imaging spectrometer configuration aligned to the centre of the OPA2 and HCF spatial profiles, we again measured the spatial chirp in the OPA2 signal before and after filtering using HCF. However in this instance, the fibre used to spatially filter the OPA2 signal had been cleaved to a shorter length, $L = 125$ mm, than previously. The shorter fibre was expected attenuate high spatial frequencies less than previously, however still retained waveguide qualities which would homogenise the spatial chirp and angular dispersion. Figure 5.19 shows the resolved imaging spectrometer data of the OPA2 signal with and without HCF modal filtering, again showing excellent spectral dispersion and frequency gradient reduction. For the centre of the

beam profile, incident upon the ∼90 µm slit of the imaging spectrometer, the normalised spatial dispersion ($dx'/d\lambda$) and frequency gradient ($d\lambda_0/dx'$) measured were 2.1×10^{-2} mm/nm and 0.37 nm/mm respectively before and 1.0×10^{-3} mm/nm and 0.13 nm/mm respectively after filtering.

Spectral Phase Characterisation

Hollow core fibres are commonly used for supercontinuum generation and self-compression of laser pulses [117]. Both of these nonlinear effects arise as a result of self-phase modulation, described in section 2.1.3, where the instantaneous frequency of a pulse is modulated by the intensity-dependent nonlinear refractive index. However, self phase modulation is non-ideal in the case where HCF is used for contrast enhancement, as a spatiotemporal filtering technique must not add additional, uncompressible, high order phase terms to a laser pulse.

The laser B integral, the total nonlinear phase shift a beam experiences, can be used to estimate an approximate threshold for problematic nonlinear effects to emerge. Laser systems are typically designed to limit the accumulated B integral to <3. From equation 2.19 and 5.2, we can approximately describe the B integral for a beam propagating through an air-filled HCF as,

$$B \simeq \frac{2\pi}{\lambda_0} \int n_2 I_0 \exp(-\alpha_{nm} z)\, dz \tag{5.4}$$

where n_2 is the nonlinear refractive index of air, measured by Schwarz et al at at 1054 nm as 2.6 $\times10^{-23}$ $\mathrm{m^2W^{-1}}$ [118] and α_{nm} (equation 5.2) is the attenuation factor, depending on the popagating mode and the fibre diameter. For the LP_{01} mode, $\alpha_{01} = 0.241$ $\mathrm{m^{-1}}$ for 200 µm diameter fibre. For a pulse with similar paramters to the OPA2 signal (150 µJ, 1.2 ps), for which ∼90% of light is coupled into the LP_{01} mode of 200 µm diameter 300 mm long HCF, and assuming that the fibre sets a constant beam radius of 100 µm in the LP_{01} mode, we arrive at a calculated B integral of 0.16, which should be safely below the limit for SPM or other nonlinear effects.

Additional bandwidth generation due to SPM would also have been visible on the previous 2D imaging spectrometer results, however a more accurate measurement can be gathered from spectral phase retrieval using a FROG. In order to characterise the effect of HCF on the spectral phase of the pulse, we used the Cerberus FROG (described in section 3.2) to characterise the beam before and after spatiotemporal filtering with 200 µm diameter HCF. The retrieved spectral phase from the the FROGed algroithm can be fitted with a 4th-order polynomial function around

$\omega' = (\omega - \omega_0)$, where the Talyor expansion of spectral phase, from 2.4, gives

$$\varphi(\omega) = \varphi^{(0)} + \varphi^{(1)}\omega' + \frac{1}{2!}\varphi_2\omega'^{(2)} + \frac{1}{3!}\varphi_3\omega'^{(3)} + ... \tag{5.5}$$

from which we can determine the linear chirp (equation 2.6), the group time delay dispersion (equation 2.7) and the third order dispersion (equation 2.8).

A systematic error was found in the in FROG alignment which resulted in the measurement of a non-symmetric spectrogram. This may have been caused a misalignment in the translation stage introducing angular walkoff between the reference and gate pulses, resulting in them not propagating parallel to one another, which would have varied the crossing angle and moved the position of best focus within the SHG crystal. This asymmetry would have resulted in a poor retrieval, as discussed in chapter 5, and therefore the measured spectrogram was analysed twice, by mirroring each side of the spectrogram around $t = 0$. Whilst this systematic error potentially prevents us making a definitive conclusion from the retrieved pulse, since the systematic error was present in both to some extent, we can infer any effect of the HCF on the differences between the two scans.

Figure 5.20 shows the FROG retrieval of the OPA2 signal, including the measured spectrogram using the Cerberus FROG (top left). There was an asymmetry present due to user misalignment in the FROG trace and therefore to minimise these effects the retrieval algorithm inverted the trace around t = 0. The retrieval algorithm was run for the entire measured trace, giving an error of 0.033, while inverting the spectrogram around the right hand side of the trace (t = $0 \rightarrow \infty$) resulted in a retrieval error of 0.026 and inverting the trace around the left hand side (t = $0 \rightarrow -\infty$) gave a retrieval error of 0.025. The minimum retrieval error for confidence is 0.02 [72], therefore we cannot draw concrete conclusions from this data, however it provides a reasonable indicator for changes in the spectral phase due to propagating a beam through HCF. The top right image of figure 5.20 shows retrieved FROGed trace, taken from the left hand side, which gives the retrieval temporal (bottom left) and spectral (bottom right) intensity profiles and phase of the signal. The temporal FWHM of the retrieval profile was found to be 1.87 ps, in addition to a central wavelength of $\lambda_0 = 1053.0$ nm and a bandwidth of $\Delta\lambda = 9.07$ nm, which correspond with previous measurements.

The spectral phase of the retrieval trace was fitted using a 4^{th}-order polynomial fit to give

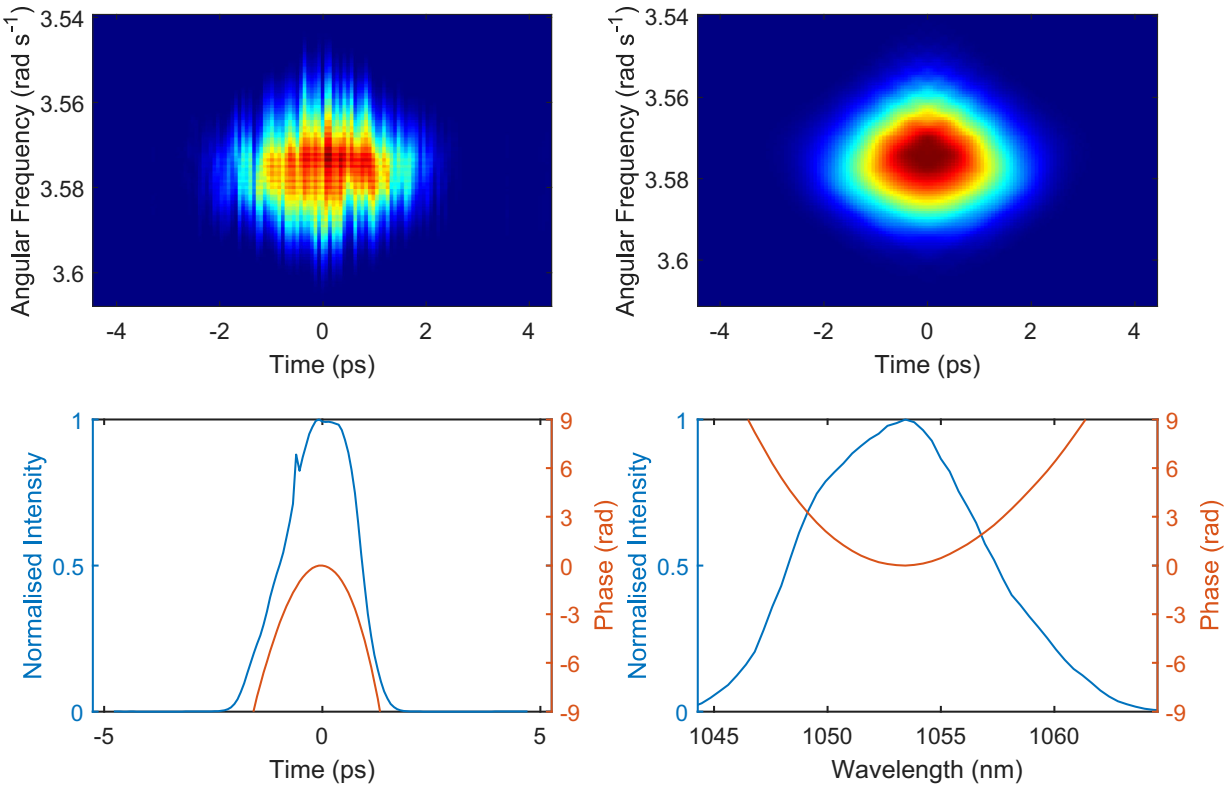


Figure 5.20: FROG retrieval of the OPA2 signal pulse. Top left: the measured spectrogram obtained using the Cerberus FROG, top right: retrieved FROG trace from FROGed code, obtained by mirroring the measured trace around delay = 0 from t = 0 $\rightarrow -\infty$, which gave a retrieval error of 0.025. Bottom left: temporal, and bottom right: spectral profiles of the retrieved FROG trace.

values for the chirp $d\nu/dt$ = 1.23±0.02 THz/ps, the group time delay dispersion (GTDD), D_λ = 0.220±0.003 ps·nm^{-1} and the third order dispersion, $D_{3,\lambda}$ = 0.7±0.3 fs·nm^{-2}. The errors here are determined by the polynomial fit factor. A chirp of $d\nu/dt$ = 1.23±0.02 THz/ps corresponds reasonably with the expected linear chirp due to the ps-OPA SF6 glass block stretcher of ∼1.06 and the measured third order dispersion would not have a significant effect on the pulse profile or compressibility.

Figure 5.21 shows the FROG retrieval of the HCF, from the measured spectrogram obtained using the Cerberus FROG (top left) and the FROGed retrieved spectrogram (top right). Similarly to figure 5.20, the measured spectrogram was cut and mirrored around the left side of the trace (t = 0 $\rightarrow -\infty$), giving a retrieval error of 0.023 (compared to 0.028 when taken from the right hand side).

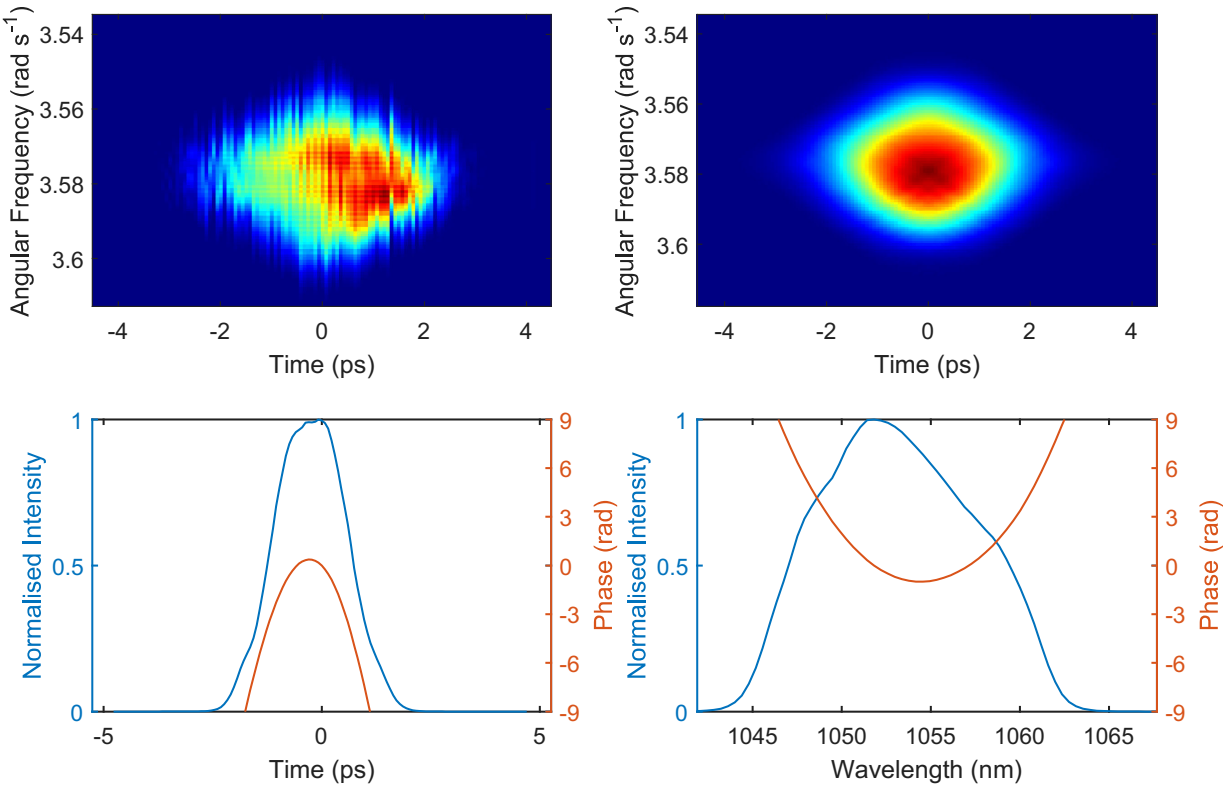


Figure 5.21: FROG retrieval of the OPA2 signal pulse, post filtering with 200 µm diameter, 300 mm long HCF. Top left: the measured spectrogram obtained using the Cerberus FROG, top right: retrieved FROG trace from FROGed code, obtained by mirroring the measured trace around delay = 0 from t = 0 $\rightarrow -\infty$, which gave a retrieval error of 0.023. Bottom left: temporal, and bottom right: spectral profiles of the retrieved FROG trace.

Analysis of the temporal (bottom left) and spectral (bottom right) intensity profiles gives a FWHM pulse duration of 1.99 ps, a central wavelength of $\lambda_0 = 1053.0$ nm and a bandwidth of $\Delta\lambda = 11.1$ nm. It is notable here that the spectral profile of the HCF signal does differ from the previous OPA2 measurement, however it still resembles spectra previously measured from OPA2 when that stage was pumped with additional pump energy (section 4.3.3). The FROG measurements for the OPA2 and HCF outputs were taken on consecutive days and therefore it is possible that changes system may have produced different spectral profiles. A fourth order polynomial fit of the spectral phase gives values for the linear chirp of $d\nu/dt = 1.26\pm0.009$ THz/ps, the group time delay dispersion (GTDD) $D_\lambda = 0.214\pm0.003$ ps·nm^{-1} and the third order dispersion $D_{3,\lambda}$ = -0.6±0.4 fs·nm^{-2}. As previously, these are in reasonable agreement with expectations and importantly do not significantly differ from the measurements of the OPA2

signal without filtration. Whilst repeated measurements would remove ambiguities in the retrieval process, these results nevertheless indicate that HCF does not impose additional high order phase terms or dispersion onto the beam profile, an observation in agreement with previous publications [109], [110].

5.4 Conclusion

As we have seen in this section, a cylindrical dielectric HCF is a capable spatial filter at high energies which also works to homogenise the spatiospectral profile of the ∼180 µJ, 1.2 ps signal pulse output of a two-stage OPA system.

As the beam propagates along the hollow core fibre, high order spatial order modes are attenuated more strongly and the beam tends further towards a Gaussian spatial profile. However, modal filtering attenuates the beam and therefore the transmission efficiency is limited by the fibre length, whilst energy can be recouped at later amplification stages there is need to establish parameters that provide adequate modal filtering within acceptable transmission efficiency losses. We have investigated spatial filtering with two diameters of HCF; the maximum transmission efficiency recorded was ∼50% for 100 µm diameter, 250 mm long fibre, robust over several hours of operation however with a limited lifetime due to damage at the input face which reduced the maximum transmission efficiency and potentially introduced additional scatter into the beam profile. A larger, 200 µm diameter, fibre was able to circumvent the damage threshold at our focused intensities, demonstrating high transmission efficiencies, >75%, approaching that of conventional spatial filters such as VSFs. Despite a larger diameter, this fibre preserved good spatial filtering qualities, with additional benefits lying in its nature as a "fixed point" for beam position, beam pointing and spatial mode in the system.

The transmission efficiency through HCF was observed to be highly dependent upon the focal spot at the input of the fibre. For robust long-term operation and to reduce the need to regularly realign the fibre an active alignment system may offer a necessary solution to this, using motorised beamsteering controllers to optimise the input into HCF. However, this could limit the maximum number of HCF stages on a laser due to the cost and complexity of integrating multiple active alignment stages. Some compromise could also be reached with a variety of HCF diameters where less critical filtering stages could have a broader fibre diameter and therefore not require such

significant active stabilisation.

The 200 µm fibre transmission efficiency scans for the in z (figure 5.13)were performed on a separate day to the measurements for x & y translation (figure 5.14), however the system was not realigned between these days. In the first set of scans, there is no sign of astigmatism whereas the difference in the variation in x, y due to translation of the HCF input suggests there may have been astigmatism in the beam present. This raises concerns that the astigmatism can develop during short periods, perhaps due to changes in the laboratory temperature or the mode-locking of the master oscillator. However, this also shows the value of HCF as a tool to filter aberrations from the spatial beam profile which may unexpectedly appear.

Whilst the transmission efficiency of HCF is important to maximise in order to preserve the gain of the OPA stages, the key interest lies in its ability to filter high order spatial modes and provide a fixed system point. The loss in energy due to transmission efficiency can be compensated for in further long pulse/low spatiospectral aberration later amplification stages. Due to further losses in the Öffner stretcher directly following the ps-OPAs, of up to ∼70%, the seed energy to the final OPA stages in the Cerberus front end beamline, the ns-OPAs, is typically of order ∼50 µJ which is amplified by a typical gain factor of ∼200. The minimum energy requirement for the ns-OPA stages, to reach a threshold for proton production in 15 µm Al foil shots, is ≈4 mJ, however the current pump energy delivered to these stages, ∼180 mJ, is below the maximum potential output of the pump beamline, ∼300 mJ, and therefore the additional loss due to HCF could potentially be recouped by increasing the pump energy delivered to these later amplification stages.

After characterising the transmission efficiency through HCF, we moved on to examining its ability to filter spatiotemporal couplings from ps-domain OPA stages. First characterising the spatial chirp present in the stages before filtering, we observed a lower spatial dispersion present in the OPA2 signal compared to OPA1 signal, which we theorised to be as a result of the inverting telescope between the stages. This is an important observation, operating two-stage OPA systems has been shown to improve the spectral stability of the output [85], however by introducing a telescope between the two stages, or by flipping the orientation of seed and pump beams, we may also compensate to some degree for spatiotemporal couplings which manifest in each individual gain stage. Additionally we were able to minimise spatial chirp arising in these stages with careful alignment and timing control. However, there was some ambiguity as to whether angular

dispersion was still present in the beam and merely minimised at the imaging spectrometer. This also illustrates the importance of alignment through two-stage ps-OPA systems as changes in the beam pointing may cause subtle spatiotemporal couplings to appear, to the detriment of the laser system contrast. As the steps to minimise spatial chirp required careful alignment of the system they are not automatically robust against changes in beam pointing or temporal wander due to changes in the relative path length in the system due to thermal effects.

HCF appears to offer a viable method of removing or minimising spatial chirp, and therefore angular dispersion, present in a pulse. We have demonstrated a significant reduction in both the spatial dispersion and frequency gradient measured in the spatiospectral profile of a laser pulse. Additionally, spectral phase characterisation using the Cerberus FROG diagnostic does not show any large additional or uncompressible spectral phase terms in the HCF filtered pulse that might result from unwanted SPM in the fibre.

The capacity for both angular dispersion reduction and pointing stability improvements make hollow core fibre an attractive candidate technique for incorporating into a potential phase-conjugate OPCPA beamline. This is a concept discussed in more detail in section 10, however in essence this involves stretching the pulse with a Treacy-style two-grating z-compressor to give a negative chirp before further amplification using OPA where the idler beam, the phase-conjugate of the signal pulse with positive chirp, is taken and compressed in a similar Treacy z-compressor. The idler inherits high order spectral phase terms from the pump beam as well as angular dispersion and is susceptible to pointing instabilities in the pump beam. HCF filtering could reduce the impact of these last two factors and increase the robustness of the ilder signal. HCF could also potentially also be used at the output of a stretcher, to compensate for spatial chirp/angular dispersion and clean up the spatial profile for efficient amplification in later gain stages.

Chapter 6

Laser-Plasma Interactions

High power lasers can act as compact particle accelerators, and are often used in experiments as drivers for x-ray radiation, high energy electrons, protons and ions and neutrons [3], [5], [34]. The intense electromagnetic fields generated at the point of focus can ionise materials and accelerate these species to high energies via several mechanisms which depend upon the initial conditions of the laser and target parameters. In this section we briefly review some of the key elements of the laser-matter interaction, but also highlight that this is a large and complex field, with many interesting themes beyond the scope of the thesis work. Here we particularly focus on processes that can be sensitive to early time optical noise or pre-pulse that might then modify the later time laser-matter interaction, using target normal sheath acceleration (TNSA) from a thin foil as an example case.

6.1 The Pondermotive Force

The pondermotive force acts upon a charged particle in the presence of an external electromagnetic field such that it accelerates the particle away from the region of high field density. Semi-classically, laser-plasma interaction is modelled between charged species in a plasma and an external electromagnetic field, $\boldsymbol{E}$ & $\boldsymbol{B}$, where the motion of charged particles is described by the Lorentz force. Fluid equations for an electron plasma with charge e and mass m_e can be written in the form

$$\frac{\partial \boldsymbol{v}}{\partial t} + \boldsymbol{v}\left(\boldsymbol{v}\dot{\nabla}\right) = -\frac{e}{m_e}\left(\boldsymbol{E} + \boldsymbol{v} \times \boldsymbol{B}\right), \tag{6.1}$$

where $\boldsymbol{v}$ is the velocity of the charged particle in the electromagnetic field. Motion is dominated by linear and nonlinear response to the external field, which can be differentiated into two responses by splitting 6.1 into 1st and 2nd order terms such that $\boldsymbol{v} = \boldsymbol{v}_1 + \boldsymbol{v}_2$. In this case, the linear response is found in the form;

$$\frac{\partial \boldsymbol{v_1}}{\partial t} = -\frac{e}{m_e}\boldsymbol{E}, \tag{6.2}$$

which, when substituting a plane wave solution for the electric field to represent the laser, yields a linearised solution in the form

$$\boldsymbol{a} = a_0 \sin(kz - \omega t)\hat{\boldsymbol{x}}, \tag{6.3}$$

where $\boldsymbol{v}_1 = c\boldsymbol{a}$, a_0 is most often called the *normalised vector potential* or *quiver* resulting from oscillations due to the external electric field.

Nonlinear responses of the charged particle quiver can be written in the form:

$$\frac{\partial \boldsymbol{v_2}}{\partial t} = -\left(\boldsymbol{v}_1\dot{\nabla}\right)\boldsymbol{v}_1 - \frac{e}{m}\left(\boldsymbol{v}_1 \times \boldsymbol{B}\right) \tag{6.4}$$

Using the identities $\boldsymbol{B} = \nabla \times \boldsymbol{A} = (m_e c/e)\nabla \times \boldsymbol{a}$ and $\boldsymbol{v}_1 = c\boldsymbol{a}$, this equation is shown to simplify as

$$\begin{aligned}\frac{\partial \boldsymbol{v_2}}{\partial t} &= -c^2\left(\boldsymbol{a}\dot{\nabla}\right)\boldsymbol{a} - c^2\left(\boldsymbol{a}\left(\nabla \times \boldsymbol{a}\right)\right) \\ &= -c^2\left(\boldsymbol{a}\dot{\nabla}\right)\boldsymbol{a} - c^2\left(\frac{1}{2}\nabla a^2 - \left(\boldsymbol{a}\dot{\nabla}\right)\boldsymbol{a}\right) \\ &= -\frac{1}{2}c^2\nabla a^2\end{aligned} \tag{6.5}$$

From this, we can clearly see a force which acts along the spatial gradient of the electric field, accelerating ions away from regions of high field density. This is called the Pondermotive force,

$$\boldsymbol{F}_P = -\frac{1}{2}m_e c^2 \nabla a^2, \tag{6.6}$$

Returning to the frame of a plane-wave electric field, described by 6.2 and 6.3, the time-averaged pondermotive force is given by,

$$\boldsymbol{F}_P = -\frac{1}{4}m_e c^2 \nabla a_0^2 = -\frac{e}{4m_e\omega^2}\nabla E_0^2 \tag{6.7}$$

Lastly, to put this in a frame to predict interactions with our laser, we can use the identities

$\omega = 2\pi c/\lambda$ and $I_0 = \epsilon_0 E_0^2/2$, yielding:

$$\boldsymbol{F}_P = -\frac{e^2 I\lambda^2}{8\epsilon_0 \pi^2 m_e c^3} \quad \propto I\lambda^2. \tag{6.8}$$

Therefore electron acceleration scales strongly with the laser intensity and wavelength.

6.2 Target Normal Sheath Acceleration

The most easily accessible regime, and most common, for ion acceleration is target normal sheath acceleration (TNSA) where electrons are accelerated from the front to the rear of a solid target and the charge separation between them and the surface of the target accelerates a beam of ions behind them. TNSA is achieved at focused intensities of $10^{16} - 10^{23}\ Wcm^{-2}$ [12], within the range of most modern high power laser systems which are reported to generate proton beams with energies approaching 100 MeV [119]. The TNSA mechanism is described in figure 6.1

The high electromagnetic field created by a focused laser means that in the case of a pulse with a Gaussian temporal profile, the leading edge of the laser pulse or elements of the pulse with intensity exceeding the threshold for field ionisation that arrive on target prior to the main pulse will pre-ionise the front surface of the target, creating a so-called 'preplasma' at the surface which then typically expands outwards at the ion sound speed, C_s. As the outer layers of the target expand fastest, this creates a density gradient at the front of the target of

$$n(z,t) = n_0 \exp(-x/C_s t) \tag{6.9}$$

where the ion sound speed is given by

$$C_s = \left(\frac{\gamma_{Cp} Z k_B T_e}{m_i}\right)^{\frac{1}{2}} \tag{6.10}$$

where γ_{Cp} is the adiabatic index, approximately unity for plasma expansion over long length scales, Z is the atomic number of the ion species in the plasma, ion mass m_i, and k_B is the Boltzmann constant.

As the interaction continues, later arriving components of the laser pulse propagate through the preplasma up to the critical surface, where the plasma wavelength is equal to the laser

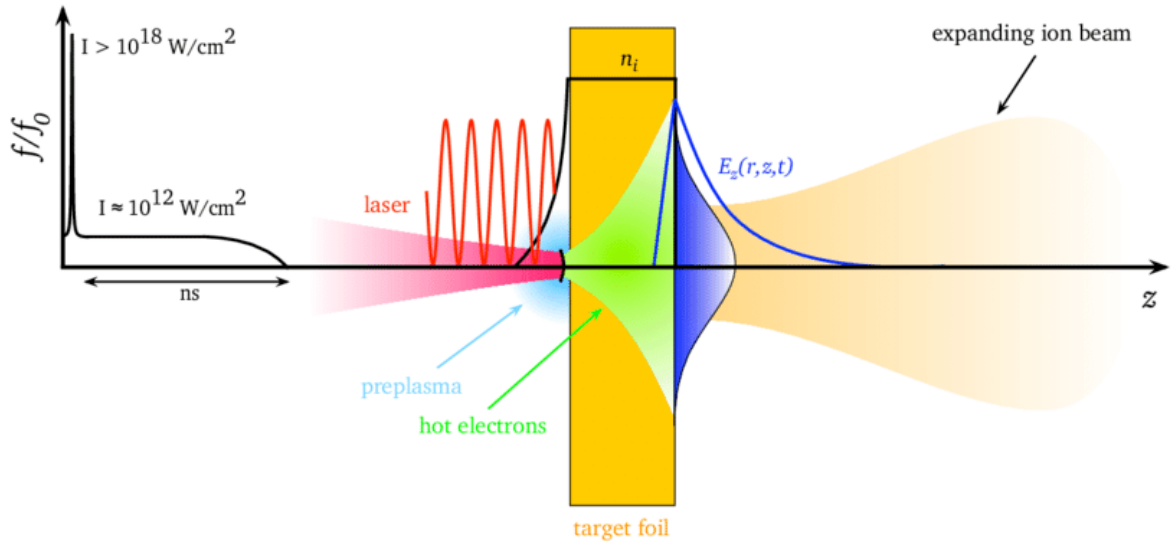


Figure 6.1: An outline of the TNSA mechanism. As the leading edge of a high power laser pulse is focused onto a thin (∼5 - 50 µm thick) metallic foil, the surface of the foil is ionised by intensities greater than 10^{12} Wcm^{-2}, creating an expanding preplasma at the front of the target. Electrons pondermotively accelerated by the main pulse may then travel through the target as 'hot electrons', escaping from the rear side and establishing a high electric field between the electron beam and the rear of the target due to charge seperation. This electric field will ionise the rear surface, accelerating ions in the direction pointing normal to the target. From Roth et al. [4]

wavelength. Within this sub-critical region the laser will deposit energy into the plasma via inverse-Bremsstrahlung at underdense regions and resonant absorption at the critical surface causing further heating and ionisation which then drives continued expansion of the plasma.

The strong electromagnetic potential of the laser accelerates electrons into the target via the pondermotive force, the distribution of these 'hot' electrons largely determined by the pondermotive potential [4], $F_P = -\nabla U_P$ (equation 6.6). The hot electron temperature is found to similarly scale linearly with the laser intensity, I, and quadratically with the wavelength, λ;

$$T_{hot} \approx U_P \approx 1MeV \times (I[\mathrm{Wcm}^{-2}]\lambda^2[\mu m^2]/10^{19})^{1/2}. \tag{6.11}$$

Assuming an exponential distribution around this temperature, and an efficiency η, the density

of hot electrons, n_0, pondermotively accelerated into the target is

$$n_0 = \frac{\eta E_L}{ct_L \pi r_0^2 k_B T_{hot}}, \tag{6.12}$$

where E_L, t_L and r_0 are the laser parameters; the energy, pulse duration and radius of focal spot respectively.

Hot electrons are screened as they travel through the target once they move inwards beyond the critical surface, however the target local electron density does result in some broadening of the electron beam through electrostatic repulsion by a characteristic broadening angle θ proportional to the target thickness, d, density and nuclear charge, Z. The density of electrons at the rear surface of the target is therefore adjusted to

$$n_{e,0} = \frac{\eta E_L}{ct_L \pi \left(r_0 + dtan\left(\theta/2\right)\right)^2 k_B T_{hot}}. \tag{6.13}$$

Charges at the rear of the target are no longer screened, this charge separation induces a large electric potential, Φ between the escaping hot electrons and the rear surface of the target which manifests as a high sheath electric field on the rear surface. The longitudinal extension of the sheath is governed by the Debye length,

$$\lambda_D = \left(\frac{\epsilon_0 k_B T_{hot}}{e^2 n_{e,0}}\right)^{1/2}, \tag{6.14}$$

which can be shown to scale quadratically with the target thickness and is inversely proportional to the laser intensity (from eqaution 6.11) [4]. A thinner target or a more intense focused laser will produce a shorter sheath field extension and therefore a stronger electric field. The theoretical derivation for 6.14 however assumes a step in the gradient of the rear target surface where within the target the electric potential is perfectly compensated, if instead there is some density gradient on the rear surface of the target, the hot electron Debye length will be reduced by the ion density scale length [120].

The maximum electric field at the rear surface of the target is given simply by

$$E_{max} = \frac{\sqrt{2} k_B T_{hot}}{e \lambda_D}, \tag{6.15}$$

and by simply substituting identities from 6.11, 6.13 and 6.14, clear scaling laws become apparent;

$$E_{max} \approx 5.2 \times 10^{11} \frac{r_0}{r_0 + d\tan\theta/2} I^{7/8} \times 10^{18} [V/m] \tag{6.16}$$

Broadly, key scaling laws and the parametric importances for TNSA are incident laser intensity and the target thickness. In addition to this, a steep density gradient on the rear surface of the target is also important to reduce ion density scale lengths. This is discussed in more detail by Robson et al 2007 [35].

This electric field created in this way is high enough to exceed the ionisation threshold for atoms at the rear surface, usually contaminants such as water vapor and hydrocarbons present on the target surface. Unconfined, these species are accelerated by the sheath field to high energies and follow the hot electrons as a tight beam. Laser driven ion sources tend to have low divergence with small source sizes and short pulse durations determined by the focal spot and pulselength of the laser, lending themselves to probing and imaging applications.

6.2.1 Influence of Contrast upon TNSA

Scaling laws for TNSA indicate that we should aim to use a high laser intensity, a thin target and a steep rear-target density gradient. Light arriving on target ahead of the main pulse which is of an intensity above the ionisation threshold for the target material will however alter the initial conditions of the TNSA process.

Ionisation of foil targets has been observed at intensities of $10^{12}\ Wcm^{-2}$ [12] and as high power laser development produces systems capable of higher focused intensities, the intensity contrast ratio of "small", early time optical features reaching the target ahead of the main pulse will increasingly exceed this threshold. Indeed, for system such as Orion or Vulcan PW which deliver intensities of $10^{21}\ Wcm^{-2}$, potential prepulse components at a 10^{-9} contrast ratio to the main pulse may lead to significant preplasma formation and expansion before the arrival of the main pulse. Even for university class systems such as Cerberus, operating at a focused intensity of $10^{19}\ Wcm^{-2}$, components of the pulse have been shown to exceed this threshold.

When the target is pre-ionised, a preplasma forms at the target surface which will expand based upon the ion sound speed. An expanding preplasma acts to attenuate the main beam, reducing on-target intensity [121]. Laser energy deposition into the expanding underdense plasma or at the

critical surface reduces the density step-gradient at the rear of the target due to bulk heating via x-ray generation or shockwaves [12] which also disrupt the internal electrical conductivity of the target which can interrupt electron transport or induce filamentation of hot electrons inside of the target and lead to greater proton beam divergences and blurring of the source [12]. Furthermore, for a sufficiently thin target, the prepulse can entirely ionise the point of focus, causing the main beam to interact solely with the preplasma [122] or may even completely ablate the target prior to arrival of main pulse [9].

Therefore while TNSA scaling parameters (laser intensity and target thickness) increase the proton yield, they also increase the susceptibility towards the effects that prepulse will have on the interaction. However, certain results have also shown that carefully controlled prepulse can instead benefit ion acceleration. Lefebvre et al. recorded increased hot electron temperature/coupling efficiency with the laser interacting with a large preplasma at the front of the target [123]. Optimal levels of prepulse have also been shown to cause the incoming laser to self-focus to higher intensity due to relativistic self-focusing in a preformed plasma in front of the target [124]. For this reason there is keen interest, not only in removing prepulse from a laser temporal profile but also in identifying the mechanisms by which they are produced to afford greater control over and temporal tuning of the temporal intensity contrast of a high power laser system.

Chapter 7

Target Areas

In this chapter we will describe two of the experimental target areas that the Cerberus laser delivers light towards, the Mega Ampere Generator for Plasma Implosion Experiments (MAGPIE) z-pinch facility and the Cerberus Multi-Terawatt Target Area which is used for laser interactions with thin (∼few µm) metallic foils and novel targets (including optically levitated microdroplets [125] and laser-launched flyers [18]).

7.1 MAGPIE

Cerberus was initially designed, in part, to supply pulsed ps to ns duration NIR and visible light to the adjacent MAGPIE z-pinch facility. MAGPIE discharges large 1.4 MA currents, over a rise time of 240 ns, through thin (∼µm scale) radial wire arrays to generate plasmas for investigating the formation of supersonic, magnetised plasma flows and shocks for laboratory astrophysics [80]. The Cerberus system is currently used for its long pulse beamline, supplementing plasma diagnostic tools including laser interferometry (shadowgraphy and schlieren imaging), Thompson scattering [126] and Faraday rotation imaging of 2D magnetic field structures [127], [128]. The Cerberus long pulse beamline (400 mJ, 1.2 ns) is sent across to an adjacent laser bay, for amplification up to 25 J through 25 mm and 50 mm aperture Nd:Glass gain storage amplifiers.

Recently, the Cerberus laser has been used to provide Faraday rotation imaging to measure the magnetic fields in shocks propagating through and interacting with sub-critical plasmas [20]. This diagnostic technique uses the optical Faraday effect, which results in polarisation rotation of a laser propagating through a plasma, by a given amount depending on the magnetic field, B [129].

The total polarisation rotation is given as,

$$\phi = \frac{\lambda_0^2}{8\pi^2 c^3}\left(\frac{e^3}{\epsilon_0 m_e^2}\right)\int n_e B dL \tag{7.1}$$

where λ_0 is the central wavelength of the diagnostic laser, propagating through a length, L, of plasma with an electron density, n_e. Here, e is the electron charge, ϵ_0 is the permittivity of free space and m_e is the mass of a single electron. Faraday rotation imaging requires a bright signal to out-compete the plasma emission and a known, stable polarisation state, high spatial uniformity and very good (few %) shot-to-shot repeatability to enable background subtraction of residual spatial features in the probe beam. As calculating the total Faraday rotation requires a known plasma electron density, the Faraday rotation beamline is also supplemented by an interferometry beamline.

7.2 Multi-Terawatt Target Area

Amplified light from the Nd:Glass/OPCPA front-end of Cerberus undergoes the final stage of amplification and compression in the 'multi-terawatt target area', for use in high intensity laser target interactions with thin foils and novel target geometries including laser accelerated "flyer" foils and optically trapped levitating droplets [130] investigating particle acceleration of x-rays and protons, x-ray source size measurement, and shock-driver experiments. High energy pulses are directed into the main target chamber, where p-polarised focused intensities of up to 10^{19} Wcm^{-2} can be produced on target using an F/3 off-axis parabola (OAP). The main target chamber is kept under vacuum for high power laser-plasma interactions. The effective repetition rate is determined by two steps, the timescale for the amplifiers to cool after a shot ($\sim$10 minutes for the 50cm rod) and the time to let up and pump back down the main target chamber to swap out targets and diagnostic packages ($\sim$1 hour).

7.2.1 Target Area Laser Diagnostics

To characterise the focused laser intensity produced on-target for each shot in an experiment, we use three separate diagnostics to measure the energy, pulse duration and focused beam diameter of the laser.

Energy Measurement

A fast (∼1 ns rise time) photodiode, is aligned to observe the 0-order diffraction from the first grating in the main pulse compressor. Calibrating the photodiode signal against the compressed pulse energy, measured with an energy meter (GENTEC QE50SP) gives a measurement of the amplified pulse energy used on shot. However, the photodiode is small compared to the beam profile of the main pulse as it propagates through the final compressor. The large path length through air from the final Nd:Glass beamline vacuum spatial filter to the main compressor means that small changes in the beam pointing on a day-to-day basis, or in the case of long experimental days shot-to-shot, will change the point along the beam profile which the photodiode measures, giving a different reading for the same energy. To account for this, the photodiode signal is calibrated prior to each shot by firing a test shot and directly measuring the main beam energy with a reference energy meter. Figure 7.1 shows the relationship between the measured main pulse energy and the photodiode signal, from this figure we can see that whilst the response is reasonably linear, by cross-correlating between these two diagnostics before each shot we are able to limit the error in our pulse energy measurement.

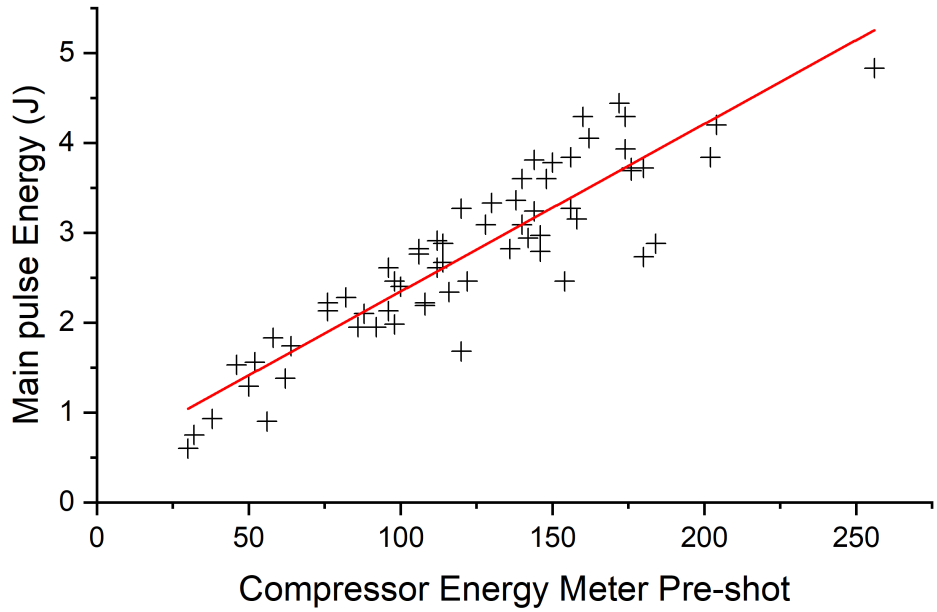


Figure 7.1: SE: Calibration of peak voltage measured by the compressor energy meter against directly measured energy. Each data point x represents a single shot, this data was taken over a time scale of several weeks

Single-shot Autocorrelator

Single-shot autocorrelators allow for us to measure the FWHM pulse duration of a single beam, based upon the principles described in chapter 3. By taking the leakage light through the back of the final mirror directing the main pulse into the target chamber, we can measure the temporal duration of an experimental laser pulse using a single-shot autocorrelator, shown in figure 7.2. The input beam is divided into two pulses which are cylindrically focused to overlap through a 1.5 mm thick beta-barium borate (BBO) nonlinear crystal. One condition for single-shot autocorrelators is that the spatial profile of the beam is smooth over the region of overlap, as well as increasing the signal to noise ratio of the autocorrelator, cylindrically focusing the beams helps us achieve this. A translation stage incorporated into one of the beampaths can be used to ensure good temporal overlap within the crystal. The same portion of each focused beam is overlapped with one another in the nonlinear crystal, however the crossing angle between the two pulses maps the relative delay onto the transverse position of the SHG signal from the nonlinear stage. The crossing angle θ, determines the maximum temporal window as,

$$\Delta\tau = 2\left(\frac{d}{c}\right)\tan(\theta/2) \simeq \frac{d\theta}{c} \tag{7.2}$$

for a beam diameter d, typically set by the crystal tolerance (up to ∼few mm). The nonlinear crystal thickness also accounts for the phase-matched bandwidth which the autocorrelator can measure, typically the thinner the crystal the more bandwidth it supports [67], the Cerberus autocorrelator's 1.5 mm thick BBO crystal theoretically supports 12.3 nm of phase-matched bandwidth, corresponding to a transform-limited pulse duration of 150 fs.

Figure 7.3 shows a single-shot, second order SHG autocorrelation taken from the 10 Hz OPCPA front-end of the system, which was propagated through to the multi-terawatt target area. The FWHM pulse duration of this trace was measured to be 680 fs. However for full power laser shots, gain-narrowing effects in the Nd:Glass flashlamp amplifiers in the front-end glass beamline and the 50 mm main pulse amplifier can limit the compressibility of the main pulse. Typically, we measure on-shot FWHM pulse durations between 700-800 fs.

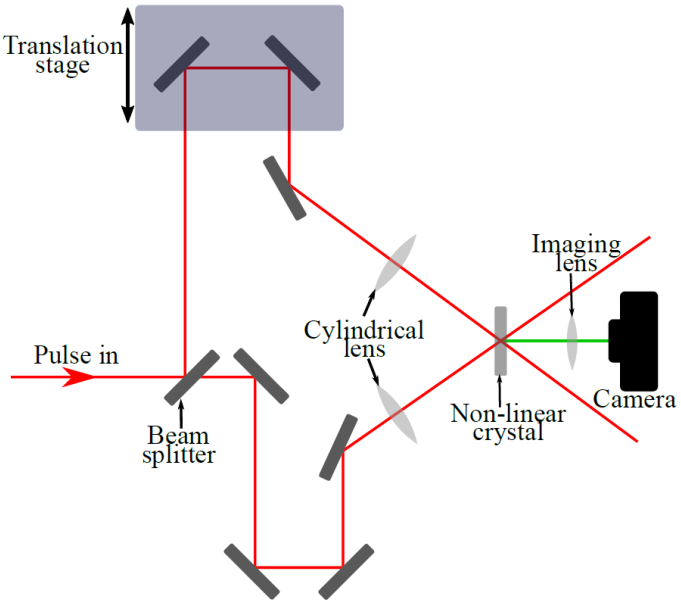


Figure 7.2: Schematic diagram of the single-shot, second order autocorrelator in the multi-terawatt target area. A small portion of the compressed laser pulse is taken and split between two beamlines, which are then cylindrically focused to overlap inside of a 1.5 mm thick beta-barium borate (BBO) non-linear crystal. The crossing angle between the two pulses encodes a time delay onto the SHG signal from the nonlinear stage, from which we can measure the temporal duration of an experimental pulse. Image credit: Samuel Eardley [15].

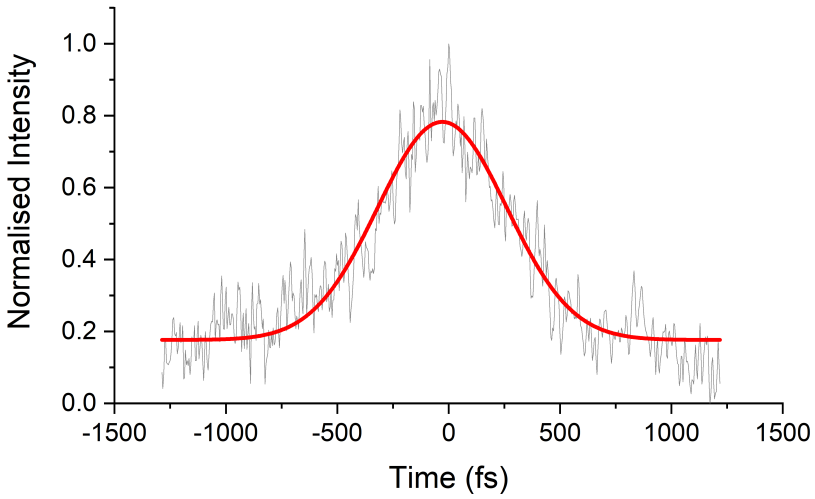


Figure 7.3: Single-shot, second order SHG autocorrelation of the Cerberus 10 Hz OPCPA front-end, with a FWHM pulse duration measured at 680 fs, assuming a Gaussian temporal pulse shape.

Focal Spot Camera

Finally, a focal spot camera can be moved into position to image the target chamber centre with a microscope objective. An example focal spot measurement with 6.3 × 5.2 µm $1/e^2$ focused beam

diameter is shown in figure 7.4. Due to the high energies involved on-shot the camera cannot measure the amplified beam, therefore pre-shot focal spot measurements are carried out on the 10 Hz OPCPA front end signal. A code to calculate the energy contained within the focal spot was written by Samuel Eardley, which works by finding the sum value of all the pixels within the $1/e^2$ beam diameter, divided by the total pixel value across the background-subtracted image. Typically 70- 80% of the laser energy is contained within the $1/e^2$ beam diameter.

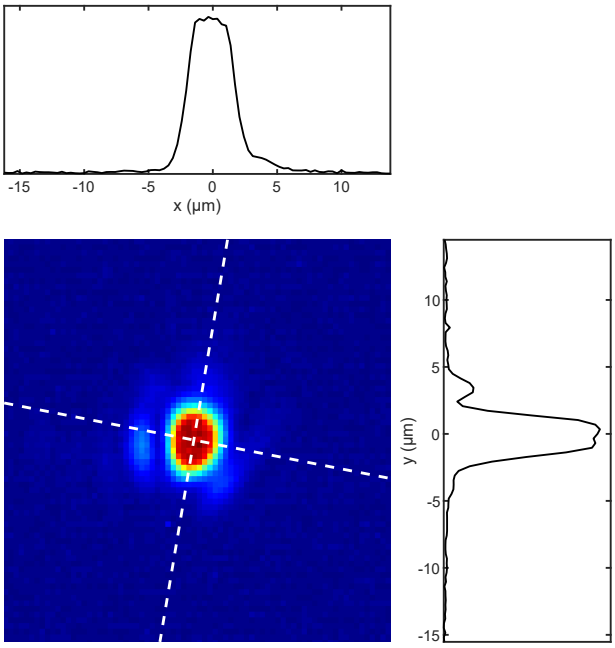


Figure 7.4: Farfield image of the Cerberus main pulse, taken using a microscope objective at the centre of the multi-terawatt target chamber.

7.2.2 Cerberus Interferometry Beamline

One key diagnostic in the multi-terawatt target chamber is a optical probe beamline which can be used for imaging interactions at the target chamber centre (TCC) with a variety of target geometries. Depending upon the configuration of imaging optics used in the interferometer, these have included optically levitated microdroplets [125], thin metallic foils, wires and laser-launched flyers [18]. Additionally, a polarised light Nomarski interferometer [131] is placed at the end of the interferometry beamline for measuring plasma electron densities in underdense regions produced by the laser interaction with the target. The optical probe pulse can be set to arrive at a specific time, relative to the main laser pulse. This allows for single interferometry measurements at a specific point in the laser-target interaction. Alternative interferometry beamlines use a

separately seeded laser source for optical probing, however the Cerberus optical probe beamline is optically-locked to the main pulse which reduces timing jitter from electronic triggers.

An optical probe beam is generated by frequency doubling the ∼60 mJ, 500±50 fs compressed interferometry beamline pulse to $\lambda_0 = 527$ nm in a 1.5 mm long potassium dihydrogen phosphate (KDP) nonlinear crystal. The combination of pulse compression and SHG here provides us with a 'sharp', bright light source which can image rapidly evolving hydrodynamic motion on a sub-ps timescale. An SHG pulse also has the advantage of probing a plasma behind the critical surface of the main laser pulse, where it deposits much of its energy. Light can penetrate through plasma up to the critical density, where the laser wavelength is equal to the plasma wavelength. The critical surface scales with wavelength as $n_{crit} \propto \lambda^{-2}$ and therefore shorter wavelength light is able to penetrate through increasingly dense plasma.

The optical probe, at the point of the interaction (TCC), is imaged by a series of lenses through a Nomarski interferometer [131] where a Wollaston prism is used to produce fringes by overlapping the image of the optical probe at TCC with a reference portion taken from elsewhere in the optical beam profile. A simplified diagram of the interferometer is shown in figure 7.5. A Wollaston prism separates light into two orthogonally polarised beams, when aligned at 45° to the polarisation of the optical probe beam, this splits the probe into two pulses with equal energy, which are recombined using a visible light polariser after the prism to create interference fringes. The Wollaston prism will introduce a small divergence angle as the image rays are focused through the Wollaston prism, by a lens, L, with a focal length of 300 mm in our initial configuration, to be resolved by a camera (Canon 350D DSLR). The fringe separation is given by

$$\delta = \frac{\lambda Z}{\alpha L} \tag{7.3}$$

for a optical probing wavelength λ, where Z is the distance between the Wollaston and the detector plane, α is the angle of the Wollaston prism and L is the distance from the focusing lens to the prism. A benefit of rotating the Wollaston prism at a 45° angle is that the two images are separated horizontally and vertically from each other, so that objects in one image do not obscure measurements in the interferogram. A laser pulse propagating through a plasma acquires a phase shift proportional to the line integral of the plasma electron density and therefore the fringe shift of the interferogram measured using the interferometer can (making some assumptions about

the overall geometry) be used to calculate the electron plasma density in front of the target at a relative time to the main laser pulse determined by the manually specified path length of the optical probe beamline.

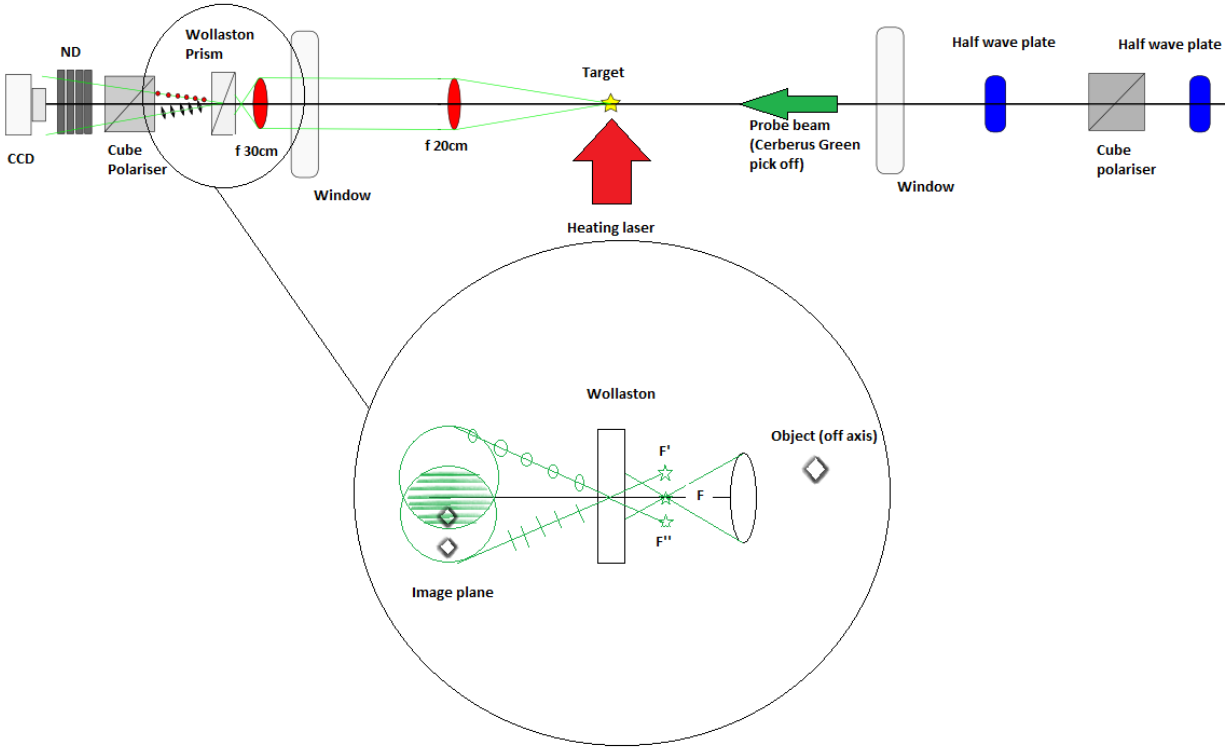
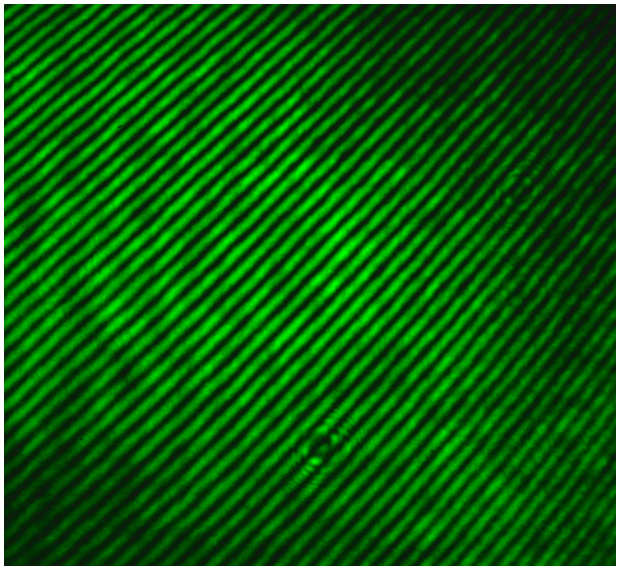
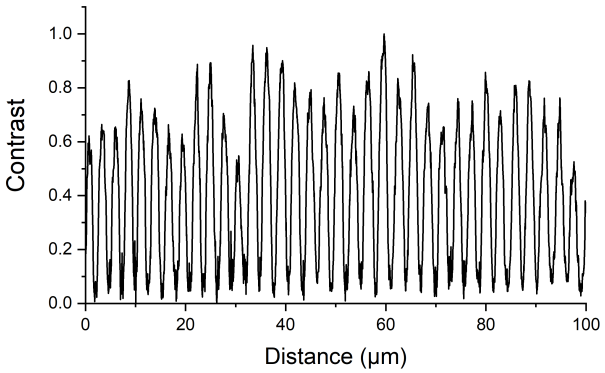


Figure 7.5: Schematic diagram of the Cerberus optical probe beamline and the Nomarski interferometer. An optical probe beam passes through the centre of the main target chamber, at which point the beam is imaged by a series of optics onto a CCD camera. A Wollaston prism, visible polariser combination is used to divide the beam into two and interfere a region of the optical probe which passed through the interaction region with an undisturbed part of the spatial profile. Image credit: Samuel Giltrap [125].

The fringe contrast is determined by the spatial and temporal coherence of the optical probe beam. Figure 7.6 shows The resolution of the optical probe was calibrated inserting a reference object with known size (typically a U.S. air force resolution test chart) into the centre of the target chamber. In its initial configuration, the optical probe beam was imaged with a 0.051 ± 0.001 µm/px resolution.



(a)



(b)

Figure 7.6: Top a) snapshot of a Cerberus Nomarski interferogram, this image has been contrast enhanced to clearly show interference fringes. Bottom b) relative contrast, taken from the unmodified interferogram, of the fringes produced by the interferometer Wollaston prism, rotated at 45°.

Chapter 8

Effect of a Discrete Prepulse on Laser-Plasma Interactions

It is well understood that "early time" features in the temporal intensity pulse profile above a certain threshold can cause pre-ionisation of a target, changing the geometry and mechanisms of a laser-plasma interaction. While target normal sheath acceleration (TNSA) scaling parameters (laser intensity and target thickness) in an ion acceleration experiment increase the proton yield, they also increase the susceptibility towards the effects that prepulse will have on the interaction. However, results published in the literature [132]–[134] have also shown that a carefully controlled prepulse can instead benefit ion acceleration. Lefebvre et al. recorded increased hot electron temperature/coupling efficiency with the laser interacting with preplasma at the front of the target [123]. Optimal levels of prepulse have also been shown to cause the incoming laser to self-focus to higher intensity due to relativistic self-focusing in a preformed plasma in front of the target [124], [133]. For this reason there is additional interest, not only in removing prepulse from a laser temporal profile but also examining the effect of re-introducing a well controlled discrete prepulse, with a specified pulse duration, relative intensity and timing relative to the main pulse, on charged particle acceleration in laser-target interactions. Previous investigations into the effect of discrete prepulses fall broadly into two categories, discrete, ∼ps, prepulses (as with the investigation here) and ns-duration pulses, with a similar temporal profile to background noise such as ASE or OPA-fluorescence.

In this chapter, we will present the results of two experimental campaigns, starting in 2018, which

investigated the effect of introducing a discrete prepulse of known temporal intensity contrast at a specific position in time before the main pulse of the Cerberus laser system at Imperial College London, an OPCPA/Nd:Glass hybrid architecture system described in chapter 4. The work discussed in this chapter was completed in association with Dr. Samuel Eardley and Dr. George Rowland, for fulfilment of their respective PhD research projects. The experiments involved Terawatt laser pulses produced by the Cerberus laser focused to high intensities ($\sim 10^{19}$ Wcm^{-2}) onto several different targets in the Multi-Terawatt target area (chapter 7.2). The first experiment, section 8.2, investigated the emission spectra of charged particles (mainly protons and electrons) and x-rays generated from thin, 14 µm, aluminium foils via the TNSA mechanism (section 6.2) for pulses with an artificial prepulse included a given time before the main pulse. This experiment was principally designed by Samuel Eardley, who coordinated the experiment and designed several diagnostics and systems, including the 'prepulser' subsystem described in section 8.1. Involvement by the author consisted of aligning and optimising the Cerberus laser system for the experiment, additional data analysis and simulation and modelling work described later in the chapter, followed by detailed re-characterisation of the laser system contrast (using the XTOAD diagnostic, discussed in chapter 3.3). More information, including an extended discussion on the data analysis techniques and errors for this experiment can be found in [15].

The second experiment described in this chapter, section 8.3, sought to characterise the source sizes for x-rays generating by laser-plasma interactions with the Cerberus laser system and several different target geometries. A prenumbral "knife-edge" imaging technique was developed to measure the x-ray source size of focused $\sim 10^{19}$ Wcm^{-2} laser pulses for thin (5 µm and 15 µm) Al foils, and investigated how the addition of a discrete prepulse affected the x-ray source sizes measured. Lastly, we conducted a source size measurement of a proton beam accelerated from 15 µm Al foil via the TNSA mechanism, comparing the measured source sizes across the profile of the proton beam to a similar measurement where a discrete prepulse was included in the laser temporal profile. This experiment was principally designed by George Rowland, more detail as to the motivation and developmental process of the source size diagnostics can be found in [18].

8.1 Cerberus Prepulser

An optical subsystem designed to generate a low-intensity prepulse of arbitrary contrast and relative temporal position to the main laser beam was designed by Samuel Eardley and integrated into the Cerberus laser system between the OPCPA front end and the glass amplification beamline (chapter 4). The optical layout of the "Prepulser" is shown in figure 8.1. This subsystem is able to add an arbitrary prepulse between 0 and 10 ns before the main pulse with a ratio of the main pulse to prepulse energy in an approximate range from $1{:}10^{-5}$ to 1:1.

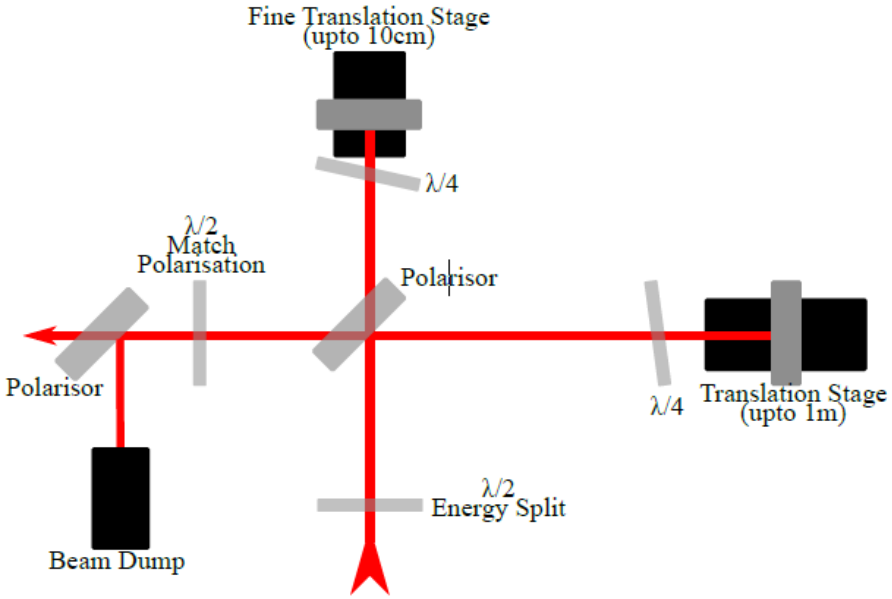


Figure 8.1: Schematic view of Cerberus Prepulser, which adds an arbitrary discrete prepulse with a relative intensity from $1{:}10^{-5}$ to 1:1, to the main pulse of the Cerberus laser system at a relative temporal position of up to 10 ns. Image credit: Samuel Eardley [15].

The Prepulser was based on a Michelson interferometer-like design, where a half-waveplate is used to determine the energy split through a polarising beamsplitter (extinction ration $\sim 10^4$:1 at 45° incidence) into two arms of the subsystem. The waveplate-polariser combination here enabled a reasonably high degree of control over the ratio of energy split between the main, reflected, pulse and the transmitted prepulse energies. The main beam is reflected from the polariser and propagates through a quarter-waveplate before it is retroreflected using a HR 0° mirror mounted on a course translation stage with up to 1 meter range of motion. The prepulse meanwhile, is transmitted through the polariser and propagated through a similar quarter-waveplate, retro-mirror combination with the retro mirror mounted onto a fine translation stage with up to 100

mm range of motion. The two stages in conjunction, offer a relative delay between the prepulse and the main pulse between 0 and -10 ns, with course adjustment on the main pulse delay stage and fine (±5 µm error) tuning with the prepulse stage. Double-passing both quarter-waveplates orthogonally rotates the polarisation of both beams such that they are transmitted and reflected by the polarising beamsplitter in the opposite orientation than previously. Therefore the prepulse and main beam are recombined to propagate collinearly, though at orthogonal polarisations to each other. Therefore finally, a half-waveplate, polariser combination is used to reestablish the same polarisation between the main and prepulse beams. This half-waveplate is set such that only ∼5% of the prepulse energy is transmitted through the polariser and ∼95% of the main pulse energy is transmitted. Each of the the waveplates in the beamline was also tilted to minimise back propagation from internal reflections, which would produce additional unwanted prepulses. At this stage in the laser system, the stretched pulse duration is approximately 740 ps, therefore the main beam and prepulse at this stage are temporally overlapped.

The relative delay between the main pulse and prepulse was calibrated using a fast photodiode and high temporal resolution oscilloscope (Tektronix DPO3054). The relative temporal position was found by measuring the position of the main pulse and then blocking the main pulse arm of the subsystem to completely eliminate its signal before recording the position of the prepulse. The additional path length due to ND filters placed in front of the photodiode to attenuate the main pulse were also accounted for.

We were aware that inhomogeneities in the polarisation state across the beamfront can cause aberrations in the spatial profile of a beam propagating through a waveplate-polariser combination when the waveplate is set towards the limits of rotating that light. We therefore carefully checked the beamfront of the prepulse by comparing the focal spot which it produced to the focal spot of the main beam using the focal spot camera at the centre of the target chamber (described in section 7.2).

8.2 Effect of a Discrete Prepulse on Particle and X-ray Emission Spectra

In this section, we describe an investigation into the effects of introducing a discrete prepulse with arbitrary relative intensity and temporal position with respect to the main pulse of the

Cerberus Laser System at Imperial College on the measured energy spectra of protons, electrons and x-rays accelerated via the TNSA mechanism. Measurements were taken from several purpose-built diagnostics, including a proton spectrometer, electron spectrometer and image plate stack. Additionally, this was supported by data from a single hit x-ray camera (ANDOR - DX434-BN) and optical interferometry beamline, described in more detail in section 7.2.1. A diagram of the target chamber, with the relative position of the diagnostics involved in this experiment, is shown in figure 8.2.

A proton spectrometer designed by S. Eardley [15] to measure a proton energy spectrum from 100 keV to <20 MeV, this was placed 300 mm away from the target chamber centre (TCC) along the axis normal to the target looking at ions accelerated via TNSA. Particle beams entered the diagnostic through a 200 µm entrance pinhole, with further background noise reduction ensured by shielding the instrument using 3 mm thick lead sheets. The basis of this diagnostic was a magnetic spectrometer based on a Thompson parabola (with E field set to zero for this work), with two 250 mT magnets (100x100 mm) held in a yoke to create a static magnetic field that deflected ions a given amount depending upon their velocity and charge to mass ratio. Charged particles in the magnetic field are subject to the Lorentz force, this force induces a circular path, the Larmor orbit, with a radius

$$r_L = \frac{p_\perp}{|q|\,B}, \tag{8.1}$$

where $p_\perp$ is the relativistic momentum for a particle with charge q in a magnetic field of magnitude B. From this radius, we can calculate the momentum and therefore energy of a particle with known charge displaced by a given amount in the direction normal to the beam axis. The dispersion curves were calculated for the spatial distribution of the magnetic field of the two magnets, which was measured using a Hall probe. Two BAS-TR image plates [135] were placed 17.5 mm behind the magnets, vertically above each other so that the higher image plate measured lower energy protons. In many cases, an external electric field is also applied to differentiate between ions, however here 14 µm Al foil was used on the higher image plate to attenuate protons with energy up to 1 MeV and ions such as carbon ions up to 16.5 MeV, oxygen ions up to 23 MeV and Al ions up to 40 MeV. A separate magnetic spectrometer, the electron spectrometer, was also placed 150 mm from TCC along the laser axis so that it would detect electrons directly accelerated by the laser field. This diagnostic consisted of a 5×0.5 mm entrance slit (normal to

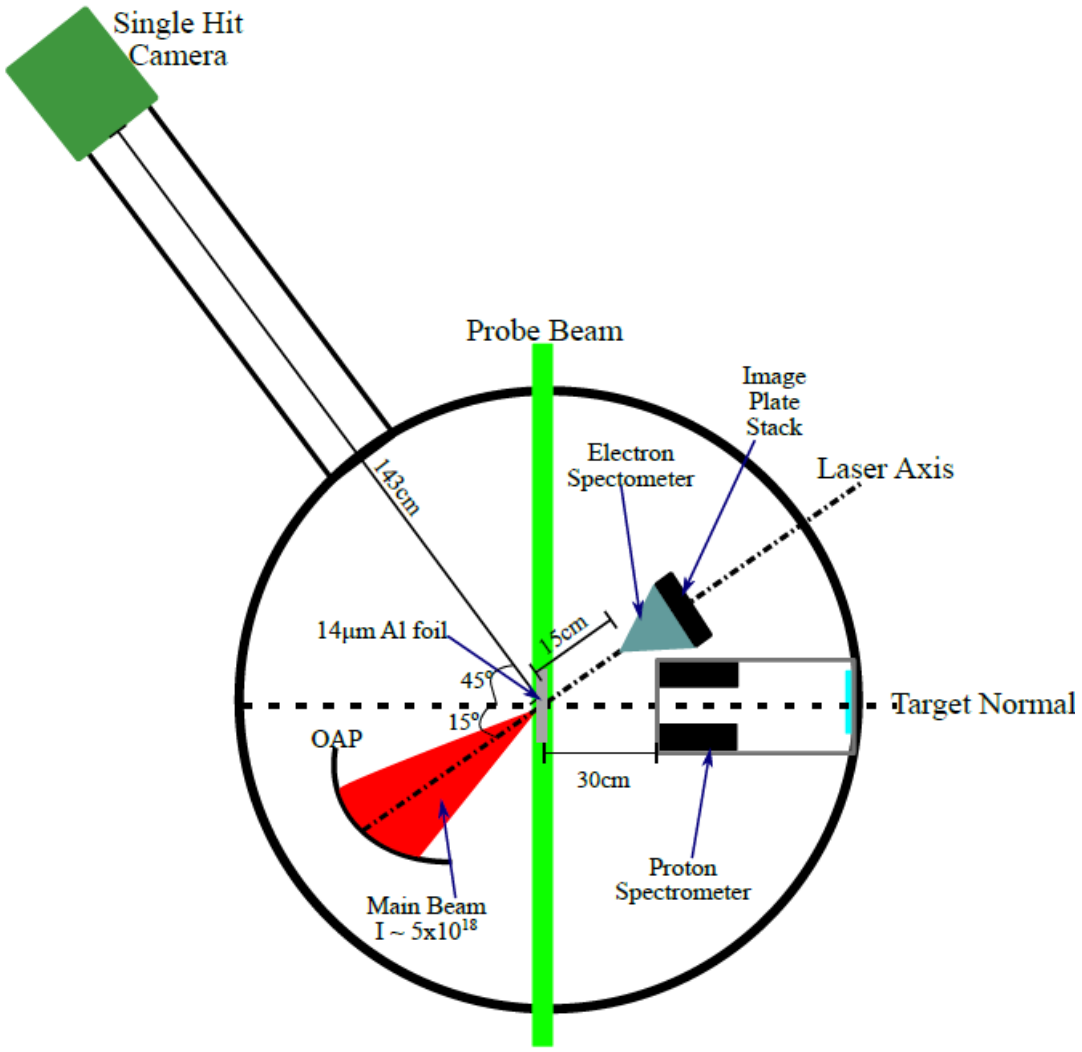


Figure 8.2: Diagram of the multi-terawatt lab target chamber setup for characterising the emission spectra of charged particles and x-rays for interactions between a $\sim 10^{18}$ Wcm^{-2} intensity focused laser pulse with an artificial $\sim 10^{-5}$ relative contrast prepulse included in the temporal intensity profile, incident at an angle of 15°, with 14 µm Al foils. Two magnetic spectrometers were included, one in the axis normal to the target rear surface to measure protons accelerated by the TNSA mechanism and one along the laser axis to measure the spectrum of electrons directly accelerated by the laser beam, with a multi-layer image plate stack to characterise the x-ray spectrum in the laser axis. Additionally, a single-hit x-ray photon counter (Andor DX434-BN) was aligned with line of sight to the target. An optical probe beam provided plasma interferometry measurements normal to the front surface of the target. Image credit: Samuel Eardley [15].

the dispersion direction) ahead of a strong, 0.1 T, magnet pair. A slit was chosen here over a pinhole, which is more typical of these diagnostics, as a compromise between high signal-to-noise ratio and small uncertainty in the energy measurement. The diagnostic was shielded against hard x-rays by two-layer conical shielding, using 2 mm thick Al cone wrapped in 3 mm thick

lead sheets. As with the proton spectrometer, the magnetic field inside of the spectrometer was spatially mapped with a Hall probe to inform the energy dispersion calculation.

Additionally, a stack of 10 image plates was placed behind the electron spectrometer to measure the energies of x-rays, which would not be deflected by the magnetic field. Each image plate was placed behind successive levels of aluminium, copper, iron and tantalum of varying thickness, filtering progressively more energetic x-rays, and sandwiched between two 300 µm kapton foils to attenuate secondary electrons. 3 mm thick lead shielding was placed on the front and back of the image plate stack, with 5 mm thick lead on the sides. The front shielding also had an additional hole, besides the entrance slit, not in the beam axis to measure the background x-ray flux. This diagnostic was used in conjunction with a single photon counting x-ray sensitive CCD (Andor DX434-BN), located 1.43 meters from TCC. This x-ray camera was used to measure the thermal electron temperature produced in the course of the experiment to cross check against the x-ray image plate results. Thermal x-ray emission was expected to be near-isotropic, provided the camera was aligned with line of sight of the target.

A laser interferometry beamline (described in section 7.2.2) was also available to measure the electron density up to >50 µm from the front surface of the target at a specific point in time relative to the main pulse, with a <ps temporal resolution. However, as described later in this section, these measurements were obscured by diffraction patterns produced between the optical probe beam and the sides of the foil target as well as bright plasma self-emission close to the interaction region.

A focused intensity of $5\pm1 \times 10^{18}$ Wcm^{-2} (2 J, 750 fs) was propagated to target, focused with an F/3 off-axis parabola (OAP) to a focal spot ∼5 µm FWHM diameter (1.7× diffraction limit), incident onto a 14 µm thick Al foil at an angle of 15° to avoid direct back reflection into the laser chain. The focused intensity for each shot was calculated using the measured focused beam diameter, the pulse energy, which varied on-shot from 1.8 J - 2.3 J, and the pulse duration, which measured using a second-order autocorrelator (section 7.2.1) between a range of 650 - 800 fs FWHM, with an average FWHM pulse duration of 750±60 fs. These parameters are predominantly affected by differences in the phase matching of the Cerberus front end OPA stages. The experiment was repeated with an artificial prepulse added to the temporal intensity profile of the main pulse at a range of times; -20 ps, -50 ps, -60 ps, -70 ps, -90 ps and -2 ns relative

to the main pulse. The amplified final energy of the prepulse could not be measured directly, due to background noise produced by the final high gain flashlamp amplifiers dominating the signal on a photodiode or energy meter. Instead, the prepulse energy was calculated based upon the response of the focal spot camera, using calibrated neutral density (ND) filters to attenuate the main pulse to a level where the intensity on the camera was approximately equal to the prepulse when the main beam was blocked. The prepulse intensity was initially measured at a relative contrast of $\sim 10^{-5}$, corresponding to a focused intensity $\sim 6 \pm 1 \times 10^{13}$ Wcm^{-2}, however this measurement technique did introduce some error as described later in this chapter. Following a discussion of the results at the end of this experiment, the XTOAD diagnostic (section 3.3) was fully commissioned and used by the author to recharacterise the prepulse intensity, this time measuring a relative contrast of 2.75×10^{-4}.

8.2.1 Results and Discussion

The results of the proton energy spectra with an artificial prepulse included at various times before the main pulse is shown in figure 8.3. The energy spectrum in presented in units of photo stimulated luminescence (PSL), corresponding to counts on the image plate, per the energy of protons which would produce signal at each point on the image plate, calculated from Larmor radius (equation 8.1), per the solid angle subtended by the 200 µm pin hole at the entrance to the spectrometer to give a value of spectral intensity in units of MeV^{-1}mStr^{-1} to MeV. More information describing the detailed analysis process is provided in [15]. A low energy cutoff was chosen at 1 MeV due to a large increase in flux observed at <1 Mev on the image plate, this may be due to unfiltered ions as 'low E image plate' was not wrapped in an Al filter. Additionally, the energy spectrum for prepulses -90 ps and -2 ns before the main pulse are not included in figure 8.3 as there, the spectrum was very highly attenuated. These results show a clear enhancement of the proton energy spectrum due to the addition of a prepulse. For shots which included a prepulse, we measured not only an increase in the maximum proton energy but also a greater proton flux onto the detector, with the greatest enhancement found for a prepulse up to 60 ps before the main pulse. Correspondingly, we also determined that the proton spectrum became 'flatter' as the prepulse approached 60 ps, taking on a non-Maxwellian distribution, with a lower flux at low energies than for a shot without prepulse, which is not characteristic for proton beams accelerated purely via TNSA. Subsequent repeat measurements of the proton energy spectrum at this delay also showed

a similar enhancement and spectral profile, indicating this was a reproducible observation and not a result of shot-to-shot variation. As the prepulse was moved further in time before the main pulse, the enhancement of the proton spectrum diminished, and for a prepulse greater than 90 ps before the main pulse the proton, and especially the electron, spectrum was highly attenuated. Figure 8.4 shows a clear peak in the maximum proton energy recorded for a prepulse around 60 ps ahead of the main pulse, ∼5.1 × greater than shots with no prepulse included.

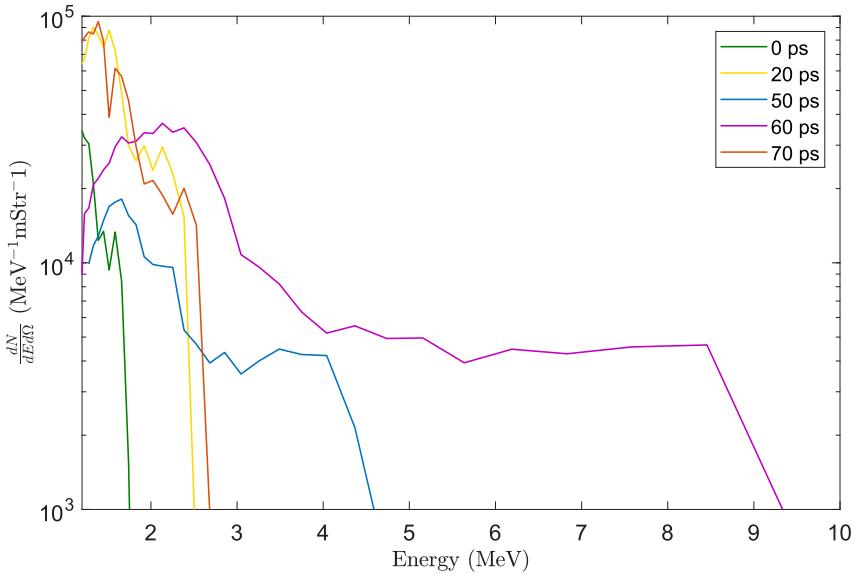


Figure 8.3: Proton energy spectra obtained by adding an artificial prepulse, with relative intensity contrast of 2.75×10^{-4}, at a relative time prior to the main Cerberus laser pulse, of focused intensity of $5\pm1\ \times10^{18}$ Wcm^{-2} (2 J, 750 fs), in interactions with 14 µm Al foils. A clear increase in the maximum particle energy can be seen for prepulse delays around 60 ps. A low energy cutoff is imposed for proton energies <1 MeV.

Electron spectrometer data, presented in figure 8.5 in units of Mev^{-1}mStr^{-1} per MeV, shows similar behaviour to the proton spectra with an enhancement in the spectrum due to a prepulse, rising with the prepulse position up to 60 ps before the main pulse before falling at further delays and becoming highly attenuated in the case of a prepulse 90 ps or more ahead of the main pulse. This is unsurprising as protons and electrons are closely associated in the TNSA model, however it is also worth noting that the electron spectrum does not change greatly in shape as was the case for protons. As such, from these results we are able to calculate the hot electron temperature, T_{eHOT}, of the population of electrons; comprising electrons directly accelerated by the laser field. Figure 8.6 shows the maximum energy and hot electron temperature measured from the electron spectra for several measurements obtained for a prepulse a given time ahead of the main laser

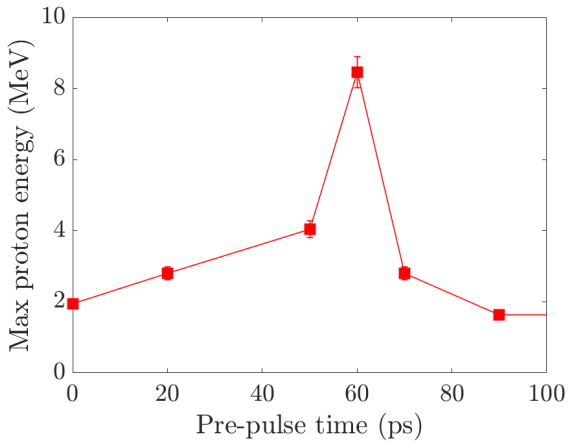


Figure 8.4: The maximum recorded proton energies obtained by adding an artificial prepulse, with relative intensity contrast of 2.75×10^{-4}, at a relative time prior to the main Cerberus laser pulse, of focused intensity of $5\pm1\ \times10^{18}$ Wcm^{-2} (2 J, 750 fs), in interactions with 14 µm Al foils. The maximum particle energy is observed to peak for prepulse with up to 60 ps relative to the main pulse.

pulse. The maximum electron energy was observed to peak as the for a prepulse around 60 ps before the main pulse, whilst T_{eHOT} was seen to peak for a prepulse 50 ps before the main pulse, with a maximum enhancement in the hot electron temperature from 160 keV, no prepulse, to 560 keV, 60 ps prepulse. It is also worth mentioning that in the measurements, the electron spectrometer noise floor was particularly high, therefore the diagnostic may not have been able to record the highest electron energies emitted by the plasma.

The energy spectrum of x-rays produced in this investigation was acquired from an image plate stack place behind the electron spectrometer. Laser-plasma interactions produce x-rays predominantly through Bremsstrahlung radiation, at energies from >100 eV to so-called "hard x-rays" >10 keV, through interactions between free electrons and ions in the plasma. The presence of two main electron distributions, hot electrons accelerated directly by the laser pulse and thermal electrons due to ionisation and reflux within the target, produces a two-temperature x-ray spectrum, which is best analysed using a two-temperature fit,

$$S(E) = A\ \exp\left(-\frac{E}{T_1}\right) \times B\ \exp\left(-\frac{E}{T_2}\right). \tag{8.2}$$

Where A and T_1 describe the population of low energy, thermal x-rays and B and T_2 describe the population of hard x-rays produced by interactions between the plasma and hot electrons. The coefficients A, T_1, B and T_2 were fitted to the image plate data using a genetic algorithm (GA)

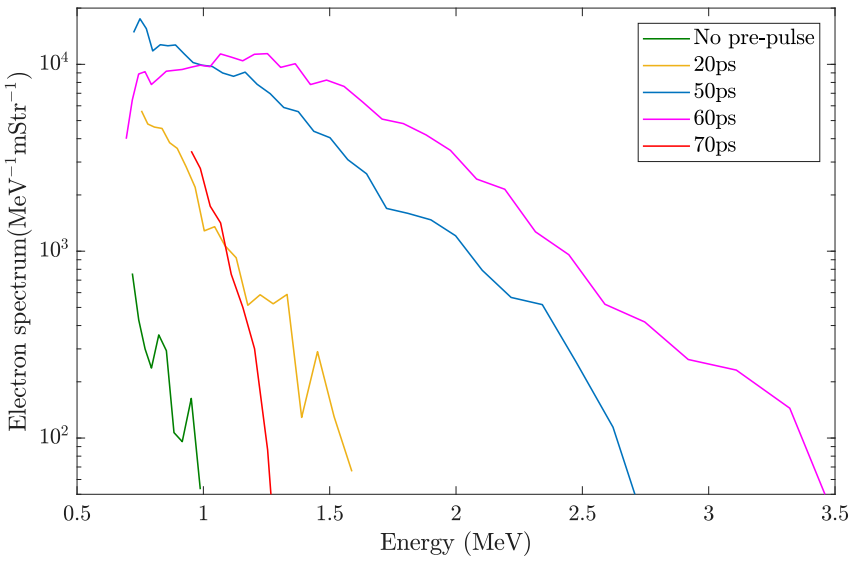


Figure 8.5: Electron energy spectra obtained by adding an artificial prepulse, with relative intensity contrast of 2.75×10^{-4}, at a relative time prior to the main Cerberus laser pulse, of focused intensity of $5\pm1\ \times10^{18}$ Wcm^{-2} (2 J, 750 fs), in interactions with 14 µm Al foils. A clear enhancement of the electron spectrum can be seen for prepulse delays around 60 ps.

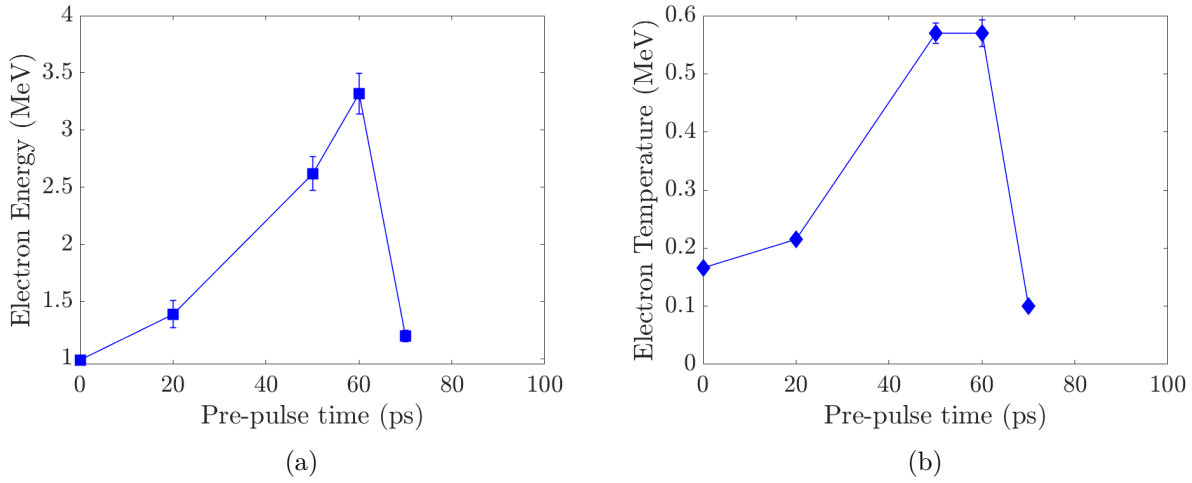


Figure 8.6: The a) maximum energy and b) hot electron temperature of electron spectra obtained by adding an artificial prepulse, with relative intensity contrast of 2.75×10^{-4}, at a relative time prior to the main Cerberus laser pulse, of focused intensity of $5\pm1\ \times10^{18}$ Wcm^{-2} (2 J, 750 fs), in interactions with 14 µm Al foils. The maximum electron energy was observed for a prepulse 60 ps before the main pulse, whilst T_{eHOT} was seen to peak for a prepulse 50 ps before the main pulse.

by Samuel Eardley described in [15], table 8.1 shows the two-temperature fitting parameters. The error represented here was calculated by the standard deviation the results produced by three final iterations of the GA. In the case of the spectrum produced with no prepulse present, the

GA arrived at the same result each time. The values for the low-temperature x-rays obtained from the image plate stack are in good agreement with the single-hit Andor results, to within an average 16.9% difference. In the case of the x-ray spectrum for the 50 ps prepulse shot, the difference between the final value for T_1 obtained was quite substantial and varied from the single-hit Andor measurement by 40%. If this datapoint is considered anomalous, the agreement between the image plate and single-hit Andor camera is within ∼10%.

Prepulse	A ($keV^{-1}mStr^{-1}$)	T_1 (keV)	B ($keV^{-1}mStr^{-1}$)	T_2 (keV)
0 ps	$(2.6 \pm 0.8) \times 10^8$	1.8 ± 0.1	$(1.1 \pm 0.1) \times 10^4$	17.7 ± 0.0
20 ps	$(2.7 \pm 0.9) \times 10^8$	1.9 ± 0.2	$(2.24 \pm 0.03) \times 10^4$	18.9 ± 1.3
50 ps	$(1.8 \pm 0.1) \times 10^8$	2.8 ± 1.4	$(4.7 \pm 0.7) \times 10^3$	17.2 ± 0.8
60 ps	$(2.9 \pm 1.3) \times 10^8$	2.1 ± 0.2	$(9.3 \pm 1.2) \times 10^3$	20.9 ± 0.5
70 ps	$(3.8 \pm 1.5) \times 10^8$	1.8 ± 0.1	$(3.5 \pm 0.1) \times 10^4$	15.7 ± 0.5

Table 8.1: Two-temperature fitting parameters, described in equation 8.2, for the measured x-ray spectrum spectra obtained by adding an artificial prepulse, with relative intensity contrast of 2.75×10^{-4}, at a relative time prior to the main Cerberus laser pulse, of focused intensity of $5 \pm 1 \times 10^{18}$ Wcm^{-2} (2 J, 750 fs), in interactions with 14 µm Al foils.

For the proton and electron data, spectral enhancement was observed to peak for a prepulse added around 50-60 ps ahead of the main pulse, however here the measurement of the hard x-ray temperature in the case of a 50 ps and 60 ps prepulse is lower than the other data. This measurement is somewhat misleading, however, as integrating beneath the x-ray spectrum to calculate the total hard x-ray energy still gives a maximum result in the case of a 60 ps prepulse, shown in figure 8.7.

We have thus far demonstrated an enhancement of the energy spectra of protons, electrons and x-rays by the inclusion of a prepulse ahead of the main pulse, with a previously measured relative contrast 10^{-5}. The maximum proton energy, as well as the energy and temperature of electrons and x-rays, was seen to peak for a prepulse 60 ps before the main pulse, before becoming increasingly suppressed as the prepulse was moved a progressively earlier time relative to the main pulse. We may be able to explain the enhancement in the observed energy spectra due to the laser self-focusing inside of the preplasma before the target. Preplasma is produced by ionisation of the front face of the target by elements of a laser pulse which arrive prior to the main pulse, these include discrete prepulses, ASE and OPA fluorescence background noise and the rising edge of the pulse. The preplasma expands from the front face of the target at

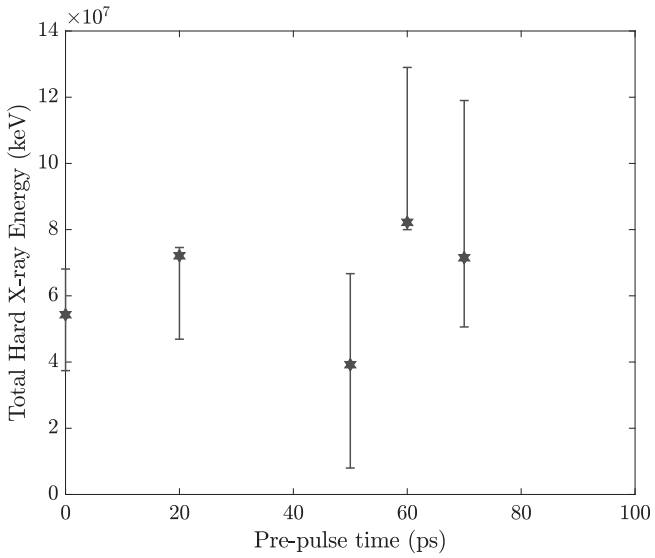


Figure 8.7: The total energy in the hard (>10 keV) x-ray spectrum obtained by adding an artificial prepulse, with relative intensity contrast of 2.75×10^{-4}, at specific time ahead of the Ceberus main laser pulse ($5\pm1\ \times10^{18}$ Wcm^{-2}), calculated by integrating the image stack x-ray PSL with respect to photon energy.

approximately the ion sound speed (equation 6.10). Hot electrons are accelerated directly by the electric field of the laser via the pondermotive force. From equation 6.8 we therefore assume, $T_{hot} \sim (I\lambda^2)^n$, where n is an empirical factor which is generally 1/3 to 1/2. To account for the observed increase in the hot electron temperature from 160 keV (no prepulse) to 560 keV (60 ps prepulse), the intensity increase due to self-focusing must be approximately a factor of 10. For a laser with our parameters, ∼2J pulse energy, ∼750 ps duration, this would indicate a focused beam diameter of approximately 1.6 µm. The self-focusing condition for a laser propagating through plasma is given by the relativistic critical power,

$$P(GW) \geq 17\frac{n_{crit}}{n_e} \tag{8.3}$$

where n_{crit} is the critical density at which point the central frequency of the laser is equal to the plasma frequency and n_e is the electron density of the plasma. If self-focusing is responsible for our observed increase in charged particle flux, for a 2 J, 750 fs laser pulse, where the critical density for light centered at 1053 nm is 7.9×10^{20} cm^{-3}, we require a minimum electron density in the preplasma of $n_{SF} \simeq 6 \times 10^{18}$ cm^{-3}.

Preplasma Electron Density Measurements

We can potentially directly measure the electron density in the preplasma using the Cerberus interferometry beamline, described in section 7.2.2. An optical probe beam, produced by frequency doubling the ∼60 mJ, 500±50 fs interferometery beamline pulse to $\lambda_0 = 527$ nm, is propagated through the target chamber, parallel to the front side of the foil. The optical probe, at the point of the interaction (TCC), is imaged by a series of lenses through a Nomarski interferometer [131] where a Wollaston prism is used to produce interference fringes by overlapping the image of the optical probe at TCC with a reference portion taken from elsewhere in the optical beam profile. The fringe shift of the interferogram measured using the interferometer can be used to calculate the electron plasma density in front of the target at a relative time to the main laser pulse determined by the path length of the optical probe beamline.

The artificial prepulse used in this investigation was initially measured at a 10^{-5} relative contrast to the main pulse. Initial simulations using Helios 4.4.0, a 1D radiation-magnetohydrodynamics code [17], with a prepulse of this intensity [15], predicted an expansion of the critical surface from 8.0 to 9.3 µm in front of the target surface due to the addition of the prepulse at -60 ps relative to the main pulse. The preplasma was predicted to expand up to ∼ 35 µm in front of the target before the main pulse arrived, with this expansion affected little by the addition of the prepulse. The on-shot interferometry data, however, is considered unsuitable for electron density measurements within ∼40 µm of the front surface of the target. The optical probe was obscured close to the surface of the target by self-emission in the second harmonic of the main pulse caused by the laser frequency at the critical surface coupling to the plasma frequency. Additionally, the interferometer was originally designed for imaging optically levitated microdroplets [125], and was therefore designed with a high magnification (∼ ×30) and small depth of field. As the foils used in this investigation were very wide (∼1 cm) compared to the depth of field, there was a significant amount of diffraction observed in the optical probe beam from across the front surface of the foil.

After further discussion of the results presented in [15], there was some ambiguity as to whether the previous prepulse intensity was significant enough to explain the large increase in emission spectra that we had measured from the target. The relative contrast between the prepulse and the main pulse was originally measured by comparing the brightness on the focal spot camera

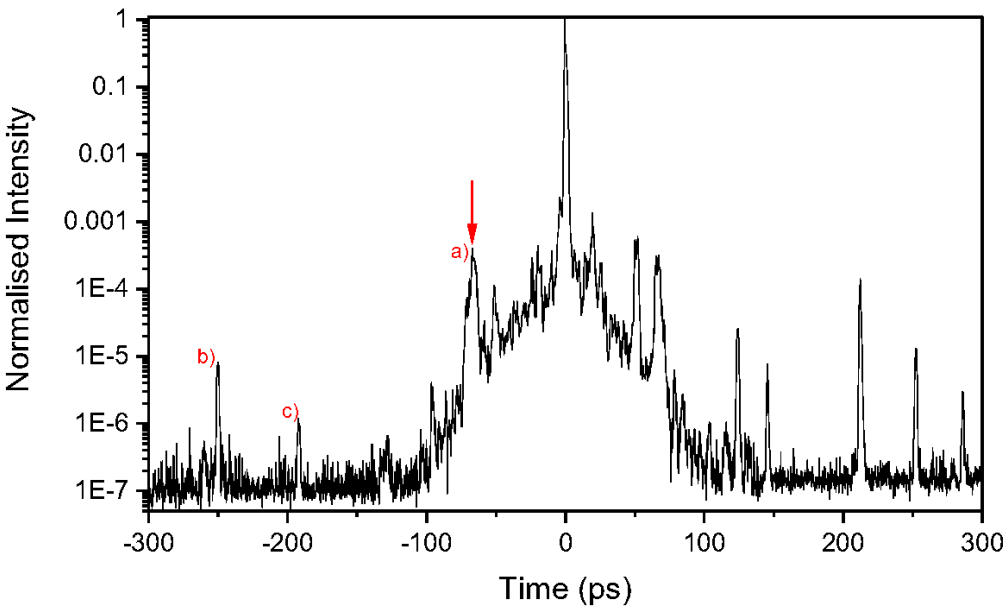


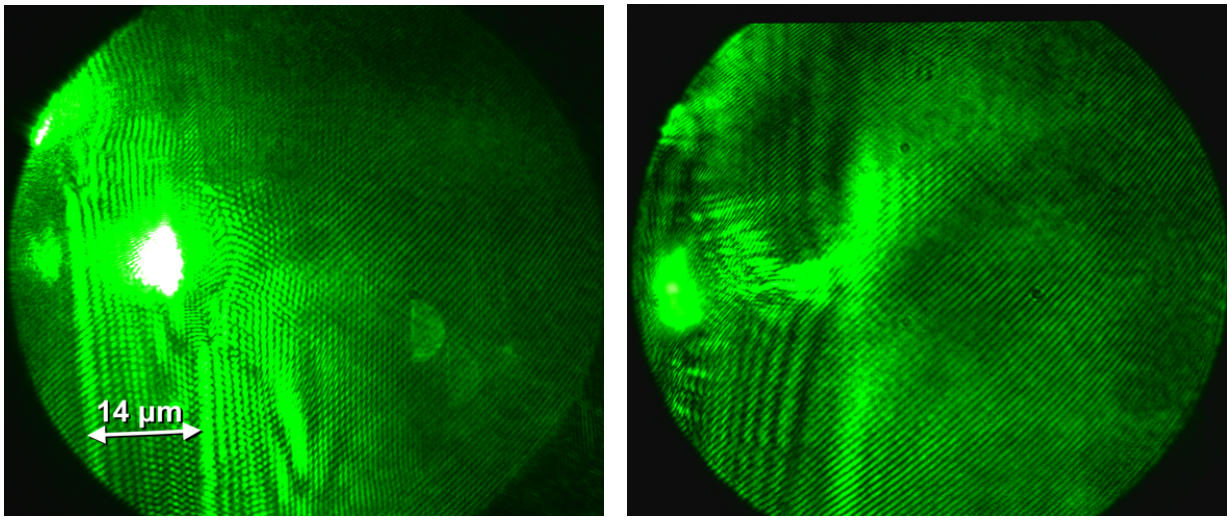
Figure 8.8: The temporal profile of Cerberus OPCPA front end, characterised with an effective dynamic range of $\sim 10^8$, using a third order autocorrelator, the XTOAD described in section 3.3, without XPW contrast enhancement engaged. Several important features can be seen on this plot including a) the discrete prepulse artificially introduced by the Cerberus Prepulser, at 65 ps before the main pulse with a relative contrast of 2.75×10^{-4} and a temporal FWHM of 3.7 ps. Two additional discrete prepulses are also observed by the scan, b) a 10^{-5} artefact produced in the diagnostic and c) a $\sim 10^{-6}$ relative contrast produced by internal reflections inside of the Cerberus prepulser. The broad 10^{-7} relative contrast pedestal is produced by fluorescence in the front end ns-OPA stages, at 10^{-7} the pedestal is an order of magnitude more intense than is typically measured for the system, this likely a factor of this contrast scan and not representative of typical system performance. Additionally, a 200 ps duration broad 'triangular' pedestal is visible up to a relative contrast of 10^{-4} due to uncompressible incoherent scattered light inside of the front end CPA stretcher.

for each beam, using calibrated neutral density (ND) filters to attenuate the main pulse. This measurement did not account for any intensity-dependence in the attenuation factors of the ND filters which were used. The relative contrast was measured from the OPCPA front end of the laser system, at 10 Hz operation, where the intensity of the main beam would have been approximately $\sim 10^{13}$ Wcm^{-2}. Ongoing development on the XTOAD diagnostic (described in section 3.3) at this time allowed a more accurate measurement of the temporal intensity profile of the laser pulse, with the prepulse included. The compressed interferometry beamline pulse, which is analogous to the main Cerberus pulse, was characterised using the XTOAD diagnostic, at this time without XPW contrast enhancement available, resulting in the scan shown in figure 8.8. From this plot, we can identify the artifical prepulse at a relative contrast of 2.75×10^{-4} and

with a temporal FWHM of 3.7 ps. On figure 8.8, the prepulse is seen ~ 65 ps before t_0, however as the beamline was realigned several times between the experiment and this measurement this is not indicative of its position in any of the previous shots.

Additional observations by the author, as well as preliminary analysis, also showed that electron density measurements could still be recovered from non-ideal interferograms by careful analysis using a phase retrieval code, Interpret, written by Jason Cole [16]. This code takes a background subtracted interferogram, and retrieves the both phase shift from the interferogram fringes and the electron density of the preplasma from the unwrapped phase. Figure 8.9 shows two interferograms produced by optically probing a 15 µm thick Al foil at -8 ps relative to the arrival of the Cerberus main pulse. Figure 8.9a is taken from a shot with a measured focused intensity of $4.9\pm1.2\times10^{18}$ Wcm^{-2}, without a prepulse added to the temporal profile and figure 8.9b shows the interferogram measured for a shot with a main pulse focused intensity, measured as $5.2\pm1.3\times10^{18}$ Wcm^{-2}, where an artificial prepulse, with an approximate intensity contrast of 2.75×10^{-4}, was included 60ps ahead of the Ceberus main laser pulse. On both of these images, bright self emission close to the interaction region obscures density measurements close to the face of the target, this is particularly bright on figure 8.9a. Additionally, diffraction from the front surface of the target can also be observed on both interferograms, the large diffraction observed in figure 8.9b may be caused by the target normal having been inadvertently rotated in the plane of the optical probe beam during alignment for this shot.

Whilst both self-emission and diffraction effects from the front surface of the target still prevented clear interferometry measurements close to the interaction region, we were still able to retrieve plasma electron density measurements from these interferograms using Interpret [16]. In the first stage of the analysis code, a fast Fourier transform (FFT) is taken of the background-subtracted interferometer image. The FFT of the Cerberus interferometer displays prominent 'side-lobes' diagonally to the left and right of the centre, due to the fringes produced by the Wollaston prism, set at a 45° angle of rotation. By carefully limiting the region of interest around these side-lobes, we are able to discriminate, to some extent, between the interferometer fringes and the diffraction from the front of the target. Additionally, a combination of noise and diffraction effects often produced errors in the phase shift retrieval algorithm which resulted in discontinuities along the retrieved electron density profile. As these error sources were present at specific points on the interferograms, we repeated the analysis process several times for several different areas



(a) Shot 78 (b) Shot 84

Figure 8.9: Interferograms showing the plasma expansion from the front of a 15 µm thick Al foil at -8ps relative to the Cerberus main pulse for two shots, a) $(4.9\pm1.2)\times10^{18}$ Wcm^{-2} focused intensity, with no additional prepulse and b) $(5.2\pm1.3)\times10^{18}$ Wcm^{-2} where an artificial prepulse, with relative intensity contrast of 2.75×10^{-4}, was included 60ps ahead of the Ceberus main laser pulse. Both a) and b) show bright self emission close to the interaction region which obscures density measurements close to the face of the target whilst b) shows significant diffraction from the optical probe beam across the front surface of the target.

of interest, to obtain a composite electron density profile of several different retrieval results which avoided the noise errors. For each of these, the phase retrieval was set around a reference cylindrical symmetry point on the interferogram for each different area of interest. Through this technique, the electron density profiles were found to be in good agreement with one another.

The plasma electron density measurements were supplemented in regions where the interometry data could not be retrieved using Helios 4.4.0 [17]. Helios simulated the preplasma expansion from a 15 µm Al foil target for two shots, with no additional prepulse and with a prepulse included 60ps ahead of the Ceberus main laser pulse. The temporal intensity profile of the laser used in each simulation was determined by the previous third order autocorrelation measurement (with and without a prepulse), multiplied by the measured focused intensity for each shot. Helios simulations were run in timesteps of $\sim$ 100 fs, from 300 ps before the arrival of the main laser pulse. At each timestep, Helios gave values of the ionisation fraction, density and temperature of electrons and ions in the plasma (with the condition $T_e \neq T_i$), fluid velocity, plasma pressure and other key plasma parameters.

Figure 8.10 shows the combined Helios and interferometry electron density measurements of a

preplasma expanding radially from the front of the target 8 ps before the arrival of the main pulse ($4.9\pm1.2\times10^{18}$ Wcm^{-2}) without a prepulse included in the beam profile. At this focused intensity, we predict the main pulse will reach the relativistic critical surface at an electron density of $1.78\pm0.15\times10^{21}$ cm^{-3}. Interpret produces an electron density profile relative to the area of interest selected for analysis on the interferometer image. To plot the electron density as a function of the radial distance, we have defined the front surface of the target from the centre of the self-emission spot. The one-dimensional electron density was taken as a lineout from Interpret 1.5 um radially from beam centre along the optical axis, to reduce the effect of errors in the density retrieval close to the centre of the beam due to symmetry effects. This gave good agreement between the interferometery results and the Helios simulation, as well as consistent agreement between each electron density profile retrieval. From Figure 8.10, at -8 ps relative to the main pulse, we can see the preplasma expansion up to ∼67.1 µm from the front of the target before the density gradient drops off. Helios simulations predict the relativistic critical surface has expanded up to 6.37 µm, while the threshold for self focusing, at $1.5\pm0.3\times10^{19}$ cm^{-3}, is seen to have expanded 64 µm from the front of the target, close to the edge of the expanding preplasma. Applying an exponential fitting function to the interferometry results, $n_e = A\exp(-Bx)$, gives fitting constants of $A = 1.54\pm0.1\times10^{20}$ cm^{-3} and $B = 3.57\pm1\times10^{4}$ m^{-1}.

This value of A corresponds to a solid density of $1.54\pm0.1\times10^{20}$ cm^{-3}, which falls short when compared to the solid Al electron density of 6.0×10^{22} cm^{-2}, however as seen in figure 8.10, the electron density gradient appears to increase closer to the surface of the target. This may be due to either heating of the preplasma by later-time increasingly intense components of the pulse profile, such as the 'triangular' pedestal feature (seen on figure 8.8 rising ∼100 ps ahead of the main pulse), or ramped shocks launched back into the preplasma by a ns-long prepulses such as the ASE background or OPA fluorescence. However, more detailed modelling, likely involving particle-in-cell (PIC) simulations, would be required to fully explain this.

Figure 8.11 shows the combined Helios and interferometry electron density of a preplasma expanding radially from the front of the target 8 ps before the arrival of the main pulse ($5.2\pm1.3\times10^{18}$ Wcm^{-2}) where a prepulse, with 2.75×10^{-4} relative intensity contrast, 3.7 ps FWHM duration, was introduced 60 ps before the main pulse. The one-dimension electron density was taken as a lineout from Interpret 1.5 um radially from beam centre along the optical axis. The inter-

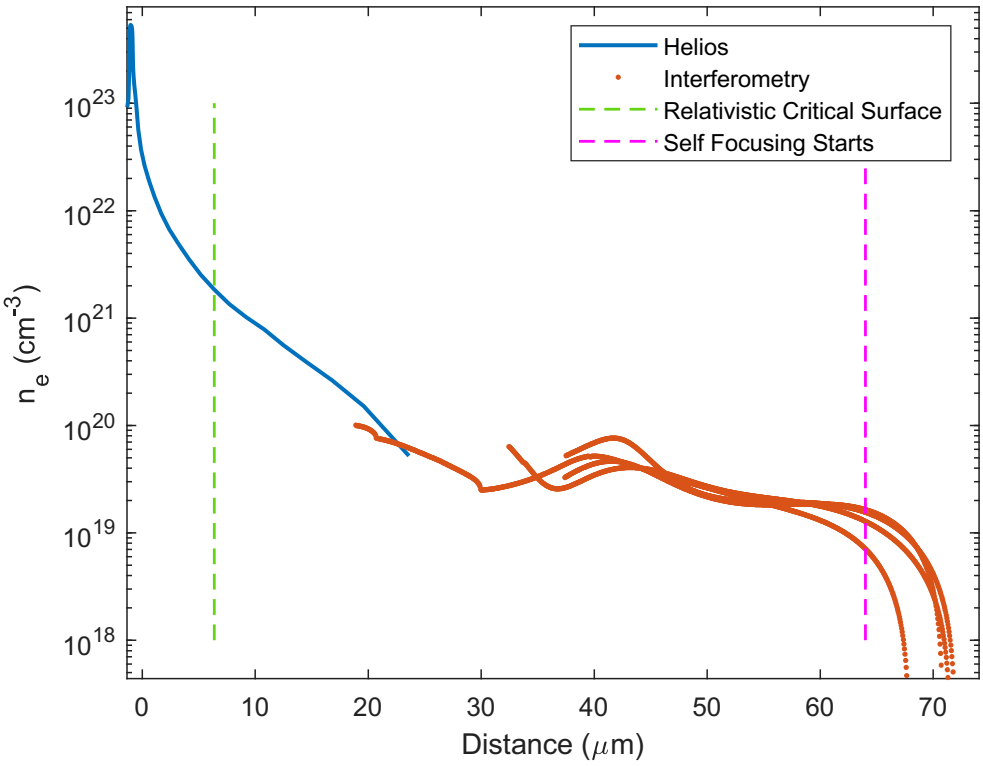


Figure 8.10: Electron density at the front of a a 15 µm Al foil, 8 ps before the arrival of the main pulse ($4.9\pm1.2\times10^{18}$ Wcm^{-2}). The electron density profile is comprised of a composite of 1D Helios hydrodynamic simulations (blue) and experimental interferometry results (orange). The threshold for laser self-focusing in the preplasma (pink) as well as the relativistic critical surface (green) are also indicated.

ferometry measurements extended up to >200 µm from surface of target, however at the time of analysis we were unsure as to whether this data was 'real' or produced by an error in the density retrieval algorithm. For a main pulse of focused intensity $5.2\pm1.3\times10^{18}$ Wcm^{-2} (2.28 ± 0.20 J, 800 ± 160 fs), we can calculate the relativistic critical surface to be at $1.81\pm0.15\times10^{21}$ cm^{-3} and the density for self focusing at $1.16\pm0.27\times10^{19}$ cm^{-3}. From figure 8.11, we therefore find the relativistic critical surface has expanded to 22 µm in front of the target at 8 ps prior to the main beam and the threshold for self focusing at 113 µm, or 221 µm if accounting for the extended electron density measurements. Fitting the interferometry results between 65 - 90 µm from the target surface, as shown in figure 8.11 provides values of $A = 3.14\pm0.01\times10^{21}$ cm^{-3} and $B = 5.0\pm0.1\times10^{4}$ m^{-1}.

Expansion of a plasma into vacuum is primarily determined by the ion sound speed, where the density gradient of an expanding plasma in one-dimension (without strong magnetic fields

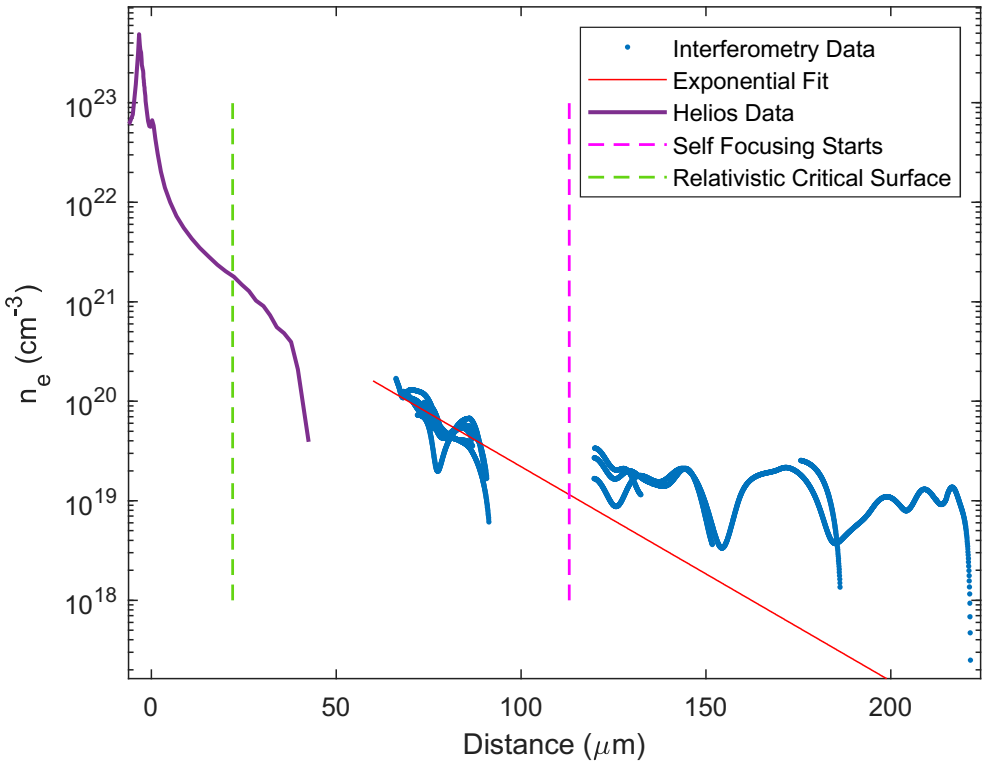


Figure 8.11: Composite electron density profile density at the front of a 15 µm Al foil, 8 ps before the arrival of the main pulse ($5.2\pm1.3 \times 10^{18}$ Wcm^{-2}) where a prepulse of 2.75×10^{-4} contrast was introduced at -60 ps relative to the main pulse. The electron density profile is comprised of combined 1D Helios hydrodynamic simulations (purple) and interferometry results (blue). The threshold for self-focusing, taken from the exponential fit of interferometry data between 65 - 90 µm from the target surface (pink), as well as the relativistic critical surface (neon green) are also indicated.

present) can be described by

$$n(x,t) = n_0 \exp(-x/c_s t) \tag{8.4}$$

where c_s is the ion sound speed and t is the expansion time. Using the fitting parameters from figures 8.10 and 8.11, we can find the ion sound speed, $1/B \cdot t$, which in turn gives an estimate for the electron temperature in the preplasma from

$$c_s = \left(\frac{\gamma_{Cp} Z k_B T_e}{m_i}\right)^{\frac{1}{2}} \tag{8.5}$$

where γ_{Cp} is the adiabatic index, approximately unity for plasma expansion over long length scales, Z is the atomic number of the ion species in the plasma, ion mass m_i, and k_B is the Boltzmann constant. The plasma expansion in figure 8.11 has a definite expansion start time, 52 ps, given from the arrival of the artificial prepulse. From this, we can calculate an ion sound

speed, $c_s = 388$ kms^{-1}. Making the, not unreasonable, assumption that the preplasma is mainly comprised of protons and electrons, we subsequently find an electron temperature of $T_e = 1.5$ keV, whilst Al ions would give a $T_e \simeq 14$ keV. This value compares well with the Helios simulation, which gives an electron temperature at this point of 1.6 keV. For the shot with no prepulse, the start of the expansion time is less obvious. Ionisation of thin metallic foils typically begins at focused intensities of 10^9-10^{12} Wcm^{-2} [12], which would suggest that the ∼ns-duration ASE pedestal could reach this threshold. However, the ASE pedestal for the Cerberus laser system (from the Nd:Glass flashlamp amplifer chain) has not been fully characterised and its exact temporal duration in not known, though expected to be of order <1 µs. Additionally, the plasma expansion due to the heating or ionisation by the triangular CPA pedestal, rising ∼100 ps before the main pulse, could overtake the plasma density at the front of the target. The Helios simulation results for the 2D electron density expansion over time is shown in figure 8.12, which indicates that the preplasma begins expanding from the front of the target approximately 150 ps before the arrival of the main pulse.

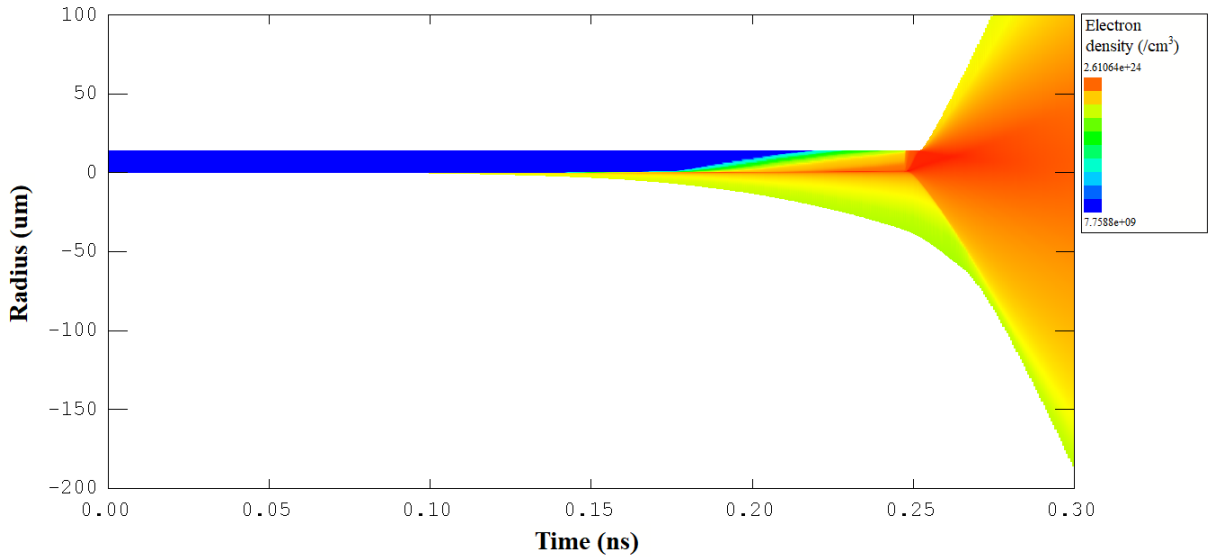


Figure 8.12: Helios model of electron density in a 14 µm thick Al foil, showing the radial expansion of preplasma produced by a 4.9±1.2×10^{18} Wcm^{-2} focused intensity laser pulse. The main pulse arrives on this figure at 0.25 ns.

Calculating the ion sound speed for the fitting parameters from figure 8.10, gives an ion sound speed of 187 kms^{-1}, with a corresponding electron temperature $T_e = 405$ eV. Cross-checking the interferometry results with our Helios simulation, however, we discover a large discrepancy

between the measured interferometry electron temperature and the Helios value of 0.31 eV, out by 3 orders of magnitude. Of these two values, we are more inclined to believe the interferometry measurements, firstly as they conform much better to our expectations and secondly as Helios simulations handle laser absorption in aluminium poorly at the low temperature limit. The opacity tables for aluminium are referenced from PROPACEOS [17], shown in figure 8.13, the absorption coefficients of Aluminium at the particular densities and temperatures involved in this interaction are not well documented and for light centered at 1054 nm (photon energy = 1.18 eV), the PROPACEOS opacity is very low for temperatures below ∼0.4 eV.

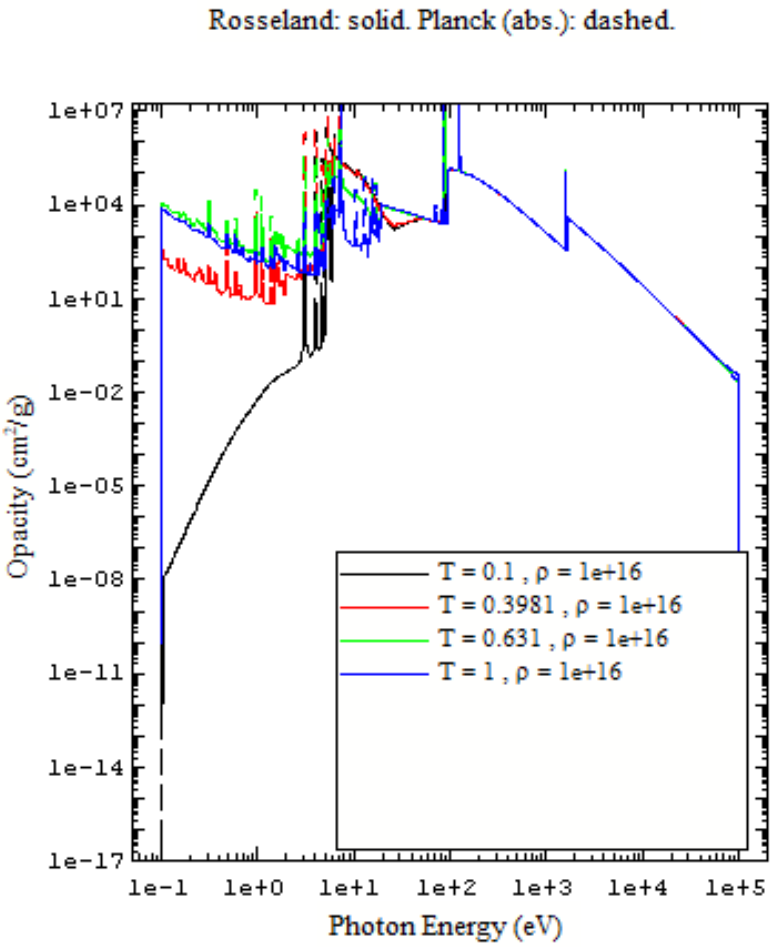


Figure 8.13: PROPACEOS Al opacities [17]

Additionally, whilst generally in good agreement with the interferometry data, the Helios simulations in figures 8.10 and 8.11 predicted the preplasma electron density to fall off much closer to the target surface than the interferometry results measured. As the preplasma could be measured by the interferometer at a much further distance, the tail end of the Helios electron density

profile is likely due to an error in the simulation. Helios is a Lagrangian plasma physics code, where the spatial grid moves with the fluid and the mass contained in 'zones' defined at the start of the simulation is kept constant. It is possible that sub-optimal zoning limited the mass able to expand during the simulation or that once again, Helios was not able to account for laser absorption in the underdense leading edge of the preplasma.

Whilst the ion sound speed determines the overall profile of the expanding preplasma, due to ioniation pressure from electrons, we can roughly find the rate of expansion for different points along the electron density gradient given its radial distance from the front of the target at our expansion time. 8.14 shows the preplasma velocities found for our interferometry measurements of both shots. We can use these velocities to calculate, assuming a rate of constant expansion, the position of the self-focusing threshold and the relativistic critical surface at t_0, when the main laser pulse arrives. For figure 8.14b, we can see that the preplasma expansion velocities for the interferometry measurements up to 221 µm from the target, which we were previously unsure of the accuracy of, nicely fit the linear trend of the other data, suggesting these are real measurements and not an error in the density retrieval algorithm. Comparing the linear trend to Helios, also gives reasonable agreement, Helios predictions for the plasma velocity at 221 µm from the target give a value of 4.83 kms^{-1}, similar to the interferometry measurement 4.26 kms^{-1}.

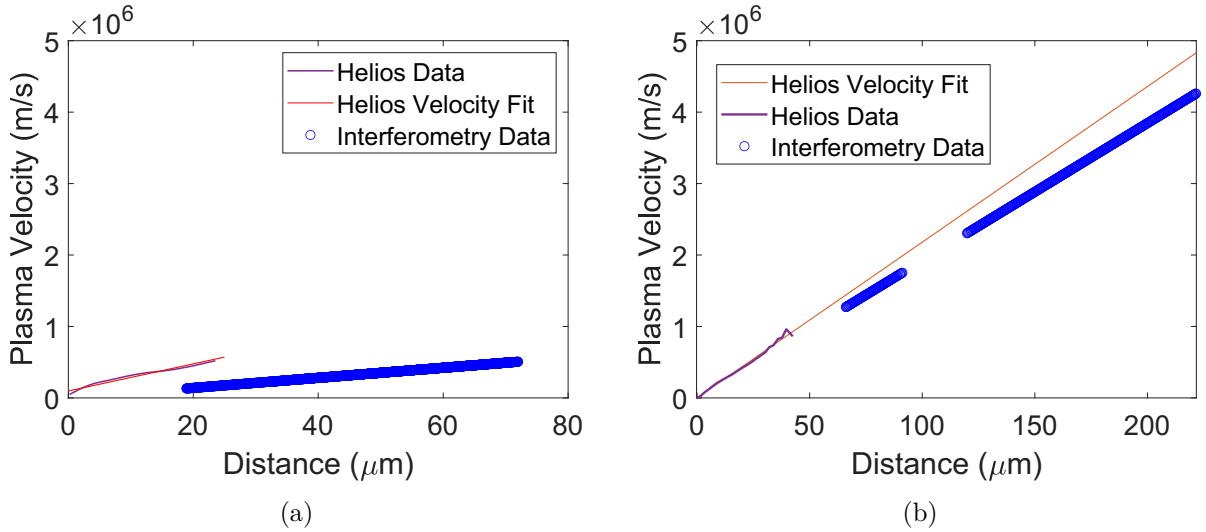


Figure 8.14: The radial velocity of preplsma expanding from the front of the target at -8 ps relative to the main pulse, calculated from the radial distance of the plasma from the target, given a specific expansion time, for two shots, a) (4.9±1.2)×10^{18} Wcm^{-2} focused intensity, with no additional prepulse and b) (5.2±1.3) × 10^{18} Wcm^{-2} where an artificial prepulse, with relative intensity contrast of 2.75×10^{-4}, was included 60ps ahead of the Ceberus main laser pulse.

With no prepulse, we predict the self-focusing threshold to have expanded to 68.5±0.5 µm from the front surface at the arrival of the main laser pulse. With the inclusion of a discrete prepulse, at a relative contrast of 2.75×10^{-4}, 60 ps ahead of the main pulse the expected threshold for self-focusing will have expanded up to 250±0.5 µm radially from the target surface, a factor ∼3.6 times further than where no prepulse was added - approximately the same factor that the beam diameter would have to be reduced by to account for the increase in our hot electron temperature measurements.

8.3 Source Size Measurement

X-ray and proton beams are effective tools for imaging matter. However, there are three main parameters of an x-ray or proton source which are important to characterise for experiments; the spectral brightness, pulse duration and source size. In this section, we discuss an experimental campaign to characterise the source size of x-rays and proton beams produced in laser-target interactions using the Cerberus laser system at Imperial College London. Additionally, we investigated the effect of adding a discrete artificial prepulse to the temporal profile of the laser on these source size measurements. In the target-normal sheath acceleration (TNSA) model, both proton and x-ray sources are associated with hot electrons directly accelerated by the laser. Investigating the effect of an added prepulse provides more insight into the dynamics of that interaction, and how it might be best optimised. Further details regarding the motivation for this experiment, the development of the diagnostic techniques involved and the data analysis methods can be found in [18].

8.3.1 X-Ray Source Size Measurements

An x-ray source size measurement technique was implemented in the Multi-Terawatt target chamber using a knife-edge configuration where a thick (∼few mm) high Z material was used to produce an abrupt obscuring edge which obstructed a portion of the x-ray light emitted at the source. A knife-edge ideally produces a sharp shadow if obscuring light emitted from a point source, however for an extended source with finite size, there will be a penumbral transition region caused by some rays produced at different points across the source, travelling along paths not blocked by the knife-edge. The size of the penumbral region, R_p, is determined by the source size, S, and the position of an ideal (perfectly opaque) knife-edge relative to the source and the detector. Shown in figure 8.15, we find that

$$R_p = \frac{q}{p} S' \tag{8.6}$$

where S' is the footprint of the source at a viewing angle θ, p is the distance from the source to the knife-edge and q is the distance from the knife-edge to the detector, it follows q/p is the magnification.

In order to produce a defined prenumbral region, it is important to select an obscuring object

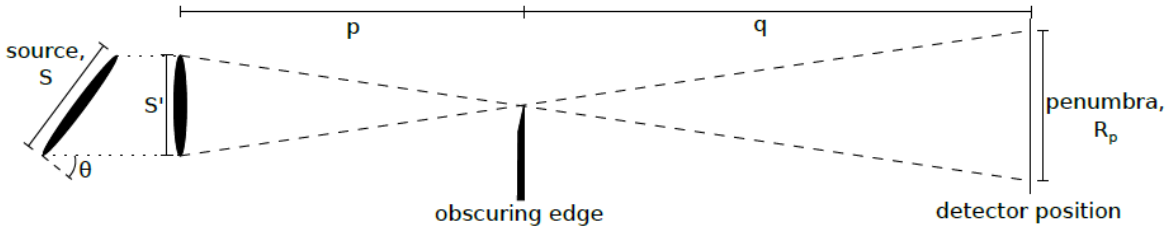


Figure 8.15: Knife-edge source size measurement technique. The size of the penumbral region, R_p, is determined by the source size, S, where S' is the footprint of the source at a viewing angle θ, p is the distance from the source to the knife-edge and q is the distance from the knife-edge to the detector.

with a sharp edge that is able to highly attenuate x-rays. A novel technique for penumbral imaging was developed using tungsten carbide ball bearings (WCBBs), 5 mm diameter, 0.025 µm surface roughness. WCBBs are spherically symmetrical, with an effective cross-sectional area which increases rapidly from the 'edge' along the radius of the sphere. This means that the effective "knife-edge" (here curved rather than straight) could be aligned with a high degree of confidence to the axis from TCC to the detector, without any tilt of the bearing relative to this axis affecting the results. A photograph of the penumbral imaging setup in the Multi-Terawatt target chamber is shown in figure 8.16. The diagnostic was aligned 326 mm from TCC, on an axis 45±1° vertically and 55±3° horizontally in the plane [normal] to the front of the target, detecting x-rays produced by laser-plasma interactions. Image plate (Fuji BAS-MS [135]) was used to measure the PSL of the x-rays across the penumbral region, the image plate was wrapped in 15 µm Al foil to block low energy charged particle flux. Two WCBBs were aligned orthogonally to one another for 2D imaging of the source size. The first was aligned 14 mm from TCC to measure the vertical axis from the target, giving a magnification of M = 23.3 and the second was aligned 6 mm from TCC in the horizontal axis of the target, giving a magnification of M = 55.7. Finally, two pairs of strong (∼45 mT) Neodymium (Nd) plate magnets were mounted in the chamber along the line of sight between TCC and the detector in order to deflect charged particles produced during the interaction away from the image plate.

Figure 8.17 shows the scanned image plate results of a source size measurement for x-rays produced in the interaction of the Cerberus main pulse, focused to a ∼10 µm focal spot diameter with a total focused intensity of $\sim 10^{19}$ Wcm^{-2} onto 15 µm thick Al foil. The vertical and horizontal penumbral edges produced by the two orthogonal WCBBs are shown, with a lineout

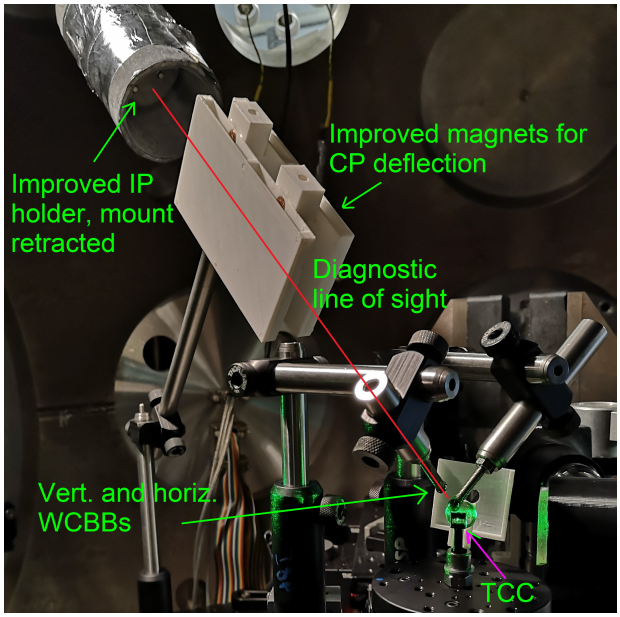


Figure 8.16: X-ray source size diagnostic layout, two tungsten carbide ball bearings (WCBBs) were used to create a sharp knife-edge for prenumbral measurements. X-rays produced at TCC were detected using Fuji BAS-MS image plate, with signal to noise improvement provided by two (∼45 mT) Neodymium (Nd) plate magnets to deflect charged particles.

taken of the vertical transition region which allows direct measurement of the source size.

A focused intensity of 5±1 $\times 10^{18}$ Wcm^{-2} (2 J, 750 fs) was achieved on target. The focal spot diameter was measured prior to each shot with an average diameter of 9.95±1.65 µm in the vertical axis of the target and 8.95±1.50 µm in the horizontal axis of the target. In each shot, the focal spot could be optimised by translating the OAP once the target chamber was under vacuum and directly capturing the farfield spatial profile using a high magnification focal spot camera. We investigated the source sizes of x-rays produced from 5 µm and 15 µm Al foils. These foils are geometrically identical in x, y for the laser and therefore we expected only a difference in the source size due to the incident angle of the beam onto the foil. Using an F/3 OAP, we focus the beam to target at a vertical angle of 15°, which would cause the vertical source size to be $\sim 3.5\%\times$ larger than the horizontal. After characterising the source size for these foils, we investigated the effect of adding an artificial prepulse 50 ps ahead of the main pulse with a relative contrast measured at 2.75×10^{-4}. A prepulse at this position was chosen as, in the previous section, we observed a peak in the hot electron energy spectrum and in the x-ray temperature for a prepulse at this point.

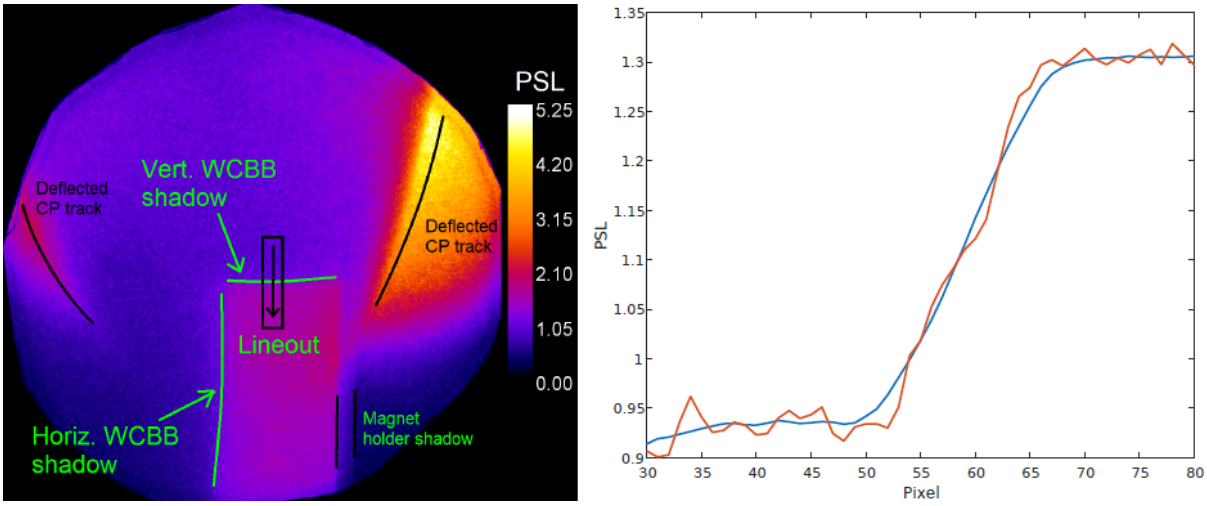


Figure 8.17: Image plate scan showing the penumbral shadows cast by two, orthogonally oriented tungsten carbide ball-bearing after a Cerberus shot upon 15 µm thick aluminium. Streaks can be seen upon the image plate caused by charged particles. The black box on the left image shows the direction in which the lineout was taken. The lineout shows the real data (red line) along with a smoothed profile (blue line) which assisted in measuring the transition width. The penumbra width was estimated to be 11.5×1.5 pixels, yielding a measured source size of 34.9×4.8 µm.

Results and Discussion

For laser-target interactions with focused intensities of $\sim 10^{18}$ Wcm^{-2}, thin foil targets (<15 µm) are completely ionised. Therefore the target thickness should determine the volume of plasma in which x-rays are produced, the divergence of the hot electrons directly accelerated by the laser through the target also scales proportionally to the target thickness. Figure 8.18 shows the x-ray source size measurements for 5 and 15 µm thick Al foils, with respect to the focused intensity of the Cerberus laser onto the target. The data here is presented with separate points on the graph for vertical and horizontal source size measurements, unless the vertical and horizontal results were measured to be within 2-3 µm of one another in which case only the average of those two values (indicated on the figure) is included. We would predict that interactions with 15 µm thick foils should produce a factor 3 greater source size than 5 µm thick Al foil, however this was not observed in the data. With fewer 5 µm Al foil measurements, it is possible that the results do not agree with our expectations due to limited statistics; there was a large variation between source size measurements, which did not clearly correlate to the laser intensity. As was predicted, the vertical source size was measured to be typically larger than the horizontal, however the difference in the source sizes is far greater than was predicted due to the angle of incidence onto the foil. This may be due to a disparity between the predicted and actual focal spot size. The focal

spot was measured before each shot was the 10 Hz output of the OPCPA front end of the laser (described in chapter 4), unamplified by the Nd:Glass flashlamp amplifiers. There is a possibility that thermal effects in the flashlamps could produce a slight cylindrical lensing term which would change the farfield profile of the laser. However, this is unlikely as the nearfield profile of the amplified laser pulse was recorded using burn paper and did not show any large differences from the 10 Hz beam profile. Another explanation for the difference in vertical and horizontal source sizes may be due to a systematic error in target alignment procedures, the targets were aligned to TCC using the focal spot camera by translating them until they were in focus on the camera. Due to the width and height of the foils, the entirety of the foil was not visible on the camera, therefore both edges of the target were aligned to focus, with the difference between the positions of focus to determine if there was any rotational misalignment in the target. If this was the case, the difference between the positions where the edges were at focus was taken as TCC and the centre of the target was translated to that position. It is possible that residual rotation in the target alignment could increase the difference between the vertical and horizontal source sizes measured.

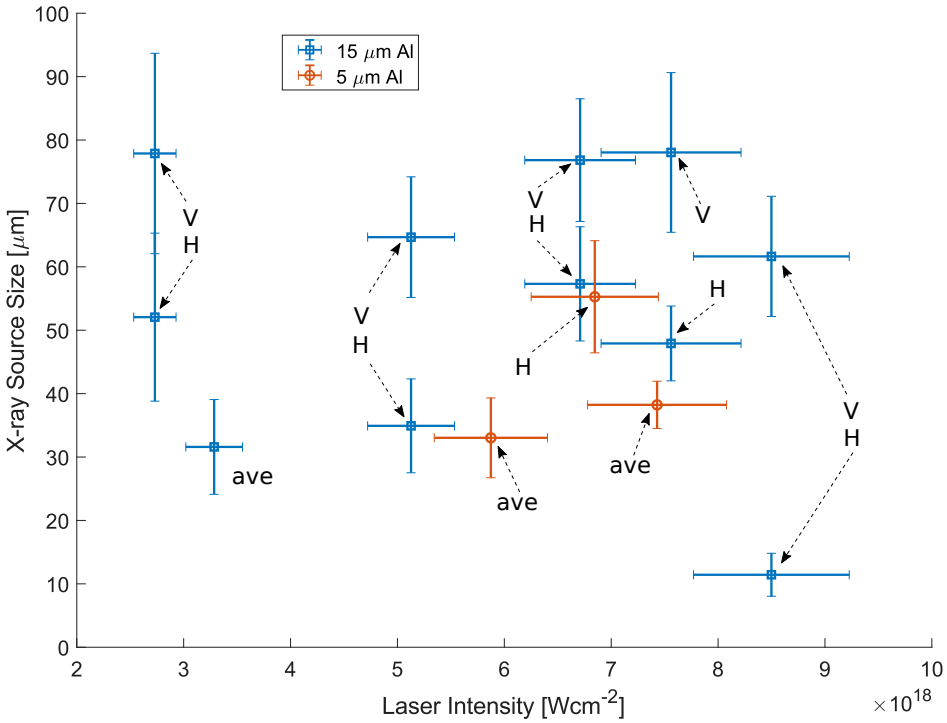


Figure 8.18: Source-size measurements of x-rays produced in the interaction between the Cerberus main laser pulse ($\sim 10^{18}$ Wcm^{-2}) and both 15 µm (blue), and 5 µm (red) thick Al foils.

An artificial prepulse, 50 ps ahead of the main pulse, was previously seen to enhance the hot

electron energy spectra and the x-ray temperature. A discrete prepulse appears to result in a smaller x-ray source size for 15 µm thick Al foils, additionally the vertical and horizontal source size measurements in the case of a prepulse are far more consistent. This is likely due to the prepulse ionising the front of the target and producing an expanding preplasma. As the preplasma expands uniformly in all directions, it creates a hemispherical plasma above the critical density at the target face, therefore the main laser pulse would be incident normal to the critical surface rather than at an angle. From this data, we can clearly see that the inclusion of the 50 ps prepulse results in a smaller measured x-ray source size. If we assume that the x-ray source size directly correlates to the diameter of the hot-electon beam accelerated by the pondermotive force (equation 6.8), then from the source size must be proportional to the focal spot diameter. With no prepulse, the average x-ray source size was found to be 70±10 µm and 38±6 µm in the vertical and horizontal axes of the target, when a prepulse was added, the average x-ray source size decreased to 40±11 µm and 31±6 µm in the vertical and horizontal axes of the target. This difference in the average source size with and without a prepulse could potentially correspond to a reduction in the focal spot diameter, produced due to self-focusing of the main beam in the pre-plasma.

Figure 8.20 shows the source size measurements from 5 µm thick Al. In this case, unfortunately, there are limited statistics to make a confident conclusion, however the source sizes measured when a prepulse was included and when it was not are more consistent than observed for 15 µm thick Al foil. This result may be due to the thickness of the target, as for a thinner foil, more of it is pre-ionisied by the laser ahead of the main beam.

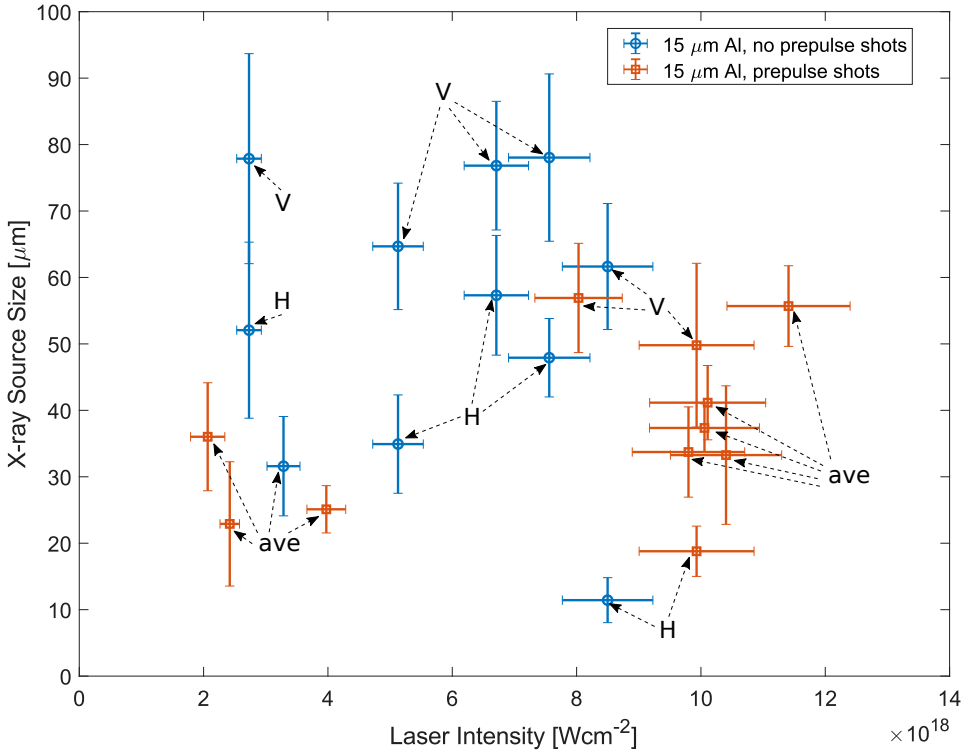


Figure 8.19: Source-size measurements of x-rays produced in the interaction between the Cerberus main laser pulse ($\sim 10^{18}$ Wcm^{-2}) and 15 µm thick Al foil, without a prepulse (blue) and with the inclusion of a discrete 2×10^{-4} relative contrast prepulse, ~50 ps before the main beam (red).

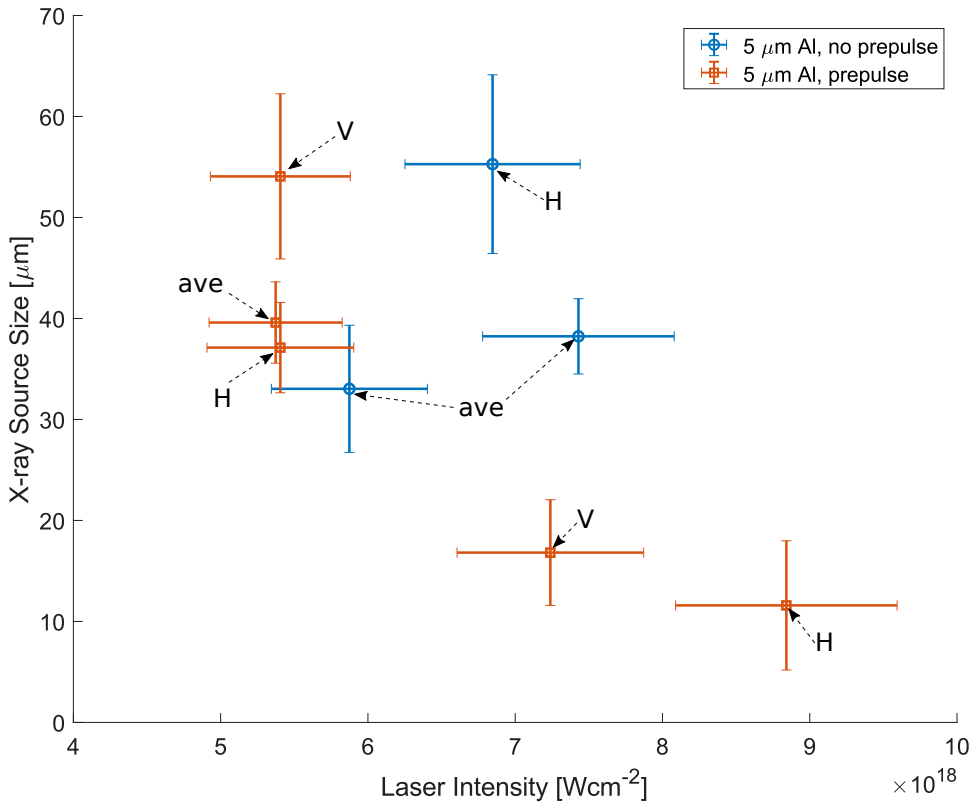


Figure 8.20: Source-size measurements of x-rays produced in the interaction between the Cerberus main laser pulse ($\sim 10^{18}$ Wcm^{-2}) and 5 µm thick Al foil, without a prepulse (blue) and with the inclusion of a discrete 2×10^{-4} relative contrast prepulse, ~50 ps before the main beam (red).

8.3.2 Proton Source Size Measurements

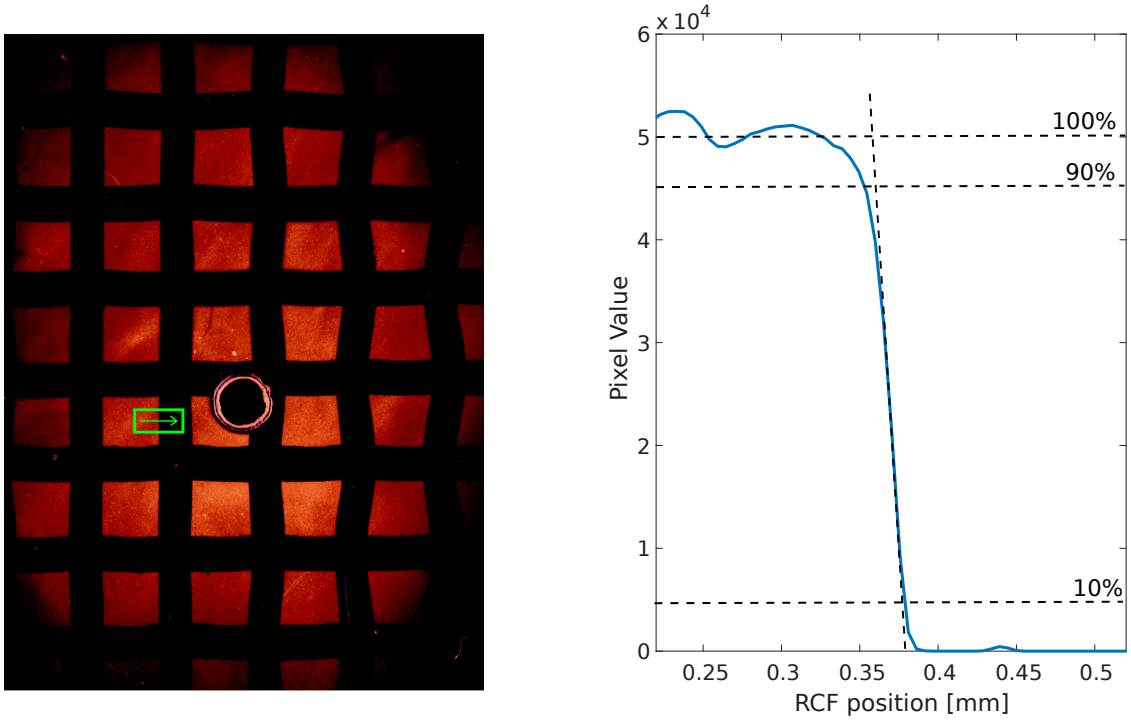
A follow on experiment on the Cerberus laser system utilised proton beams generated by interactions between the main laser and 15 µm Al foils to radiograph laser-launched flyers to investigate the electromagnetic field around or carried by the flyers [18]. Therefore we were required to characterise the source size of proton beams generated on the system. Proton source size decreases with increasing pulse energy, determined by the sheath field potential created by hot electrons escaping from the rear surface of the target. Experimental measurements [4] have also shown a strong correlation between the radial distribution of proton source sizes with the hot electron temperature and the density at the rear surface of the target,

$$E(z) \propto \frac{k_B T_{eHOT}}{\lambda_D} \propto \sqrt{k_B T_{eHOT} n_e} \tag{8.7}$$

corresponding to equation 6.15, where k_B is the Boltzmann constant and λ_D is the Debye length.

The proton source size was measured using a similar knife-edge penumbral imaging technique as in the previous section. In this instance however, a woven copper mesh, constructed of 0.25 mm copper wire, intersecting to produce a 0.4 mm square aperture, was used to imprint a regular pattern onto the proton beam profile which allowed penumbral imaging across the spatial profile. The grid was placed 9.5 mm from TCC, along the axis normal to the rear face of the target, giving a magnification of M $\sim$ 3. One layer of Radiochromic film (RCF) (Gafchromic EBT2 [136]) was used as a detector, this was placed 38.5 mm from TCC and wrapped in 15 µm thick Al foil to attenuate x-rays and low energy ions. After the shot, lineouts were taken at each point of the imprinted grid on the proton beam profile to give source size measurements across the spatial profile of the proton beam, figure 8.21 shows an example of this penumbral imaging process.

Proton source size measurements were carried out on two shots, both with 15 µm Al foil as the target, with and without a discrete prepulse included in the temporal profile, 50 ps ahead of the main pulse. The focused intensity of the laser was measured in each case, 6.8×10^{18} Wcm^{-2} in the first shot and 9.8×10^{18} for the shot with a $\sim$2 $\times 10^{-4}$ relative contrast prepulse, 50 ps before the main laser pulse.



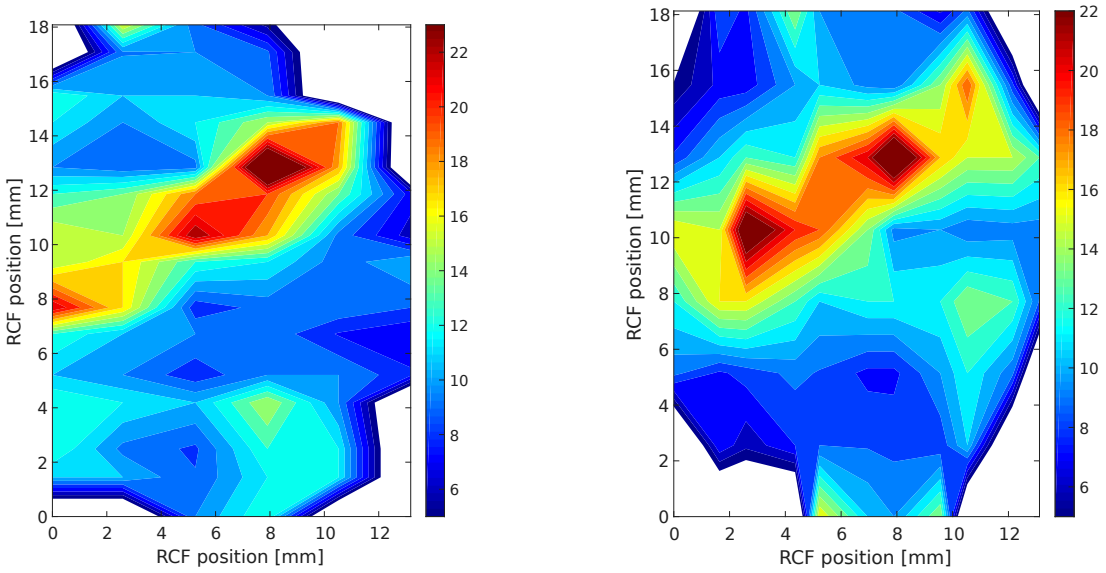
(a) (b)

Figure 8.21: (a) the spatial profile, recorded using one layer of RCF (Gafchromic EBT2) of a proton beam generated by the Cerberus main laser pulse ($\sim 10^{18}$ Wcm^{-2}) and 15 µm thick Al foil. The grid pattern on (a) was produced by a woven copper mesh, placed between the Al foil and the RCF. A lineout on (a) shows a penumbral transition, (b), which can be measured to extract the effective proton source size given at that point in the spatial profile of the proton beam.

Results and Discussion

Figure 8.22 shows proton source sizes across the spatial profile of a proton beam accelerated by a measured focused intensity of 6.8×10^{18} Wcm^{-2} from 15 µm thick Al foil. The effective proton source size was found to vary across the spatial profile of the beam, from 5 - 25 µm. The error associated with these source size measurements was expected to be related to poor fitting analysis through the penumbral region, repeat analysis the analysis for a penumbral transition, with lines of "worst fit", gave a source size error of ±0.9 µm.

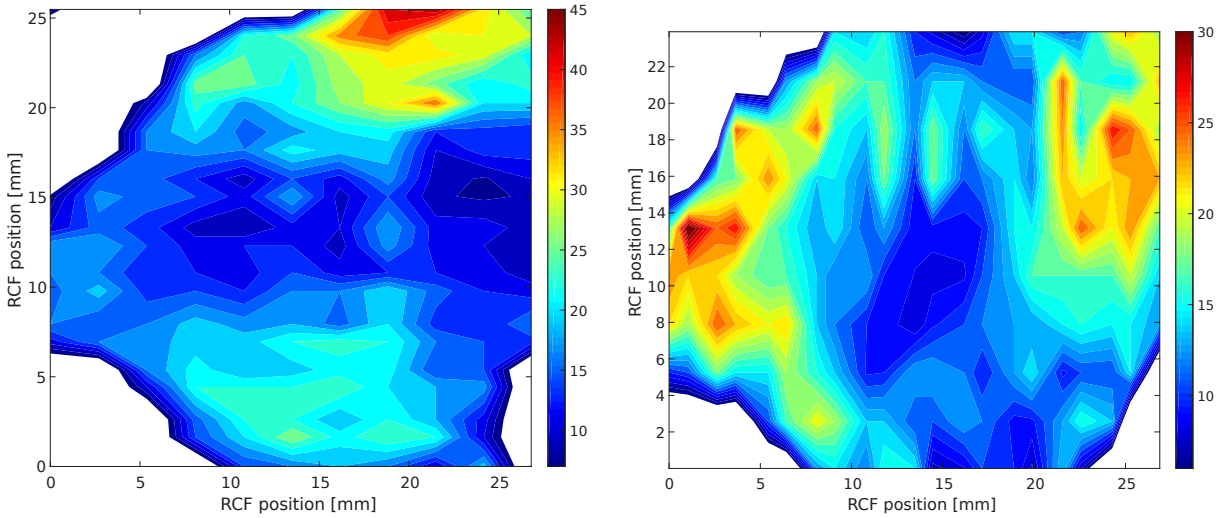
Figure 8.23 shows the proton source size measurements, in units of µm, across the spatial profile of a proton beam accelerated by a 9.8×10^{18} focused intensity laser pulse with a $\sim 2 \times 10^{-4}$ relative contrast prepulse included 50 ps prior to the main pulse, from the rear surface of a 15 µm thick Al foil target. A larger proton beam size was recorded for this shot, in addition to a greater range of source sizes compared to the shot with no prepusle was measured, varying from 5 - 40 µm.



(a) (b)

Figure 8.22: Source size measurements, in units of µm, of a proton beam accelerated by a 3.4 J, 6.8×10^{18} Wcm^{-2} focused intensity laser pulse onto 15 µm Al foil. The a) vertical and b) horizontal source sizes were observed to vary across the spatial profile of the proton beam.

Proton source size is expected to decrease with increasing hot electron temperature, and as we have previously measured an increased hot electron temperature by including a prepulse before the main pulse, this result appears to contradict our expectations. Comparing figures 8.22 and 8.23, we observe the lowest source size measurements (∼5 - 18 µm) in the centre of the proton spatial profile in the presence of a prepulse as opposed to figure 8.22, where the centre of the proton spatial profile shows a peak in proton source size (up to ∼25 µm). This perhaps indicates that protons directly accelerated via TNSA are produced from a smaller source size in the centre of the proton beam, corresponding to the hotter electron temperature. One known consequence of poor contrast, in this case a discrete prepulse, is an expansion of the rear surface of the target, which increases the scale length of the plasma and inhibits the formation of the sheath field [12] and can produce blurring of the proton source [137]. Shocks launched by ns-duration low-contrast pedestals or heating of the target leads to this expansion, which increases the the proton source size.



(a) (b)

Figure 8.23: Source size measurements, in units of µm, of a proton beam accelerated by a 9.8×10^{18} focused intensity laser pulse with a $\sim2\times10^{-4}$ relative contrast prepulse, 50 ps prior, pulse onto 15 µm Al foil. The a) vertical and b) horizontal source sizes were observed to vary across the spatial profile of the proton beam.

8.4 Conclusion

Particularly in the case of TNSA, high temporal intensity contrast is often a key design goal of high-power, short pulse CPA laser systems, however in this chapter we have shown that the ability to reintroduce discrete prepulses to the temporal intensity profile can result in an enhancement of the energy spectra of protons, electrons and x-rays accelerated from thin foils by the Cerberus laser system. We have shown the results of two investigations, involving this discrete prepulse, to characterise how the emission spectra of protons, electrons and x-rays is affected by the relative timing of a prepulse with a contrast of 2.75×10^{-4} relative to the main $\sim10^{18}$ Wcm^{-2} intensity laser pulse.

The addition of an artificial prepulse, 60 ps before the arrival of the main pulse, with a measured relative contrast of 2.75×10^{-4}, produced an overall enhancement in the maximum proton energy, hot electron temperature and total hard x-ray energy measured from the interaction. Evidence seems to suggest self-focusing in preplasma is responsible for this spectral enhancement, with electron density measurements collected by analysing the Cerberus interferometry results showing that a 60 ps prepulse causes preplasma at the threshold for self-focusing to expand a factor 3.6 times further at the arrival of the main pulse than for electron density measurements where a

prepulse was not present. This was additionally supported by x-ray source size measurements, which also measured an overall decrease in the source-size for x-ray generation when a prepulse was added 50 ps before the arrival of the main pulse.

Whilst all of this data strongly supports the hypothesis of self-focusing, calculation of the actual beam intensity at the relativistic surface still requires additional modelling. Relativistic interactions between lasers and plasmas are best handled by particle in cell (PIC) simulations which would give an accurate account of the self-focusing of the main pulse in the preplasma and also the associated effects of a intense beam propagating through this underdense region such as j×B heating or electron hole boring, which can also change the shape of the electron density gradient in front of the target. The prepulse may also be responsible for 'preforming' the preplasma, modulating the refractive index to produce steeper self-focusing, which would also require PIC simulations to investigate.

Further data analysis is also required to explain the drop off in emissions as the prepulse is moved past -60 ps relative to the main pulse. This could be due to the prepulse launching shock waves through the target which could increase plasma scale length at the rear side, screening out the formation of electron sheath fields. However, rear expansion or heating of the target would only be expected to affect the proton spectrum, in our investigation we also observed a drop in the hot electron temperature and hard x-ray populations.

For future PIC simulations, we require an accurate measurement of the electron density in front of the target. Unfortunately, Helios is not accurate at the low temperature limit, which reduces the reliability of the electron density gradient it predicts. The Cerberus interferometry measurements proved to be more reliable for measuring electron density, however these were obscured by bright self-emission from the interaction region. In the next chapter we will discuss the design and development of a supercontinuum source for optical probing at off-harmonic wavelengths, which allows us to filter bright self-emission from the Cerberus interferometer results.

Additionally, the prepulser was observed to introduce unaccounted for 10^{-6} relative contrast prepulses into the Cerberus temporal profile. Redesigning the prepulser to use a Mach Zehnder configuration would avoid these unwanted extra features from the wave plates in a Michaelson-type design.

Chapter 9

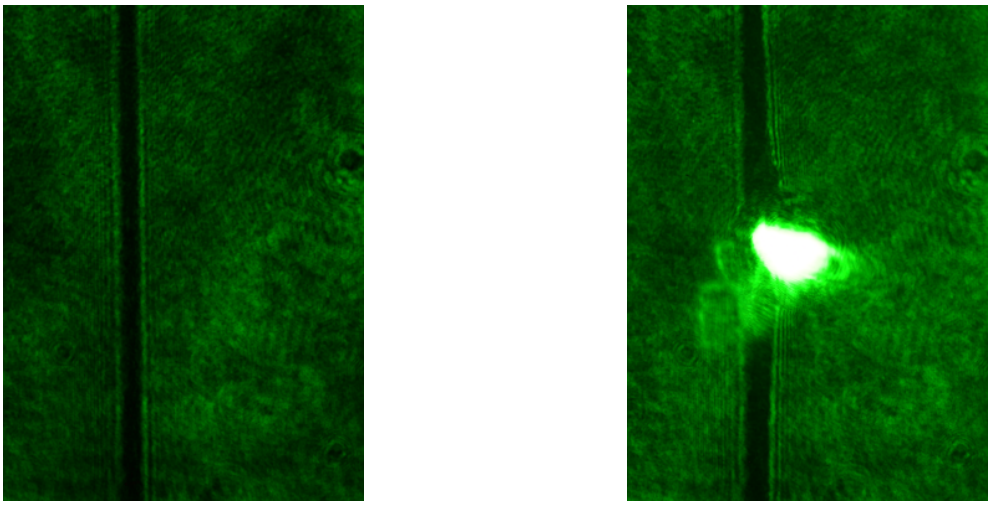
Supercontinuum-Source Based Optical Probe

In the last chapter, we discussed the results of a recent experiment on the Cerberus laser system which showed enhancement in the energy spectrum of protons, electrons and x-rays produced from thin (14 µm) aluminium foils with the addition of a discrete prepulse to the Cerberus laser temporal profile, at specific times before the main pulse [15]. It is theorised that this enhancement is most likely due to the main laser pulse self-focusing in the extended preplasma produced by the prepulse. However, in order to accurately predict the degree to which the main pulse self-focuses, we require a quantitative measurement of the electron density of the preplasma close to the front surface of the target. For this purpose, a Nomarski interferometer [131] was used in coordination with a ∼500 fs pulse duration probe beam, centered at $\lambda_0 = 527$ nm. This interferometer and the optical probe beamline are described in more detail in section 7.2.2. However, harmonic self-emission produced by the laser-plasma interaction at the same wavelength as the optical probe can be problematic in diagnostic systems of this kind, here obscuring the interferogram close to the interaction region, restricting our measurements of the preplasma electron density closer than ∼0.04 mm from the front of the target.

In this chapter, we present progress on creating an off-harmonic optical probe for laser interferometry derived from a liquid-cell supercontinuum source. By developing a source that probes the target at "off-harmonic" wavelengths, we are better able to filter out self-emission from the laser-plasma interaction and probe closer to the surface of the target. This work builds upon an

aqueous salt solution (K_2ZnCl_4) white light source previously demonstrated on the Cerberus laser system by Timothy Robinson et al. [138], which reported the stable generation of a supercontinuum pulse spanning ∼600 nm spectral range with a total energy of ∼40 µJ across the output at 3-4% RMS stability over 50 shots. We have extended this investigation to characterise the output energy as well as the spectral and spatial properties of this supercontinuum source for greater input energies of up to 50 mJ for 500±50 fs duration pulses centered at $\lambda_0 = 1054$ nm. Once characterised, the supercontinuum beam was propagated through the optical probe beamline of the Multi-Terawatt Target Area (described in section 7.2.2) to the Nomarski interferometer. By inserting different bandpass filters into the interferometer we are able to select a range of probe wavelengths, and here we discuss the interferograms produced by this probe and finally present the off-harmonic interferometry results of a laser-target interaction.

Laser-plasma interactions produce harmonic self-emission at the critical surface, where the laser wavelength is equal to the plasma wavelength [139]. Figure 9.1 shows a point of bright self-emission near 527nm in the optical probe image of a Cerberus laser shot with a 15 µm thick Al foil, here the interaction region is heavily obscured by this self-emission close to the critical surface which prevents interferometry directly adjacent to the target face.



(a) (b)

Figure 9.1: Optical probe image of a laser-target interaction with a 15 µm thick Al foil viewed edge on. The probe light was centered at 527 nm, with a pulse duration of ∼500 fs. Figure a) shows the target geometry prior to the shot, whilst figure b) shows the optical probe image ∼10 ps before the main pulse arrives, the interaction is obscured by bright self-emission from the target, integrated over 100ms by the camera exposure time.

Multi-wavelength interferometry has previously been demonstrated on the Cerberus interferom-

etry beamline at the first, second and fourth harmonics of a 1054 nm laser pulse [140]. However, it was determined that self-emission from laser-plasma interactions would still be present in the beam at these probe wavelengths, motivating the development of an off-harmonic probe. An "off-harmonic" probe, is an optical probe for interferometry at a wavelength that does not coincide with any of the harmonic light generated by the laser-plasma interaction. Optical probing at off-harmonic wavelengths enables interferometry at wavelengths which are both below the critical density of the plasma close to the interaction region and where the self-emission can be filtered from the beam. Off-harmonic probes have been developed based upon secondary laser systems, where the relative timing between the main laser pulse and the optical probe beam is determined by an electronic trigger [141], [142], or by frequency shifting the probe beam away from the laser harmonic via stimulated Raman scattering (SRS) [143], [144].

The Cerberus laser is often used to investigate laser-matter interactions with novel target geometries, including optically levitated 7 - 10 µm oil droplets which were trapped by a focused 2W, 532nm laser (Verdi, Coherent laser) [125], [130] or thin (∼15 µm) Al foil flyers, which were laser-launched using an external Q-switched, Nd:YAG laser operated at 1064 nm (∼ 150 J, 20 ns) [18]. These different experiments require the inclusion of separate laser beamlines propagating through the target chamber which may complicate optical probing of the target; for example, levitated targets may scatter the trapping laser light into the interferometry beamline. Additionally, a separate mid-infrared system, the Chimera laser [145], is currently in the final stages of development at Imperial College London, primarily designed by Nicholas Stuart for ultra-high contrast and mid-IR laser wakefield acceleration [146]. The Chimera laser generates $\lambda_0 = 3.7$ µm mid-IR pulses with ∼500 nm bandwidth, sufficient for a 3 cycle pulse, to a current maximum uncompressed pulse energy of 32 mJ. Additionally, a high energy $\lambda_0 = 1.6$ µm idler signal is also produced at the difference frequency generation stages. The master oscillators for both Cerberus laser and Chimera are synchronised by way of a rubidium atomic clock timing module (Stanford Research Systems DG645, Rb timebase option) which governs the laser oscillator round trip frequency for both systems, with the intention being that they could potentially be used for joint operation on experiments in the future. With the range of central wavelengths of each different light sources that may be used on experiments in the target chamber, as well as to future-proof against the addition of future systems with different central wavelengths, there was significant interest in developing a wavelength-tunable optical probe for interferometry at wavelengths not

covered by any of the harmonics of lasers involved in experiments.

A white light source was previously developed on the Cerberus laser system as an optical limiter and contrast diagnostic by Timothy Robinson [19], [138]. Here, a supercontinuum was generated from an 80 mm long liquid cell filled with an aqueous salt solution of both Potassium Chloride (KCl), ∼4.25 mol, and Zinc Chloride ($ZnCl_2$), ∼2.1 mol at a saturated concentration of 652±7 g/L. This choice in liquid source was informed by previous reported enhanced spectral broadening via SPM in concentrated salt solutions [147] as well as the very high solubility of $ZnCl_2$ salts (3.95 kgL^{-1}). Compressed pulses from the Cerberus OPCPA front end, with an energy of 1 - 2.5 mJ (controlled using a $\lambda/2$ waveplate-polariser pair) and a ∼500 fs FWHM duration, were focused into the liquid cell with short focal length lenses (F/6). At the output of the liquid cell, the light was recollimated before the residual 1054 nm beam was picked off using an HR mirror. For an input energy of 1 - 2.5 mJ, the total energy across the supercontinuum, as well as the spectrum within a range of 300 - 1100 nm, was characterised. A diagram of the experimental setup used is shown in figure 9.2.

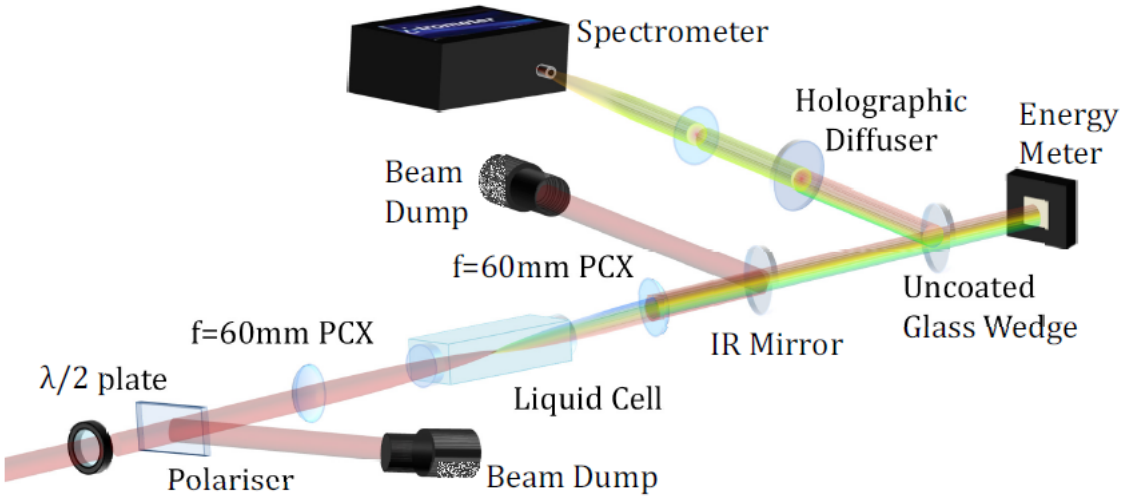


Figure 9.2: TR: Layout of the setup used to acquire spectra for analysis of the supercontinuum source's spectral stability. A holographic diffuser was used to spatially smooth the pulses in order to isolate the overall pulse-to-pulse spectral stability. Image credit: Timothy Robinson [138]

Timothy Robinson et al. reported generation of a ∼600 nm bandwidth supercontinuum with a efficiency in the input beam to total energy contained in the supercontinuum at output of approximately 10^{-2}. This white light source has been used to calibrate the resonse of optical streak cameras for optical pyrometry diagnostics at the AWE Orion laser facility [83] and test

the viability of a 630 nm off-harmonic optical probe in the Cerberus interferometry beamline by selecting a narrow portion of the supercontinuum spectrum using interference filters [140]. A potential 630 nm probe was investigated by Samuel Giltrap and Samuel Eardley, based on Raman shifting a 527 nm optical probe beam with (∼1 mJ, 500 fs) in a 150 mm long methanol liquid cell, however the signal was ultimately deemed unsuitable for optical probing due to relatively poor energy and pointing instability in the signal. Additionally, the energy difference between 10 Hz operation and 'on-shot' energies of up to 150 mJ resulted in a highly different Raman output, primarily due to undesired filamentation inside of the methanol cell, which also introduced substantial error in low power alignment of the 630 nm probe beam.

9.1 Supercontinuum Generation

Spectral broadening up to and beyond hundreds of nm can be achieved by propagating intense pulses through media with a high nonlinear refractive index [148], such as crystalline solids (e.g. YAG [149]) or gas [110], [111], [117], [150], [151] and liquid filled hollow core fibres [152]. As these pulses exhibit often high spatial coherence along with this bandwidth generation, they are good candidates for ultrafast pulse creation; high spectral bandwidth results in a very short transform limited pulse duration, to the few-cycle regime [150]. Supercontinuum generation, however, is more accurately described as an umbrella term for several nonlinear processes which each work together to produce spectral broadening of a laser pulse, including self phase modulation (described in section 2.1.3), soliton self-frequency shift [153], optical wave breaking [154] and stimulated Raman scattering.

Optical wave breaking [154] occurs as a result of the group velocity dispersion (GVD) associated with the broad bandwidth of a supercontinuum pulse. Due to the GVD, parts of the pulse which travel faster, or slower, through the medium can overtake oneanother and produce further SPM due to the interference of these pulses. Optical wave breaking generates light with a central wavelength determined by the difference in frequency between the two interfering pulses in well-defined spectral sidelobes.

Vibrational modes in materials can be quantised as quasi-particle phonon waves. Raman scattering is a $\chi^{(3)}$ nonlinear process where photons inelastically scatter off of optical phonons, (or in plasmas, plasmons) which results in a frequency shift where one pump photon is converted

into a lower energy signal photon, with the frequency difference between the two carried by an optical phonon in the material. This nonlinear process can be stimulated, named stimulated Raman scattering (SRS), when two pulses with different central wavelengths propagate together through a Raman-active medium, where the longer-wavelength beam (the Stokes pulse) receives amplification from the shorter wavelength beam. In a supercontinuum, Stokes pulses lead or trail the main peak based on their GVD, U_{Stokes} through the cell medium

$$T_{Stokes} - T_{USC} = \Delta x \left(\frac{1}{U_{Stokes}} - \frac{1}{U_{USC}} \right) \tag{9.1}$$

where Δx is the cell length and U_{USC} is the average group velocity dispersion for a bandwidth region [155].

9.1.1 Filamentation in liquids

Self-phase modulation can be extended within a laser filament, produced when self-focusing acts to reduce the pulse spatial profile (which may be balanced by diffraction or plasma defocusing), and the beam collapses into a guided plasma channel with high local density. Filamentation occurs when the input laser power is greater than critical power,

$$P_{crit} = \frac{\alpha \lambda_0^2}{n_0 n_2} \tag{9.2}$$

where λ_0 is the central wavelength, α is a parameter related to the initial spatial profile of the beam ($\alpha = 0.148$ for Gaussian beams) and n_0 and n_2 are the ordinary and nonlinear refractive indices of a material. However, when the laser power is much greater than the critical power, $P \gg P_{crit}$, non-uniformities in the spatial profile of the laser pulse can also cause it to break down into many filaments [156]. From this point, if a focusing geometry through the nonlinear medium is used, then the multiple filaments can converge and collapse into a single so-called 'superfilament' [157] which propagates with high spatial coherence as a single beam. This process was initially observed in air, but has also been reported for filamentation in water [158].

For a K_2ZnCl_4 aqueous salt solution, the nonlinear refractive index is approximately 1.36×10^{-19} m^2W^{-1} [147] at $\sim$ 1 µm. Therefore the critcal power, $P_{crit} \simeq 9.1 \times 10^5$ W, gives a lower limit for filimentation of $\sim$0.45 µJ. The Cerberus optical probe beamline operates between 1 - 60 mJ,

500±50 fs compressed pulse duration and therefore is well above the threshold for filamentation, likely in the superfilamentation regime.

9.2 Experimental Setup

Previously, supercontinuum generation was investigated at a relatively low energy (1-2.5mJ), limited by the output of the OPCPA front of the Cerberus laser system. However, for on-shot interferometry, a bright source is required for both high contrast and to outcompete broadband plasma emission and residual second harmonic light which is transmitted through interference filters. The OPCPA front end output is amplified by a series of Nd:Glass flashlamp amplifiers described in chapter 4, after these amplifiers, the beam is split between two beamlines, one which undergoes further amplification up to 10 TW, 500 fs FWHM duration for laser-target interactions and the other for interferometry. As the split between the main and probe beamlines is post-Nd:Glass amplification, the optical probe is amplified by the same gain as the main beam. This means that there is a greater energy budget for supercontinuum generation, however the dynamics of the nonlinear interactions inside of the liquid cell, such as the length of the filament formed, are intensity-dependent and must be characterised at these higher energies.

The experimental setup shown in figure 9.2 was recreated in the interferometry beamline. A saturated aqueous solution of zinc and potassium salts was prepared by dissolving a K_2ZnCl_4 salt solution in deionised water (conc. 652±7 g/L). With this solution, we filled an 80x30x30 mm cuboid liquid cell. Two 8 mm thick UV-fused silica windows were mounted at each end of the length of the cell, with the window at the input face AR coated @ 1054 nm at the air-glass interface and uncoated on the glass-liquid interface to match the refractive index of the solution, the window at the output face was similarly uncoated at the liquid-glass interface and broadband AR coated (650 - 1050 nm) at the output. Pulses, with a compressed 500±50 fs duration and a pseudo-flat top spatial profile with a D4σ beam width of 10±1 mm, were focused into the liquid cell with short, f = 60 mm, focal length lenses. As with the previous experiment, a shorter focal length lens more strongly focuses the input beam to enhance nonlinear effects within a smaller liquid volume. Previously, water absorption was shown to dominate the supercontinuum generation efficiency through the liquid cell [19], therefore a tight focus and short cell mitigates losses due to water absorption. Currently, ion acceleration experiments specify upwards of 3J onto

target, leaving a maximum energy of ∼60 mJ in the optical probe beamline after compression. The surface damage threshold of fused silica for laser pulses centered at ∼1 µm, with a pulse duration of 500 fs is approximately 2.5 Jcm^{-2} [25], at the current experimental configuration, this gives an upper energy limit of roughly 500 mJ at the inner surface, assuming a Gaussian beam profile. The use of short focal length lenses here at the input both therefore decreases loss due to attenuation in water and also results in a larger beam diameter through the glass window, suggesting possible scalability to higher energies. Additionally, salt solutions are self-healing with regards to laser photoionisation as the salt ions are already dissociated in the liquid [159].

At the output of the liquid cell, the pulse was collimated using an f = 60 mm lens (AR coated 650 - 1050 nm). Residual 1054 nm light was removed with a HR mirror, we previously characterised the reflectivity of the mirror over 400 - 1000 nm against a known white light source (Thorlabs SLS201L) as well as by measuring the liquid cell supercontinuum spectrum at low input energy. The transmitted supercontinuum energy, of light generated between an input energy of 1.8±0.1 - 57.2±1.3 mJ, was characterised using a broad band surface absorbing energy meter (Gentec QE12SP), calibrated for a spectral range 0.193 - 20 µm. The spectral profile of the supercontinuum was characterised separately, using a combination ground glass diffuser and lens to focus the spatially homogenised supercontinuum pulse onto a CCD spectrometer (Thorlabs CCS175) which could be electronically triggered by the Cerberus laser. In some cases, it was necessary to attenuate the supercontinuum light so as not to saturate the spectrometer, to do this a reflective ND filter stack was used, the spectral transmission of each of the filters was also characterised before use.

9.3 Supercontinuum Source Characterisation

The total energy of the generated supercontinuum (within a spectral range of 200 - <1000 nm) was first characterised as a function of input energy. Figure 9.3 shows the 50-shot average energy measured with respect to input energies from 1.8±0.1 - 57.2±1.3 mJ. In the previous investigation, the supercontinuum energy was seen to agree well to a second order polynomial function [138], which is also the case for figure 9.3 at input energies <10 mJ, however at higher energies the efficiency of this process appears to saturate. Using a boltzmann sigmoidal fit function, we can predict that the supercontinuum energy would begin to saturate at 0.71±0.06 mJ. The maximum

generated supercontinuum energy recorded, averaged over 50 shots, was 0.68±0.03 mJ with an RMS stability of 3.9%, recorded for an input of 56.9±1.0 mJ and corresponding to a conversion efficiency of $\sim 10^{-2}$.

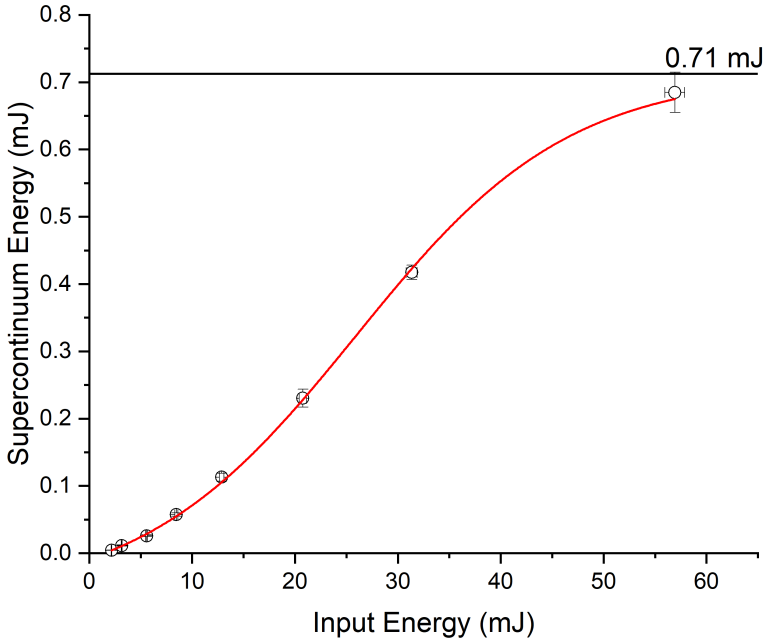


Figure 9.3: Total energy generated in a supercontinuum source with ∼600 nm spectral range, with respect to the input energy of a 1054 nm, 500fs driving pulse. The supercontinuum generation efficiency was observed to begin to saturate at high input energies, with a predicted saturated energy of 710±60 µJ.

Water attenuation is major limiting factor to supercontinuum generation in aqueous salt solutions [19]. The absorption coefficient of water at 1054 nm was measured by Hale et al. at $\alpha = 0.56990$ cm^{-1} [160], which for an 8 cm long liquid cell, approximately corresponds to a transmitted fraction of the input light of ∼1.0%. We measured a total transmitted energy (IR + supercontinuum) of 65.2±1.7 µJ for an total input energy of 1.2±0.2 mJ, corresponding to a 5±1% transmission efficiency. As the water attenuation at wavelengths in the visible spectrum is significantly lower than the infrared, this suggests that increasing the efficiency of the supercontinuum generation process increases the efficiency of total transmission.

A broad supercontinuum spectrum was measured over a range of ∼600 nm, shown in figure 9.4, with two main peaks around ∼610 nm and 900 nm, stable over 50 shots to ∼3.7% RMS. The spectral profile of the supercontinuum was not observed to vary with input energy and even cor-

responded well with the spectral profile measured in [138] at driving energies far lower than those used in this investigation, suggesting that this is dominated by the wavelength dependent linear absorption of water. SPM should produce spectral broadening around the central laser driving wavelength, the shape of the spectral profile measured is therefore likely to be a combination of nonlinear effects mentioned such as optical wave breaking, SRS, second harmonic generation in ionised plasma channels, or a combination of these. The spectral profile was found to be heavily dependent upon the absorption spectrum of water [19] and whilst the spectrometer used to characterise the spectrum only had a range of 400 - 1000 nm, it is unlikely that the supercontinuum spectrum extends past 1.2 µm due to high attenuation in water at longer wavelengths. Figure 9.4 shows the 20-point moving average of the spectral intensity, the spectrometer we used, Thorlabs CCS175, has a resolution of 6 pixels/nm and therefore the data shown is the moving average over 3.3 nm. Taking a moving average of the spectrum clearly reveals fringes with an average spacing of ∼20 nm.

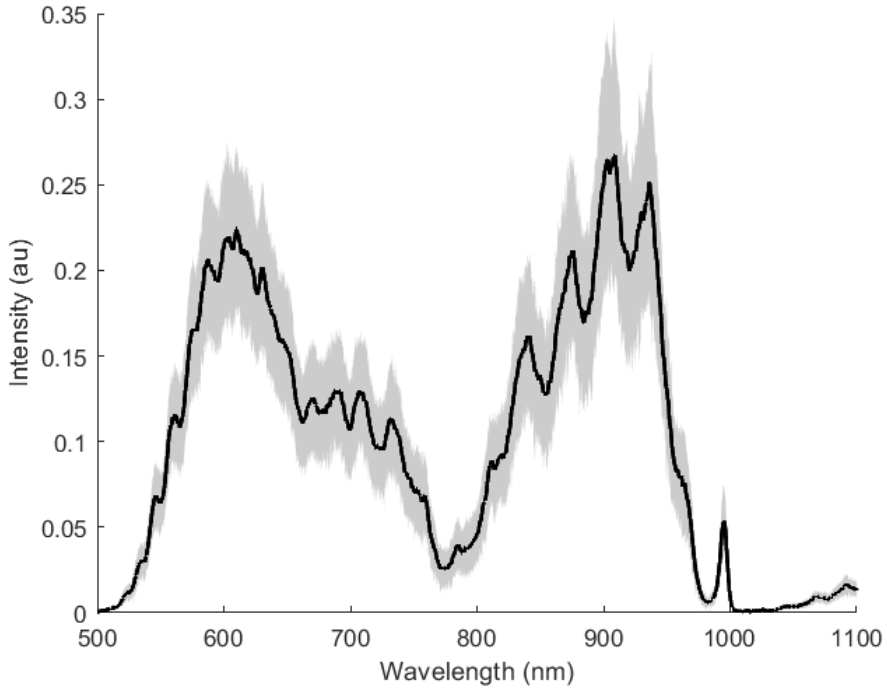


Figure 9.4: The spectral profile of a supercontinuum generated by a ∼40 mJ energy, 500 fs FHWM duration, pulse centered at 1054 nm. The black line represents the 20-point moving average supercontinuum spectrum, averaged measured over 50 shots, whilst the shaded area shows the standard deviation at each wavelength.

Light at wavelengths >1 µm was removed using a HR mirror, coated at 1054 nm, however this

mirror also produced these spectral fringes, which may originate due to the fact that the mirror used was not a wedged optic, and that the rear surface was uncoated. Figure 9.5 shows the comparison between a 20-point moving intensity average of the 50-shot average spectrum, where an HR mirror was used to remove residual >1 µm light (red), and the spectrum generated with ∼10 mJ, 1054 nm pulse energy, where IR light was not removed but the liquid cell output was attenuated by two reflective ND filters before measurement (grey), the spectral transmission of these filters was characterised beforehand using a white light source (Thorlabs SLS201L) and not shown to affect the measured spectrum. By comparing the two profiles, it is clear that an HR mirror introduces spectral fringes into the supercontinuum profile.

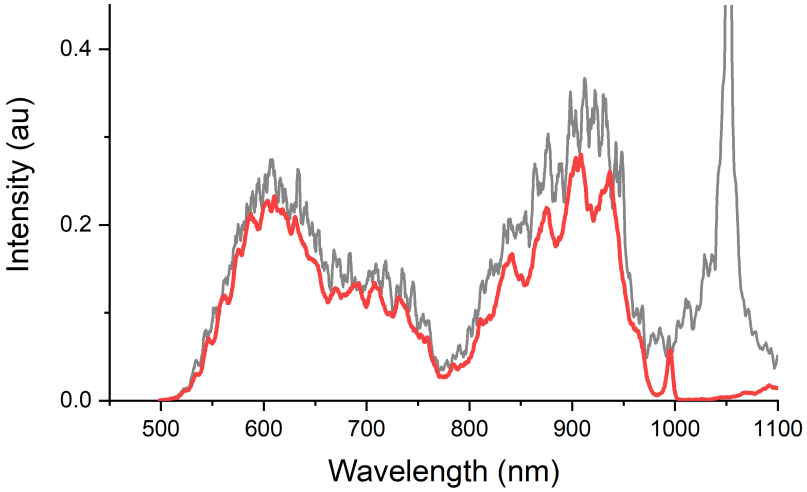
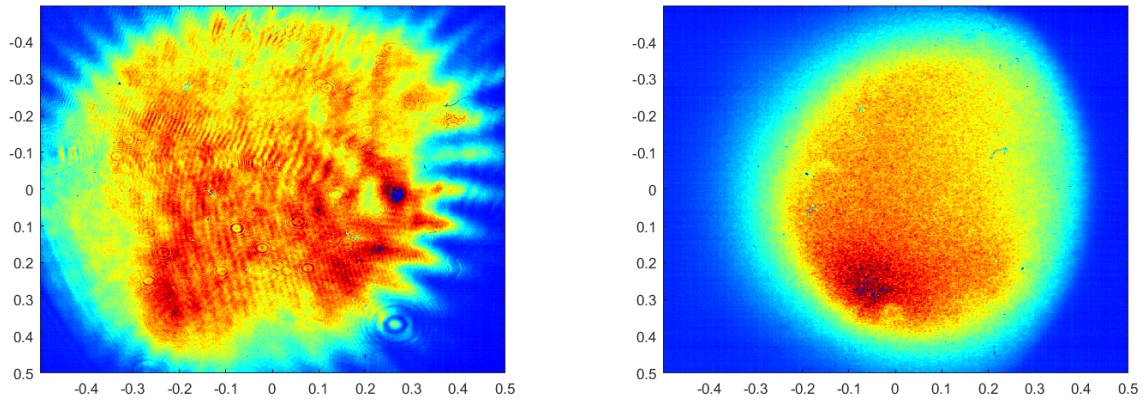


Figure 9.5: Comparison between the spectra measured for supercontinuum generation with a ∼40 mJ pulse energy (red), where an HR mirror was used to remove residual >1 µm light, and the spectrum generated for ∼10 mJ pulse energy, where IR light was not removed (grey). By comparing the two profiles, it is clear that an HR mirror introduces spectral fringes into the supercontinuum profile.

Lastly, the spatial profile of the supercontinuum source was measured and compared to the spatial profile of the input beam. As nonlinear interactions are intensity dependent, often the most intense points across the spatial profile of a laser beam contribute most to these nonlinear effects, and that low intensity distortions in the beam can be spatially filtered. Additionally, at the superfilamentation regime [157], the beam may collapse to a central high density plasma channel within the liquid cell, which acts as a waveguide. The normal filamentation threshold for the zinc chloride solution used in this investigation, at ∼1 µm central wavelength, is approximately 0.91 MW [147], and therefore for an input energy of ∼40 mJ (80 GW), we are well within the

superfilimentation regime. A beam profiler (WinCamD-LCM – 1" CMOS) was used to capture the spatial profile of the laser before the liquid cell (9.6a) and the filtered supercontinuum spatial profile, collimated and propagated a distance of ∼1 m (9.6b). A serrated pattern can be seen at the edges of the input beam, likely due to a spatial apodiser before the final vacuum spatial filter (VSF) in the Nd:Glass flashlamp amplifier beamline (described in chapter 4), which was not fully spatially filtered. Additionally, the beam is down-collimated by a factor ∼5:1 at the output of optical beamline compressor by a 500, -200 mm focal length lens pair, which is sensitive to alignment and can potentially introduce aberrations into the beam profile. The supercontinuum optical probe beam was observed to be well-collimated over >10 m propagation to the multi-terawatt target chamber and showed clear spatial filtering of the input beam, with a pseudo-flat top beam profile with an average point-to-point variation of 1.2% of the mean intensity across the profile.



(a) (b)

Figure 9.6: The measured spatial profiles (WinCamD-LCM) of the a) input λ_0= 1054 nm, ∼80 GW input light and the b) generated supercontinuum, collimated and propagated a distance of ∼1 m. The 'triangular' profile on a) is produced by imperfect spatial filtering in a VSF stage, where a imprint on the spatial apodiser is left on the beam.

9.4 Wavelength Selectable Interferometry

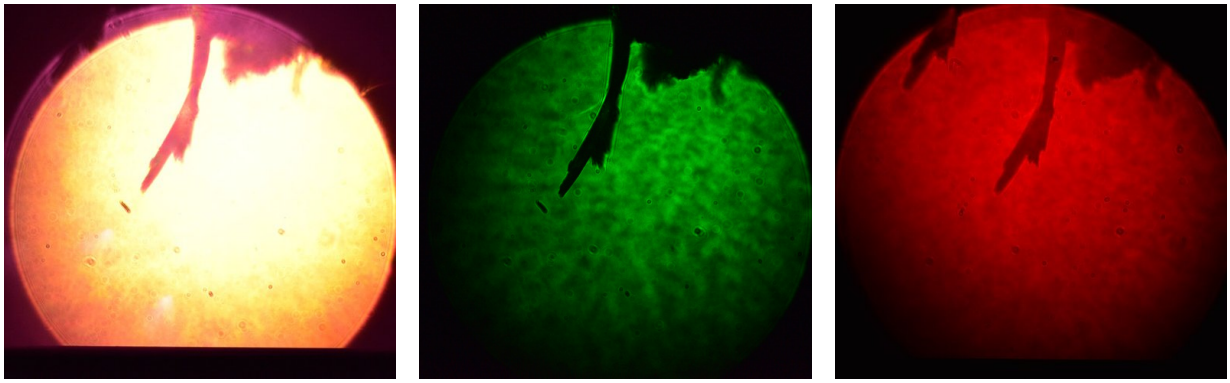
With the supercontinuum source characterised at input energies <60 mJ, the next step was to propagate the supercontinuum optical probe beam through the Cerberus interferometry beamline and assess its viability for on-shot probing of high intensity laser matter interaction experiments. One benefit of a supercontinuum pulse, is that it is generated collinearly with the input beam.

Therefore, the interferometry beamline could be aligned at 'low-power' 10 Hz operation before scaling to higher energies. Whilst filamentation at higher powers was expected to affect the collimation of the optical probe, the divergence of the low-power beam was not seen to be sufficient enough to affect alignment. After initial 10 Hz alignment, fine alignment was completed with the laser in single-shot mode at amplified pulse energies. The D4σ beam width of the optical probe was large with respect to the interferometer's area of interest and therefore shot-to-shot pointing instabilities did not greatly affect the probe image.

A good interferometry source requires enough intensity to outcompete background light from the interaction it is probing as well as high spatial coherence and that can provide high fringe contrast. It must also be 'short' on the timescale of the interaction, this is why typically the second harmonic is used as an optical probe source as it has a pulse duration a factor $\sim \sqrt{2}$ shorter than the main beam. However, group velocity dispersion was a concern with regards to supercontinuum sources, the pulse may be temporally stretched by the medium and become unsuitable for high time resolution optical probing. Previously, the liquid cell supercontinuum pulse duration was measured at approximately 5ps using an optical streak camera with 1 ps time resolution [83]. Additionally, Ho et al [155] measured that for a supercontinuum generated by an 8 ps duration pulse, centered at 530 nm in a 200 mm long CCl_4 liquid cell, that isolated 10 nm bandwidth portions of the SC were shorter than the initial pulse duration; each approximately 6 ps.

This experiment was run concurrently another which used the second harmonic optical probe beam to measure the plasma density around laser-launched thin Al foil flyers [18]. Therefore, realignment of the interferometry beamline to optimise for different interferometric wavelengths or changes to the diameter of the supercontinuum probe beam would have interfered with this other experiment. The Wollaston prism in the interferometer is a wavelength-dependent optic, therefore it should require realignment when switching to a different probe wavelength. The Cerberus laser interferometry beamline was initially designed for an optical probe wavelength of $\sim$527 nm, however, using a red HeNe laser (λ_0 $\sim$632.8 nm) to test the alignment, we still saw the presence of clear fringes in the interferometer camera.

Figure 9.7 shows three optical probe images, captured at the end of the Nomarski interferometer, produced by the supercontinuum optical probe beam. The probe image resolution was found by



(a) (b) (c)

Figure 9.7: Optical probe images captured with the supercontinuum source. These images were taken following a Cerberus laser shot onto 15 µm Al foil, with the target remnants seen in frame. Optical probe images were recorded with a) the full supercontinuum spectrum, b) a 527 nm interference filter and c) a 630 nm interference filter. No fringes were produced on images a) and b) as the interferometer's Wollaston prism rotated out for these shots.

imaging an object of known size, giving a calibration of 0.20 µm/px. These images were taken following a high power laser shot onto 15 µm thick Al foil and therefore show the remnants of the foil target. Optical probe images were recorded with the full supercontinuum spectrum (9.7a), a 527 nm interference filter (9.7b) and a 630 nm interference filter (9.7c).

Figure 9.8 shows a section of figure 9.7c, close to the target chamber centre (TCC). The upper image, which has been contrast-enhanced here for clearer visibility, shows uniform fringes with an average of separation 2.9±0.3 µm, and suggests good spatial coherence in the optical probe at this wavelength. The lower graph on figure 9.8 shows the contrast of the original probe image along a 120 µm lineout from the target surface. Whilst clear fringes are visible here, the contrast is also observed to vary across the spatial profile. Non-uniformity in the beam profile may be due to multiple filaments forming in the liquid cell which propagate as individual beamlets in the probe. Whilst the initial laser pulse is orders of magnitude greater than the critical power, there may be portions of the beam at the temporal or spatial wings of the pulse which do not collapse into the superfilament. Additionally, the low F-number of the focusing optics into the liquid cell may produce a large divergence past focus which could inhibit superfilamentation. This low-level spatial variation in the beam profile could potentially be removed using spatial filtering, such as with a VSF or hollow core fibre spatial filtering technique similar to that described in chapter 5.

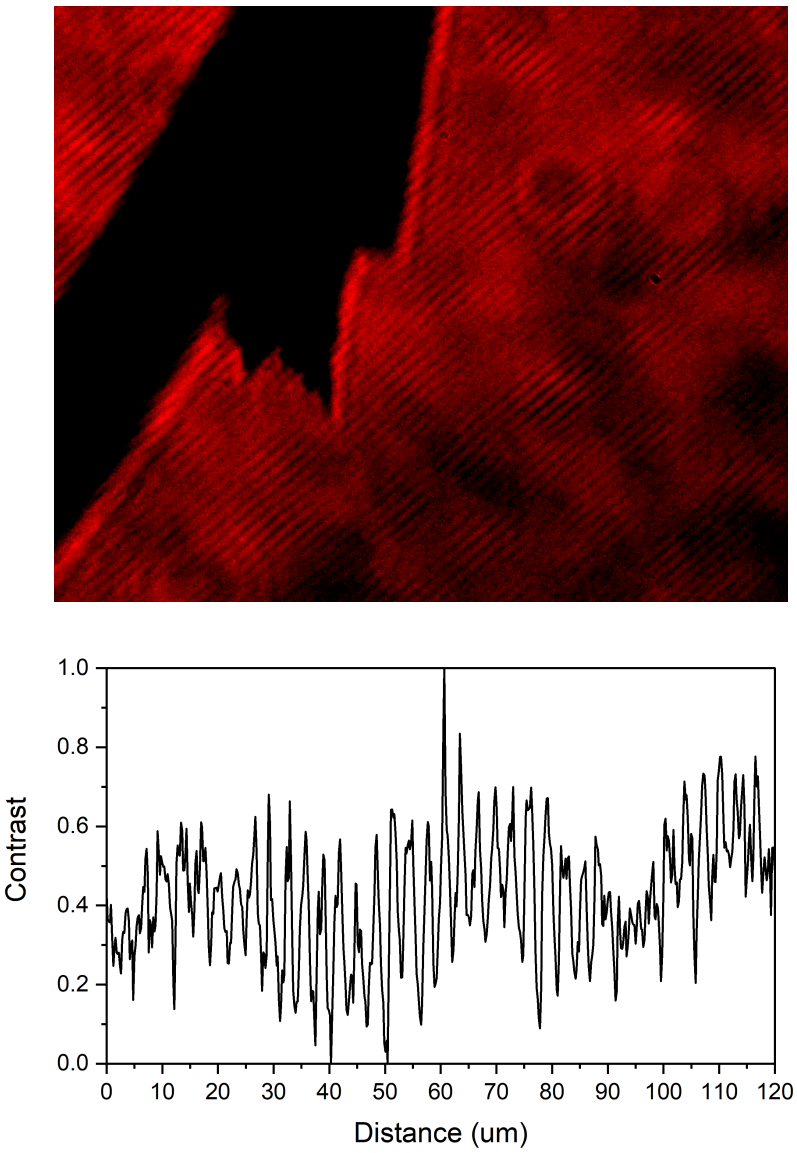


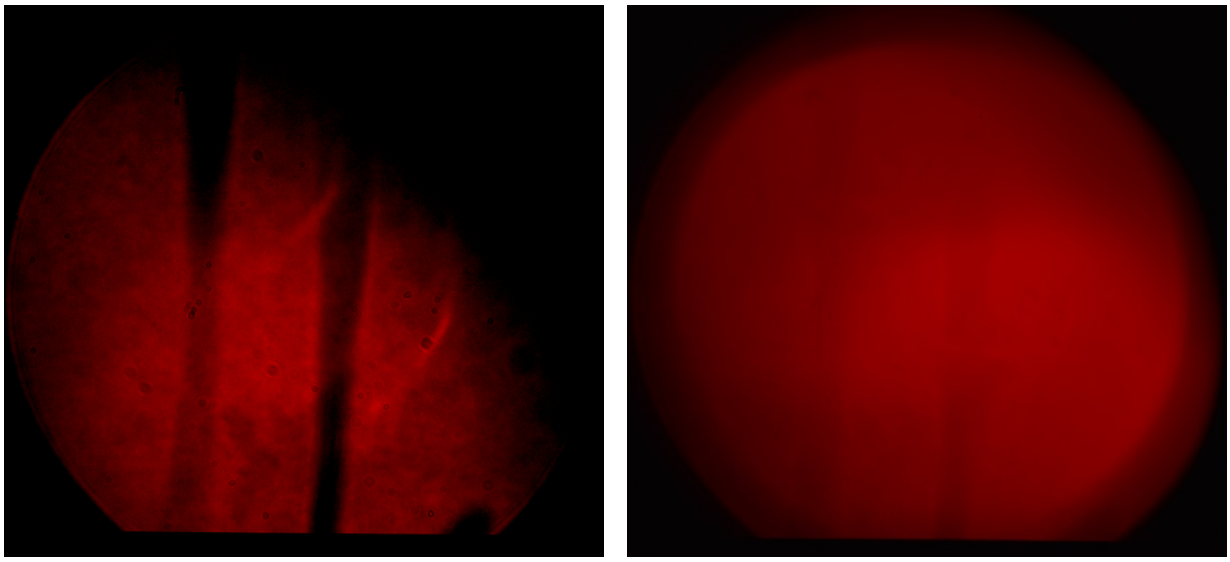
Figure 9.8: Top: contrast enhanced snapshot of figure 9.7c, to clearly show interference fringes. Bottom: the relative contrast of a 120 µm lineout from the target surface from figure 9.7c.

9.4.1 On-Shot Off-Harmonic Interferometry

The off-harmonic probe was employed for a laser-target interaction, with a $\sim 5\times10^{18}$ Wcm^{-2} intensity laser pulse focused onto a 15 µm thick Al foil. The supercontinuum optical probe was propagated through the multi-terawatt target chamber, probing the interaction at approximately the same time as the main pulse arrives at the target. At the front of the interferometer, second harmonic self-emission from the target was rejected using a 532 nm HR mirror, with a previously characterised spectral transmission, and a narrow portion of the transmitted spectrum was

selected around 630 nm using an interference filter.

Figure 9.9 shows two optical probe images, taken before the shot as a background and the image on-shot, to coincide approximately with the arrival of the main pulse. These probe images show that an off-harmonic probe allows us to conclusively filter second harmonic self-emission from laser-plasma interferometry. However, the on-shot probe image is largely drowned out by background optical noise which would prevent clear measurement of the plasma density. This background noise is not well-imaged by the interferometer, suggesting that it is not produced directly in the interaction region. This may therefore be due to probe light scattering off of the target and being reflected back down the interferometry beamline by surfaces inside of the target chamber. There is a metallic flange surrounding the window on the side of the target chamber which the probe enters. During alignment with a seperate red HeNe laser, a small amount of reflection could be seen from this flange due to this laser scattering off of a target at TCC. Therefore, a possible solution to reduce this background noise would be to prevent reflections from inside of the chamber using non-reflective coatings on surfaces which could introduce background noise.



(a) (b)

Figure 9.9: Off-harmonic optical probe images of a Cerberus laser shot onto a 15 µm thick Al foil. a) pre-shot background image, and b) the optical probe image on-shot with a relative timing to approximately coincide with the arrival of the laser pulse.

The self-emission spectrum of the interaction between the Cerberus main pulse and a thin Al foil target was also measured by using a series of lenses to image the centre of the interaction into

an integrating sphere, connected to a spectrometer (Flame-S-VIS-NIR). Figure 9.10 shows the emission spectrum measured, between 200 - 1000 µm, for a $\sim 5 \times 10^{18}$ Wcm^{-2} intensity laser pulse focused onto a 15 µm thick Al foil. The self-emission spectrum shows a clear peak at 527 nm, due to second harmonic self-emission, as well as a small peak above background at 656 nm. It is possible therefore that optical-probing at different wavelengths could decrease the background noise on the interferogram.

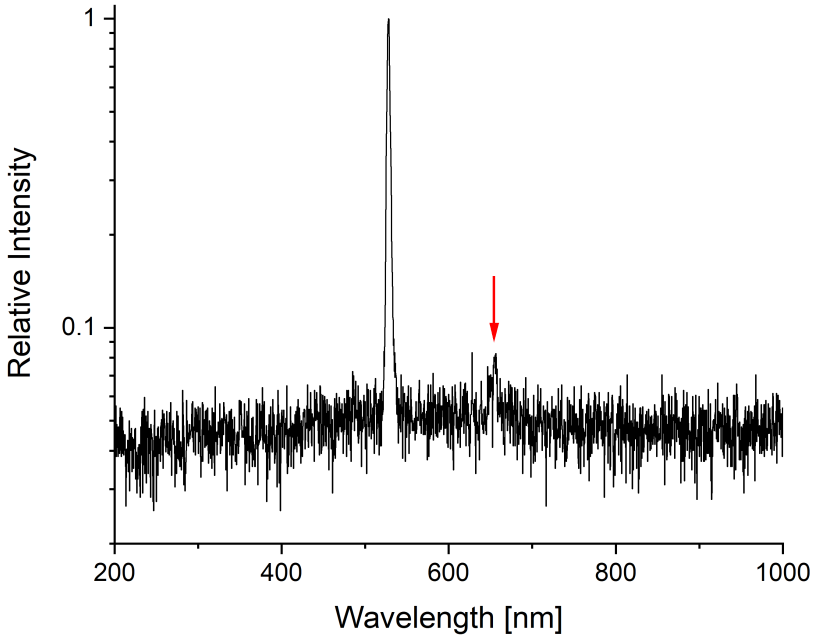


Figure 9.10: Self-emission spectrum measured from a Cerberus shot onto a 15 µm Al foil. A bright self-emission peak is seen at the second harmonic (527 nm) as well as a small peak above background, centered at 656 nm.

9.5 Conclusion and Further Work

In this chapter, we have shown a proof of concept off-harmonic optical probe based on a supercontinuum light source. Whilst we have shown that the supercontinuum source can be used to obtain reasonably high contrast interference fringes, and that it can be employed on-shot for interferometry whilst second harmonic self-emission from the target is effectively filtered, there is ultimately more developmental work required before this technique can become a permanent fixture in the interferometry beamline.

An off-harmonic probe must be able to out-compete background noise. Therefore, future work on this technique would involve scaling the probe to higher intensities. Using the current liquid cell, the supercontinuum pulse energy is expected to saturate at approximately 710 µJ. Increasing the length of the liquid cell could allow for supercontinuum generation over longer lengths, especially when combined with an enhanced filamentaion regime. Subsequently to this investigation, water filamentation on the Cerberus laser system has been investigated by Samuel Eardley, characterising filament formation using the compressed Cerberus laser pulse at wavelengths centered at 1054 nm and 527 nm. Additionally, the optical probe intensity could be increased by compressing the supercontinuum pulse with a simple 2-prism compressor or -GVD material stretcher. A more long term suggestion for further amplification would involve a subsequent broadband OPA stage or Ti:Sapphire amplifier.

For future applications of the interferometry beamline, it may also be reasonable to characterise the spatiotemporal profile of the supercontinuum source. One option that has been discussed is the characterisation of the spectral profile over time by using a simple spectrometer in combination with an optical streak camera. The spectrum of the dispersed pulse could be resolved onto the entrance slit of the optical streak camera, which would provide a spectrogram measurement of the supercontinuum pulse.

Finally, the supercontinuum source presented here also provides an opportunity for multiple-time interferometry. For a broadband optical probe, with a known chirp and temporal profile, 2D time resolved electron plasma density measurement could be taken using a series of narrowband HR coated mirrors which split the optical probe down multiple interferometric beamlines. Multiple-time interferometers have previously been demonstrated on laser plasma interactions, for plasma electron density measurements with a Nomarski-type interferometer at discrete times using optical pulse trains generated via an optical ring cavity [161], as well as line-integrated plasma electron density measurements have also been demonstrated based upon the phase difference of two discrete probing wavelengths [162]. Additionally, a technique called Single-shot supercontinuum spectral interferometry (SSSI) has been used to measure time-resolved dynamics of intense, ultrashort laser interaction with various targets – gases, nanometer-sized clusters, and plasma waveguides [163] as well as the effect on nonlinear phenomena, such as SPM or Kerr-induced cross-phase modulation (XPM), on a reference pulse [164].

Chapter 10

Conclusion

High power laser systems are a sum of their parts. A laser leverages multiple technologies to create and amplify a pulse of light to within certain parameters that are ideally tuned for specific experimental applications. The experimental requirements inform the design of the system, however amplification and pulse-control techniques in high power laser systems can often contribute background noise or pulse artefacts which degrade the temporal intensity profile of the laser. The temporal contrast of a laser system has been shown to significantly affect high intensity laser-matter interactions, including the energy spectrum and distribution of proton beams produced by target normal sheath acceleration (TNSA). There is an international effort to understand and control the contrast of a high power laser and as the landscape of high power lasers moves to ever higher focused intensities, contrast improvement becomes a crucial step in the design of these next generation of these laser systems. Front-end contrast enhancement is particularly important for university-scale laser systems which may lack the required funding or optical table space for more invasive and complex contrast enhancement techniques such as plasma mirrors. Additionally, as the next generation of high power laser systems move to increasingly high repetition rates [11], plasma-based contrast enhancement techniques may not be able to operate at the timescales required for these systems.

In this work, we have used the Cerberus laser system at Imperial College London to investigate sources of temporal intensity contrast degradation, with diagnostics including a FROG for characterising the spectral phase of front end optical parametric amplifiers, and an 'artefact-free' extended third order autocorrelator (X-TOAD), with careful optimisation yielding a maximum

dynamic range 7.8×10^{11}. We have also used a 2D imaging spectrometer to characterise the manifestation of spatial chirp and angular dispersion, two spatiospectral effects which can limit the final compressibilty of a laser pulse, in the two front-end picosecond domain optical parametric amplification (OPA) stages. We have presented a contrast enhancement technique, based upon focusing the ∼180 µJ, 1.2 ps signal pulse output of a two-stage OPA system through 10s of cm lengths of a cylindrical dielectric hollow core fibre (HCF). We have demonstrated high transmission efficiencies, >75%, using 200 µm diameter fibre which approaches that of conventional spatial filters. HCF appears to offer a viable method of removing or minimising spatial chirp from a ps-duration laser pulse as we have demonstrated a significant reduction in both the spatial dispersion and frequency gradient as measured with a 2D imaging spectrometer.

The addition of a discrete artificial prepulse, with a 2.75×10^{-4} relative contrast to the main pulse, may be a good pathway for enhanced charged particle generation from thin foil targets, as well as a potential step towards increasing the proton energy flux for radiography and compact particle accelerators. We have demonstrated that an artificial prepulse, arriving 60 ps before the main (∼10 TW) laser pulse, results in an enhancement in the electron and proton energies generated from a 15 µm thick aluminium foil by a factor of ∼5. Preliminary results thus far suggest that the preplasma expansion from the front surface of the target leads to self-focusing of the main laser pulse and a $\sim 10\times$ intensity boost as a result.

Finally, we have also extended the development of an off-harmonic optical probe based on a supercontinuum source which can better characterise the dynamics of these measurements close to the target surface at wavelengths not obscured by bright self-emission from the laser-plasma interaction region. We have presented results of a supercontinuum generation, with ∼600 nm spectral width, in an 80 mm long liquid cell containing a saturated solution of zinc and potassium salts using an up to ∼60 mJ, 500±50 fs FWHM duration laser pulse centered at $\lambda_0 = 1054$ nm. A portion of the supercontinuum centered at 630 nm was isolated using interference filters and was shown to produce a high contrast interferogram for probing laser-plasma dynamics.

10.1 Further Work: Phase Conjugate OPCPA Beamline

The characteristic 'triangular' pedestal, observed to rise up to 200 ps before the main pulse, to a maximum intensity contrast of $\sim 10^{-4}$, has been largely shown to originate due to the

imaging properties of stretchers such as the commonly used Öffner stretcher. Imaging optics in Martinéz and Öffner stretchers capture scattered light from diffraction gratings and large optics which results in incoherent phase noise which is propagated down the beamline and ultimately remains uncompressed at the end of the system. CPA subsystems which lack these imaging optics capture less scattered light, and a system designed to avoid imaging stretchers in favour of other alternatives such as the Treacy design could have potential to significantly reduce the triangular pedestal.

However, imaging optics in stretchers invert the beam, producing positive group-velocity dispersion (GVD) and therefore positive chirp, compressors such as the Treacy compensate for this with the opposite sign GVD. Without imaging optic CPA subsystems, the beam would not be able to be recompressed once stretched. A phase-conjugate OPCPA scheme could circumvent this limitation and would involve taking the idler from an OPA as the signal for amplification, as the idler inherits the opposite sign chirp to the seed (-ve chirp) it can be recompressed by a positive dispersion grating pair. This allows the beam to be stretched and compressed without need of imaging CPA subsystems that degrade the contrast profile. This principle is demonstrated in the figure below. However, the idler produced from an OPA stage inherits additional chirp and high order phase of the pump in addition to angular dispersion and greater pointing instabilities. In order for a phase-conjugate OPCPA beamline to be implemented well, these issues must be compensated for. Hollow core fibre has been demonstrated to be able to filter both angular dispersion from a beam as well as act as a fixed point for pointing stability enhancement. HCF filtering could thus reduce the impact of these factors as well as increase the robustness of the idler signal for stable operation in a future high-contrast phase-conjugate OPCPA laser system.

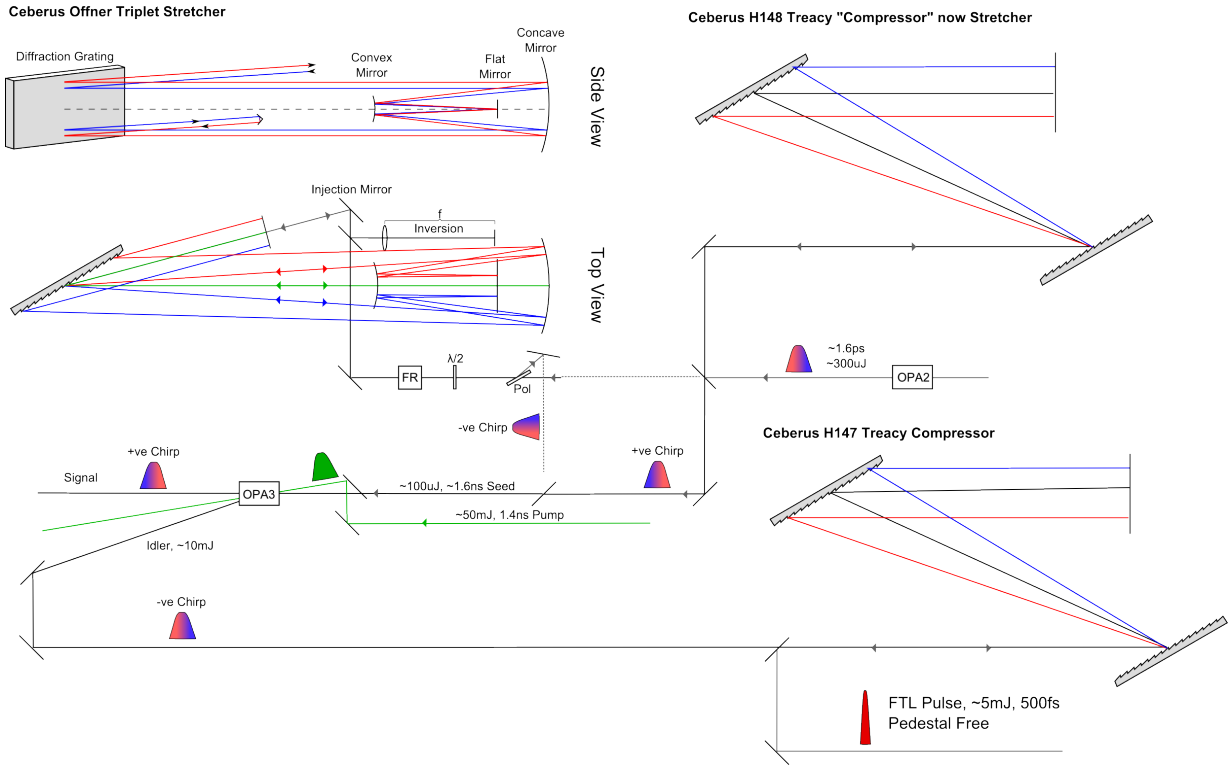


Figure 10.1: Overview of the phase-conjugate OPCPA principle, taking the idler from an OPA as the signal for amplification, as the idler has the opposite sign chirp to the seed (-ve) it can be recompressed by a positive dispersion grating pair. Image credit: Nicholas Stuart [36].

Bibliography

[1] R. Betti and O. A. Hurricane, "Inertial-confinement fusion with lasers," *Nature Physics*, vol. 12, no. 5, pp. 435–448, May 2016, Number: 5 Publisher: Nature Publishing Group, ISSN: 1745-2481. DOI: 10.1038/nphys3736.

[2] B. A. Remington, "High energy density laboratory astrophysics," *Plasma Physics and Controlled Fusion*, vol. 47, no. 5, A191, Apr. 19, 2005, Publisher: IOP Publishing, ISSN: 0741-3335. DOI: 10.1088/0741-3335/47/5A/014.

[3] S. P. D. Mangles, C. D. Murphy, Z. Najmudin, *et al.*, "Monoenergetic beams of relativistic electrons from intense laser–plasma interactions," *Nature*, vol. 431, no. 7008, pp. 535–538, Sep. 2004, Number: 7008 Publisher: Nature Publishing Group, ISSN: 1476-4687. DOI: 10.1038/nature02939.

[4] M. Roth and M. Schollmeier, "Ion acceleration—target normal sheath acceleration," *CERN Yellow Reports*, 231 Pages, Feb. 16, 2016. DOI: 10.5170/cern-2016-001.231.

[5] S. P. Hatchett, C. G. Brown, T. E. Cowan, *et al.*, "Electron, photon, and ion beams from the relativistic interaction of petawatt laser pulses with solid targets," *Physics of Plasmas*, vol. 7, no. 5, pp. 2076–2082, Apr. 19, 2000, ISSN: 1070-664X. DOI: 10.1063/1.874030.

[6] R. Hovden and D. A. Muller, "Electron tomography for functional nanomaterials," *MRS Bulletin*, vol. 45, no. 4, pp. 298–304, Apr. 1, 2020, ISSN: 1938-1425. DOI: 10.1557/mrs.2020.87.

[7] M. Prall, M. Durante, T. Berger, *et al.*, "High-energy proton imaging for biomedical applications," *Scientific Reports*, vol. 6, no. 1, p. 27 651, Jun. 10, 2016, Number: 1 Publisher: Nature Publishing Group, ISSN: 2045-2322. DOI: 10.1038/srep27651.

[8] C. M. Brenner, S. R. Mirfayzi, D. R. Rusby, *et al.*, "Laser-driven x-ray and neutron source development for industrial applications of plasma accelerators," *Plasma Physics and Controlled Fusion*, vol. 58, no. 1, p. 014 039, Nov. 2015, Publisher: IOP Publishing, ISSN: 0741-3335. DOI: 10.1088/0741-3335/58/1/014039.

[9] J. Fuchs, P. Antici, E. d'Humières, *et al.*, "Laser-driven proton scaling laws and new paths towards energy increase," *Nature Physics*, vol. 2, no. 1, pp. 48–54, Jan. 2006, Bandiera_abtest: a Cg_type: Nature Research Journals Number: 1 Primary_atype: Research Publisher: Nature Publishing Group, ISSN: 1745-2481. DOI: 10.1038/nphys199.

[10] C. Danson, D. Hillier, N. Hopps, and D. Neely, "Petawatt class lasers worldwide," *High Power Laser Science and Engineering*, vol. 3, 2015, ISSN: 2095-4719, 2052-3289. DOI: 10.1017/hpl.2014.52.

[11] C. N. Danson, C. Haefner, J. Bromage, *et al.*, "Petawatt and exawatt class lasers worldwide," *High Power Laser Science and Engineering*, vol. 7, 2019, Publisher: Cambridge University Press, ISSN: 2095-4719, 2052-3289. DOI: 10.1017/hpl.2019.36.

[12] McKenna Paul, Lindau Filip, Lundh Olle, Neely David, Persson Anders, and Wahlström Claes-Göran, "High-intensity laser-driven proton acceleration: Influence of pulse contrast," *Philosophical Transactions of the Royal Society A: Mathematical, Physical and Engineering Sciences*, vol. 364, no. 1840, pp. 711–723, Mar. 15, 2006. DOI: 10.1098/rsta.2005.1733.

[13] M. Sharpe and D. Irish, "Stray light in diffraction grating monochromators," *Optica Acta: International Journal of Optics*, vol. 25, no. 9, pp. 861–893, Sep. 1, 1978, ISSN: 0030-3909. DOI: 10.1080/713819858.

[14] N. H. Stuart, D. Bigourd, R. W. Hill, *et al.*, "Direct fluorescence characterisation of a picosecond seeded optical parametric amplifier," *Optics Communications*, vol. 336, pp. 319–325, Feb. 1, 2015, ISSN: 0030-4018. DOI: 10.1016/j.optcom.2014.09.032.

[15] S. Eardley, "Optimising secondary particle and radiation sources in high-intensity laser interaction experiments," Accepted: 2021-07-06T08:02:10Z Publisher: Imperial College London, Ph.D. dissertation, Jan. 2020.

[16] J. Cole, *Interpret*, original-date: 2014-06-09T15:51:12Z, Dec. 29, 2022.

[17] J. J. MacFarlane, I. E. Golovkin, and P. R. Woodruff, "HELIOS-CR – a 1-d radiation-magnetohydrodynamics code with inline atomic kinetics modeling," *Journal of Quantitative Spectroscopy and Radiative Transfer*, Radiative Properties of Hot Dense Matter, vol. 99, no. 1, pp. 381–397, May 1, 2006, ISSN: 0022-4073. DOI: 10.1016/j.jqsrt.2005.05.031.

[18] G. Rowland, "New diagnostic tools for probing collapsing voids driven by hypersonic impact," Accepted: 2022-07-05T11:29:05Z Publisher: Imperial College London, Ph.D. dissertation, Mar. 2022.

[19] T. Robinson, "Laser-plasma interaction experiments using high energy, high contrast OPCPA lasers," Ph.D. dissertation, Imperial College London, Mar. 2018, 211 pp.

[20] D. R. Russell, G. C. Burdiak, J. J. Carroll-Nellenback, *et al.*, "Perpendicular subcritical shock structure in a collisional plasma experiment," *Physical Review Letters*, vol. 129, no. 22, p. 225 001, Nov. 22, 2022, Publisher: American Physical Society. DOI: 10.1103/PhysRevLett.129.225001.

[21] T. H. Maiman, "Stimulated optical radiation in ruby," *Nature*, vol. 187, no. 4736, pp. 493–494, Aug. 1960, Number: 4736 Publisher: Nature Publishing Group, ISSN: 1476-4687. DOI: 10.1038/187493a0.

[22] L. E. Hargrove, R. L. Fork, and M. A. Pollack, "LOCKING OF he–ne LASER MODES INDUCED BY SYNCHRONOUS INTRACAVITY MODULATION," *Applied Physics Letters*, vol. 5, no. 1, pp. 4–5, Jul. 1964, Publisher: American Institute of Physics, ISSN: 0003-6951. DOI: 10.1063/1.1754025.

[23] E. Ippen, C. Shank, and A. Dienes, "Passive mode locking of the cw dye laser," *Applied Physics Letters*, vol. 21, no. 8, pp. 348–350, Oct. 15, 1972, Publisher: American Institute of Physics, ISSN: 0003-6951. DOI: 10.1063/1.1654406.

[24] D. Strickland and G. Mourou, "Compression of amplified chirped optical pulses," *Optics Communications*, vol. 56, no. 3, pp. 219–221, Dec. 1, 1985, ISSN: 0030-4018. DOI: 10.1016/0030-4018(85)90120-8.

[25] B. C. Stuart, M. D. Feit, S. Herman, A. M. Rubenchik, B. W. Shore, and M. D. Perry, "Optical ablation by high-power short-pulse lasers," *Journal of the Optical Society of*

America B, vol. 13, no. 2, p. 459, Feb. 1, 1996, ISSN: 0740-3224, 1520-8540. DOI: 10.1364/JOSAB.13.000459.

[26] J. Kerr, "XLIII. on rotation of the plane of polarization by reflection from the pole of a magnet," *The London, Edinburgh, and Dublin Philosophical Magazine and Journal of Science*, vol. 3, no. 19, pp. 321–343, May 1, 1877, Publisher: Taylor & Francis _eprint: https://doi.org/10.1080/14786447708639245, ISSN: 1941-5982. DOI: 10.1080/14786447708639245.

[27] E. Treacy, "Optical pulse compression with diffraction gratings," *IEEE Journal of Quantum Electronics*, vol. 5, no. 9, pp. 454–458, Sep. 1969, Conference Name: IEEE Journal of Quantum Electronics, ISSN: 1558-1713. DOI: 10.1109/JQE.1969.1076303.

[28] O. Martinez, "3000 times grating compressor with positive group velocity dispersion: Application to fiber compensation in 1.3-1.6 µm region," *IEEE Journal of Quantum Electronics*, vol. 23, no. 1, pp. 59–64, Jan. 1987, ISSN: 0018-9197. DOI: 10.1109/JQE.1987.1073201.

[29] A. Offner, "54 UNIT POWER MAGING CATOPTRIC ANASTIGMAT," p. 8,

[30] G. Cheriaux, B. Walker, L. F. Dimauro, P. Rousseau, F. Salin, and J. P. Chambaret, "Aberration-free stretcher design for ultrashort-pulse amplification," *Optics Letters*, vol. 21, no. 6, p. 414, Mar. 15, 1996, ISSN: 0146-9592, 1539-4794. DOI: 10.1364/OL.21.000414.

[31] G. New, *Introduction to Nonlinear Optics*. Cambridge: Cambridge University Press, 2011, ISBN: 978-0-521-87701-5. DOI: 10.1017/CBO9780511975851.

[32] H. Kiriyama, A. S. Pirozhkov, M. Nishiuchi, *et al.*, "Status and progress of the j-KAREN-p high intensity laser system at QST," *High Energy Density Physics*, vol. 36, p. 100 771, Aug. 1, 2020, ISSN: 1574-1818. DOI: 10.1016/j.hedp.2020.100771.

[33] J. Šulc and H. Jelínková, "5 - solid-state lasers for medical applications," in *Lasers for Medical Applications*, ser. Woodhead Publishing Series in Electronic and Optical Materials, H. Jelínková, Ed., Woodhead Publishing, Jan. 1, 2013, pp. 127–176, ISBN: 978-0-85709-237-3. DOI: 10.1533/9780857097545.2.127.

[34] J. T. Mendonça, J. R. Davies, and M. Eloy, "Proton and neutron sources using terawatt lasers," *Measurement Science and Technology*, vol. 12, no. 11, pp. 1801–1812, Nov. 1, 2001, ISSN: 0957-0233, 1361-6501. DOI: 10.1088/0957-0233/12/11/307.

[35] L. Robson, P. T. Simpson, R. J. Clarke, *et al.*, "Scaling of proton acceleration driven by petawatt-laser–plasma interactions," *Nature Physics*, vol. 3, no. 1, pp. 58–62, Jan. 2007, Bandiera_abtest: a Cg_type: Nature Research Journals Number: 1 Primary_atype: Research Publisher: Nature Publishing Group, ISSN: 1745-2481. DOI: 10.1038/nphys476.

[36] N. Stuart, "Generation of high-contrast, terawatt to petawatt OPCPA laser pulses," Ph.D. dissertation, Imperial College London, Sep. 2016, 199 pp.

[37] N. Stuart, T. Robinson, D. Hillier, *et al.*, "Comparative study on the temporal contrast of femtosecond mode-locked laser oscillators," *Optics Letters*, vol. 41, no. 14, p. 3221, Jul. 15, 2016, ISSN: 0146-9592, 1539-4794. DOI: 10.1364/OL.41.003221.

[38] J. Peebles, C. McGuffey, C. M. Krauland, *et al.*, "Impact of pre-plasma on fast electron generation and transport from short pulse, high intensity lasers," *Nuclear Fusion*, vol. 56, no. 1, p. 016 007, Dec. 2015, Publisher: IOP Publishing, ISSN: 0029-5515. DOI: 10.1088/0029-5515/56/1/016007.

[39] N. V. Didenko, A. V. Konyashchenko, A. P. Lutsenko, and S. Y. Tenyakov, "Contrast degradation in a chirped-pulse amplifier due to generation of prepulses by postpulses," *Optics Express*, vol. 16, no. 5, pp. 3178–3190, Mar. 3, 2008, Publisher: Optical Society of America, ISSN: 1094-4087. DOI: 10.1364/OE.16.003178.

[40] A. Kon, M. Nishiuchi, H. Kiriyama, *et al.*, "Single-shot measurement of post-pulse-generated pre-pulse in high-power laser systems," *Crystals*, vol. 10, no. 8, p. 657, Aug. 2020, Number: 8 Publisher: Multidisciplinary Digital Publishing Institute. DOI: 10.3390/cryst10080657.

[41] C. Hooker, Y. Tang, O. Chekhlov, *et al.*, "Improving coherent contrast of petawatt laser pulses," *Optics Express*, vol. 19, no. 3, pp. 2193–2203, Jan. 31, 2011, Publisher: Optical Society of America, ISSN: 1094-4087. DOI: 10.1364/OE.19.002193.

[42] D. N. Papadopoulos, P. Ramirez, K. Genevrier, *et al.*, "High-contrast 10 fs OPCPA-based front end for multi-PW laser chains," *Optics Letters*, vol. 42, no. 18, pp. 3530–3533, Sep. 15, 2017, ISSN: 1539-4794. DOI: 10.1364/OL.42.003530.

[43] T. Oksenhendler, P. Bizouard, O. Albert, S. Bock, and U. Schramm, "High dynamic, high resolution and wide range single shot temporal pulse contrast measurement," *Optics*

Express, vol. 25, no. 11, pp. 12 588–12 600, May 29, 2017, ISSN: 1094-4087. DOI: 10.1364/OE.25.012588.

[44] V. A. Schanz, V. A. Schanz, M. Roth, M. Roth, V. Bagnoud, and V. Bagnoud, "Picosecond contrast degradation by surface imperfections in chirped-pulse-amplification stretchers," *JOSA A*, vol. 36, no. 10, pp. 1735–1742, Oct. 1, 2019, Publisher: Optical Society of America, ISSN: 1520-8532. DOI: 10.1364/JOSAA.36.001735.

[45] C. Dorrer and J. Bromage, "Impact of high-frequency spectral phase modulation on the temporal profile of short optical pulses," *Optics Express*, vol. 16, no. 5, pp. 3058–3068, Mar. 3, 2008, Publisher: Optical Society of America, ISSN: 1094-4087. DOI: 10.1364/OE.16.003058.

[46] Y. Tang, D. Egan, C. Hooker, *et al.*, "Quantitatively evaluating impact of large optics in the stretcher on compressed pulse contrast (conference presentation)," in *Short-pulse High-energy Lasers and Ultrafast Optical Technologies*, vol. 11034, International Society for Optics and Photonics, May 13, 2019, 110340E. DOI: 10.1117/12.2523003.

[47] M. D. Perry, T. Ditmire, and B. C. Stuart, "Self-phase modulation in chirped-pulse amplification," *Optics Letters*, vol. 19, no. 24, pp. 2149–2151, Dec. 15, 1994, Publisher: Optical Society of America, ISSN: 1539-4794. DOI: 10.1364/OL.19.002149.

[48] G. Pretzler, A. Kasper, and K. J. Witte, "Angular chirp and tilted light pulses in CPA lasers," *Applied Physics B*, vol. 70, no. 1, pp. 1–9, Jan. 1, 2000, Company: Springer Distributor: Springer Institution: Springer Label: Springer Number: 1 Publisher: Springer-Verlag, ISSN: 1432-0649. DOI: 10.1007/s003400050001.

[49] K. Osvay, A. P. Kovács, G. Kurdi, *et al.*, "Measurement of non-compensated angular dispersion and the subsequent temporal lengthening of femtosecond pulses in a CPA laser," *Optics Communications*, vol. 248, no. 1, pp. 201–209, Apr. 1, 2005, ISSN: 0030-4018. DOI: 10.1016/j.optcom.2004.11.099.

[50] Z. Sacks, G. Mourou, and R. Danielius, "Adjusting pulse-front tilt and pulse duration by use of a single-shot autocorrelator," *Optics Letters*, vol. 26, no. 7, p. 462, Apr. 1, 2001, ISSN: 0146-9592, 1539-4794. DOI: 10.1364/OL.26.000462.

[51] C. Fiorini, C. Sauteret, C. Rouyer, N. Blanchot, S. Seznec, and A. Migus, "Temporal aberrations due to misalignments of a stretcher-compressor system and compensation," *IEEE Journal of Quantum Electronics*, vol. 30, no. 7, pp. 1662–1670, Jul. 1994, Conference Name: IEEE Journal of Quantum Electronics, ISSN: 1558-1713. DOI: 10.1109/3.299499.

[52] L. Ionel, "Spatio-temporal analysis of the distorted chirped pulse amplification laser beam in focus," *Optoelectronics and Advanced Materials - Rapid Communications*, vol. 7, pp. 481–484, July-August 2013 Jul. 11, 2013, Publisher: OAM-RC, ISSN: 1842-6573.

[53] S. Akturk, M. Kimmel, P. O'Shea, and R. Trebino, "Measuring spatial chirp in ultrashort pulses using single-shot frequency-resolved optical gating," *Optics Express*, vol. 11, no. 1, pp. 68–78, Jan. 13, 2003, ISSN: 1094-4087. DOI: 10.1364/OE.11.000068.

[54] A. Zaukevičius, V. Jukna, R. Antipenkov, *et al.*, "Manifestation of spatial chirp in femtosecond noncollinear optical parametric chirped-pulse amplifier," *JOSA B*, vol. 28, no. 12, pp. 2902–2908, Dec. 1, 2011, ISSN: 1520-8540. DOI: 10.1364/JOSAB.28.002902.

[55] L. Ranc, L. Ranc, L. Ranc, *et al.*, "Improvement in the temporal contrast in the tens of ps range of the multi-PW apollon laser front-end," *Optics Letters*, vol. 45, no. 16, pp. 4599–4602, Aug. 15, 2020, Publisher: Optical Society of America, ISSN: 1539-4794. DOI: 10.1364/OL.401272.

[56] G. J. Dunning and M. L. Minden, "Scattering from high efficiency diffraction gratings," *Applied Optics*, vol. 19, no. 14, pp. 2419–2425, Jul. 15, 1980, ISSN: 2155-3165. DOI: 10.1364/AO.19.002419.

[57] S. Roeder, Y. Zobus, C. Brabetz, and V. Bagnoud, "How the laser beam size conditions the temporal contrast in pulse stretchers of chirped-pulse amplification lasers," *High Power Laser Science and Engineering*, vol. 10, e34, 2022, Publisher: Cambridge University Press, ISSN: 2095-4719, 2052-3289. DOI: 10.1017/hpl.2022.18.

[58] M. Nantel, J. Itatani, A.-C. Tien, *et al.*, "Temporal contrast in ti:sapphire lasers, characterization and control," *IEEE Journal of Selected Topics in Quantum Electronics*, vol. 4, no. 2, pp. 449–458, Mar. 1998, Conference Name: IEEE Journal of Selected Topics in Quantum Electronics, ISSN: 1558-4542. DOI: 10.1109/2944.686755.

[59] N. Minkovski, S. M. Saltiel, G. I. Petrov, O. Albert, and J. Etchepare, "Polarization rotation induced by cascaded third-order processes," *Optics Letters*, vol. 27, no. 22, pp. 2025–2027, Nov. 15, 2002, Publisher: Optical Society of America, ISSN: 1539-4794. DOI: 10.1364/OL.27.002025.

[60] F. Albert, A. G. R. Thomas, S. P. D. Mangles, *et al.*, "Laser wakefield accelerator based light sources: Potential applications and requirements," *Plasma Physics and Controlled Fusion*, vol. 56, no. 8, p. 084 015, Aug. 1, 2014, ISSN: 0741-3335, 1361-6587. DOI: 10.1088/0741-3335/56/8/084015.

[61] C. Thaury, F. Quéré, J.-P. Geindre, *et al.*, "Plasma mirrors for ultrahigh-intensity optics," *Nature Physics*, vol. 3, no. 6, pp. 424–429, Jun. 2007, Number: 6 Publisher: Nature Publishing Group, ISSN: 1745-2481. DOI: 10.1038/nphys595.

[62] V. Chvykov, P. Rousseau, S. Reed, G. Kalinchenko, and V. Yanovsky, "Generation of 10^{11} contrast 50 TW laser pulses," *Optics Letters*, vol. 31, no. 10, pp. 1456–1458, May 15, 2006, Publisher: Optical Society of America, ISSN: 1539-4794. DOI: 10.1364/OL.31.001456.

[63] "Photodiodes." (), [Online]. Available: https://www.thorlabs.com/newgrouppage9.cfm?objectgroup_id=285 (visited on 07/02/2021).

[64] J. A. Armstrong, "Measurement of picosecond laser pulse widths," *Applied Physics Letters*, vol. 10, no. 1, pp. 16–18, Jan. 1, 1967, Publisher: American Institute of Physics, ISSN: 0003-6951. DOI: 10.1063/1.1754787.

[65] R. Trebino and E. Zeek, "The autocorrelation, the spectrum, and phase retrieval," in *Frequency-Resolved Optical Gating: The Measurement of Ultrashort Laser Pulses*, R. Trebino, Ed., Boston, MA: Springer US, 2000, pp. 61–99, ISBN: 978-1-4615-1181-6. DOI: 10.1007/978-1-4615-1181-6_4.

[66] R. Trebino, "FROG beam geometries," in *Frequency-Resolved Optical Gating: The Measurement of Ultrashort Laser Pulses*, R. Trebino, Ed., Boston, MA: Springer US, 2000, pp. 117–139, ISBN: 978-1-4615-1181-6. DOI: 10.1007/978-1-4615-1181-6_6.

[67] R. Trebino, *Frequency-Resolved Optical Gating: The Measurement of Ultrashort Laser Pulses*. Boston, MA: Springer US, 2000, ISBN: 978-1-4613-5432-1 978-1-4615-1181-6. DOI: 10.1007/978-1-4615-1181-6.

[68] C. Bourassin-Bouchet and M.-E. Couprie, "Partially coherent ultrafast spectrography," *Nature Communications*, vol. 6, no. 1, p. 6465, Mar. 6, 2015, ISSN: 2041-1723. DOI: 10.1038/ncomms7465.

[69] P. O'Shea, M. Kimmel, X. Gu, and R. Trebino, "Highly simplified device for ultrashort-pulse measurement," *Optics Letters*, vol. 26, no. 12, pp. 932–934, Jun. 15, 2001, Publisher: Optica Publishing Group, ISSN: 1539-4794. DOI: 10.1364/OL.26.000932.

[70] C. Iaconis and I. Walmsley, "Self-referencing spectral interferometry for measuring ultrashort optical pulses," *IEEE Journal of Quantum Electronics*, vol. 35, no. 4, pp. 501–509, Apr. 1999, Conference Name: IEEE Journal of Quantum Electronics, ISSN: 1558-1713. DOI: 10.1109/3.753654.

[71] R. Trebino, "FROG," in *Frequency-Resolved Optical Gating: The Measurement of Ultrashort Laser Pulses*, R. Trebino, Ed., Boston, MA: Springer US, 2000, pp. 101–115, ISBN: 978-1-4615-1181-6. DOI: 10.1007/978-1-4615-1181-6_5.

[72] M. J. V. Streeter, "Ultrafast dynamics of relativistic laser plasma interactions," Ph.D. dissertation, Imperial College London, Sep. 2013.

[73] D. Kane, "Real-time measurement of ultrashort laser pulses using principal component generalized projections," *IEEE Journal of Selected Topics in Quantum Electronics*, vol. 4, no. 2, pp. 278–284, Apr. 1998, ISSN: 1077260X. DOI: 10.1109/2944.686733.

[74] S. Luan, M. H. R. Hutchinson, R. A. Smith, and F. Zhou, "High dynamic range third-order correlation measurement of picosecond laser pulse shapes," *Measurement Science and Technology*, vol. 4, no. 12, pp. 1426–1429, Dec. 1993, Publisher: IOP Publishing, ISSN: 0957-0233. DOI: 10.1088/0957-0233/4/12/018.

[75] A. Jullien, J.-P. Rousseau, B. Mercier, *et al.*, "Highly efficient nonlinear filter for femtosecond pulse contrast enhancement and pulse shortening," *Optics Letters*, vol. 33, no. 20, pp. 2353–2355, Oct. 15, 2008, Publisher: Optica Publishing Group, ISSN: 1539-4794. DOI: 10.1364/OL.33.002353.

[76] L. P. Ramirez, D. N. Papadopoulos, A. Pellegrina, *et al.*, "Efficient cross polarized wave generation for compact, energy-scalable, ultrashort laser sources," *Optics Express*, vol. 19,

no. 1, pp. 93–98, Jan. 3, 2011, Publisher: Optical Society of America, ISSN: 1094-4087. DOI: 10.1364/OE.19.000093.

[77] M. Querry, "Optical constants of minerals and other materials from the millimeter to the ultraviolet," CHEMICAL RESEARCH DEVELOPMENT AND ENGINEERING CENTER ABERDEEN PROVING GROUNDMD, Nov. 1, 1987, Section: Technical Reports.

[78] I. H. Malitson, "Interspecimen comparison of the refractive index of fused silica*,†," *JOSA*, vol. 55, no. 10, pp. 1205–1209, Oct. 1, 1965, Publisher: Optica Publishing Group. DOI: 10.1364/JOSA.55.001205.

[79] L. Bergé, C. Gouedard, J. Schjødt-Eriksen, and H. Ward, "Filamentation patterns in kerr media vs. beam shape robustness, nonlinear saturation and polarization states," *Physica D-nonlinear Phenomena - PHYSICA D*, vol. 176, pp. 181–211, Mar. 1, 2003. DOI: 10.1016/S0167-2789(02)00740-6.

[80] S. V. Lebedev, D. J. Ampleford, S. N. Bland, *et al.*, "Implosion dynamics of wire array z-pinches: Experiments at imperial college," *Nuclear Fusion*, vol. 44, no. 12, S215–S220, Nov. 2004, Publisher: IOP Publishing, ISSN: 0029-5515. DOI: 10.1088/0029-5515/44/12/S12.

[81] S. Patankar, "High-power laser systems for driving and probing high energy density physics experiments," Ph.D. dissertation, Imperial College London, 2013.

[82] M. Mason, "A sub-60 fs titanium sapphire chirped pulse amplification system," Ph.D. dissertation, Imperial College London, 2000.

[83] S. Patankar, E. T. Gumbrell, T. S. Robinson, *et al.*, "Absolute calibration of optical streak cameras on picosecond time scales using supercontinuum generation," *Applied Optics*, vol. 56, no. 24, pp. 6982–6987, Aug. 20, 2017, Publisher: Optica Publishing Group, ISSN: 2155-3165. DOI: 10.1364/AO.56.006982.

[84] I. N. Ross, P. Matousek, G. H. C. New, and K. Osvay, "Analysis and optimization of optical parametric chirped pulse amplification," *Journal of the Optical Society of America B*, vol. 19, no. 12, p. 2945, Dec. 2, 2002, ISSN: 0740-3224, 1520-8540. DOI: 10.1364/JOSAB.19.002945.

[85] D. Bigourd, S. Patankar, S. I. Olsson Robbie, *et al.*, "Spectral enhancement in optical parametric amplifiers in the saturated regime," *Applied Physics B*, vol. 113, no. 4, pp. 627–633, Dec. 1, 2013, ISSN: 1432-0649. DOI: 10.1007/s00340-013-5519-x.

[86] A. Offner, "Unit power imaging catoptric anastigmat," U.S. Patent 3748015A, Jul. 24, 1973.

[87] G. Figueira and M. Fernandes, "Spatio-temporal distortions and propagation of wavefront-aberrated beams in grating pairs," *AIP Conference Proceedings*, vol. 1228, no. 1, pp. 150–158, Apr. 16, 2010, Publisher: American Institute of Physics, ISSN: 0094-243X. DOI: 10.1063/1.3426046.

[88] B. Webb, M. J. Guardalben, C. Dorrer, S. Bucht, and J. Bromage, "Simulation of grating compressor misalignment tolerances and mitigation strategies for chirped-pulse–amplification systems of varying bandwidths and beam sizes," *Applied Optics*, vol. 58, no. 2, p. 234, Jan. 10, 2019, ISSN: 1559-128X, 2155-3165. DOI: 10.1364/AO.58.000234.

[89] "Dazzler - Ultrafast pulse shaper - Fastlite." (), [Online]. Available: https://fastlite.com/produits/dazzler-ultrafast-pulse-shaper/ (visited on 03/13/2023).

[90] A. Jullien, O. Albert, F. Burgy, *et al.*, "10^-10 temporal contrast for femtosecond ultraintense lasers by cross-polarized wave generation," *Optics Letters*, vol. 30, no. 8, pp. 920–922, Apr. 15, 2005, Publisher: Optical Society of America, ISSN: 1539-4794. DOI: 10.1364/OL.30.000920.

[91] H. Yan-Lan, Z. Hao-Bin, T. Ji-Chun, *et al.*, "Two-dimensional non-spatial filtering based on holographic bragg gratings," *Chinese Physics B*, vol. 19, no. 7, p. 074 215, Jul. 2010, ISSN: 1674-1056. DOI: 10.1088/1674-1056/19/7/074215.

[92] D. Bigourd, P. Morin, J. Dubertrand, *et al.*, "Parametric gain shaping from a structured pump pulse," *IEEE Photonics Technology Letters*, vol. 31, no. 3, pp. 214–217, Feb. 2019, ISSN: 1041-1135. DOI: 10.1109/LPT.2018.2888731.

[93] M. Nisoli, S. De Silvestri, and O. Svelto, "Generation of high energy 10 fs pulses by a new pulse compression technique," *Applied Physics Letters*, vol. 68, no. 20, pp. 2793–2795, May 13, 1996, ISSN: 0003-6951, 1077-3118. DOI: 10.1063/1.116609.

[94] S. Hädrich, M. Kienel, M. Müller, *et al.*, "Energetic sub-2-cycle laser with 216 w average power," *Optics Letters*, vol. 41, no. 18, pp. 4332–4335, Sep. 15, 2016, Publisher: Optica Publishing Group, ISSN: 1539-4794. DOI: 10.1364/OL.41.004332.

[95] G. Fan, G. Fan, P. A. Carpeggiani, *et al.*, "70 mJ nonlinear compression and scaling route for an yb amplifier using large-core hollow fibers," *Optics Letters*, vol. 46, no. 4, pp. 896–899, Feb. 15, 2021, Publisher: Optica Publishing Group, ISSN: 1539-4794. DOI: 10.1364/OL.412296.

[96] O. H. Heckl, C. R. E. Baer, C. Kränkel, *et al.*, "High harmonic generation in a gas-filled hollow-core photonic crystal fiber," *Applied Physics B*, vol. 97, no. 2, p. 369, Oct. 14, 2009, ISSN: 1432-0649. DOI: 10.1007/s00340-009-3771-x.

[97] J. C. Travers, T. F. Grigorova, C. Brahms, and F. Belli, "High-energy pulse self-compression and ultraviolet generation through soliton dynamics in hollow capillary fibres," *Nature Photonics*, vol. 13, no. 8, pp. 547–554, Aug. 2019, ISSN: 1749-4893. DOI: 10.1038/s41566-019-0416-4.

[98] T. Miura, F. Koyama, Y. Aoki, A. Matsutani, and K. Iga, "Hollow optical waveguide for temperature-insensitive photonic integrated circuits," *Japanese Journal of Applied Physics*, vol. 40, no. 7, p. L688, Jul. 2001, Publisher: IOP Publishing, ISSN: 1347-4065. DOI: 10.1143/JJAP.40.L688.

[99] E. A. J. Marcatili and R. A. Schmeltzer, "Hollow metallic and dielectric waveguides for long distance optical transmission and lasers," *The Bell System Technical Journal*, vol. 43, no. 4, pp. 1783–1809, Jul. 1964, ISSN: 0005-8580. DOI: 10.1002/j.1538-7305.1964.tb04108.x.

[100] F. Poletti, N. V. Wheeler, M. N. Petrovich, *et al.*, "Towards high-capacity fibre-optic communications at the speed of light in vacuum," *Nature Photonics*, vol. 7, no. 4, pp. 279–284, Apr. 2013, Number: 4 Publisher: Nature Publishing Group, ISSN: 1749-4893. DOI: 10.1038/nphoton.2013.45.

[101] S. John, "Strong localization of photons in certain disordered dielectric superlattices," *Physical Review Letters*, vol. 58, no. 23, pp. 2486–2489, Jun. 8, 1987, Publisher: American Physical Society. DOI: 10.1103/PhysRevLett.58.2486.

[102] E. Yablonovitch, "Inhibited spontaneous emission in solid-state physics and electronics," *Physical Review Letters*, vol. 58, no. 20, pp. 2059–2062, May 18, 1987, Publisher: American Physical Society. DOI: 10.1103/PhysRevLett.58.2059.

[103] P. Yeh and A. Yariv, "Bragg reflection waveguides," *Optics Communications*, vol. 19, no. 3, pp. 427–430, Dec. 1, 1976, ISSN: 0030-4018. DOI: 10.1016/0030-4018(76)90115-2.

[104] T. Hidaka, T. Morikawa, and J. Shimada, "Hollow-core oxide-glass cladding optical fibers for middle-infrared region," *Journal of Applied Physics*, vol. 52, no. 7, pp. 4467–4471, Jul. 1981, ISSN: 0021-8979, 1089-7550. DOI: 10.1063/1.329373.

[105] J. J. Degnan, "Waveguide laser mode patterns in the near and far field," *Applied Optics*, vol. 12, no. 5, pp. 1026–1030, May 1, 1973, Publisher: Optical Society of America, ISSN: 2155-3165. DOI: 10.1364/AO.12.001026.

[106] B. Mahieu, D. Gauthier, M. Perdrix, *et al.*, "Spatial quality improvement of a ti:sapphire laser beam by modal filtering," *Applied Physics B*, vol. 118, no. 1, pp. 47–60, Jan. 2015, ISSN: 0946-2171, 1432-0649. DOI: 10.1007/s00340-014-5953-4.

[107] "LUCA," SLIC : Saclay Laser-matter Interaction Center. (), [Online]. Available: https://iramis.cea.fr/slic/LUCA.php (visited on 03/13/2023).

[108] Y. Gao, J. Sun, G. Chen, and C. Sima, "Demonstration of simultaneous mode conversion and demultiplexing for mode and wavelength division multiplexing systems based on tilted few-mode fiber bragg gratings," *Optics Express*, vol. 23, no. 8, p. 9959, Apr. 20, 2015, ISSN: 1094-4087. DOI: 10.1364/OE.23.009959.

[109] G. Cirmi, G. Cirmi, G. Cirmi, *et al.*, "Novel method for the angular chirp compensation of passively CEP-stable few-cycle pulses," *Optics Express*, vol. 28, no. 3, pp. 3171–3178, Feb. 3, 2020, Publisher: Optical Society of America, ISSN: 1094-4087. DOI: 10.1364/OE.384290.

[110] J. Hu, X. Wang, X. Liu, *et al.*, "Angular dispersion compensation for ultra-broadband pulses by using a cascaded prism and hollow-core fiber configuration," *Optics Express*, vol. 30, no. 21, pp. 37 293–37 302, Oct. 10, 2022, Publisher: Optica Publishing Group, ISSN: 1094-4087. DOI: 10.1364/OE.470545.

[111] K. F. Mak, M. Seidel, O. Pronin, *et al.*, "Compressing uj-level pulses from 250 fs to sub-10 fs at 38-mhz repetition rate using two gas-filled hollow-core photonic crystal fiber stages," *Optics Letters*, vol. 40, no. 7, pp. 1238–1241, Apr. 1, 2015, Publisher: Optica Publishing Group, ISSN: 1539-4794. DOI: 10.1364/OL.40.001238.

[112] S. Prahl, *Laserbeamsize: ISO 11146 calculation of laser beam center, diameter, and m^2*, version 1.9.4.

[113] S. Akturk, X. Gu, E. Zeek, and R. Trebino, "Pulse-front tilt caused by spatial and temporal chirp," *Optics Express*, vol. 12, no. 19, pp. 4399–4410, Sep. 20, 2004, ISSN: 1094-4087. DOI: 10.1364/OPEX.12.004399.

[114] X. Gu, S. Akturk, and R. Trebino, "Spatial chirp in ultrafast optics," *Optics Communications*, vol. 242, no. 4, pp. 599–604, Dec. 2004, ISSN: 00304018. DOI: 10.1016/j.optcom.2004.09.004.

[115] C. Tralie and E. Dempsey, *Exact, parallelizable dynamic time warping alignment with linear memory*, Aug. 4, 2020. DOI: 10.48550/arXiv.2008.02734. arXiv: 2008.02734[cs, eess].

[116] "Distance between signals using dynamic time warping - MATLAB dtw - MathWorks united kingdom." (), [Online]. Available: https://uk.mathworks.com/help/signal/ref/dtw.html (visited on 03/14/2023).

[117] B. Debord, F. Amrani, L. Vincetti, F. Gérôme, and F. Benabid, "Hollow-core fiber technology: The rising of "gas photonics"," *Fibers*, vol. 7, no. 2, p. 16, Feb. 2019, Number: 2 Publisher: Multidisciplinary Digital Publishing Institute. DOI: 10.3390/fib7020016.

[118] J. Schwarz, P. Rambo, M. Kimmel, and B. Atherton, "Measurement of nonlinear refractive index and ionization rates in air using a wavefront sensor," *Optics Express*, vol. 20, no. 8, pp. 8791–8803, Apr. 9, 2012, Publisher: Optica Publishing Group, ISSN: 1094-4087. DOI: 10.1364/OE.20.008791.

[119] A. Higginson, R. J. Gray, M. King, *et al.*, "Near-100 MeV protons via a laser-driven transparency-enhanced hybrid acceleration scheme," *Nature Communications*, vol. 9, no. 1, p. 724, Feb. 20, 2018, Number: 1 Publisher: Nature Publishing Group, ISSN: 2041-1723. DOI: 10.1038/s41467-018-03063-9.

[120] A. J. Mackinnon, M. Borghesi, S. Hatchett, *et al.*, "Effect of plasma scale length on multi-MeV proton production by intense laser pulses," *Physical Review Letters*, vol. 86, no. 9, pp. 1769–1772, Feb. 26, 2001, Publisher: American Physical Society. DOI: 10.1103/PhysRevLett.86.1769.

[121] K. Ogura, M. Nishiuchi, A. S. Pirozhkov, *et al.*, "Proton acceleration to 40 MeV using a high intensity, high contrast optical parametric chirped-pulse amplification/ti:sapphire hybrid laser system," *Optics Letters*, vol. 37, no. 14, pp. 2868–2870, Jul. 15, 2012, Publisher: Optical Society of America, ISSN: 1539-4794. DOI: 10.1364/OL.37.002868.

[122] T. Utsumi, K. Matsukado, H. Daido, T. Esirkepov, and S. Bulanov, "Numerical simulation of melting and evaporation of a cold foil target irradiated by a pre-pulse," *Applied Physics A*, vol. 79, no. 4, pp. 1185–1187, Sep. 1, 2004, ISSN: 1432-0630. DOI: 10.1007/s00339-004-2700-4.

[123] E. Lefebvre and G. Bonnaud, "Nonlinear electron heating in ultrahigh-intensity-laser–plasma interaction," *Physical Review E*, vol. 55, no. 1, pp. 1011–1014, Jan. 1, 1997, Publisher: American Physical Society. DOI: 10.1103/PhysRevE.55.1011.

[124] T. Z. Esirkepov, J. K. Koga, A. Sunahara, *et al.*, "Prepulse and amplified spontaneous emission effects on the interaction of a petawatt class laser with thin solid targets," *Nuclear Instruments and Methods in Physics Research Section A: Accelerators, Spectrometers, Detectors and Associated Equipment*, vol. 745, pp. 150–163, May 1, 2014, ISSN: 0168-9002. DOI: 10.1016/j.nima.2014.01.056.

[125] S. B. Giltrap, "Optically levitated targets as a source for high brightness x-rays and a platform for mass-limited laser-interaction experiments," Ph.D. dissertation, Imperial College London, 2017, 251 pp.

[126] A. J. Harvey-Thompson, S. V. Lebedev, S. Patankar, *et al.*, "Optical thomson scattering measurements of plasma parameters in the ablation stage of wire array z pinches," *Physical Review Letters*, vol. 108, no. 14, p. 145 002, Apr. 3, 2012, Publisher: American Physical Society. DOI: 10.1103/PhysRevLett.108.145002.

[127] S. N. Bland, S. C. Bott, G. N. Hall, *et al.*, "Diagnostics for studying the dynamics of wire array z pinches," *Review of Scientific Instruments*, vol. 77, no. 10, 10F326, Oct. 2006, Publisher: American Institute of Physics, ISSN: 0034-6748. DOI: 10.1063/1.2336470.

[128] G. F. Swadling, S. V. Lebedev, G. N. Hall, *et al.*, "Diagnosing collisions of magnetized, high energy density plasma flows using a combination of collective thomson scattering, faraday rotation, and interferometry (invited)," *The Review of Scientific Instruments*, vol. 85, no. 11, 11E502, Nov. 2014, ISSN: 1089-7623. DOI: 10.1063/1.4890564.

[129] S. N. Bland, D. J. Ampleford, S. C. Bott, *et al.*, "Use of faraday probing to estimate current distribution in wire array z pinches," *Review of Scientific Instruments*, vol. 77, no. 10, 10E315, Oct. 2006, Publisher: American Institute of Physics, ISSN: 0034-6748. DOI: 10.1063/1.2227443.

[130] C. J. Price, T. D. Donnelly, S. Giltrap, *et al.*, "An in-vacuo optical levitation trap for high-intensity laser interaction experiments with isolated microtargets," *Review of Scientific Instruments*, vol. 86, no. 3, p. 033 502, Mar. 1, 2015, Publisher: American Institute of Physics, ISSN: 0034-6748. DOI: 10.1063/1.4908285.

[131] R. Benattar, C. Popovics, and R. Sigel, "Polarized light interferometer for laser fusion studies," *Review of Scientific Instruments*, vol. 50, no. 12, pp. 1583–1586, Dec. 1979, ISSN: 0034-6748, 1089-7623. DOI: 10.1063/1.1135764.

[132] Y. Sentoku, V. Bychenkov, K. Flippo, *et al.*, "High-energy ion generation in interaction. of short laser pulse with high-density plasma," *Applied Physics B*, vol. 74, no. 3, pp. 207–215, Mar. 1, 2002, ISSN: 1432-0649. DOI: 10.1007/s003400200796.

[133] P. McKenna, D. C. Carroll, O. Lundh, *et al.*, "Effects of front surface plasma expansion on proton acceleration in ultraintense laser irradiation of foil targets," *Laser and Particle Beams*, vol. 26, no. 4, pp. 591–596, Dec. 2008, Publisher: Cambridge University Press, ISSN: 1469-803X, 0263-0346. DOI: 10.1017/S0263034608000657.

[134] D. Wang, Y. Shou, P. Wang, *et al.*, "Enhanced proton acceleration from an ultrathin target irradiated by laser pulses with plateau ASE," *Scientific Reports*, vol. 8, no. 1, p. 2536, Feb. 7, 2018, Number: 1 Publisher: Nature Publishing Group, ISSN: 2045-2322. DOI: 10.1038/s41598-018-20948-3.

[135] P. Martin, H. Ahmed, D. Doria, *et al.*, "Absolute calibration of fujifilm BAS-TR image plate response to laser driven protons up to 40 MeV," *Review of Scientific Instruments*, vol. 93, no. 5, p. 053 303, May 2022, Publisher: American Institute of Physics, ISSN: 0034-6748. DOI: 10.1063/5.0089402.

[136] "GAFCHROMIC ® EBT 2 SELF-DEVELOPING FILM FOR RADIOTHERAPY DOSIMETRY," 2009.

[137] M. Kaluza, J. Schreiber, M. I. K. Santala, *et al.*, "Influence of the laser prepulse on proton acceleration in thin-foil experiments," *Physical Review Letters*, vol. 93, no. 4, p. 045 003, Jul. 20, 2004, Publisher: American Physical Society. DOI: 10.1103/PhysRevLett.93.045003.

[138] T. S. Robinson, S. Patankar, E. Floyd, N. H. Stuart, N. Hopps, and R. A. Smith, "Spectral characterization of a supercontinuum source based on nonlinear broadening in an aqueous k_2ZnCl_4 salt solution," *Applied Optics*, vol. 56, no. 35, pp. 9837–9845, Dec. 10, 2017, Publisher: Optical Society of America, ISSN: 2155-3165. DOI: 10.1364/AO.56.009837.

[139] K. Tanaka, W. Seka, L. M. Goldman, *et al.*, "Evidence of parametric instabilities in second harmonic spectra from 1054 nm laser-produced plasmas," *The Physics of Fluids*, vol. 27, no. 8, pp. 2187–2190, Aug. 1984, Publisher: American Institute of Physics, ISSN: 0031-9171. DOI: 10.1063/1.864845.

[140] S. Patankar, E. T. Gumbrell, T. S. Robinson, *et al.*, "Multiwavelength interferometry system for the orion laser facility," *Applied Optics*, vol. 54, no. 36, pp. 10 592–10 598, Dec. 20, 2015, ISSN: 1539-4522. DOI: 10.1364/AO.54.010592.

[141] K. Zeil, C. Bernert, S. Kraft, *et al.*, "Off-harmonic optical probing of high-intensity laser interaction with hydrogen targets using a stand-alone probe laser system (conference presentation)," in *Laser Acceleration of Electrons, Protons, and Ions V*, vol. 11037, SPIE, May 14, 2019, p. 1 103 704. DOI: 10.1117/12.2520884.

[142] C. Bernert, S. Assenbaum, F.-E. Brack, *et al.*, "Off-harmonic optical probing of high intensity laser plasma expansion dynamics in solid density hydrogen jets," *Scientific Reports*, vol. 12, no. 1, p. 7287, May 4, 2022, Number: 1 Publisher: Nature Publishing Group, ISSN: 2045-2322. DOI: 10.1038/s41598-022-10797-6.

[143] O. Willi, P. Rumsby, and S. Sartang, "Optical probe observations of nonuniformities in laser-produced plasmas," *IEEE Journal of Quantum Electronics*, vol. 17, no. 9, pp. 1909–1917, Sep. 1981, Conference Name: IEEE Journal of Quantum Electronics, ISSN: 1558-1713. DOI: 10.1109/JQE.1981.1071350.

[144] M. P. Kamath, A. P. Kulkarni, S. Jain, *et al.*, "Development of raman-shifted probe laser beam for plasma diagnosis using polaro-interferometer," *Pramana*, vol. 75, no. 5, pp. 883–888, Nov. 1, 2010, ISSN: 0973-7111. DOI: 10.1007/s12043-010-0170-0.

[145] C. N. Danson, M. White, J. R. M. Barr, *et al.*, "A history of high-power laser research and development in the united kingdom," *High Power Laser Science and Engineering*, vol. 9, e18, 2021, ISSN: 2095-4719, 2052-3289. DOI: 10.1017/hpl.2021.5.

[146] J. Wood, S. Mangles, and Z. Najmudin, "Simulated optimisation of a 10 mJ class, mid-IR driven laser wakefield accelerator demonstrating a high charge, MeV electron source created via extreme laser redshifting," CENTRAL LASER FACILITY Annual Report 2017 - 2018, 2017, Type: dataset. DOI: 10.14469/HPC/2232.

[147] T. Jimbo, V. L. Caplan, Q. X. Li, Q. Z. Wang, P. P. Ho, and R. R. Alfano, "Enhancement of ultrafast supercontinuum generation in water by the addition of zn^{2+} and k^{+} cations," *Optics Letters*, vol. 12, no. 7, pp. 477–479, Jul. 1, 1987, Publisher: Optica Publishing Group, ISSN: 1539-4794. DOI: 10.1364/OL.12.000477.

[148] R. R. Alfano, Ed., *The Supercontinuum Laser Source*, New York: Springer-Verlag, 2006, ISBN: 978-0-387-24504-1. DOI: 10.1007/b106776.

[149] F. Silva, D. Austin, A. Thai, *et al.*, "Multi-octave supercontinuum generation from mid-infrared filamentation in a bulk crystal," *Nature Communications*, vol. 3, p. 807, May 1, 2012, ISSN: 2041-1723. DOI: 10.1038/ncomms1816.

[150] M. Nisoli, S. D. Silvestri, O. Svelto, *et al.*, "Compression of high-energy laser pulses below 5 fs," *Optics Letters*, vol. 22, no. 8, pp. 522–524, Apr. 15, 1997, Publisher: Optica Publishing Group, ISSN: 1539-4794. DOI: 10.1364/OL.22.000522.

[151] G. Cirmi, R. E. Mainz, M. A. Silva-Toledo, *et al.*, "Optical waveform synthesis and its applications," *Laser & Photonics Reviews*, vol. 2200588, p. 40, n/a 2023, _eprint: https://onlinelibrary.wiley.com/doi/pdf/10.1002/lpor.202200588, ISSN: 1863-8899. DOI: 10.1002/lpor.202200588.

[152] M. Chemnitz, M. Gebhardt, C. Gaida, *et al.*, "Hybrid soliton dynamics in liquid-core fibres," *Nature Communications*, vol. 8, no. 1, p. 42, Jun. 29, 2017, ISSN: 2041-1723. DOI: 10.1038/s41467-017-00033-5.

[153] F. M. Mitschke and L. F. Mollenauer, "Discovery of the soliton self-frequency shift," *Optics Letters*, vol. 11, no. 10, pp. 659–661, Oct. 1, 1986, Publisher: Optica Publishing Group, ISSN: 1539-4794. DOI: 10.1364/OL.11.000659.

[154] W. J. Tomlinson, R. H. Stolen, and A. M. Johnson, "Optical wave breaking of pulses in nonlinear optical fibers," *Optics Letters*, vol. 10, no. 9, pp. 457–459, Sep. 1, 1985, Publisher: Optica Publishing Group, ISSN: 1539-4794. DOI: 10.1364/OL.10.000457.

[155] P. P. Ho, Q. X. Li, T. Jimbo, Y. L. Ku, and R. R. Alfano, "Supercontinuum pulse generation and propagation in a liquid carbontetrachloride," *Applied Optics*, vol. 26, no. 14, pp. 2700–2702, Jul. 15, 1987, Publisher: Optica Publishing Group, ISSN: 2155-3165. DOI: 10.1364/AO.26.002700.

[156] M. Centurion, Y. Pu, M. Tsang, and D. Psaltis, "Dynamics of filament formation in a kerr medium," *Physical Review A*, vol. 71, no. 6, p. 063 811, Jun. 17, 2005, ISSN: 1050-2947, 1094-1622. DOI: 10.1103/PhysRevA.71.063811.

[157] G. Point, Y. Brelet, A. Houard, *et al.*, "Superfilamentation in air," *Physical Review Letters*, vol. 112, no. 22, p. 223 902, Jun. 4, 2014, Publisher: American Physical Society. DOI: 10.1103/PhysRevLett.112.223902.

[158] F. V. Potemkin, E. I. Mareev, A. A. Podshivalov, and V. M. Gordienko, "Highly extended high density filaments in tight focusing geometry in water: From femtoseconds to microseconds," *New Journal of Physics*, vol. 17, no. 5, p. 053 010, May 2015, Publisher: IOP Publishing, ISSN: 1367-2630. DOI: 10.1088/1367-2630/17/5/053010.

[159] D. Hammer, R. Thomas, G. Noojin, B. Rockwell, P. Kennedy, and W. Roach, "Experimental investigation of ultrashort pulse laser-induced breakdown thresholds in aqueous media," *IEEE Journal of Quantum Electronics*, vol. 32, no. 4, pp. 670–678, Apr. 1996, Conference Name: IEEE Journal of Quantum Electronics, ISSN: 1558-1713. DOI: 10.1109/3.488842.

[160] G. M. Hale and M. R. Querry, "Optical constants of water in the 200-nm to 200- µm wavelength region," *Applied Optics*, vol. 12, no. 3, pp. 555–563, Mar. 1, 1973, Publisher: Optica Publishing Group, ISSN: 2155-3165. DOI: 10.1364/AO.12.000555.

[161] M. Börner, J. Fils, A. Frank, *et al.*, "Development of a nomarski-type multi-frame interferometer as a time and space resolving diagnostics for the free electron density of

laser-generated plasma," *Review of Scientific Instruments*, vol. 83, no. 4, p. 043 501, Apr. 2012, Publisher: American Institute of Physics, ISSN: 0034-6748. DOI: 10.1063/1.3701366.

[162] T. Lan, S. Zhang, W. Ding, *et al.*, "Long-time measurements of line-integrated plasma electron density using a two-color homodyne optical fiber interferometer," *Review of Scientific Instruments*, vol. 92, no. 9, p. 093 506, Sep. 2021, Publisher: American Institute of Physics, ISSN: 0034-6748. DOI: 10.1063/5.0055570.

[163] K. Y. Kim, "Diagnostic of laser-plasmas: Single-shot supercontinuum spectral interferometry," in *AIP Conference Proceedings*, ISSN: 0094243X, vol. 737, Stony Brook, New York (USA): AIP, 2004, pp. 407–413. DOI: 10.1063/1.1842571.

[164] D. Patel, D. Jang, S. W. Hancock, H. M. Milchberg, and K.-Y. Kim, "Simplified single-shot supercontinuum spectral interferometry," *Optics Express*, vol. 28, no. 8, pp. 11 023–11 032, Apr. 13, 2020, Publisher: Optica Publishing Group, ISSN: 1094-4087. DOI: 10.1364/OE.386631.